ABSTRACT

Title of Dissertation:	FUNCTIONAL PARTICLE GENERATION BY AEROSOL-ASSISTED PROCESSES
	Yujia Liang, Doctor of Philosophy, 2018
Dissertation directed by:	Sheryl H. Ehrman Department of Chemical and Biomolecular Engineering

Aerosol-assisted processes are continuous with short residence times, simple operating procedures, and facile equipment requirements. They are scalable and promising for fabrication of functional particles as conductive pastes in solar cell metallization and interference packaging, electrode materials in energy storage devices, and photocatalysts in energy conversion. Although aerosol-assisted processes have long been used in manufacturing and their fundamentals have been intensively explored, further investigation is still required to better understand the particle formation mechanisms of different aerosol-assisted processes. In this dissertation, three different aerosol-assisted processes are investigated, spray pyrolysis, colloidal spray pyrolysis (CSP), and spray drying. These processes can be conducted under mild reaction conditions with simple operation procedures. The product particles are controllable. The effects of process variables on the product particles are studied. Furthermore, the prospects of applying these three aerosol-assisted processes in

generating functional particles in applications, including solar cell metallization, battery, and photocatalysis are assessed.

Part 1) includes Chapters 3-5. I first present Cu-Sn binary particle generation by spray pyrolysis. Through studying the particle oxidation behaviors under different reaction conditions, the Cu-Sn binary particles exhibit high oxidation-resistance. The one-dimensional and two-dimensional structures fabricated by direct printing inks containing Cu-Sn powders display low resistivity. They all suggest that Cu-Sn binary particles produced by spray pyrolysis are promising materials in the inks in printed electronics and in the conductive pastes in solar cell metallization and interference packaging.

In Part 2), Chapters 6, a novel aerosol-assisted process, CSP, is developed. This process addresses one restriction of conventional spray pyrolysis which can only be used to fabricate particles from precursor solutions containing high-solubility salts. By applying CSP, tin@carbon (Sn@C) composite particles are produced with controllable interior structures. These composite particles exhibit high-performance as the anode materials for Li-ion and Na-ion batteries.

In Part 3), Chapter 7, spray drying is utilized to fabricate photocatalysts from precursor solutions containing SnO_2 colloids and edge-oxidized graphene oxide (eo-GO) sheets. The particle morphology, element distribution, and band structures were investigated by various tools. The photocatalytic activity of the composite particles is five times that of commercialized TiO_2 (P25) in reducing CO_2 into CH_4.

FUNCTIONAL PARTICLE GENERATION BY AEROSOL-ASSISTED PROCESSES

by

Yujia Liang

Dissertation submitted to the Faculty of the Graduate School of the
University of Maryland, College Park, in partial fulfillment
of the requirements for the degree of
Doctor of Philosophy
2018

Advisory Committee:
Professor Sheryl Ehrman, Chair
Dr. Howard Glicksman
Professor Chunsheng Wang
Professor Dongxia Liu
Professor Bao Yang

Dedicated to Qingnian Liang, Weiyi Zhang, and Sixing Lu

To my 20s.

Acknowledgement

I sincerely want to thank my advisor, Dr. Sheryl Ehrman, for her guidance during the years. Her support assisted me to accomplish this dissertation. She is a model for me to learn as a scholar, advisor, and leader. I would like to thank Dr. Howard Glicksman for his suggestions and advice during my research. I want to express my gratitude to National Science Foundation (CBET-1336581) and DuPont Company for their financial support of this project. I also want to thank Dr. Chunsheng Wang and Dr. Dongxia Liu for their assistance on our collaborated projects and serving on my committee. I am also grateful to Dr. Bao Yang for serving on my committee and providing me with valuable suggestions. I want to thank Dr. Sz-Chian Liou for training me to be an expert in TEM, Dr. Peter Zavalij for instructing me to acquire the knowledge of Rietveld refinement, and Dr. Karen Gaskell for XPS data analysis.

I want to thank lab mates, Dr. Kai Zhong, Dr. Alex Langrock, Dr. Tim Vinciguerra, and Trang Nguyen. I would also like to thank my collaborators, Chao Luo, Fudong Han, Fei Wang, Yangang Liang, Huajun Tian, Yong Yang, Sucheun Oh, Ji Chen, Wei Wu, Peng Wang, Huilong Hou, and all other people who have ever helped me during my research.

At last, I want to send my special acknowledgment to my parents in China, Qingnian Liang and Weiyi Zhang. It is always your love that helps and supports me to go through ups and downs in my life. For my wife, Dr. Sixing Lu, I owe you a lot during the years for your endless patience and encouragement. The spatial distance (between College Park, MD and Tucson, AZ) strengthened our love and forced us concentrate on our research. We both become PhDs in less than 5 years.

Table of Contents

List of Tables

List of Figures

Chapter 1: Introduction and overview

This dissertation is focused on developing aerosol-assisted processes to generate functional particles used in conductive pastes in solar cell metallization and interference packaging, anode and cathode materials for energy storage devices, and photocatalysts for energy conversion. In this chapter, motivations, strategies, and significant results of this work are outlined.

1.1 Motivations

Aerosol-assisted approaches have long been recognized as promising for mass production of functional particles at an industrial-scale, because they are continuous one-step processes with facile equipment requirements and minimal waste production (Glicksman et al. 1996; Gurav et al. 1993; Nandiyanto and Okuyama 2011; Song et al. 2004; Zhong et al. 2013a). Therefore, aerosol-assisted methods have been intensively investigated to produce materials that can be used in inks in printed electronics and in the conductive pastes used in solar cell metallization and interference packaging (Comiskey et al. 1998; Faddoul et al. 2012; Glicksman et al. 1997; Glicksman et al. 1995; Hsien-Hsueh et al. 2005; Kim et al. 2004; Leenen et al. 2009; Li et al. 2005; Ma et al. 2014; Matienzo et al. 2008; Perelaer et al. 2010; Songping and Shuyuan 2006; Wang et al. 2007a; Wu et al. 2016; Yiwei et al. 2007; Zhong et al. 2012), anode and cathode materials in energy storage (Luo et al. 2017; Strobel and Pratsinis 2007; Xu et al. 2013a; Zhu et al. 2017), and photocatalysts (Nie et al. 2016; Strobel et al. 2006; Wang et al. 2011). However, several obstacles still exist and restrict the further application of aerosol-assisted methods in these fields. Although the formation mechanisms of various aerosol processes have been researched (Gurav et al. 1993; Nandiyanto and Okuyama 2011), the particle structure and

composition are difficult to design in advance (Shen et al. 2014b). Other issues are also remained to be addressed to promote the applications of aerosol-assisted methods in these applications. I will discuss these issues in this section.

Spray pyrolysis has long been proven as an effective approach to fabricate particles used in the conductive pastes in solar cell metallization and interference packaging. The most common material used in these applications is silver (Ag). Ag powders can be facilely prepared by spray pyrolysis (Glicksman and Yang 2004; Kodas et al. 1995; Pingali et al. 2005; Pluym et al. 1993). However, in 2016, 562 million ounces of silver were used globally for industrial applications including electronics, photovoltaic metallization, and solders (O'Connell et al. 2017). Considering the high price of silver (18 USD/oz, (Bloomberg 2017)), replacing it with inexpensive materials, such as Cu (0.18 USD/oz, (Bloomberg 2017)) can greatly reduce manufacturing costs. To facilitate the scale up in industry, Cu particles have been successfully prepared by a continuous process by using a high flash-point co-solvent (ethylene glycol, EG) without direct addition of H_2 gas (Zhong et al. 2012). Nevertheless, several challenges, such as the ease of oxidation of copper materials and the high mobility of copper in silicon (a common substrate in the electronics industry), have to be addressed before further application of copper-based powders (Istratov et al. 2000; Kim et al. 2004).

For the applications of aerosol-assisted approaches in producing anode and cathode materials in energy storage, spray pyrolysis (Luo et al. 2017; Xu et al. 2013a; Zhu et al. 2017) and spray drying (Jung et al. 2013; Ma et al. 2015) have been successfully utilized. However, one prerequisite of aerosol-assisted methods to achieve uniform particle-to-particle composition and structure is a stable precursor solution, restricting their usage to

highly soluble salts for spray pyrolysis and reactions in single phase for spray drying. Unfortunately, for some promising anode materials, such as Sn (theoretical specific capacity: 993 $mAhg^{-1}$ for Li-ion batteries (LIBs)) (Huang et al. 2015; Winter and Besenhard 1999), it is difficult to obtain stable and uniform aqueous solution containing tin salts, because tin salts are easily hydrolyzed in aqueous solutions (Perry 2011).

For high-performance photocatalysts, titania (TiO_2) has been intensively studied as the catalyst for the artificial photosynthesis since the pioneering work of Inoue *et al*. (Inoue et al. 1979). However, it exhibits low catalytic efficiency that can be ascribed to three factors: 1) the low CO_2 adsorption on the surface, 2) rapid recombination of the photo-generated electrons and holes, and 3) catalyst deactivation due to adsorption of less reactive intermediates (Chang et al. 2016; Habisreutinger et al. 2013). On the other hand, the innovation of catalyst normally requires investment on the equipment. The fabrication processes are complex. For the photocatalyst fabrication, as the widespread approach, hydrothermal process endures the long processing time, safety concerns raised by the accumulation pressure in the reactor, and sophisticated post-production treatment (Hsieh et al. 2014; Ide et al. 2016; Sun et al. 2015). Alternative approaches have also been developed, including molecular beam epitaxy (MBE), sol-gel, and ion-exchange (AlOtaibi et al. 2015; Li et al. 2015a; Tahir and Amin 2015). Nevertheless, MBE requires significant equipment investment. Sol-gel and ion-exchange approaches have sophisticated operating procedures and long processing time.

1.2 Research strategies and objectives

To address the aforementioned issues in Section 1.1, three aerosol-assisted processes will be developed to fabricate functional particles as conductive pastes in solar cell metallization and interference packaging, anode and cathode materials in energy storage devices, and photocatalysts in CO_2 reduction. I will concentrate on process development, study of underlying mechanisms, and materials characterizations.

In Chapter 2, I review approaches to develop oxidation-resistant Cu powders as alternative materials to Ag in applications including printed electronics. Then an overall description of the methods to fabricate anode materials is given. In the end, the reported strategies of preparing photocatalysts are provided. This chapter introduces the specific motivations of developing three different aerosol-assisted processes.

In Chapter 3, a method will be presented to generate micron-sized Cu-Sn binary particles via spray pyrolysis. Copper nitrate and tin chloride are selected as the metal sources. Water and EG are used as solvent and co-solvent, respectively. The effects of experimental conditions (reaction temperature, EG concentration, residence time, and quench gas flow rate) on the final particle properties (morphologies, crystallinity, and metal distribution within the particles) are investigated.

As a next step, in Chapter 4, we will present a detailed investigation of the oxidation behavior of $CuSn_y$ (y is the atomic ratio of Sn/Cu in the product) solid particles fabricated by spray pyrolysis. A quantitative understanding of the phase evolution of $CuSn_y$ particles during oxidation is obtained through Rietveld refinement analysis of the X-ray diffraction (XRD) patterns. To better understand the oxidation behavior of $CuSn_y$ particles under high temperature, *in-situ* XRD measurements are conducted in ambient air. Kinetics

experiments are performed to determine the oxidation kinetics of $CuSn_y$ particles and the oxidation mechanisms at different temperatures. Together, these results are used to identify the $CuSn_y$ particle composition that has optimal oxidation resistance and spherical morphology

In Chapter 5, I will assess the prospect of applying Cu-Sn powders in the inks of printed electronics by *in-situ* measurement of the resistivities of one-dimensional and two-dimensional $CuSn_y$ structures. These structures are fabricated by direct printing inks containing $CuSn_y$ powders. The resistivity measurements are conducted under various conditions including continuously changing the measurement temperature from 2 K to 400 K in oxygen-free environment and heating $CuSn_y$ patterns at 573 K in ambient air for 90 min, enabling a systematic study of the effects of temperature and oxidation on the resistivities of $CuSn_y$ structures.

In Chapter 6, I will present colloidal spray pyrolysis (CSP), a process that can generate functional particles with uniform particle-to-particle composition and structure from stable multiphase precursor solutions, which could be a promising strategy to prepare uniform electrode materials in LIBs and sodium-ion batteries (SIBs). The structure and composition of particles are pre-designable based on our models. Several distinguishable advantages of CSP make it unique when compared to conventional aerosol processes. Unlike spray pyrolysis, CSP can process low solubility salts, expanding the application of spray pyrolysis to a wider range of functional materials. CSP uses an aqueous precursor solution, with no direct addition of H_2 gas or pure organic solvents, which makes CSP safer and simpler for scale-up manufacturing. CSP is also different from multi-step spray drying, where colloids are used as templates to be etched away in the end (Boissiere et al. 2011;

Jung et al. 2013). CSP is a one-step process with a short residence time where colloids are involved in *in-situ* solid-state reactions and structural evolution.

A novel photocatalyst engineering process will be developed in Chapter 7 to produce efficient nanocomposites as catalysts for artificial photosynthesis. Spray drying, a continuous and scalable process, is applied here to fabricate nanocomposites, comprising of eo-GO sheets and nano-sized SnO_2 colloids. The obtained powders are termed TinGOx, where *x* is the mass ratio of SnO_2 to eo-GO in the precursor. The eo-GO sheets have large intact sp^2 carbon network to deliver large surface area, excellent electron transfer ability, sufficient active sites of negatively charged O atoms, and narrow band gap. The utilization of nano-sized SnO_2 can efficiently trap the photogenerated electron and create a defect state to narrow its wide bandgap. State-of-art techniques are utilized to reveal the configuration of nanocomposites, including EELS in low-loss and core-level regions. A detailed investigation on the photoreduction of CO_2 is conducted to understand the photocatalytic activity, optimal SnO_2/eo-GO mass ratio, and reaction mechanism. The best TinGOx photocatalyst exhibits superior performance in photoreducing CO_2 into CH_4 with high yield and selectivity compared to bare eo-GO, SnO_2, and the commercial TiO_2 (P25).

Based on the results and discussions in the previous chapters, conclusions are given for the process developments of aerosol-assisted approaches to fabricate functional particles in Chapter 8. Cu-Sn binary particles have been successfully produced by spray pyrolysis as conductive pastes in solar cell metallization and interference packaging. CSP has been utilized in generating Sn@C particles as anode materials. TinGOx photocatalysts have been fabricated by spray drying. Future work is also provided in this chapter to discuss possible projects that can be conducted based on the results presented in this dissertation.

Chapter 2: Background information

In this chapter, a review will be presented on reported strategies to address issues in 1) developing alternatives to Ag particles in applications such as printed electronics, 2) generating high-performance anode materials, and 3) photocatalyst fabrication.

2.1 Developing alternatives to Ag particles in applications of printed electronics, interference packaging, and solar cell metallization

Metal particles have been widely applied in printed electronics (Comiskey et al. 1998; Li et al. 2005), interference packaging (Faddoul et al. 2012; Wang et al. 2007a), and solar cell metallization (Mokkapati et al. 2009; Temple and Bagnall 2011). Gold and silver are by far the most commonly used materials in these fields due to their high electrical conductivity and oxidation resistance (Comiskey et al. 1998; Faddoul et al. 2012; Li et al. 2005; Mokkapati et al. 2009; R et al. 2015; Temple and Bagnall 2011; Wang et al. 2007a). However, the high cost of these noble metals has increased interest in developing alternative cost-efficient materials such as copper (Cu) (Huang and Sheen 1997; Songping and Shuyuan 2006; Yonezawa et al. 2015a; Yonezawa et al. 2015b; Zhong et al. 2012) for these applications. However, copper particles are easily oxidized even at room temperature, which could increase the resistivity (Kim et al. 2004).

Particle engineering with an oxidation-resistant layer on a Cu core has been proposed as an effective configuration. The oxidation preventing layer can be secondary metals, for example, Au (Xu et al. 2012), Ag (Hai et al. 2013; Jung et al. 2011; Li et al. 2016a), Ni (Sharma et al. 2014), and Al (Noor et al. 2015). To synthesize Cu-Au nanoparticles, $HAuCl_4$ and $Cu(acac)_2$ were reduced in 1,2-hexadecanediol and oleylamine (Xu et al.

2012). The solution was then heated at 160 ^{o}C for 2 h. The Cu-Au nanoparticles were collected after washing the precipitates with ethanol and centrifugation. Hai et al. reported a technique to coat the Cu powder with an Ag layer (Hai et al. 2013). 5-μm-sized Cu particles were dispersed in distilled water under vigorous agitation. The surface oxide layers of Cu particles were removed by adding a solution comprising of ammonium hydroxide (NH_4OH) and ammonium sulfate ($(NH_4)_2SO_4$) into the powders. Then potassium tartrate ($C_4H_4O_6K_2$) was added to the solution. In the end, an aqueous solution containing $AgNO_3$ and NH_4OH was added dropwise to obtain the product. The particles were collected by centrifugation. All the procedures were completed in a closed system bubbled with Ar gas. Jung et al. used spray pyrolysis to fabricated Ag-coated Cu powders (Jung et al. 2011). An aqueous precursor solution containing $AgNO_3$ and $Cu(NO_3)_2$ was atomized and carried into a reactor by H_2 (5 vol.%) and Ar mixture gas. The reaction temperature was 900 ^{o}C and the residence time was 2.1 s in generating the Cu-Ag particles. Sharma et al. fabricated Cu-Ni nanopowders by flame-driven aerosol method (Sharma et al. 2014). Precursors containing copper nitrate and nickel nitrate were delivered into the throat of the nozzle. The high-velocity hot gas stream atomizes the precursor solution and assists the formation of Cu-Ni nanopowders. Cu-Al particles were synthesized by an improved electric explosion of wire (EEW) method (Noor et al. 2015). Al and Cu were twisted in wires and placed in the production chamber, which was filled with Ar gas. A high voltage power unit applied a high current in the order of 10^5 A/mm^2 to the wires. The mixtures of superheated vapor and boiling droplets of the exploding wires were cooled down in Ar gas. Based on the above discussion, spray pyrolysis has its unique advantages in fabricating metal powders with simple operating procedures, short processing time, and

minimal waster production. Unfortunately, adding the reported secondary metals will increase the cost of the Cu particle manufacturing because of their high materials costs (Bloomberg 2017).

Organic compounds have also been proposed as the passivation layers to protect Cu from being oxidized (Jianfeng et al. 2011; Yonezawa et al. 2015a). Jianfeng et al. utilized a polyol method to synthesize Cu nanoparticles (Jianfeng et al. 2011). A mixture of polyvinylpyrrolidone (PVP), sodium hypophosphite, and EG was heated at 90 ^{o}C. A solution of copper nitrate in EG liquid was then added into the previous mixture. After the formation of PVP-coated Cu nanoparticles, they were centrifuged and washed several times. Yonezawa et al. mixed gelatin and CuO microparticles in hot water. An aqueous ammonia solution was introduced to adjust the pH to 11. After the formation of fine particles, the pH of the dispersion was reduced to 8.5 by adding saturated aqueous citric acid into the mixture. Then gelatin-coated Cu powders were collected by decantation. Before using these particles, the organic coating needs to be removed because the organic layer on the Cu particle surface could result in a significant increase of the resistivity. Therefore, there is a need to explore other strategies from a comprehensive view of cost and electrical conductivity.

Jeong et al. reported that by tuning the molecular weight of poly(N-vinylpyrrolidone), which is the capping molecules, the Cu nanoparticles fabricated from polyol method can have minimal surface oxidation (Jeong et al. 2008). The surface oxidized layer can prevent the further oxidation of Cu particle (Jeong et al. 2008). Although this particle configuration has been proven can fabricate low-resistivity patterns, the sophisticated particle generation process (polyol method) requires other particle fabrication process. Based on this work, I

propose that utilizing a reactive metal to form the sacrificial oxide layer can effectively increase the oxidation resistance of the particles. One obstacle in this strategy is to find a reactive metal, whose oxide has relatively high conductivity.

Based on these ideas, I developed a spray pyrolysis process to fabricate Cu-Sn powders with inexpensive raw materials, one-step operating, and enhanced oxidation-resistance. Details will be presented in Chapters 3-5.

2.2 Approaches to fabricate high-performance anode materials

As discussed by Goriparti et al., alloys and metals (such as Sn, Ge, and Sb) are promising anode materials in LIBs with high capacity density (Goriparti et al. 2014). Nevertheless, the salts of these metals can easily hydrolyze in aqueous solutions (Table 2.1). The hydrolysis of these salts increases the instability of the precursor solutions, resulting in the early precipitation in the precursor solutions. This could lead to the uncontrollable particle-to-particle composition and structure.

Table 2.1. Salt solubilities of corresponding metals as high-performance battery materials listed in (Goriparti et al. 2014)

Metal salts	**Solubility**
$Si(OC_2H_5)_4$ (TEOS)	Reacts with H_2O
$GeCl_4$	Hydrolysis H_2O
$AlCl_3$	Dissolve in H_2O evolving HCl
$SnCl_4$	Hydrolysis H_2O
$SbCl_2$	9881. g/ 100 g H_2O

*The solubility data are summarized from (Perry 2011).

Reactions between phases are more difficult and require significantly longer processing time than those within single phases because of interphase mass transport resistance. It will be significantly more difficult for a continuous and scalable process to produce materials from multiphase reaction system than single phase reaction system.

Several techniques have been reported to produce the high-capacity materials. Here, I use Sn as an example, since these fabrication techniques can also be used to produce other metals. The hydrothermal approach has been reported to synthesize Sn/C composite particles (Youn et al. 2016). $SnCl_4$ and citric acid monohydrate were mixed and dissolved in water and stirred for 3 h. Then the mixture was heated at 300 ^oC in a muffle furnace for 1.5 h, following by calcining the precipitates under flowing Ar at 650 ^oC for 3h.

Wet chemistry method has also been applied to produce Sn-based materials for batteries (Derrien et al. 2007; Eom et al. 2015; Zhu et al. 2014a). $SnCl_4$ and trisodium citrate dehydrate were dissolved in EG, then $NaBH_4$ was added into the solution to reduce $SnCl_4$ (Eom et al. 2015). Methanol and deionized water were used to wash the products. After the product was washed and centrifuged for 5 times, it was collected and dried at 120 ^oC for 24 h under vacuum. Nano-Sn powders were then formed. In another method, $SnCl_2$ and salenH_2 ligand were dissolved into ethanol (Zhu et al. 2014a). Triethylamine was added to the solution, then the mixture was stirred at 85 ^oC for 24 h. The product was washed and filtered by ethanol and then sintered at 650 ^oC for 2 h in Ar. Derrien et al. mixed resorcinol, sodium carbonate, and formaldehyde in water for 2 h at 70 ^oC (Derrien et al. 2007). The product was washed with water and then immersed in tertiobutanol and filtered for several times. Then it was stirred in tributylphenyltin (TBPT) and tertiobutanol overnight. In the

end, the mixture was placed in Ar flux at 700 ^{o}C for 2 h to form the nanostructured Sn-C composite.

Alternative approaches have also been proposed to fabricate Sn-based materials. For example, a solution containing citric acid, $SnCl_2$, NaCl, and H_2O was stored at -20 °C for 24 h (Qin et al. 2014). Then freeze-drying technology was used to remove the H_2O. The dry gel was then ground to powders and annealed at 750 ^{o}C for 2 h under H_2. After washing the sample several times with water, 3D Sn@G-PGNWs were obtained. Tao et al added $SnCl_4 \cdot 5H_2O$ and s. platensis in absolute ethanol to form precursor solution (Tao et al. 2014). Then, the solution was filtered and sintered at 80 ^{o}C. The powders were later mixed with a solution prepared by dissolving polystyrene (PS) in dimethylformamide. After calcining the sample at 600 °C in N_2 for 3 h, anode materials were prepared.

Based on the above discussion, it can be seen the reported methods have sophisticated experimental procedures and long operating time. Therefore, spray pyrolysis has been utilized to facilitate the potential scale-up production (Hong and Kang 2015; Xu et al. 2013a; Zhang et al. 2014a). Xu et al. dissolved $SnCl_2$ and PVP into ethanol (Xu et al. 2013a). The precursor solution was ultrasonically atomized into droplets and transported into furnaces by Ar-H_2 mixture gas flow. The reaction temperature is 900 ^{o}C. The process of spray pyrolysis reported by Zhang et al. is complicated (Zhang et al. 2014a). The resorcinol and formaldehyde were polymerized to form resorcinol formaldehyde. It was mixed with $SnCl_2$ in ethanol to form the precursor solution. The precursor solution was atomized and carried by Ar gas into the furnace with the set point of 800 ^{o}C. Hong et al. prepared the precursor solution by dissolving Sn (II) oxalate (C_2O_4Sn) and PVP (Kanto,

Mw: 40,000) into water (Hong and Kang 2015). The spray pyrolysis was conducted at 650 ^{o}C with N_2 as the carrier gas.

As we can find in the above discussions, the reduction of tin salts to tin is challenging. To ensure the single-phase reaction, pure organic solvents are commonly utilized to dissolve the tin salts. In addition, the operating procedures are complicated and time-consuming. Even though spray pyrolysis has been applied to fabricate Sn-based materials, pure organic solvents are still utilized. Moreover, H_2 gas is added directly into the reaction system to guarantee the complete reduction of tin salts to tin. All of these issues need to be addressed to promote the mass-production of Sn-based anode materials. In that case, a new process, CSP, will be discussed in Chapter 6, to continuously generate the Sn-based composite particles with mild reaction condition.

2.3 Methods to fabricate photocatalysts

Up to now, the hydrothermal approach has been the most commonly utilized to fabricate photocatalysts (Hsieh et al. 2014; Ide et al. 2016; Sun et al. 2015). Hsieh et al. firstly made a solution containing $TaCl_5$, iced H_2O, KOH, and methanol (Hsieh et al. 2014). Then this solution was mixed with $InCl_3$ and hydrothermally heated at 150 ^{o}C for 4 h. After the reaction, the products were washed and centrifuged several times and dried at 90 ^{o}C to obtain tantalum-based pyrochlore and indium hydroxide. Sun et al. prepared a solution containing $CdCl_2$, NH_2CSNH_2 and ethylenediamine (Sun et al. 2015). The solution was hydrothermally heated in a Teflon-lined, stainless-steel autoclave at 160 ^{o}C for 48 h. Then, the products were mixed with $Ni(NO_3)_2$, yellow phosphorus, and ethylenediamine to make a solution, which is hydrothermally heated in Teflon-lined, stainless-steel autoclave for the

second time at 140 ^{o}C for 12 h. The powders were dried in vacuum overnight at 60 ^{o}C to obtain Ni_2P/CdS nanorods. Ide et al. hydrothermally heated a solution containing TiO_2 (P25), tetrapropylammonium hydroxide (TPA), H_2O, and NH_4F in a Teflon-lined stainless-steel autoclave 170 ^{o}C for 7 days (Ide et al. 2016). The products were then washed and centrifuged several times to obtain the zeolite-TiO_2.

Alternative approaches have also been reported to fabricate Ti-based photocatalysts. Li et al rapidly heated the iced aqueous solution containing $TiCl_4$ to 100 ^{o}C within 5 min (Li et al. 2015b). Then the solution was dried in air for 24 h at 80 ^{o}C. The product was calcined in a muffle furnace at 400 ^{o}C for 2h to form the sub-10 nm rutile titanium dioxide nanoparticles. Tan et al. heated the solutions containing graphene oxide (GO), TiO_2, and H_2O at 80 ^{o}C for 2h (Tan et al. 2015). Then the product was dried in air overnight to form the oxygen-rich TiO_2/GO. Long et al. stirred the solution containing TiO_2 nanosheets, PVP, ascorbic acid (AA), and KBr in an oil bath at 80 ^{o}C for 10 min (Long et al. 2017). Then, K_2PdCl_4 and $CuCl_2$·were added into the previous solutions and heated in air at 80 ^{o}C for 3 h. Pd_xCu_1-TiO_2 hybrid was obtained after washing and centrifugation several times of the previous solids. Tahir et al. used the sol-gel method to fabricate In-doped TiO_2 (Tahir and Amin 2015). A solution containing $Ti(C_4H_9O)_4$, C_2H_5OH, CH_3COOH, isopropanol, and acetic acid was hydrolyzed at 30 ^{o}C for 24 h. Then indium nitrate was added to the previous solution and stirred for 12 h. After that, the powder was dried in an oven in air at 80 ^{o}C for 12 h. In the end, the product was calcined in a muffle furnace at 500 ^{o}C for 5h.

Other photocatalysts have also been fabricated by non-hydrothermal methods. Li et al. dried a mixture at 80 ^{o}C overnight (Li et al. 2016b). The mixture contained containing urea, $Ce(NO_3)_3$, SiO_2 particles, and water. The powders were calcined at 550 ^{o}C for 2h. Then,

the product was reacted with NH_4HF_2 to form CeO_2/g-C_3N_4. Shown et al. used the microwave approach to fabricate Cu/GO hybrid (Shown et al. 2014). Suspensions containing GO, $Cu(NO_3)_2$, and EG was microwaved for 180 s under 350 W. EG was removed by centrifugation. Then, the solids were dried under vacuum overnight to form the final product. In preparation of $BiVO_4/V_2O_5$, the purchased NH_4BEA zeolite was firstly calcined in air at 500 ^oC for 6 h (Murcia-López et al. 2017). Then the powders were dissolved into a solution containing $VOSO_4$ and water. After that, the solution was dried overnight at 80 ^oC and calcined at 500 ^oC for 6 h in dry air flow. The solids were dissolved into a solution containing $Bi(NO_3)_3$ and water. The solution was dried overnight at 80 ^oC, calcined at 500 ^oC for 6 h in dry air flow to form the final product. To fabricate $SrTiO_3$:La, Rh/Au/$BiVO_4$:Mo photocatalyst sheet, Wang et al. suspended $SrTiO_3$:La (La-doped $SrTiO_3$), $BiVO_4$:Mo (Mo-doped $BiVO_4$), and Rh in isopropanol and drop-cast on a glass substrate (Wang et al. 2016). After drying at room temperature, a thin gold layer was deposited by thermal vacuum evaporation at 400 ^oC with a rate of 20 nm/s under a base pressure of 2.6×10^{-3} Pa. The final product was obtained by heating the sample at 200 ^oC to 500 ^oC for 10 to 30 min. AlOtaibi et al. used the MBE method to grow Rh/Cr_2O_3 on GaN nanowires (AlOtaibi et al. 2015). The Si wafer was firstly cleaned by acetone, methanol, and HF. Then GaN nanowire was grown by MBE on Si substrate. Precursor solutions containing Na_3RhC_6, CH_3OH, K_2CrO_4, chloroplatinic acid, CH_3OH, and water were used to photodeposit Rh/Cr_2O_3 on GaN nanowires under irradiation of 300 W xenon lamp to obtained the desired product.

The hydrothermal method normally results in accumulation of pressure in the reactor, resulting in the potential safety concern. Other approaches exhibit complicated

experimental procedures, time-consuming process, and huge instrumental investment. Therefore, in Chapter 7, a spray drying process was developed to fabricate high-performance photocatalysts by one-step operating.

Chapter 3: Cu-Sn binary particle generation by spray pyrolysis

3.1 Abstract

Cu-Sn binary particles were generated via spray pyrolysis from metal salt precursors with ethylene glycol as the co-solvent and reducing agent. The morphology, crystallinity, and elemental distribution of particles were tunable by changing the reaction temperature, residence time, and quench gas flow rate. Hollow porous particles were fabricated with a higher Sn concentration on the particle surface when the furnace set point was 500 ^{o}C, while solid particles with a lower surface Sn concentration were generated when the furnace set point was 1000 ^{o}C. Particles with spherical morphologies were obtained at long residence time conditions (4.5 s). Cu-Sn binary particles with irregular structures (*e.g.*, pores on the particle surface, fragmented spherical particles, and lamellar fragments) were formed at short residence time conditions (0.92 s). A possible spray pyrolysis mechanism was proposed that incorporates chemical reaction steps and structural progression. By this mechanism, the metal salts are believed to sequentially undergo hydrolysis to metal hydroxides, decomposition to metal oxides, reduction to metals, and finally diffusion of Sn into the Cu matrix to generate the Cu-Sn solid solution.

3.2 Introduction

Metal particles have attracted a large amount of interest due to their wide application in the fields of electronics, catalysis, and plasmonics (Kim et al. 2002; Li et al. 2005; Talley et al. 2005). It is of great importance to develop scalable processes for the fabrication of metal particles with controllable morphologies, crystal phases, and composition. Plenty of methods have been reported to solve this problem, *e.g.*, seed-growth procedures (Cho et al.

2010; Xie et al. 2014), polyol processes (Fievet et al. 1993; Park et al. 2007), sonochemical treatments (Dhas et al. 1998; Fujimoto et al. 2001), and spray pyrolysis (Kim et al. 2006; Pluym et al. 1993; Xia et al. 2001a). Spray pyrolysis is advantageous because it is a continuous one-step process with facile equipment requirements and less waste production (Song et al. 2004; Zhong et al. 2013a). Spray pyrolysis consists of three steps: (i) atomization of a precursor into droplets; (ii) reaction and solvent evaporation in the isolated droplets surrounded by carrier gas; and iii) final product collection. As the precursor droplets have the same droplet-to-droplet composition, spray pyrolysis can be used to obtain relatively uniform powders containing single or multiple components (Lenggoro et al. 2000).

Various metals, *e.g.*, Ag (Pingali et al. 2005), Ni (Xia et al. 2000; 2001a), Co (Gürmen et al. 2006), and Cu (Kim et al. 2003; Zhong et al. 2012), have been synthesized by this technique. To produce the metals from metal salts, H_2 was first introduced with carrier gas to generate oxide-free metal powders (Gurav et al. 1993). However, addition of H_2 above the lower explosion limit was required (Kim et al. 2003; Zhong et al. 2012). To solve this problem, ammonium ion has been used as a reducing agent to obtain metal particles (Xia et al. 2000). Nevertheless, this method required the precise control of the molar ratio of ammonium to metal salt in the precursor and the removal of residual ammonium salts from the product (Xia et al. 2000; 2001a). Co-solvents, *e.g.*, formic acid and ethanol have also been successfully utilized to fabricate the metals (Kim et al. 2003; Xia et al. 2001b). However, the low flash points of formic acid (69 ^{o}C) and ethanol (13 ^{o}C) have led to exploration of alternative co-solvents (Yaws 1999). Recently, EG has attracted attention

for its higher flash point (111 ^{o}C) and reducing ability in metallic powder fabrication (Yaws 1999; Zhong et al. 2013a).

Copper particles, especially solid and spherical particles with narrow size distribution, have potential for applications in conductive pastes, integrated materials, and interference packaging (Huang and Sheen 1997; Youngil et al. 2008; Zhong et al. 2012). They are favored because of the relatively inexpensive raw materials, high solubility salts ($Cu(NO_3)_2 \cdot 3H_2O$: 145 g/100 g H_2O, 25 ^{o}C) (Lide 2007-2008), and low resistivity (nanocrystalline Cu, 1.8×10^{-7} Ω·m, 300 K) (Lu et al. 2004). However, some obstacles still need to be addressed before their further application: (i) copper particles will oxidize at room temperature once exposed to air, increasing the resistivity (Kim et al. 2004), and (ii) high copper mobility in silicon could reduce device efficiency (copper can diffuse through a standard 0.625 mm thick intrinsic silicon wafer in about 3 h at room temperature) (Istratov et al. 2000; Morinaga et al. 1996). The diffusivity of Cu in Si is 4×10^{-2} cm^2/s at 1073 K, and the diffusivity of Si in Cu is 3.7×10^{-2} cm^2/s at the same temperature (Degang et al. 1998). For reference, the thickness of a 4-inch Si wafer, widely used in the electronics industry, is only 0.525 mm (semiwafer.com). To remedy these challenges, $Cu_{core}Ag_{shell}$ particles were fabricated to prevent copper oxidation while maintaining high conductivity (Grouchko et al. 2009). However, there is still a need to explore other methods utilizing less expensive materials.

Tin was selected as the secondary material in copper-based materials because of its higher reaction activity towards oxidation than copper. It has been shown that the formation of sacrificial tin oxides can protect copper from being oxidized while maintaining relatively high conductivity in the case of Cu-Sn binary nanowires (Chen et al. 2014). Another benefit

of doping with tin is the low diffusivity of copper in tin. Tin and tin oxides have been reported as effective copper diffusion barrier materials (Liu et al. 2005; Liu et al. 2007a; Mei et al. 1992). However, reported methods for Cu-Sn material synthesis focus on producing nano-sized particles (Cao et al. 2014; Jo et al. 2011) and thin films (Kumar et al. 2011; Polat et al. 2014). Therefore, it is desirable to develop a continuous and potentially scalable process to fabricate micron-sized Cu-Sn powders, because they are favored for applications such as conductive pastes and interference packaging (Deshpande et al. 2005; Wu et al. 2009). Here, a method is presented to generate micron-sized Cu-Sn binary particles via spray pyrolysis. In this work, $Cu(NO_3)_2$ and $SnCl_2$ were selected as the metal sources. Water and EG were used as solvent and co-solvent, respectively. The effects of experimental conditions (reaction temperature, EG concentration, residence time, and quench gas flow rate) on the final particle properties (morphologies, crystallinity, and metal distribution within the particles) were investigated.

3.3 Experimental

3.3.1 Preparation of precursor

All chemicals were purchased from the companies listed and used without further purification. $Cu(NO_3)_2 \cdot 3H_2O$ (99.5% purity, Strem Chemicals, Newburyport, MA, USA) was first dissolved into distilled water. $SnCl_2 \cdot 2H_2O$ (Fisher Scientific, Waltham, MA, USA) was added into EG (≥99%, Sigma Aldrich, St. Louis, MO, USA). The two solutions were mixed to make a solution of 1 M $Cu(NO_3)_2$, 0.1 M $SnCl_2$, and 3.6 M, 4.8 M, or 5.9 M EG based on different experiments. To ease the hydrolysis of $SnCl_2$, HNO_3 (SIGMA-ALDRICH, 70%) was added with a final concentration of 0.1 M.

3.3.2 Spray pyrolysis procedures

The setup of the spray pyrolysis is the same as reported in previous work (Zhong et al. 2012). In brief, precursor was transported into the atomizer (with a 1.7 MHz ultrasonic generator) by a peristaltic pump. The atomized droplets of precursor had a volume average diameter ~5 μm (Zhong et al. 2012). Once the droplets were formed, they were transported by carrier gas (N_2, 99.5%, Arigas, Rador, PA, USA) into a quartz tube (inner diameter = 19 mm), which was heated by two furnaces in series (total heated length = 81.3 cm). The carrier gas flow rate (CGFR) was varied from 1 L/min to 5 L/min based on the experimental design with the residence times shown in Figure 3.1c. At the end of the tube, a polytetrafluoroethylene (PTFE) filter (with a diameter of ~9.5 cm) was utilized to collect the powders. Quench gas (N_2, AIRGAS, 99.5%) was introduced at ~8 L/min to reduce the temperature at the filter.

To better understand the heating conditions in the system, the temperature along the centerline of the quartz tube and immediately downstream of the filter was measured within the heated range (81.3 cm) by a K-type thermocouple. Distilled water was atomized as a surrogate for the precursor during the measurement. N_2 gas was used as the carrier gas, the same as during the actual particle generation process.

To estimate the residence time of the double furnace reactor of 81.3 cm length, $N = 32$ calculation elements were selected. It was assumed that the temperature was uniform within each element. Thus, the average time required for each droplet (or particle) to traverse the element can be calculated using a plug-flow reactor approach. The reactor can be divided into a number of sub-volumes along the axial direction. In each sub-volume the

reaction extent is treated as spatially uniform (Fogler 1999). Therefore, residence time per sub-volume can be calculated as:

$$t_i = \frac{A \times l}{F} \times \frac{T_{room}}{T_i} \qquad (3.1)$$

Here, A is the cross sectional area of the tube, l is the length of the calculation element, F is the CGFR, T_{room} is the room temperature, and T_i is the temperature in each element which can be found in Figure 3.1a-b. Thus, the total residence time (τ) can be estimated as:

$$\tau = \sum_1^N t_i \qquad (3.2)$$

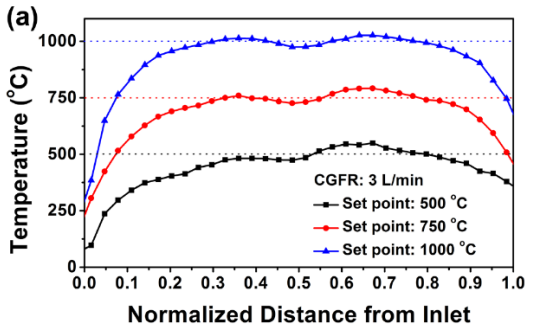

(c)

Temperature (°C)	500	750			1000
CGFR (L/min)	3	1	3	5	3
Residence time (s)	2.0	4.5	1.5	0.92	1.2

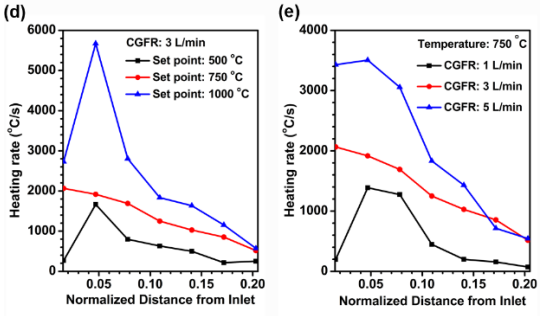

Figure 3.1. Temperature profile of a double furnace reactor of 81.3 cm in length with (a) fixed CGFR at 3 L/min and various temperatures; (b) fixed temperature at 750 °C and different CGFRs; (c) estimated residence time. (d) and (e) The heating rates in the reactor with respect to the conditions in (a) and (b), respectively.

3.3.3 Mechanism exploration

Conditions of high temperatures (500 °C, 750 °C, and 1000 °C) and long residence times (~0.92 s) were utilized to fabricate the Cu-Sn binary powders, as discussed in the previous section. To investigate the mechanism of the particle formation process,

experiments were conducted at lower temperatures and shorter residence times to identify reaction intermediates. The precursor contained 1 M $Cu(NO_3)_2$, 0.1 M $SnCl_2$, and 0.1 M HNO_3. EG was added with a concentration of 5.9 M. The spray pyrolysis was conducted at i) 300 ^oC with CGFR = 5 L/min and quench gas at ~5.2 L/min; and ii) 500 ^oC with CGFR = 10 L/min and quench gas at ~10.8 L/min. During those two experiments, only a single furnace was used, and the residence time was less than 0.74 s in both cases.

3.3.4 Characterization and data analysis

Scanning electron microscopy (SEM, Hitachi SU-70, Hitachi, Tokyo, Japan) was used to observe the particle morphologies. Transmission electron microscopy (TEM, Jeol Jem 2100 LaB6, Jeol Jem, Tokyo, Japan) was utilized to understand the details of the particle structures. Before conducting the SEM and TEM observations, powders were suspended in ethanol. After sonication for ~1 min, the mixture was added dropwise onto a silicon wafer or TEM grid, and dried under ambient conditions. X-ray diffractometer (XRD, Bruker D8 advance, Bruker, Billerica, MA, USA) was used to obtain crystallographic information of powders. Particles were also examined by X-ray photoelectron spectroscopy (XPS, Kratos Axis 165, Kratos Axis, Manchester, UK) to determine the elemental distribution on the powder surface. In addition, the powders were sputtered in vacuum by argon ions for 20 min to collect the sub-surface concentration profile. The sputtering gun was set at 4 kV and 5 mA.

3.4 Results and discussion

3.4.1 Reaction temperature

To identify the composition of the products, powder XRD with Cu Ka radiation was utilized, as shown in Figure 3.2. When the set point of the furnaces was 500 ^oC, Cu and

Cu13.7Sn were the main phases. The residence time of the process was 2 s. When the temperature increased to 750 ^{o}C, the residence time of the process was 1.5 s. Powders displayed higher quality crystallinity with sharp peaks of Cu13.7Sn without Cu peaks. However, there was one peak at 32.6^{o}, which could not be identified as Cu or Cu13.7Sn. It may be attributed to intermediate salt phase(s) of small quantity, with low peak intensity compared to the major Cu13.7Sn peaks. The increase of temperature could promote the forming of a Cu-Sn solid solution, which is thermodynamically favorable. A similar phenomenon has also been reported in other alloy particles that a particle composed of a single alloy phase will have lower free energy compared to a particle containing multiple phases (Zhong et al. 2013a). When the temperature was increased to 1000 ^{o}C, the residence time was 1.2 s. The intensity of the unidentified peak (32.6^{o}) was negligible compared to the strong peaks of Cu13.7Sn. The XRD diagram exhibited high quality crystallinity with Fm-3m symmetry, implying complete reaction to generate Cu13.7Sn particles.

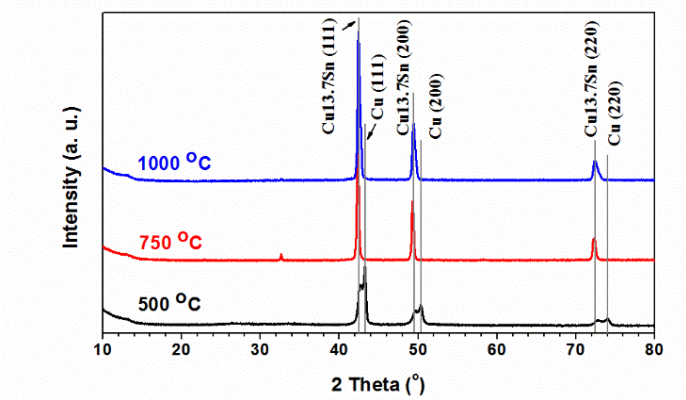

Figure 3.2. XRD results of powders generated from systematic conditions. The precursor contained 1 M $Cu(NO_3)_2$, 0.1 M $SnCl_2$, 0.1 M HNO_3, and 4.8 M EG. The CGFR was fixed at 3 L/min. The powders were generated at 500 ^{o}C, 750 ^{o}C, and 1000 ^{o}C. The major peaks are from Cu13.7Sn (ICDD with PDF No. 03-065-6821) and Cu (ICDD PDF No. 01-070-3038).

The morphologies of particles generated at different reaction temperatures with 4.8 M EG in the precursor are shown in Figure 3.3 with additional images in Figure 3.4. When the temperature was set at 500 ^{o}C, hollow porous particles could be seen with primary particles (marked by solid line circle) on the surface, as shown in Figure 3.3a. The number mean diameter of the hollow porous particles and the primary particles are 1.5 µm and 150 nm, respectively (Figure 3.3d). The TEM observations of these particles further validate the porous hollow structure with primary particles scattered within the shell, as shown in Figure 3.5a.

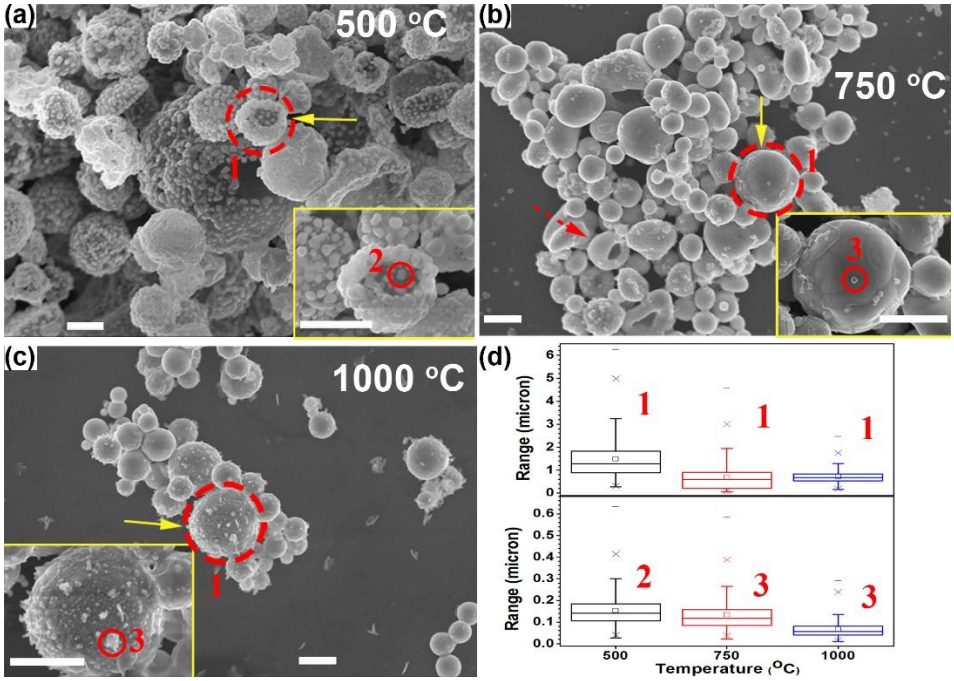

Figure 3.3. SEM images of powders generated from the precursor solution with 1 M $Cu(NO_3)_2$, 0.1 M $SnCl_2$, 0.1 M HNO_3, and 4.8 M EG. The reaction temperatures were 500 ^{o}C (a), 750 ^{o}C (b), and 1000 ^{o}C (c). The CGFR was fixed at 3 L/min. Insets are higher magnification images of selected regions marked by solid arrows. The scale bars in all figures are 1 µm. (d) The summary of the diameter of the particles marked as 1, 2, and 3 in (a)–(c). Detailed size distributions for each condition can be found in Figure 3.6.

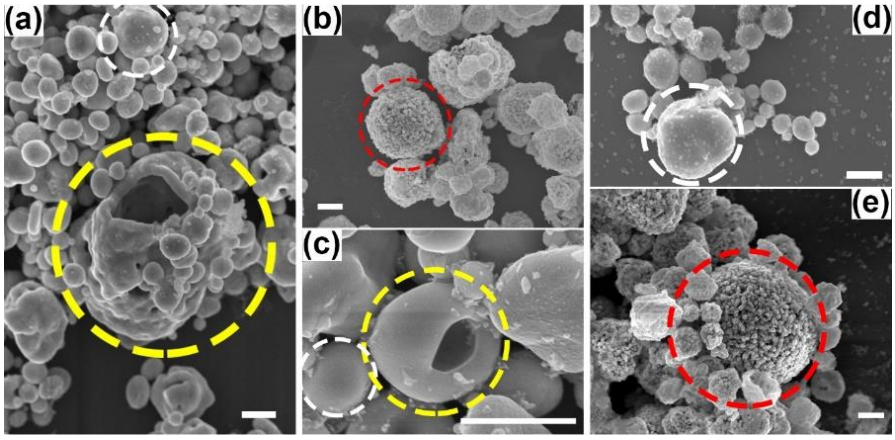

Figure 3.4. Samples generated at 750 ^{o}C with EG concentration of 3.6 M (a), 4.8 M (b)-(c), and 5.9 M (d)-(e). The concentrations of $Cu(NO_3)_2$, $SnCl_2$, and HNO_3 were 1 M, 0.1 M, and 0.1 M, respectively. The scale bars of the SEM images are 1 μm.

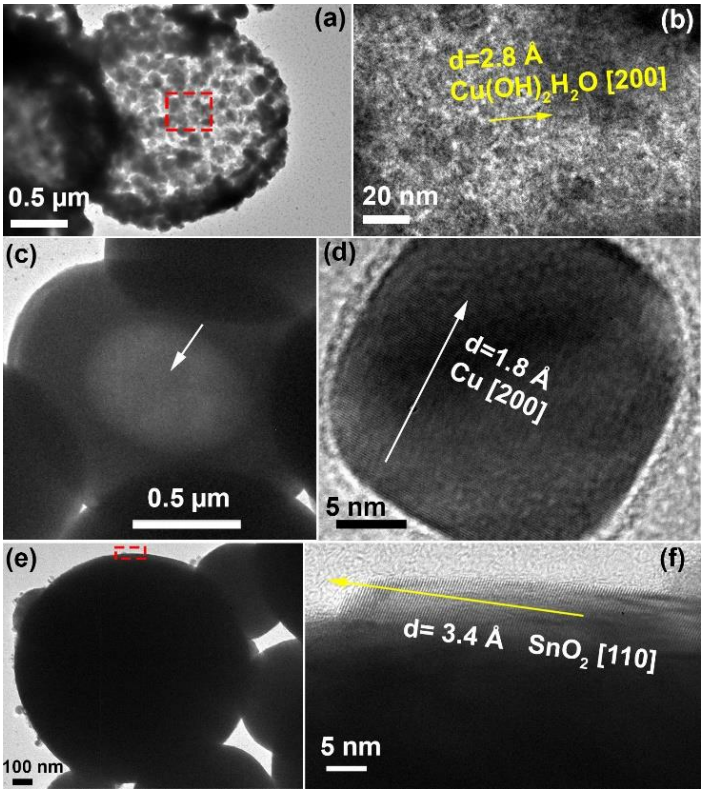

Figure 3.5. TEM images of particles fabricated by precursors with 1 M $Cu(NO_3)_2$, 0.1 M $SnCl_2$, and 0.1 M HNO_3. The CGFR was fixed at 3 L/min. (a)–(b) Particles generated at

500 °C, with 5.9 M EG. (c)–(d) Particles obtained at 750 °C, with 4.8 M EG. (e)–(f) Particles obtained at 1000 °C, with 4.8 M EG.

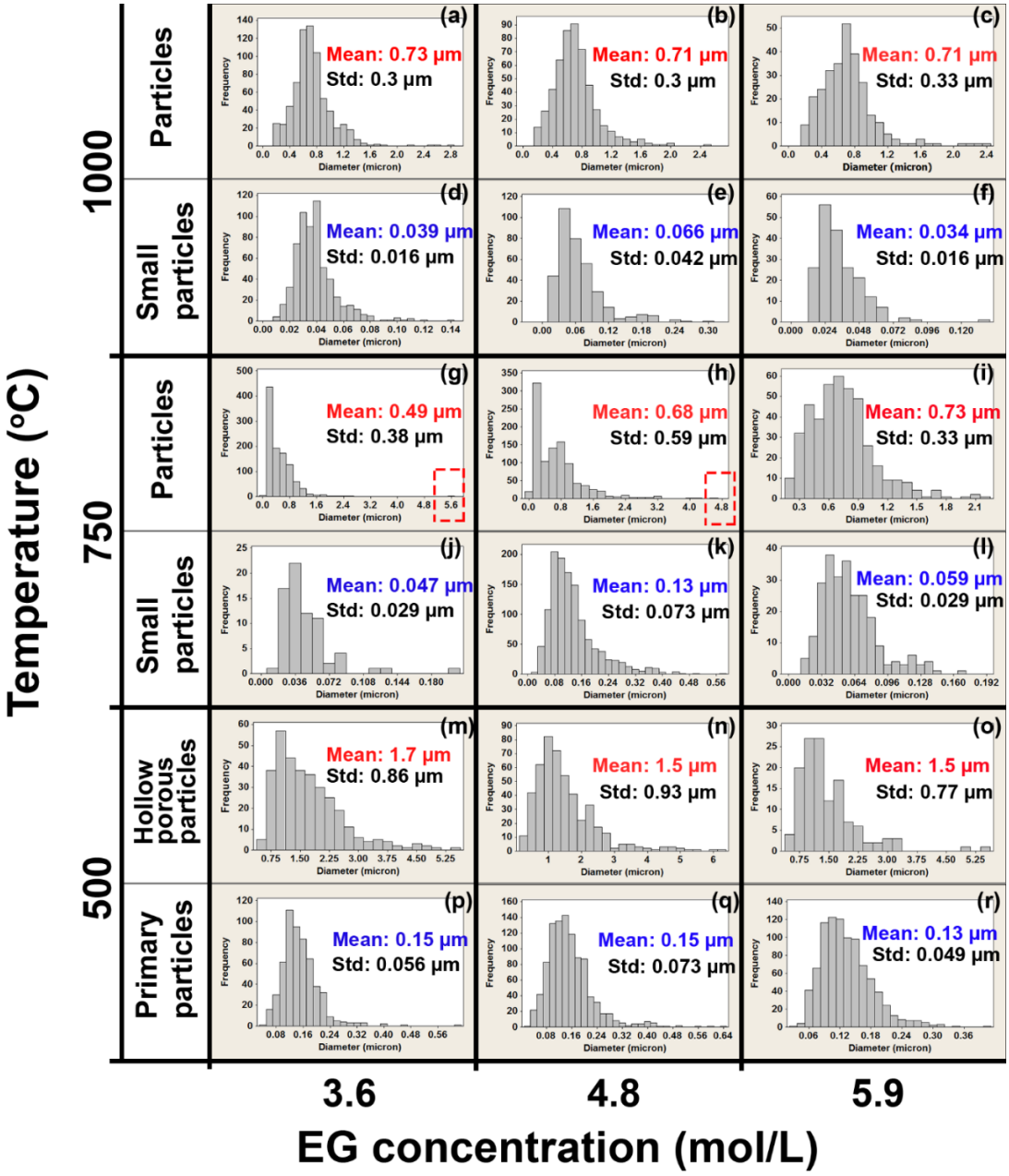

Figure 3.6. Diameter distributions of the products generated at systematic conditions. The concentrations of $Cu(NO_3)_2$, $SnCl_2$, and HNO_3 were 1 M, 0.1 M, and 0.1 M, respectively.

According to reported results, the hollow structures were caused by a solute concentration gradient within the droplets which led to solute precipitation on the surface of the droplets (Gurav et al. 1993). The granular precipitates within the precursor droplets could concentrate on the droplet surface for the maximum structural stability during the solvent evaporation (Nandiyanto and Okuyama 2011). After the solvents vaporized and solutes reduced to metals, hollow porous particles were formed with primary particles comprising the shell (morphologies shown in Figure 3.3a). Pressure may accumulate within the shell during evaporation of the solvent, leading the droplets to burst (Gurav et al. 1993). Thus, semispherical particles can be observed, as shown in the inset of Figure 3.3a.

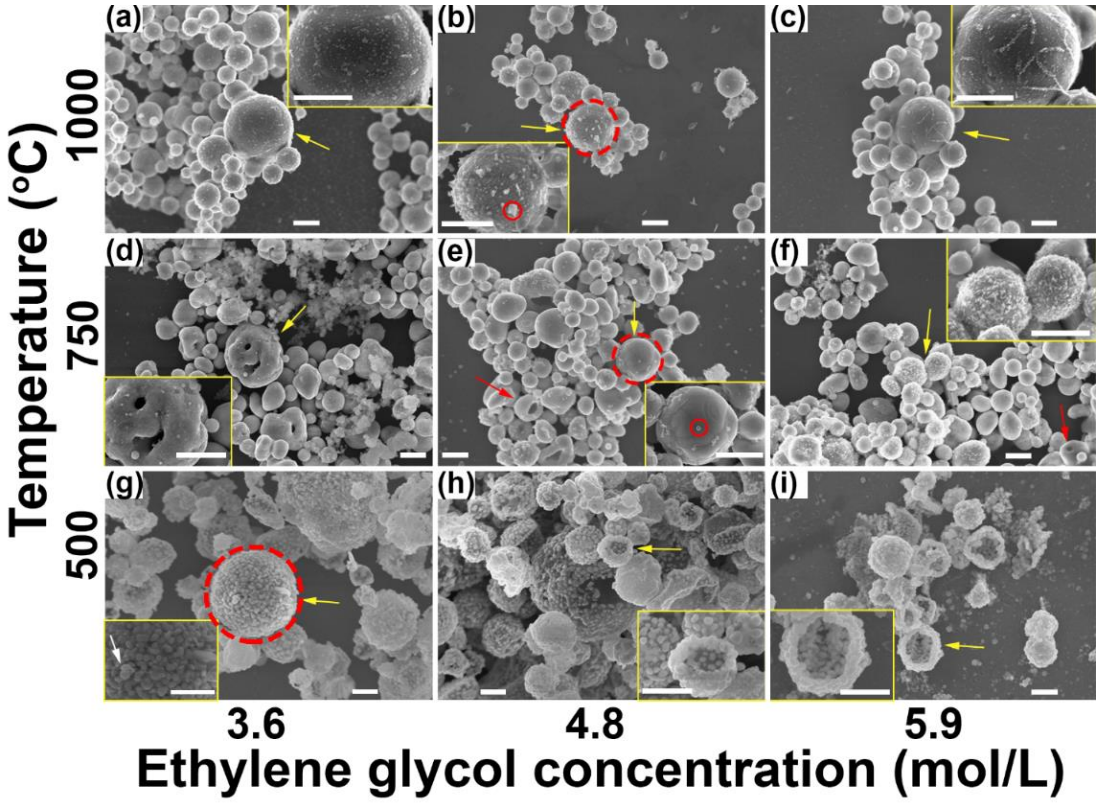

Figure 3.7. SEM images of powders generated from systematic conditions. EG concentration was tuned at 3.6 M, 4.8 M, and 5.9 M at 500 °C, 750 °C, and 1000 °C, respectively. The concentrations of $Cu(NO_3)_2$, $SnCl_2$, and HNO_3 in the precursor were 1

M, 0.1 M, and 0.1 M, respectively. The CGFR was fixed at 3 L/min. Insets highlighted by yellow squares are higher magnification images of selected regions marked by yellow arrows. The scale bars in all figures are 1 μm.

When the furnace set point temperature was increased to 750 ^{o}C, the amount of primary particles was significantly decreased. Instead, hollow particles with a crust on the surface can be seen in Figure 3.3b. The particles in the TEM image (Figure 3.5c) also exhibit the hollow structure, with the dark part representing the crust and bright area (marked by white arrow) representing the hollow core. The number mean diameter of these particles is 0.68 μm (Figure 3.3d), which is smaller than that of the hollow porous particles generated at the 500 ^{o}C. The decrease of the number mean diameter supports the hypothesis that the hollow crusted particles in Figure 3.3b are caused by the coagulation of the primary particles and shrinking of the hollow porous structure in Figure 3.3a. Size can affect the melting point of Cu and Sn (Ju et al. 2015; Karabacak et al. 2006). The reported melting point of bulk tin is ~230 ^{o}C (Ju et al. 2015; Wronski 1967). The melting of bulk Cu-Sn alloy ranges from 1085 ^{o}C (Sn at % = 0) to 945 ^{o}C (Sn at % = 10%) (Saunders and Miodownik 1990). Copper nanorods with a length of 2.3 μm and a diameter of 100 nm have also been found to melt below 550 ^{o}C (Karabacak et al. 2006). The fragmented spherical particles may stem from the melting of the fragmented hollow particles (inset of Figure 3.3a) obtained at 500 ^{o}C. Thus, other morphologies, *e.g.*, spherical particles with pores (inset of Figure 3.7d) and fragments (marked by a dashed arrow in Figure 3.3b, and circled by dashed lines in Figure 3.4c) were seen at this temperature, which indicates these particles may stem from the coagulation of the primary particles in Figure 3.3a. Based on Figures 3.3b,3.4, it can be concluded that the morphologies of particles at 750 ^{o}C showed the evolution from hollow

to solid. The hollow to solid transition occurred between 500 ^{o}C and 1000 ^{o}C. In spray pyrolysis, reaction temperature is a critical factor influencing the particle structure. With the increase of temperature, particle structure could evolve either from hollow to solid (Ortega et al. 1991) or from solid to hollow (Eslamian and Ashgriz 2006) based on the chemical properties and precipitation rates of the salts in the precursor (Eslamian and Ashgriz 2006). In our system, the evaporation of HNO_3 ($P_{vap,\ HNO3}$ = 172 kPa at 373 K) from precursor droplet into the gas phase promotes hydrolysis of $SnCl_2$ (Yaws 1995). Based on the prior reports, $SnCl_2$ prefers to hydrolyze to form hydroxides and decompose to SnO, even at room temperature (Cohen and West 1972). SnO is likely formed at the droplet surface. Thus, with the increase of reaction temperature, the Cu-Sn particles shifted from hollow to solid due to the melting of the primary particles and densification of the Cu-Sn particles. This mechanism may also be applicable to other systems with rapidly precipitating components.

Small particles can be seen on the surface of the hollow crusted particles at 750 ^{o}C (inset of Figure 3.3b, solid line circle). The small particles, with number mean diameter of 0.13 μm (Figure 3.3d), were believed to form by gas-to-particle conversion, which has been reported in spray pyrolysis (Fotou et al. 2000; Schulz et al. 2005; Tsai et al. 2004). One possible formation mechanism is that the volatized $Cu(NO_3)_2$ vaporizes into the gas once it has precipitated from the solvent. The vapor pressure of $Cu(NO_3)_2$ at 495.8 K is 480 Pa (Addison and Hathaway 1958). $Cu(NO_3)_2$ may vaporize below 500 K and decompose to CuO, NO_2, and O_2 above 500 K (Stern 1972). CuO may nucleate into small oxide particles in the gas phase. With the reducing environment created by EG, it is rational to believe the CuO will be reduced to Cu, and then the small particles, as shown in Figure

3.3b,c, were formed. For reference, the vapor pressures of CuO and SnO at 1000 ^{o}C are $P_{vap,CuO} = 1.1\times10^{-2}$ Pa (Mack et al. 1923) and $P_{vap,SnO} = 370$ Pa (Platteeuw and Meyer 1956) and the vapor pressures of the pure metals are even lower, $P_{vap,Sn} = 1.5\times10^{-2}$ Pa and $P_{vap,Cu} = 6.0\times10^{-3}$ Pa, at 1000 ^{o}C (Smithells et al. 2004). Another possible mechanism is that after the solvent in the precursor droplets evaporated, the Cu and Sn may be reduced by the EG. The metals in the particles would vaporize, nucleate, and grow into particles with a diameter less than 100 nm in the gas phase. A similar mechanism has also been reported by other researchers (Tsai et al. 2004). In the TEM observation, the small particles were found to be pure Cu particles (Figure 3.5d), which further validated the hypothesis that the small particles are likely generated by gas-to-particle conversion.

When the temperature was increased to 1000 ^{o}C, the particles underwent further densification to form spherical solid particles (Figure 3.3c) with a number mean diameter of 0.71 μm (Figure 3.3d). The TEM image (Figure 3.5e) also provides evidence of this conclusion. Small particles are still seen with number mean diameter of 0.13 μm on the particle surfaces, which are also believed to be formed by gas-to-particle conversion. The SnO_2 seen in Figure 3.5f is believed to be caused by the oxidation of the Sn on the particle surface.

To further understand the elemental distributions and chemical states on and beneath the Cu-Sn particle surface, XPS analysis was utilized together with ion-beam sputtering. As shown in Figure 3.8, the Cu/Sn ratio was lower on the surface (before sputtering) than under the surface (after sputtering). Both cases exhibited Sn enrichment compared to the Cu/Sn ratios in the precursor and the major crystal phase (Cu13.7Sn). In addition, the low temperature led to a lower Cu/Sn ratio than the high temperature. This Sn enrichment on

the particle surface is likely responsible for the difference in the Cu/Sn ratio observed from XRD measurements (13.7) compared to that in the precursor (10). A mass balance calculation was made assuming that the Cu-Sn particles were encapsulated by an amorphous Sn layer that would not appear in the XRD. From this calculation, the overall Cu/Sn ratio in the product particles is maintained at 10, if the ratio of the calculated thickness of Sn crust to the radius of Cu-Sn core (with Cu/Sn ratio = 13.7) is 0.008. Therefore, for particles obtained at 1000 ºC, with a mean diameter of 710 nm (Figure 3.6), a thickness of 3 nm Sn enrichment layer would explain the Cu/Sn ratio observed with XRD. Thus, both the calculated and XPS results indicates that Sn accumulates on the particle surface (Figure 3.8).

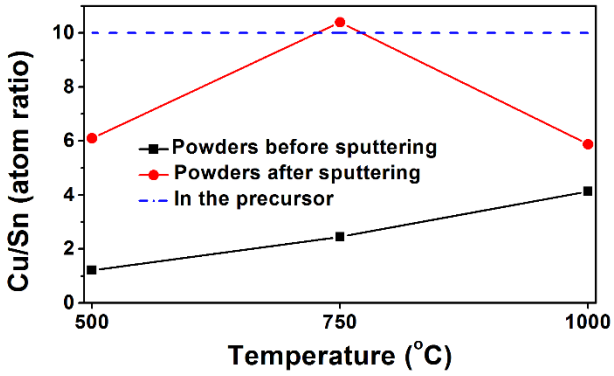

Figure 3.8. The Cu/Sn ratios summarized from XPS results. The precursor contained 1 M $Cu(NO_3)_2$, 0.1 M $SnCl_2$, 0.1 M HNO_3, and 4.8 M EG. The CGFR was set at 3 L/min. Sputtering was conducted in vacuum by argon ions for 20 min.

The dominant tin species on the particles surface can be identified as SnO_2 (Figure 3.9a,d,g, before sputtering). After sputtering the XPS peaks representing metallic tin increased significantly in all tested samples. For copper, the signal from Cu 2p is shown in

Figure 3.9b,e,h (after sputtering). From the reference, metallic copper has a major peak at 932.4 eV (Fleisch and Mains 1982), which is marked by a grey line in Figure 3.9b,e,h. It can be seen that the powders contained metallic copper on and beneath the particle surface at all three temperatures. To better understand the copper states on and beneath the sample surface, the signals from Cu LMM auger electrons were collected. The shoulder peaks around 565 eV, as shown in Figure 3.9c,f,i, are strong evidence for the existence of metallic copper (Fleisch and Mains 1982), However, the peaks of the 1000 ^{o}C sample were weak around 565 eV (Figure 3.9c, before sputtering), which means the metallic copper presents a small amount on the surface. Peaks around 570 eV are evidence for the existence of copper oxides. Unfortunately, as the shape and peak position of CuO and Cu_2O are similar (Fleisch and Mains 1982), it is hard to distinguish between them in all samples. Results shown here can only confirm that there are copper oxides on the surface. However, a qualitative conclusion still can be made based on the relative intensity of the peak around 570 eV to the peak around 565 eV. The amount of copper oxides increased with temperature. The Cu/Sn ratio increased on the Cu-Sn binary particle surface with the increase of temperature. Therefore, Cu was more readily oxidized at high temperatures because of insufficient Sn to form sacrificial oxides, which may protect Cu from being oxidized. After sputtering, the intensity of the peak around 570 eV decreased, making it negligible compared to the peaks around 565 eV (Figure 3.9c,f,i, after sputtering). This indicates the existence of metallic copper as the main component beneath the particle surface.

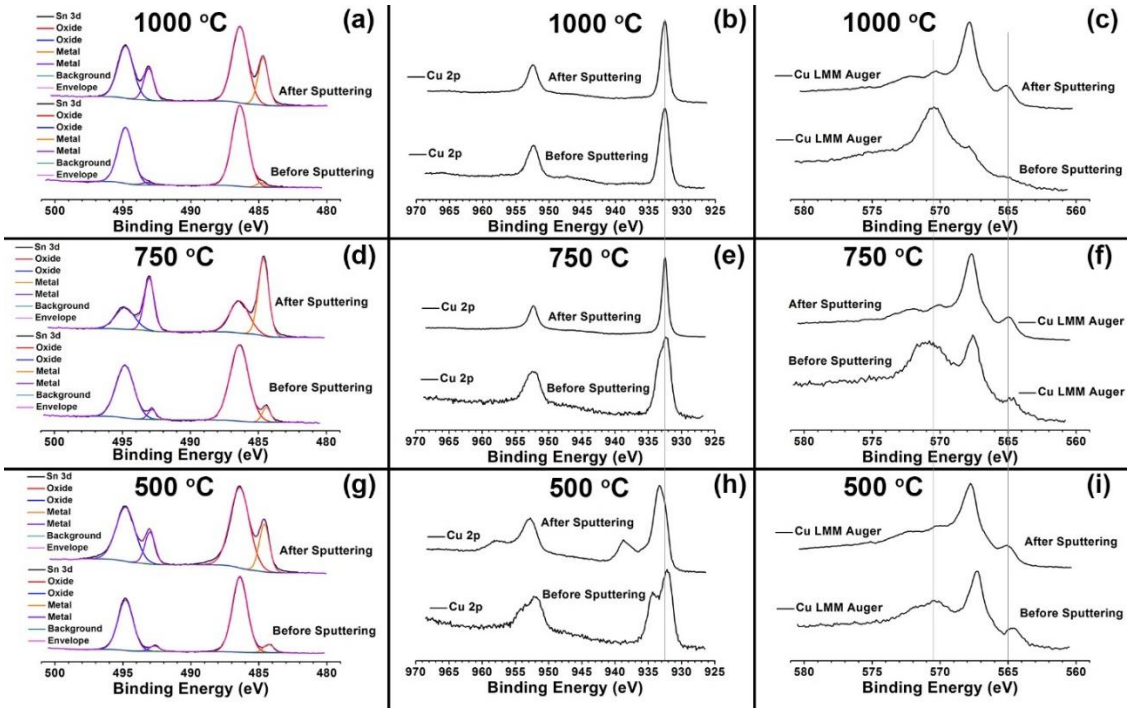

Figure 3.9. XPS signals collected at different temperatures. The concentrations of $Cu(NO_3)_2$, $SnCl_2$, and HNO_3 were 1 M, 0.1 M, and 0.1 M, respectively. The EG concentration was fixed at 4.8 M. The CGFR was set at 3 L/min. The temperature was set at 1000 ^oC (a)-(c); 750 ^oC (d)-(f); 500 ^oC (g)-(i); (a), (d), and (g) represent the data from Sn 3d electrons. (b), (e), and (h) illustrate the data from Cu 2p electrons. (c), (f), and (i) are the data from Cu LMM Auger electrons.

For a mixture of H_2O and EG, the evaporation of H_2O is faster than EG, because the vapor pressure of H_2O is higher than EG (Table 3.1). Solutes would be expected to precipitate on the droplet surface with EG remaining as the inner core. During this process, a fast formation of SnO is possible because of the evaporation of HNO_3 and hydrolysis of $SnCl_2$ as discussed above. With the further evaporation of the solvent, copper salts would reach the saturation point and precipitate. Therefore, the Cu/Sn ratio was lower on the

particle surface than beneath the surface, as shown in Figure 3.8. It led to the concentration difference of Cu and Sn between the particle surface and inner core, which could provide the driving force for the diffusion of Cu towards the particle surface ($D_{\text{Cu-in-Sn}}$: 7.57×10^{-11} m^2/s, 220 ^oC; $D_{\text{Sn-in-Cu}}$: 5.09×10^{-24} m^2/s, 220 ^oC) (Mei et al. 1992). Therefore, the increase of reaction temperature could promote the diffusion of Cu towards the particle surface, causing the increasing Cu/Sn ratio on the particle surface, as seen in the XPS results in Figure 3.8.

Table 3.1. Vapor pressure of water and EG

Temperature (^{o}C)	P_{water} **(mm Hg) (Speight 2004)**	P_{EG} **(mm Hg) (Jordan 1954)**
60	149.38	1.6
70	233.7	3
80	355.1	5.3
90	525.76	9
100	760	15
110	1074.56	25
120	1489.14	40

3.4.2 Ethylene glycol volume percentage in the precursor

The co-solvent, acting as the solute carrier, and reducing agent, is one of the most critical factors affecting the precursor properties. Before EG was identified as an effective co-solvent to generate oxide-free copper particles (Zhong et al. 2012), ethanol was applied in spray pyrolysis as the co-solvent (Kim et al. 2003). As reported, 10 vol % of ethanol in aqueous solution can promote the formation of phase pure copper powder from copper

nitrate precursor at temperatures above 600 ^{o}C (Kim et al. 2003). This was attributed to the high H_2 yield of ethanol decomposition during spray pyrolysis. Experimental measurements showed that 2.2 moles of H_2 could be generated from every mole of ethanol (Zhong et al. 2013b). It has been experimentally proven that every mole of EG can generate 0.81 mol of H_2 during spray pyrolysis (Zhong et al. 2013b). Therefore, metal salts can be reduced to metal particles by H_2, the product of ethanol and EG decomposition. Compared to ethanol as the co-solvent, the consumption of EG would be greater to reduce the same amount of metal salt. Though ethanol can create a better reducing atmosphere during spray pyrolysis, EG is still favored due to its higher flash point (Zhong et al. 2012). As reported, the decomposition of EG to H_2 has several different mechanisms (Yue et al. 2012):

$$C_2H_6O_2 \rightarrow 2CO + 3H_2 \qquad (3.3)$$

$$C_2H_6O_2 \rightarrow C_2H_{6-x}O_2 + \frac{x}{2}H_2 \qquad (3.4)$$

here, Formula (3.3) is the complete decomposition of EG, and Formula (3.4) is the general dehydrogenation of EG.

During the experiments, the relative EG amount needs to be controlled. High EG volume percentages in the precursor can lead to high H_2 production in the reactor, which can promote the generation of oxide-free Cu-Sn binary particles. However, excessive EG will result in a precursor solution too viscous to be atomized and H_2 above the lower flammability limit.

The dynamic viscosities and densities of the precursors with various EG concentrations (Figure 3.10) were measured because they have been reported as two of the factors affecting the precursor droplet size (Avvaru et al. 2006; Ramisetty et al. 2013; Tsai et al.

2009). As shown in Figure 3.10, the viscosity of the precursor increased rapidly with EG concentration compared to density. For the conditions with EG concentration > 5.9 M (viscosity > 3 mPa·s), it was difficult to atomize the precursor in the experiments because of the high viscosity. Similar results were observed and discussed by other researchers with similar transducers (1.7 MHz), who found the precursor cannot be atomized when the viscosity exceeded 2 mPa·s in their experiments (Wang et al. 2008).

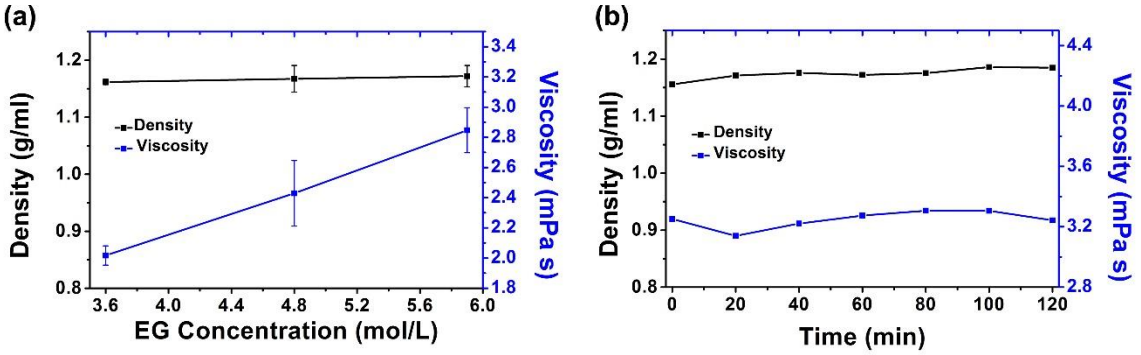

Figure 3.10. (a) Densities and viscosities of precursors with 3.6 M, 4.8 M, and 5.9 M EG. The concentrations of $Cu(NO_3)_2$, $SnCl_2$, and HNO_3 were 1 M, 0.1 M, and 0.1 M, respectively. (b) Densities and viscosities of precursor with 1 M $Cu(NO_3)_2$, 0.1 M $SnCl_2$, 0.1 M HNO_3, and 5.9 M EG during the spray pyrolysis.

To further understand the effect of EG concentration on the product crystallinity and morphology, XRD and SEM images of the powders obtained from the precursor solutions with different EG concentrations (*i.e.*, 3.6 M, 4.8 M, and 5.9 M) at different temperatures (500 ^{o}C, 750 ^{o}C, and 1000 ^{o}C) was taken as shown in Figures 3.7,3.11. There was no significant morphological difference between the tested EG concentrations. However, the morphologies and number mean diameters of particles varied significantly between

different temperatures, consistent with the discussion in Section 3.4.1. Generally, the particles were within the range of 0.5 to 2.5 μm, which is consistent with previous results (Zhong et al. 2012).

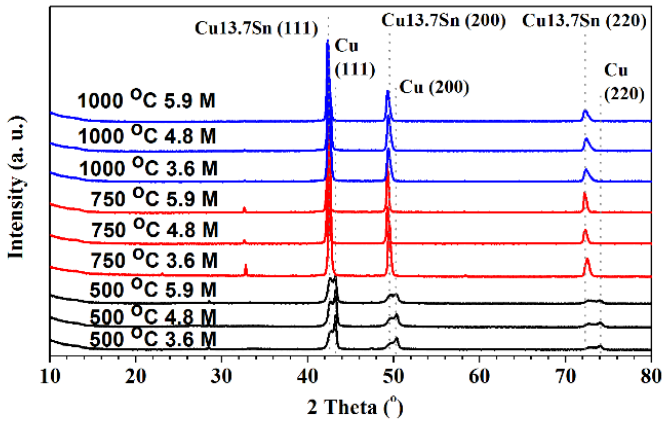

Figure 3.11. XRD results of powders generated from systematic conditions. The concentrations of $Cu(NO_3)_2$, $SnCl_2$, and HNO_3 in the precursor were 1 M, 0.1 M, and 0.1 M, respectively. The CGFR was fixed at 3 L/min. The powders were generated at 500 °C (black), 750 °C (red), and 1000 °C (blue), with EG concentration varied at 3.6 M, 4.8 M, and 5.9 M (from bottom to top), respectively. The major peaks are from Cu13.7Sn (ICDD with PDF No. 03-065-6821) and Cu (ICDD PDF No. 01-070-3038).

XRD measurements were conducted to analyze the detailed crystal information of these samples. As shown in Figure 3.11, no significant difference can be seen between the samples generated at various EG volume percentages with the same temperature, which is consistent with the SEM results. Based on the results, it can be concluded that the EG can effectively reduce the metal salts at concentrations as low as 3.6 M in the precursor.

However, the EG concentration had no significant effect on the particle morphology and crystallinity in the tested EG volume percentages.

One important thing needs to mention here is the composition change during the spray pyrolysis. It is difficult to understand the composition of precursor solution directly because there are various variables to be determined, for example, the concentrations of $Cu(NO_3)_2$, $SnCl_2$, HNO_3, and EG. I still attempted to understand this issue by monitoring the density and viscosity changes of the precursor solution during the spray pyrolysis. As shown in Figure 3.10b, the densities and viscosities of precursor solution which contains 1 M $Cu(NO_3)_2$, 0.1 M $SnCl_2$, 0.1 M HNO_3, and 5.9 M EG were measured every 20 min during the spray pyrolysis. Although fluctuations can be observed in the density and viscosity measurements, densities and viscosities of the precursor solution varied within narrow ranges. This indicates that the composition of the precursor can remain within a narrow range during the spray pyrolysis.

3.4.3 Residence time

To explore the effect of residence time on powder formation, spray pyrolysis was conducted at 750 ^oC with various carrier gas flow rates (CGFRs). 750 ^oC was chosen because it represented the transition conditions (as discussed in Section 3.4.1), highlighting an observable difference in the morphology. The residence times were 4.5 s, 1.5 s, and 0.92 s for CGFR = 1, 3, and 5 L/min, respectively (Figure 3.1). EG concentration was 4.8 M. As shown in Figure 3.12, the morphologies of the particles varied under different residence times. The long residence time (4.5 s) promoted the generation of spherical particles with smooth surfaces (Figure 3.12a), which are at the lowest surface energy state. Few small particles were observed under this experimental condition. Short residence time (0.92 s)

favored the formation of irregular shapes (*e.g.*, pores on the particle surface, fragmented spherical particles, and lamellar fragments, marked by dashed arrows in Figure 3.12c). The longer residence time may have led to the loss of small particles by thermophoretic deposition on the tube walls (Nguyen et al. 2002). Thus, small particles could not be seen on the filter (Figure 3.12a). The temperature difference between the centerline and wall position has been reported for similar gas flow rates, reactor tube dimensions, and furnace set point temperatures to range from 150 ºC to 200 ºC (Damour et al. 2005). Considering the mean particle sizes at 750 ºC (small particles: 79 nm, big particles: 630 nm, Figure 3.6), the system is in the continuum regime and the thermophoretic velocity (c_t) can be calculated as (Talbot et al. 2006):

$$c_t = \frac{2C_s\nu\left(\frac{k_g}{k_p}+C_t\frac{2l_p}{d_p}\right)C\frac{dT/dr}{T_0}}{\left(1+3C_m\frac{2l_p}{d_p}\right)\left(1+2\frac{k_g}{k_p}+2C_t\frac{2l_p}{d_p}\right)} \qquad (3.5)$$

where C_s (thermal slip coefficient), C_t (a numerical factor of order unity), and C_m (momentum exchange coefficient) are suggested to be 1.2, 2.2, and 1.1, respectively (Loyalka 1968; Talbot et al. 2006). For the radial temperature gradient, dT/dr = 16,000 K/m, when the temperature difference between the center line and tube wall was assumed to be 150 ºC. Other parameters of ν (kinematic viscosity), l_p (mean free path), and k_g/k_p (thermal conductivity ratio of gas to particle) are 3.7×10^{-5} m^2/s, 0.14 nm, and 2×10^{-4}, respectively (Yaws 1999). Based on the mean diameter of particles and small particles at 750 ºC, C (slip correction factor) are 1.3 and 5.0, respectively in each case (Friedlander 2000). By Equation (3.5), the thermophoretic velocities of large particles and small particles are 4.0×10^{-3} mm/s and 0.15 mm/s, respectively. Therefore, the difference between

the thermophoretic velocities of big and small particles could cause the results observed in Figure 3.12.

For the situation where residence time was short, particles had insufficient time to form spheres. Lamellar structures (inset of Figure 3.12c) can be seen, which may have originated from metal hydroxide intermediates (Zhong et al. 2012). Pores on the surface of the particles were formed as a result of the rapid evaporation caused by the short residence time. The powders generated at medium residence time (1.5 s) exhibited an intermediate morphology between the long (4.5 s) and short (0.92 s) residence time conditions.

To further understand the effect of residence time on the crystallinity of Cu-Sn binary particles, XRD measurement was performed. As shown in Figure 3.12d, there was no significant difference in crystal structure among particles fabricated at different residence times. All samples exhibited high quality crystallinity with sharp Cu13.7Sn peaks, similar to the powders generated at other conditions. The small peaks around 32.6^{o} are still believed to be unidentified intermediate(s) as discussed previously.

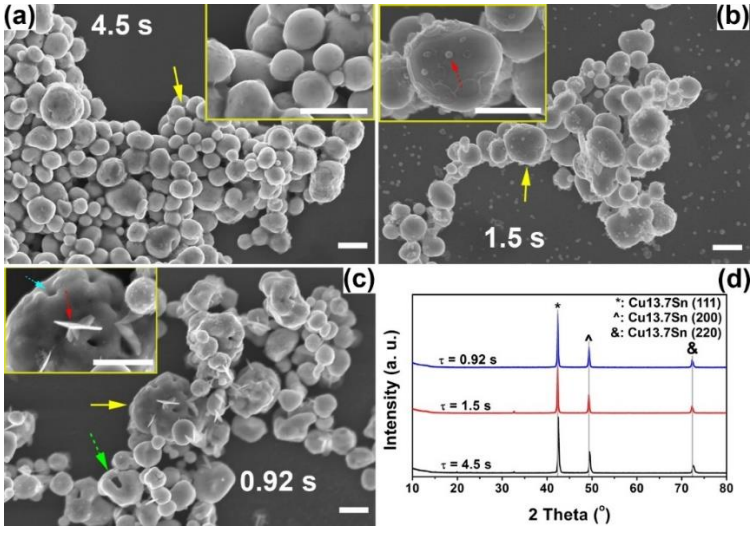

Figure 3.12. SEM images of powders obtained at 750 ^{o}C from precursors with 1 M $Cu(NO_3)_2$, 0.1 M $SnCl_2$, 0.1 M HNO_3, and 4.8 M EG. The residence times are: 4.5 s (a),

1.5 s (b), and 0.92 s (c). The insets of each figure are higher magnification images of the area marked by arrows. Arrows show irregular structures. (d) The XRD results of the powders obtained at the conditions of (a)–(c). The peaks are attributed to Cu13.7Sn (ICDD with PDF No. 03-065-6821). All scale bars in the SEM images are 1 μm.

When the set point of the furnaces were 750 ^{o}C, the residence times for each condition are 4.5 s (CGFR=1 L/min), 1.5 s (CGFR=3 L/min), and 0.92 s (CGFR=5 L/min). Long residence time (4.5 s) would cause a large quantity loss of products. Particles would more readily stick to the tube walls due to the thermophoretic force. Thus, the production rate was low. Furthermore, it became difficult to collect enough powder for future characterization within 2 h. The color map of the as-sprayed filters for different residence times are shown in Figure 3.13. For the 4.5 s condition, as the production rate was low, powders could be seen only in a circular area at the filter center. The powder production rate increased significantly under the other two conditions when the residence time was decreased to 1.5 s and 0.92 s.

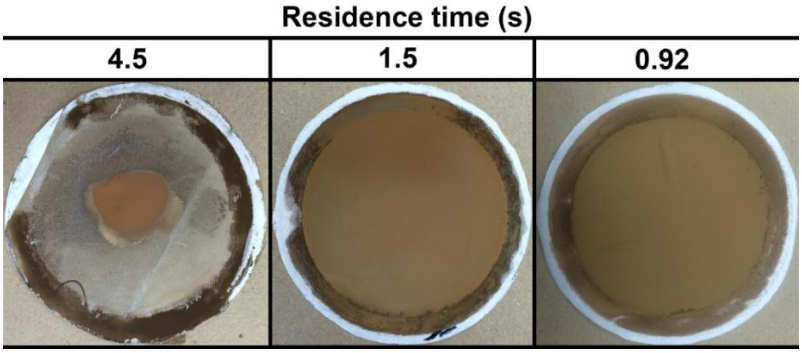

Figure 3.13. Images of as-sprayed filters generated from precursors with $Cu(NO_3)_2$, $SnCl_2$, and HNO_3 of 1 M, 0.1 M, and 0.1 M, respectively. The EG concentration was 4.8 M. The temperature was set at 750 ^{o}C. The diameters of the filters are ~ 9.5 cm.

As shown in Figure 3.1, low CGFR led to a long residence time, which may increase the possibility that tin would diffuse into the center of the particles, consequently reducing the tin concentration on the particle surface. For the particles fabricated with residence time was 4.5 s, the Cu/Sn = 7.14 on the particle surfaces before sputtering. Therefore, with such a low concentration of Sn, metallic tin was not observed on the Cu-Sn binary particle surfaces (Figure 3.14g, before sputtering) for particles generated at 1 L/min. The major peak (around 932.4 eV) in the powder prior to sputtering at 500 ^{o}C (Figure 3.14h) was attributed to metallic copper (Fleisch and Mains 1982). The absence of peaks around 565 eV, and existence of a peak around 570 eV in the Cu LMM Auger diagram (Figure 3.14i) were strong evidence that demonstrated copper oxides were the major component on the particle surface (Sen et al. 2009). When the residence time was 1.5 s, the Cu/Sn ratio decreased to 2.5 on the particle surface prior to sputtering. With such a high tin concentration on the particle surface, tin oxides were observed together with metallic tin (Figure 3.14d, before sputtering). For the copper with the protection by tin, metallic copper existed on the particle surface before sputtering, which can be validated by the peaks around 932.4 eV in Figure 3.14e, and 565 eV in Figure 3.14f (Fleisch and Mains 1982). However, peaks belonging to copper oxides were still seen around 570 eV in Figure 3.14f, before sputtering (Sen et al. 2009). For particles generated with a residence time of 0.92 s, irregular shapes were seen in Figure 3.12c, with pores and holes on the particle surface which increased the surface area. Therefore, a higher possibility for the metal oxidation was expected. Before sputtering, the intensity of the metallic tin peaks were low and no metallic copper peaks can be found around 565 eV (Figure 3.14a,c, respectively) (Fleisch and Mains 1982). After sputtering, all samples generated at 4.5 s, 1.5 s, and 0.92 s displayed

a Cu/Sn ratio around 10, which was the input Cu/Sn ratio in the precursor solutions. In addition, metallic tin peaks exhibited higher intensities compared to the tin oxides in Figure 3.14a,d,g, after sputtering. The existence of metallic copper was validated by the peaks at 932.4 eV (Figure 3.14b,e,h, after sputtering) and peaks at 565 eV (Figure 3.14c,f,i, after sputtering) (Fleisch and Mains 1982). The amount of copper oxides was negligible compared to the metallic copper after sputtering, which can be proven by the low intensities of the peaks at 570 eV in Figure 3.14c,f,i (Fleisch and Mains 1982).

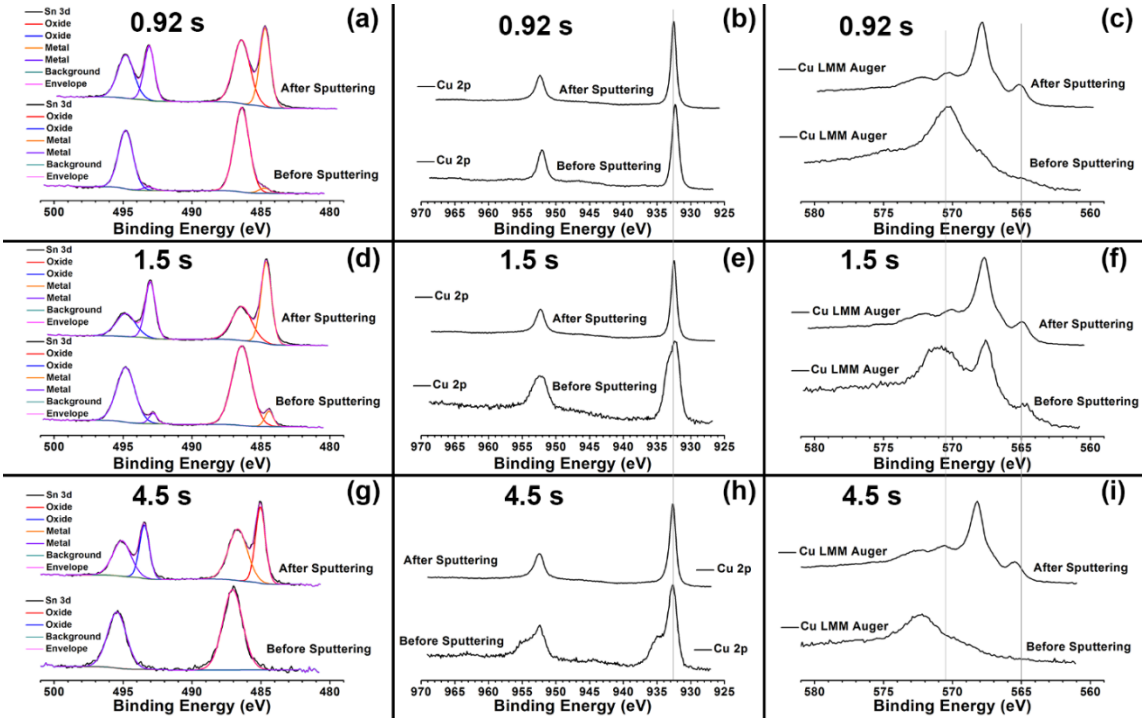

Figure 3.14. XPS signals collected at different CGFRs. The concentrations of $Cu(NO_3)_2$, $SnCl_2$, and HNO_3 were 1 M, 0.1 M, and 0.1 M, respectively. The EG concentration was fixed at 4.8 M. The temperature was set at 750 ^oC. The CGFR was set at 5 L/min (a)-(c); 3 L/min (d)-(f); 5 L/min (g)-(i); (a), (d), and (g) are the data from Sn 3d electrons. (b), (e), and (h) are the data from Cu 2p electrons. (c), (f), and (i) are the data from Cu LMM Auger electrons.

3.4.4 Effects of quench

As discussed previously, Cu and Sn were thought to evaporate into the carrier gas in the heated zone. Gas-to-particle conversion may lead to small particles after the carrier gas was cooled by the quench gas. To validate this hypothesis, a control experiment was designed, and conducted at the same conditions following the same procedures, except no quench gas was introduced. Thus, the temperature at the filter increased from 105 ^{o}C (with quench) to 175 ^{o}C (without quench). The cooling rate decreased from 162 ^{o}C/s (with quench) to 66 ^{o}C/s (without quench). To better investigate the effect of quench on the products, $SnCl_2$ concentration was set to 0.05 and 0.1 M in the precursor to investigate the origin of the small particles. The concentrations of $Cu(NO_3)_2$ and EG were still kept at 1 M and 4.8 M in both cases, respectively. During spray pyrolysis, the set point of the furnaces was 750 ^{o}C. The residence time was 1.5 s.

As shown in Figure 3.15a,c, powders generated with quench gas displayed a large quantity of small particles (marked by arrows). Without quench gas, the amount of small particles decreased significantly (Figure 3.15b,d). This observation supports the hypothesis that small particles originated from gas-to-particle conversion, since increase the cooling rate (by introducing quench) would enhance the homogeneous and heterogeneous nucleation (Schulz et al. 2005). In addition, sharp edges can be observed on the particle surface, as shown in Figure 3.15b,d, marked by arrows. These flat structures were attributed to the (111) planes of copper, indicating the doping of other elements (Chatain et al. 2004). From Figure 3.15a,c, the amount of small particles did not change significantly. Together with Figure 3.5d, it could be concluded that the copper species may be the main source for the small particles instead of tin species.

The powders generated from the four experimental conditions mentioned above were also characterized by XRD to explore the effect of quench on the final particle crystallinity. The products fabricated by precursors with 0.1 M $SnCl_2$ exhibited Cu13.7Sn as the major peaks (Figure 3.15e). For products fabricated from precursors of 0.05 M $SnCl_2$, the peaks were also sharp (Figure 3.15e) with positions close to those of Cu13.7Sn. However, the peaks were also close to other two standard peaks in the ICDD database. The standard peaks of the possible candidates are presented below the XRD diagram in Figure 3.15e. It seems that the different input Cu/Sn ratio in the precursor may lead to the formation of solid solutions other than Cu13.7Sn in the products. Therefore, intermediate products, *i.e.*, (Cu32Sn)0.12 and Cu matrix were seen in the XRD results. In addition, there was no significant difference between the XRD results of the samples generated at the same $SnCl_2$ concentration with or without quench.

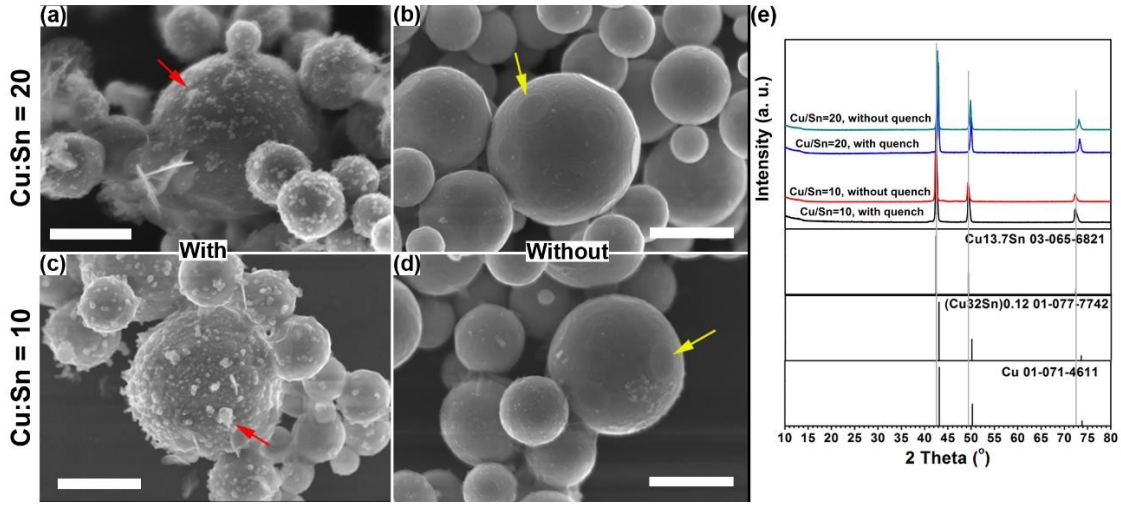

Figure 3.15. The effect of quench gas on the morphologies and crystallinities of the powders obtained at 1000 °C. The precursors contained 1 M $Cu(NO_3)_2$, 0.1 M HNO_3, and 4.8 M EG. The $SnCl_2$ concentration was 0.05 M (a)–(b) and 0.1 M (c)–(d). SEM images of the prepared powders are shown in (a), (c) with quench gas, and (b), (d) without quench

gas. (e) The XRD results of the generated powders at the four conditions. Standard peaks from Cu13.7Sn, (Cu32Sn)0.12, and Cu are displayed below the XRD results for reference. Scale bars in the SEM images are 1 μm.

3.4.5 Mechanism

After understanding how temperature, residence time, quench gas, and EG concentration affect the powder morphology, crystallinity, and elemental distribution, the mechanism of Cu-Sn binary particle formation was investigated from two perspectives: chemical reaction steps and structural progression. To explore the chemical process of Cu-Sn binary particles generation from the precursor, two conditions were chosen at low temperature and low residence time to identify reaction intermediates. 300 ^{o}C was chosen because the initial decomposition temperature of EG is ~240 ^{o}C (Yue et al. 2012). As the droplets have not fully evaporated in this condition, the crystallinity of the powder was poor with an obvious amorphous background in the XRD diagram (Figure 3.16), compared to previous XRD results. The peaks in the Figure 3.16 were attributed to metal hydroxide salts ($Cu_2Cl(OH)_3$ and $SnCl_2(H_2O)_2$) and metal (Sn).

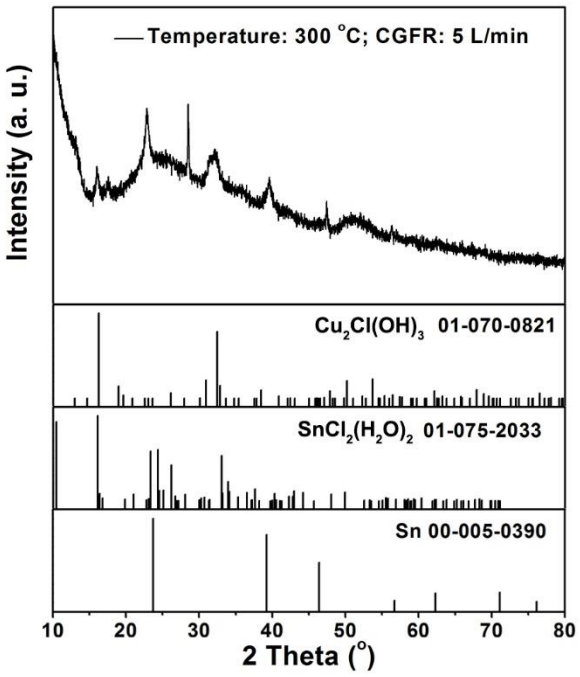

Figure 3.16. XRD diagram of powders fabricated from precursors containing 1 M $Cu(NO_3)_2$, 0.1 M $SnCl_2$, 0.1 M HNO_3, and 5.9 M EG in a total volume of 150 ml aqueous solution. Spray pyrolysis was conducted at 300 ^oC with CGFR = 5 L/min and a quench gas velocity of ~ 5.2 L/min. Possible phases are $Cu_2Cl(OH)_3$ (ICDD, PDF No. 01-070-0821), $SnCl_2(H_2O)_2$ (ICDD, PDF No. 01-075-2033), and Sn (ICDD, PDF No. 00-005-0390).

To further explore the particle formation process, the temperature was increased to 500 ^oC and the CGFR was increased to 10 L/min to keep the residence time less than 0.74 s. As shown in Figure 3.17, the samples generated from 500 ^oC consisted of metal hydroxide salts ($Cu_2Cl(OH)_3$ and $Cu_2(NO_3)(OH)_3$), metal oxides (Cu_2O and CuO), and solid solutions (Cu13.7Sn). Based on the discussion above, it is proposed that the spray pyrolysis process of converting precursor to Cu-Sn binary particles is composed of the following chemical reaction steps.

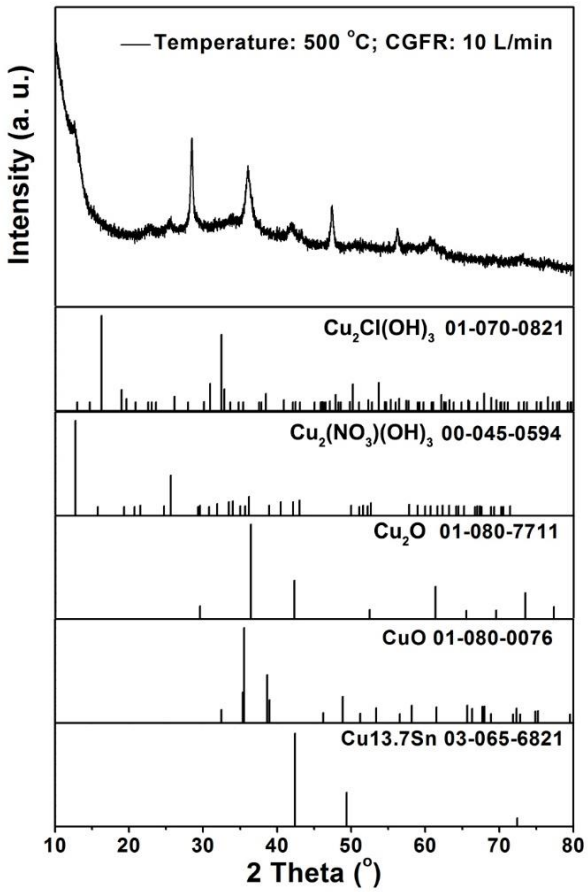

Figure 3.17. XRD diagram of powders fabricated from precursors containing 1 M $Cu(NO_3)_2$, 0.1 M $SnCl_2$, 0.1 M HNO_3, and 5.9 M EG. Spray pyrolysis was conducted at 500 ºC with CGFR = 10 L/min and a quench gas velocity of ~ 10.8 L/min. Possible phases are: $Cu_2Cl(OH)_3$ (ICDD, PDF No. 01-070-0821), $Cu_2(NO_3)(OH)_3$ (ICDD, PDF No. 00-045-0594), Cu_2O (ICDD, 01-080-7711), CuO (ICDD, PDF No. 01-080-0076), and Cu13.7Sn (ICDD, 03-065-6821).

i) Hydrolysis of the salts

With the increase of temperature within the droplets (Figure 3.1d,e) and the relative solute concentration (caused by the solvent evaporation), metal salts gradually hydrolyze

to hydroxides (Cohen and West 1972; Munnik et al. 2011). Thus, the possible reactions are:

$$2Cu(NO_3)_2 + 3H_2O \rightarrow Cu_2(NO_3)(OH)_3 + 3HNO_3 \quad (3.6)$$

$$2SnCl_2 + 3H_2O \rightarrow Sn_2Cl(OH)_3 + 3HCl \quad (3.7)$$

These products were observed in Figures 3.16,3.17. $CuCl_2$ may be formed from ion exchange, which is possible for the lower solubility of $CuCl_2$ (43.8 g in 100 g H_2O) compared to $Cu(NO_3)_2$ (60.1 g in 100 g H_2O) (Perry 2011). $CuCl_2$ may also hydrolyze in a similar way.

$$2CuCl_2 + 3H_2O \rightarrow Cu_2Cl(OH)_3 + 3HCl \quad (3.8)$$

This product phase was observed in Figure 3.16.

ii) Formation of metal oxides

With the further increase of temperature, the hydroxides begin to decompose to oxides:

$$Cu_2(NO_3)(OH)_3 \rightarrow 2CuO + HNO_3 + H_2O \quad (3.9)$$

$$Cu_2Cl(OH)_3 \rightarrow 2CuO + HCl + H_2O \quad (3.10)$$

$$Sn_2Cl(OH)_3 \rightarrow 2SnO + HCl + H_2O \quad (3.11)$$

Similar results have also been reported (Cohen and West 1972; Munnik et al. 2011). CuO was detected in XRD measurements (Figure 3.17).

iii) Reduction of the metal oxides to metals

As EG can create a reducing environment (Yue et al. 2012), metal oxides will finally be reduced to Cu and Sn. The evidence for the existence of copper and tin can be seen in the Figures 3.2,3.16, respectively. Cu_2O was detected in the XRD (Figure 3.17).

iv) Diffusion of Sn to form a solid solution

Finally, the Sn will dissolve into the Cu crystal matrix to form the Cu-Sn solid solution. However, the solid solution formation would not be completed at low temperature such as 500 ^oC. Therefore, both Cu and Cu13.7Sn phases were observed in the XRD diagram (Figure 3.2, black peaks). Based on Cu-Sn phase diagram, the phases in the Cu-Sn binary system with same Cu/Sn ratio at 500 ^oC should be Cu and Cu3.73Sn (Miettinen 2008). The formation of Cu13.7Sn could be attributed to three causes: i) The cooling effect caused by introducing quench gas could cause the product to be trapped in a nonequilibrium state; ii) Cu and Cu13.7Sn share the same Fm-3m point group symmetry, with close lattice spacing (Cu: 3.625 Å; Cu13.7Sn: 3.688 Å) (Andresen 1958; Srinivasan and Anantharaman 1963); iii) The accumulation of Sn on the particle surface may increase the Cu/Sn ratio in the bulk compared to the Cu/Sn ratio in the precursor (10). Cu13.7Sn is a stable phase with Cu/Sn ratio higher and close to 10 (Chatterjee and Gupta 1975). When the set point of the furnaces was 750 ^oC, the increased temperature would promote the formation of Cu-Sn solid solution. Thus, only Cu13.7Sn was observed in Figure 3.2 (red peaks). When the temperature was further increased to 1000 ^oC, the high temperature would lead to the system in the liquid state (Booth et al. 1977), implying facile diffusion of tin into copper matrix to form the Cu13.7Sn phases. Therefore, Cu13.7Sn was found in Figure 3.2 (blue peaks). Peaks in Figure 3.12d were also belonged to Cu13.7Sn for the same reasons.

A general mechanism has been proposed to explain the particle formation in spray pyrolysis using multi-source precursors (Gurav et al. 1993). Applying this mechanism to our specific Cu-Sn system, hydrolysis of $SnCl_2$ may lead to the precipitation of SnO in the droplets before precipitation of $Cu(NO_3)_2$. The formation of Cu-Sn particles involves a structural evolution from granular precipitates to a dense solid solution of Cu-Sn. The detailed process can be summarized as follows, together with the schematic illustration presented in Figure 3.18:

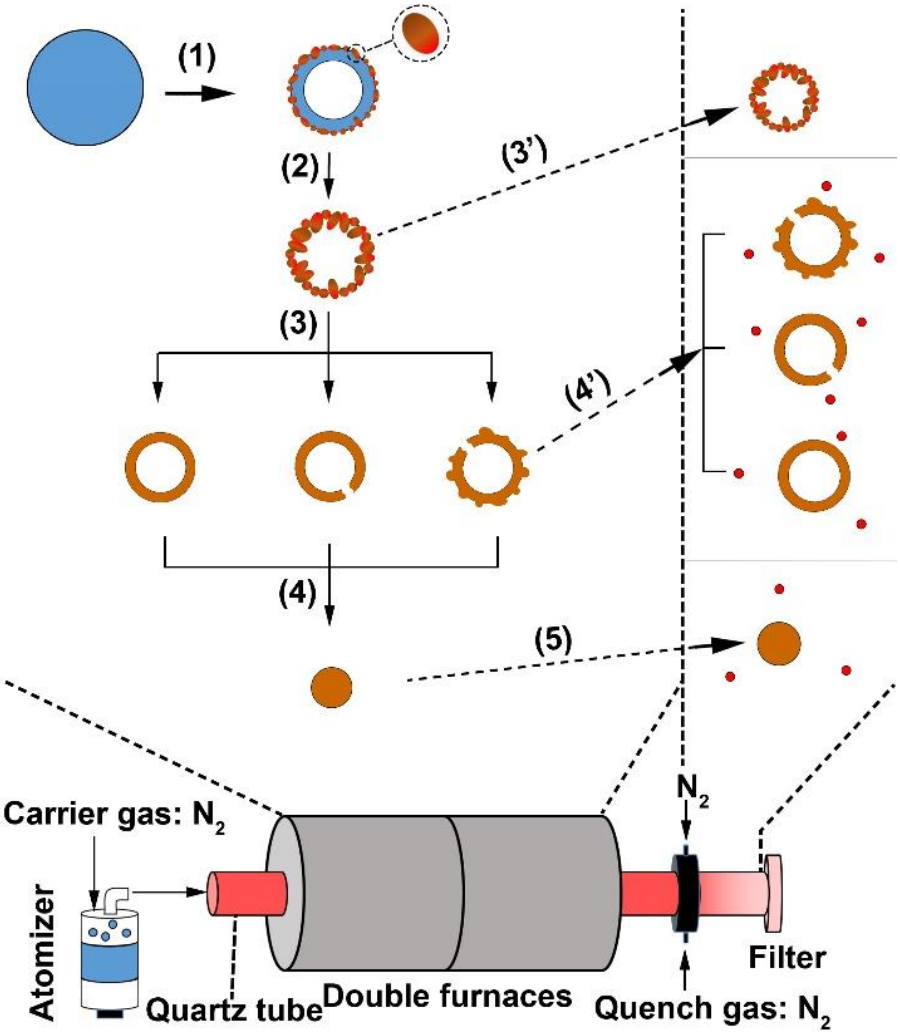

Figure 3.18. Schematic illustration of the proposed Cu-Sn binary particle formation process. The circle in Step (1) represents the precursor droplet. The magnified image of the

Step (1) product illustrate the Cu-Sn solid solution and the metallic copper, respectively. The small circles are the metal particles formed by gas-to-particle conversion.

a) Precipitation on the droplet surfaces

After the precursor droplets were carried into the furnaces, rapid evaporation of HNO_3 and solvents, particularly H_2O (due to a higher vapor pressure than EG) (Speight 2004; Yue et al. 2012), would occur. It could assist the hydrolysis of tin salts, forming the precipitates (Perry 2011), as well as generate a concentration gradient of the dissolved solutes within the droplets. Precipitation will readily occur when the solute concentration reaches the saturation point. Thus, droplets with primary particle shells and liquid EG cores would take shape.

The reduction of precipitates to metals occurs by reaction with H_2 which is produced from EG decomposition. In the magnified image of the Step 1 product (Figure 3.18), the brown part represents the Cu-Sn solid solution, while the red part illustrates the metallic copper. These substances were both found in XRD results at 500 ^oC (Figure 3.2). Once the solvents evaporate, hollow structures would be formed with primary particles comprising the shell (Step 2, Figure 3.18). If the process is ceased here, porous hollow particles would be generated (Step 3', Figure 3.18). The hollow porous structure has been observed in Figure 3.3a and 3.5a. In some cases, bursting of the droplets may occur due to the buildup of pressure caused by solvent evaporation (Gurav et al. 1993). Then fragmented, hollow, and porous particles can be found, as shown in the insets of Figure 3.3a.

b) Melting and shrinking of the hollow structure

After the hollow porous structure is generated, the primary particles will begin to sinter at the high temperatures, possibly caused by melting. In the meantime, Sn may diffuse into the Cu matrix to form a solid solution (Step 3, Figure 3.18). Hollow structures with rough crusted shells would be fabricated if the process stops here, as shown in Figure 3.5c. Other structures *e.g.*, fragmented spherical particles (Figure 3.3b, marked by red arrow), could also be regarded as products of the interconnection of primary particles seen in the powders at 500 ^{o}C (inset of Figure 3.3a). In addition, the evaporation of solvent may cause pore formation on the particle surfaces (Figure 3.7d). Therefore, morphologies as shown in Figures 3.3b,3.7d-f can be seen once the process is stopped after the gas-to-particle conversion (step 4', Figure 3.18).

c) Solidification

In the final step, solidification would be achieved once the residence time is long enough and temperature is high enough (step 4, Figure 3.18). After being cooled by the quench, small particles could be generated by gas-to-particle conversion (step 5, Figure 3.18). The detailed gas-to-particle conversion is presented in Section 3.4.1. On the filter, the small particles tend to attach on the particles instead of coating on the surface of big particles. Thus, morphologies as shown in Figures 3.3c,3.5e could be observed.

Micron-sized solid particles are favored for applications including conductive thick film pastes used for printing conductive lines and interference packaging (Huang and Sheen 1997; Wu et al. 2009). Based on our experimental results, high temperature (1000 ^{o}C) and long residence time (4.5 s) promotes the formation of micron-sized solid Cu-Sn particles, a potential condition for the further real application. The accumulation layer of Sn on the particle surface may protect the particle from being oxidized. The exploration of

Cu/Sn oxidation resistance and conductivity as a function of composition and processing environment is the subject of following chapters.

3.5 Summary of this chapter

Cu-Sn binary particles were fabricated by spray pyrolysis with EG as the co-solvent and reducing agent. By tuning the temperature, residence time, and quench gas flow rate, particles could be generated with controllable morphologies, crystallinities, and elemental distributions, which may broaden the further application of Cu-Sn bimetallic particles. Hollow porous particles were generated at 500 ^{o}C, with primary particles comprising the surface. The existence of Cu and Cu13.7Sn indicated that the generation of Cu-Sn binary particles may be incomplete at 500 ^{o}C. Cu13.7Sn phase was formed because of the cooling by introducing quench, the increased Cu/Sn ratio in the bulk caused by Sn enrichment on the particle surfaces, and the thermodynamic stability of Cu13.7Sn phase. With the increase of temperature, a transition occurred, causing the particle morphology to shift from hollow to solid, which has been validated by samples generated at 750 ^{o}C. At 1000 ^{o}C, solid particles could be generated with high quality crystallinity, and only Cu13.7Sn peaks were present in the XRD diagram. The Cu/Sn ratio was further increased on the particle surface at 1000 ^{o}C. The small particles were likely formed likely via gas-to-particle conversion.

The residence time and quench gas flow rate mainly contributed to the morphological differences. At the condition where the residence time was 4.5 s, spherical particles with smooth surfaces were obtained. The increase of the CGFR decreased the residence time, leading to insufficient time for the thermophoretic deposition of small particles on the tube walls, which could significantly reduce the loss. Thus, small particles became observable

when the residence time was 1.5 s. Particles with irregular morphologies were synthesized at the condition where residence time was 0.92 s. However, high quality crystallinity of Cu13.7Sn could be seen in all samples at 750 ^{o}C regardless of the CGFR changes.

From the experimental results, the mechanism of Cu-Sn binary particle generation can be explained through two perspectives: chemical reaction steps and structural progression. Substances in the precursor were first hydrolyzed into hydroxides. Then the hydroxides decomposed into metal oxides. Subsequently, the metal oxides were reduced to metals, and a solid solution formed. For the structural evolution, precipitation of the solutes occurred during solvent evaporation of the precursor droplets. Thus, hollow structures could be generated. Finally, the shrinking of the hollow particles continued until solid particles were formed. The accumulation of Sn on the particle surfaces could protect Cu from being oxidized. In addition, the method of generating Cu-Sn binary particles combined with the investigation of the underlying mechanism provides a foundation for fabricating other bimetallic particles.

Chapter 4: Oxidation behavior of Cu-Sn binary particle

4.1 Abstract

Micron-sized solid Cu-Sn particles have been considered as a replacement for more expensive materials (*e.g.*, Ag, Pd, and Au) in conductive pastes used in printed electronics, solar cell metallization, and interference packaging. With formation of a tin oxide layer, Cu-Sn particles could combine relatively low electrical resistivity with high oxidation resistance. However the oxidation behavior of this system is not well understood. In this chapter, the oxidation of $CuSn_y$ solid particles, fabricated by spray pyrolysis without direct addition of H_2, was investigated. Our experimental results and theoretical analysis suggest that at a low oxidation temperature (300 ^oC), the migration of O^{2-} through the oxide layer controls the oxidation. At high temperature (500 ^oC), the grain growth of the oxide layer is believed to be the rate-limiting step. Among the $CuSn_y$ particles tested, $CuSn_{0.1}$ powders exhibited the best particle structure (solid and spherical) and highest oxidation resistance.

4.2 Introduction

Metal particles have been widely applied in printed electronics (Comiskey et al. 1998; Li et al. 2005), interference packaging (Faddoul et al. 2012; Wang et al. 2007a), and solar cell metallization (Mokkapati et al. 2009; Temple and Bagnall 2011). Gold and silver are by far the most commonly used materials in these fields due to their high electrical conductivity and oxidation resistance (Comiskey et al. 1998; Faddoul et al. 2012; Li et al. 2005; Mokkapati et al. 2009; R et al. 2015; Temple and Bagnall 2011; Wang et al. 2007a). However, the high cost of these noble metals has increased interest in developing alternative cost-efficient materials such as copper (Cu) (Abhinav K et al. 2015; Yonezawa

et al. 2015a; Yonezawa et al. 2015b) for these applications. Several challenges, such as the ease of oxidation of copper materials and the high mobility of copper in silicon (a common substrate in the electronics industry), have to be addressed before widespread application of copper-based powders (Istratov et al. 2000; Kim et al. 2004). The oxidation behavior of Cu is known to be complex since many processes, including electron migration across the metal/oxide interface, recrystallization of the pseudomorphic oxide layer, external/internal diffusion of O_2 gas, and chemical reactions, can happen simultaneously (Cabrera and Mott 1949; Feng et al. 2003; Fujita et al. 2013; Levenspiel 1999). Particle engineering with an oxidation-resistant layer on a Cu core has been proposed as an effective configuration. The oxidation-passivation layer can be metals (*e.g.*, Ag, Zn, Ni, and Au) or organic compounds (Jianfeng et al. 2011; Jung et al. 2011; Kim et al. 2013; Li et al. 2016a; Sharma et al. 2014; Xu et al. 2012; Yonezawa et al. 2015a; Yuan et al. 2013). Nevertheless, there is a need to explore other strategies from a comprehensive view of cost and electrical conductivity.

Tin (Sn) has been reported as an effective protector against copper oxidation, since tin is more reactive towards oxygen than copper and tin oxides maintain relatively high conductivity (Liu et al. 2005; Liu et al. 2007a). In addition, tin is a diffusion barrier between copper and silicon, which provides extra benefit for practical applications, in particular, in solar cell metallization (Liu et al. 2005; Liu et al. 2007a). Recently, the electrical resistivity of $Cu_{core}Sn_{shell}$ nanowires fabricated by electroplating method was found to remain at the same order of magnitude after being oxidized for 25 h, while the resistivity of Cu nanowires increased by 10^7 in 15 min under the same oxidation conditions (Chen et al. 2014). However, rather than nanowires, micron-sized solid particles are favored by industry for applications such as conductive pastes and interference packaging (Deshpande et al. 2005;

Wu et al. 2009). To address this issue, Cu-Sn binary powders with Sn-enriched surface layer have been produced by a scalable process, spray pyrolysis, without the direct addition of H_2 (Chapter 3).

As a next step, here, we present a detailed investigation of the oxidation behavior of $CuSn_y$ (*y* is the atomic ratio of Sn/Cu in the product) solid particles fabricated by spray pyrolysis. A quantitative understanding of the phase evolution of $CuSn_y$ particles during oxidation was obtained through Rietveld refinement analysis of the X-ray diffraction (XRD) patterns. To better understand the oxidation behavior of $CuSn_y$ particles under high temperature, *in-situ* XRD measurements were conducted in ambient air. Kinetics experiments were performed to determine the oxidation kinetics of $CuSn_y$ particles and the oxidation mechanisms at different temperatures. Together, these results were used to identify the $CuSn_y$ particle composition that has optimal oxidation resistance and spherical morphology.

4.3 Experimental

4.3.1 $CuSn_y$ particle preparation

We synthesized the $CuSn_y$ particles following procedures discussed in Chapter 3. In brief, a 150 mL aqueous precursor solution that contained 1 M $Cu(NO_3)_2$ (99.5%, STREM CHEMICALS), 0.1 M HNO_3 (70%, SIGMA-ALDRICH), and 4.8 M ethylene glycol (EG, 98% SIGMA-ALDRICH) was firstly prepared. $SnCl_2$ (≥98% FISHER SCIENTIFIC) was used as the tin source and then added to the aqueous precursor solution with a concentration based on the targeted Sn/Cu atomic ratio (from 0 to 1) in the product particles. The precursor solution was atomized by a 1.7 MHz ultrasonic generator into droplets with

volume mean dimeter of 5 μm, measured experimentally under similar experimental conditions (Zhong et al. 2012). The droplets were carried by N_2 (99.5%, AIRGAS) into a quartz tube reactor heated by two furnaces in series both set at 1000 ^oC. A polytetrafluoroethylene (PTFE) filter was used to collect the products at the end of the quartz tube after the powders were cooled down by N_2 gas. The residence time of the process was estimated to be 1.2 s, measured and calculated by the same procedures reported in Chapter 3.

4.3.2 $CuSn_y$ powder characterization

Scanning electron microscopy (SEM, HITACHI SU-70) and transmission electron microscopy (TEM, JEOL 2100 FEG) with energy dispersive X-ray spectroscopy (EDS) were utilized to understand the particle morphology, structure, and elemental distributions. $CuSn_y$ powders were suspended and sonicated in ethanol for 1 min before being added dropwise onto silicon wafers for SEM and TEM grids for TEM. X-ray photoelectron spectroscopy (XPS, Kratos Axis 165) was performed to understand the element distributions on the powder surface and sub-surface (sputtered in vacuum by argon ions for 20 min with the sputtering gun set at 4 kV and 5 mA).

X-ray diffractometry (Bruker D8 advance) was used to obtain crystallographic information of the $CuSn_y$ powders. Rietveld refinement was conducted by Topas-5 software from Bruker to determine the phase composition of the powders. *In-situ* XRD (Bruker C2 Discover) was performed to continuously monitor the phase evolutions of the $CuSn_y$ powders during oxidation. Powders were placed on a Pt plate and heated by a programmed hot stage in ambient air. When the powders reached the targeted temperature, the hot stage was kept at that temperature for 15 min for the XRD measurements. After the

XRD measurements were completed, the temperature of the Pt plate was raised to the next target. Thermogravimetric (TG) and differential scanning calorimetry (DSC) results were measured by a SDT Q600 (TA Instruments) to understand the weight gain and heat flow during the oxidation. Alumina pans containing ~2 mg $CuSn_y$ powders were heated from room temperature to 600 °C at a rate of 5 ^oC/min under 100 mL/min of compressed O_2 flow.

4.3.3 Oxidation kinetics investigation

The oxidation kinetics of $CuSn_y$ particles was studied by performing the reaction in a U-shape tubular quartz reactor with a 10 mm inner diameter. Typically, 0.5 g of the particle powder was loaded into the quartz reactor, and the reactor was placed inside a furnace (National Electric Furnace FA120 type) controlled by a Watlow Controller (96 series). A K-type thermocouple was placed inside the furnace to monitor the particle temperature by attaching the tip of the thermocouple to the outer wall of the powder bed. The particle powder was heated to the desired temperature in He atmosphere (30 mL/min) at a ramp rate of 5 ^oC/min. Afterwards, O_2 (1 mL/min, 99.9993% purity, Airgas) diluted in N_2 (as internal standard) (15 mL/min, 99.95% purity, AIRGAS) and He (as balance gas) (35 mL/min, 99.9993% purity, AIRGAS) was introduced to the reactor through heated transfer lines held at 70 ^oC. The O_2 concertation in the reaction system was quantified using a gas chromatograph (Agilent Technologies, 6890N) equipped with a ShinCarbon ST packed column connected to a thermal conductivity detector (TCD). The volume percent of O_2 in the feed stream was set to be 1.4 % and 10 %, respectively, by changing the flow rate of O_2 and balancing the total flow using He.

4.4 Results and discussion

4.4.1 $CuSn_y$ particle preparation by spray pyrolysis

The $CuSn_y$ particles were obtained by reducing the corresponding metal salts during spray pyrolysis. After the precursor was atomized into droplets, the droplets were transported by carrier gas into the quartz tube reactor. In the reactor, $Cu(NO_3)_2$ and $SnCl_2$ were hydrolyzed into hydroxides. Subsequently, the hydroxides were decomposed into metal oxides, which were then reduced to metals by the reducing gases (H_2 and CO) generated through the decomposition of EG (Yue et al. 2012; Zhong et al. 2012). At the same time, a series of processes occurred, including solvent evaporation, solute precipitation, chemical reaction, nucleation, and crystal growth, leading to the formation of particles. Based on our previous findings in Chapter 3, high temperatures and long residence times promote the formation of solid particles. Herein, the $CuSn_y$ particles were produced at 1000 ºC with a residence time of 1.2 s, based on the experimental results presented in Chapter 3.

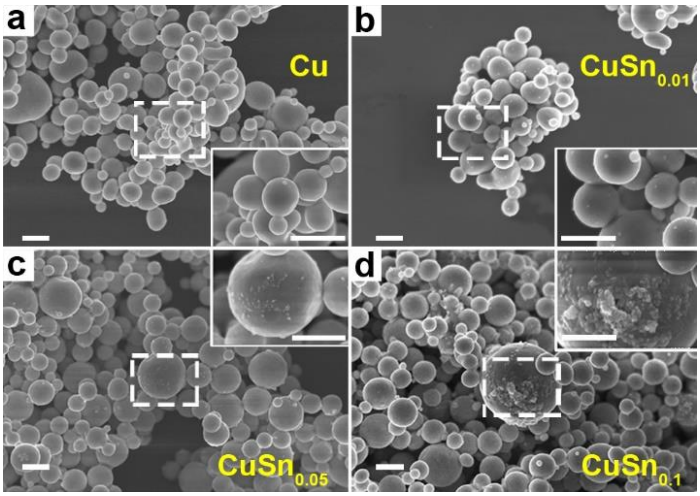

Figure 4.1. SEM images of Cu (a), $CuSn_{0.01}$ (b), $CuSn_{0.05}$ (c), and $CuSn_{0.1}$ (d) particles. The insets in each panel are the high magnification images of the selected regions marked by dashed squares. The scale bars are 1 μm for all the images.

Cu particles display solid and spherical structures with smooth surfaces, as demonstrated by SEM (Figure 4.1a) and TEM (Figure 4.2a) images. The lattice fringes in Figure 4.2b represent the (111) plane of Cu (PDF No. 01-070-3038) with a d-spacing of 2.1 Å. The corresponding diffraction pattern attributed to the Cu (111) plane (inset of Figure 4.2b) is obtained by performing fast Fourier transform (FFT), suggesting a high degree of crystallinity. This hypothesis is also validated by the pronounced Cu peaks in XRD spectrum (Figure 4.3).

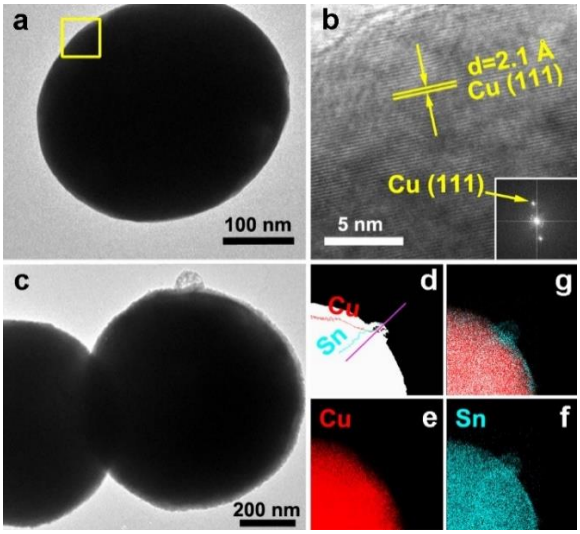

Figure 4.2. TEM images of Cu particle (a) with corresponding HRTEM image (b) of selected area in (a). The inset of (b) is the fast Fourier transform (FFT) of the HRTEM. TEM image of $CuSn_{0.01}$ particles (c) with HAADF image and line scan results of Cu and Sn (d), elemental mapping of Cu (e) and Sn (f), and overlap mapping (g).

With increasing Sn concentration, the $CuSn_y$ particles retain spherical and solid structure when $y \leq 0.1$, as shown in SEM (Figure 4.1b-d) and TEM (Figure 4.2c,4.4a-b) images. The number mean diameter of the $CuSn_y$ particles is 710 nm, same as the results

in Chapter 3. Small particles are observable on the surface of $CuSn_y$ ($y \leq 0.1$) sample. These small particles are mainly composed of Sn, validated by EDS mapping of Cu and Sn elements (Figure 4.2e-g). We believe these small Sn particles originate from evaporation and gas-to-particle conversion. The vapor pressures of SnO and Sn at 1000 ^oC are 370 Pa and 1.5×10^{-2} Pa, respectively (Gale and Totemeier 2003; Platteeuw and Meyer 1956). The evaporated SnO may be reduced to Sn by the reducing gases from EG decomposition and nucleate into small particles. With the increase of the relative concentration of Sn in the powder, Sn began to dissolve into Cu matrix to form a Cu-Sn solid solution, resulting in a blue shift of the Cu peaks to $Cu_{13.7}Sn$ (PDF No. 03-065-6821) peaks, as shown in Figure 4.3. For the $CuSn_{0.1}$ powders, the existence of $Cu_{13.7}Sn$ phase is attributed to i) the similar crystal structure and same Fm-3m point group symmetry of Cu and $Cu_{13.7}Sn$ (Saunders and Miodownik 1990); ii) the lower Sn/Cu ratio (less than that of precursor=0.1) in the particle center due to the Sn enrichment on the particle surface; iii) stable phase of $Cu_{13.7}Sn$ when Sn/Cu atomic ratio is close to 0.1 (Chatterjee and Gupta 1975).

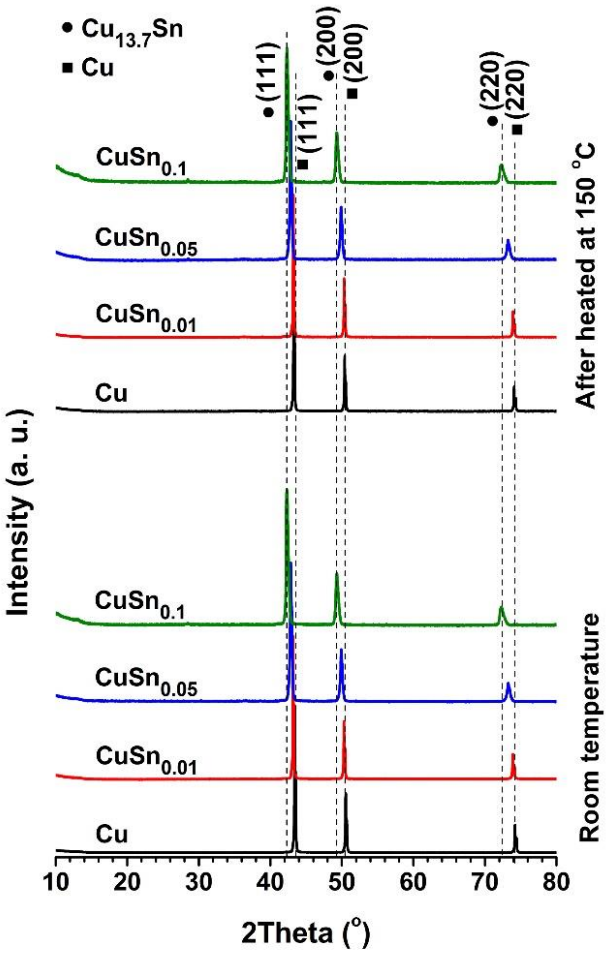

Figure 4.3. XRD diagrams of $CuSn_y$ solid particles at room temperature (bottom) and after being heated at 150 °C for 10 min in ambient air (top). The positions marked by circles and squares are standard peaks of $Cu_{13.7}Sn$ (circles, PDF No. 03-065-6821) and Cu (squares, PDF No. 01-070-3038), respectively.

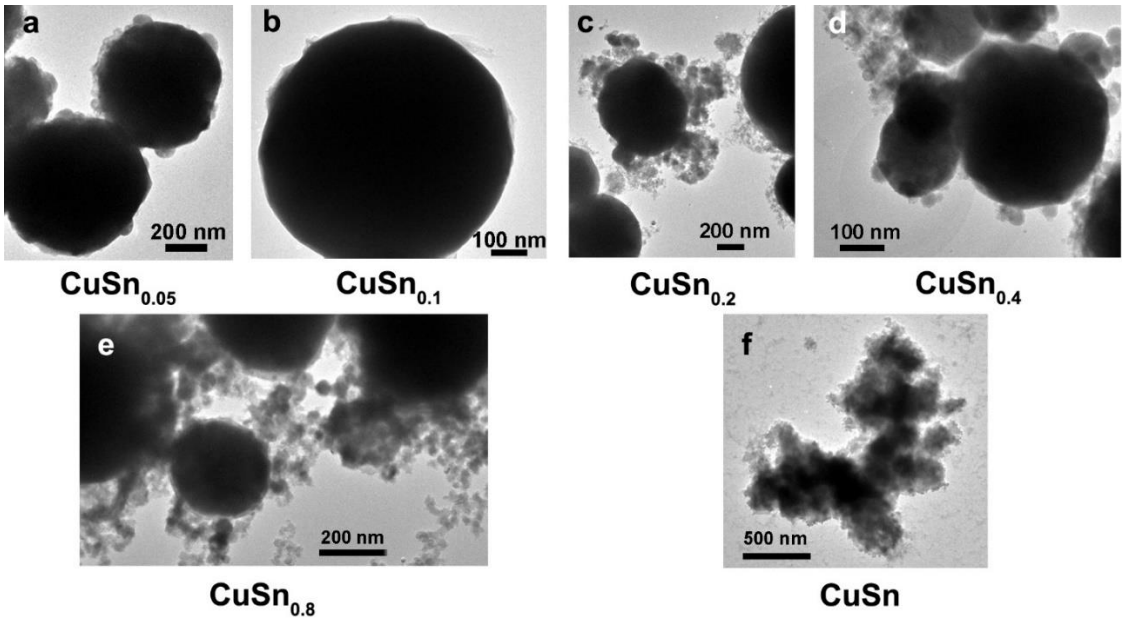

Figure 4.4. TEM images of $CuSn_{0.05}$ (a), $CuSn_{0.1}$ (b), $CuSn_{0.2}$ (c), $CuSn_{0.4}$ (d), $CuSn_{0.8}$ (e), and CuSn (f) products.

For $CuSn_y$ ($y \geq 0.1$) particles, the small Sn particles on the particle surface tend to coagulate into bigger structures (Figures 4.4c-f,4.5). Since the set points of the furnaces (1000 ^oC) are higher than the melting point of bulk Sn (230 ^oC) (Ju et al. 2015), melted Sn may have formed the interconnection between adjacent particles when y = 0.2 and 0.4 (highlighted by dashed circles in Figure 4.5a-b) and even led to the coalescence of $CuSn_{0.8}$ and CuSn particles at the surface into islands (Figures 4.4e-f,4.5c-d). The melting points of Cu (1085 ^oC) and Cu-Sn solid solutions (from 1085 ^oC (Sn at % = 0) to 945 ^oC (Sn at % = 10%)) are much higher than that of Sn (Saunders and Miodownik 1990). Thus, the coalescence of the $CuSn_y$ also indicates that a Sn-enriched layer is on the particle surface.

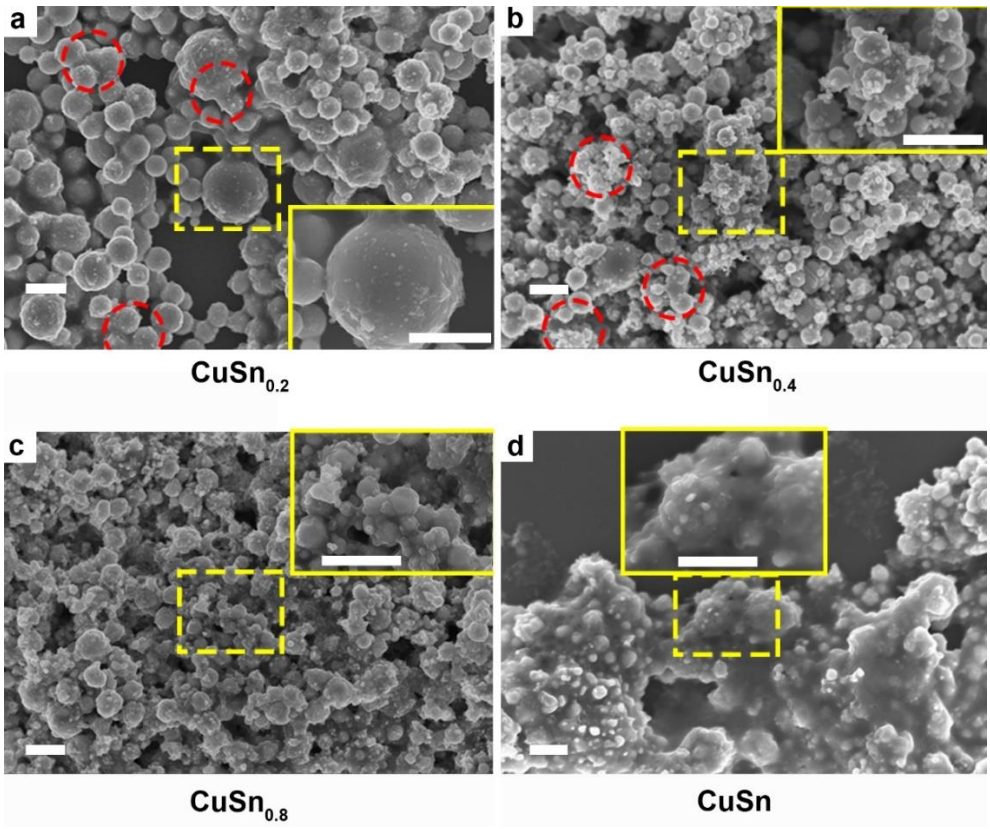

Figure 4.5. SEM images with the corresponding high magnification images of the areas marked by dashed boxes of $CuSn_{0.2}$ (a), $CuSn_{0.4}$ (b), $CuSn_{0.8}$ (c), and CuSn (d). The scale bars in all images are 1 μm.

To test this hypothesis, XPS measurements and EDS line scan characterizations were performed on the particle samples. Based on the XPS results shown in Figure 4.6, the Sn/Cu atomic ratio is significantly higher on the particle surface (before sputtering) than beneath the surface (after sputtering) or in the precursor. In Figure 4.7, for Cu 2p electrons, metallic copper has a major peak at 932.4 eV (Fleisch and Mains 1982). For Cu LMM Auger electrons, shoulder peaks around 565 eV are attributed to metallic copper, while peaks around 570 eV are evidence for the existence of copper oxides (Fleisch and Mains 1982; Sen et al. 2009). The EDS line scan also validates that hypothesis. The relative Sn/Cu

atomic ratio is higher on the particle surface than in the core (Figures 4.2d,4.8). This difference of Sn and Cu distribution along particle radius may stem from the different precipitation rates between the salts and subsequent mass diffusion (Gurav et al. 1993). The reported diffusivities are $D_{\text{Cu-in-Sn}} = 7.57\times10^{-11}$ m^2/s, $D_{\text{Sn-in-Cn}} = 5.09\times10^{-24}$ m^2/s, and $D_{\text{Cu-in-Cu}} = 6.22\times10^{-26}$ m^2/s at 220 ^{o}C (Mei et al. 1992). In spray pyrolysis, the components with lower solubility precipitate earlier than those with higher solubility during the evaporation of droplet solvent (Gurav et al. 1993). With the evaporation of HNO_3 during the solvent evaporation, the hydrolysis of $SnCl_2$ may accelerate the precipitation of SnO, while $Cu(NO_3)_2$ still remains dissolved in the droplet solvent (Perry 2011). Together with the aforementioned small Sn particles depositing on the surface of $CuSn_y$ particles, attributed to gas-to-particle conversion, a Sn-enriched layer is formed on the particle surface. The fluctuations of Sn/Cu atomic ratio (before sputtering, Figure 4.6) are possibly caused by the irregular structures as shown in Figures 4.4,4.5,4.8. Based on the mass balance calculations between the precursors and the product particles (mean diameter: 710 nm), the $CuSn_{0.1}$ particle is composed of a $Cu_{13.7}Sn$ core and a 3 nm-Sn layer as the shell (discussed in Chapter 3). For $CuSn_{0.05}$ particle, a 2.1 nm Sn-enriched layer is estimated on a $Cu_{32}Sn$ core. For $CuSn_{0.01}$ particles, the Cu core is encapsulated by a 1.2 nm Sn-enriched layer. Although only for a single particle, the EDS mapping results are consistent with this calculated Sn shell thickness. A summary of the experimental conditions to obtain the spherical $CuSn_y$ ($y\leq0.1$) particles and their particle configuration is shown in Table 4.1.

The previously reported particle engineering methods mainly focus on the core-shell configuration to improve oxidation resistance (Grouchko et al. 2009; Jianfeng et al. 2011; Kim et al. 2013; Kobayashi and Sakuraba 2008; Yamauchi et al. 2010). However, core-

shell particle production may incorporate sophisticated operating procedures, restricting the future scale-up production. Our $CuSn_y$ particles with Sn enrichment on surface, produced from one-step process, can protect Cu by forming a sacrificial oxide layer. As solid spherical particles are favored in the fields of solar cell metallization and interference packaging, the oxidation behavior of $CuSn_y$ ($y \leq 0.1$) powders was investigated next.

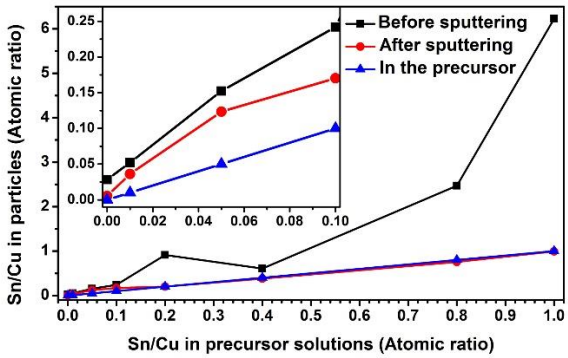

Figure 4.6. The Sn/Cu atomic ratios summarized from XPS results (Figure 4.7). The inset represents the regime where Sn/Cu ratio is below 0.1. Sputtering was conducted in vacuum by argon ions for 20 min.

Table 4.1. Summary of the configurations of $CuSn_y$ particles ($y \leq 0.1$) based on mass balance calculation and experimental conditions to obtain these particles

		Cu	$CuSn_{0.01}$	$CuSn_{0.05}$	$CuSn_{0.1}$
Particle configuration	Core	Cu	Cu	$Cu_{32}Sn$	$Cu_{13.7}Sn$
	Shell		1.2 nm Sn	2.1 nm Sn	3 nm Sn
$[SnCl_2]$ in precursor solution (mol/L)		0	0.01	0.05	0.1
$[Cu(NO_3)_2]$ in precursor solution (mol/L)		1			
Reaction temperature (^oC)		1000			
Residence time (s)		1.2			

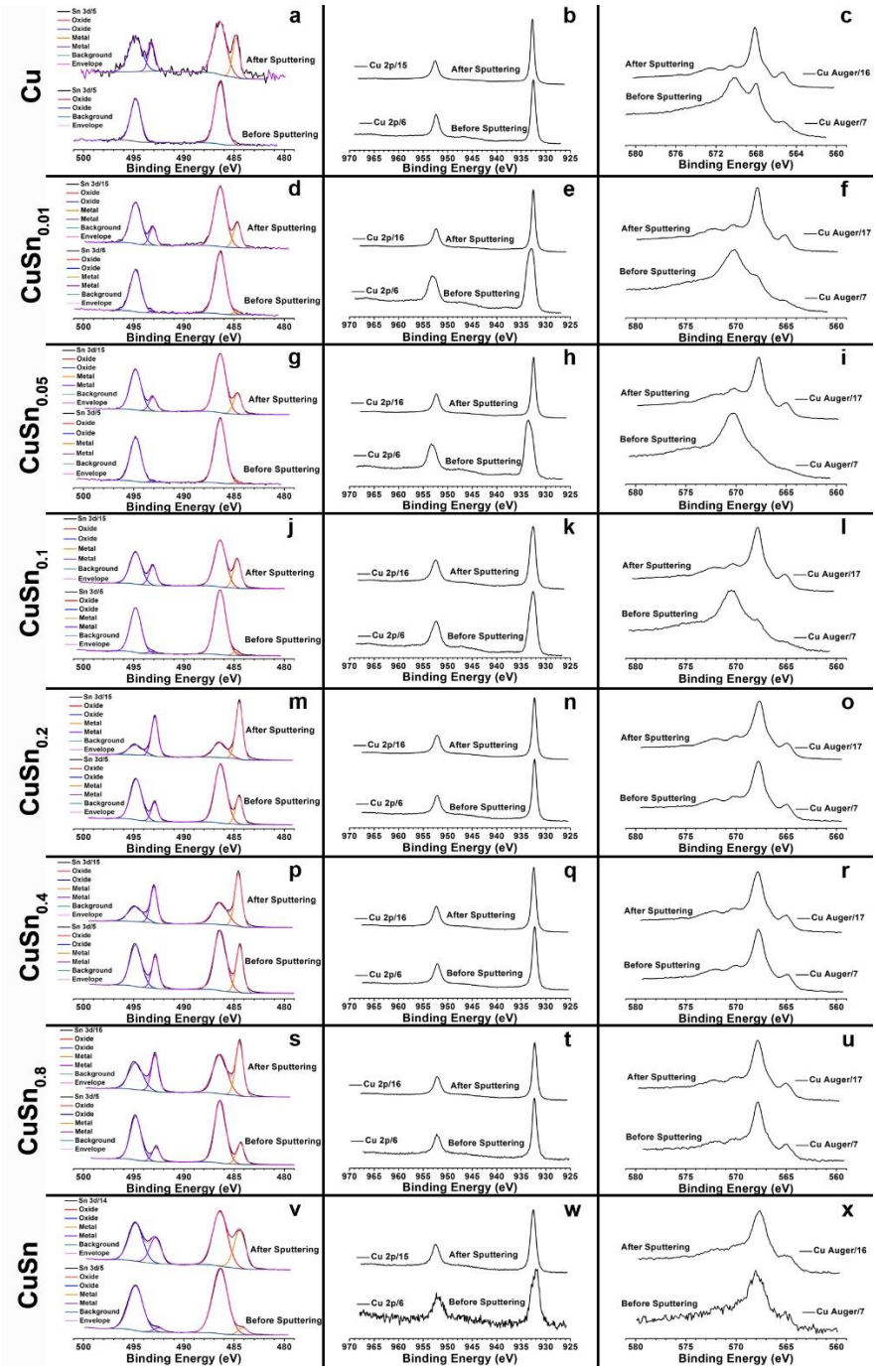

Figure 4.7. XPS signals of Cu (a-c), $CuSn_{0.01}$ (d-f), $CuSn_{0.05}$ (g-i), $CuSn_{0.1}$ (j-l), $CuSn_{0.2}$ (m-o), $CuSn_{0.4}$ (p-r), $CuSn_{0.8}$ (s-u), and CuSn (v-x) particles before and after sputtering. Images in the left column represent the spectra from Sn 3d electrons. Images in the middle column illustrate the spectra from Cu 2p electrons. Images in the right column are the spectra from Cu LMM Auger electrons.

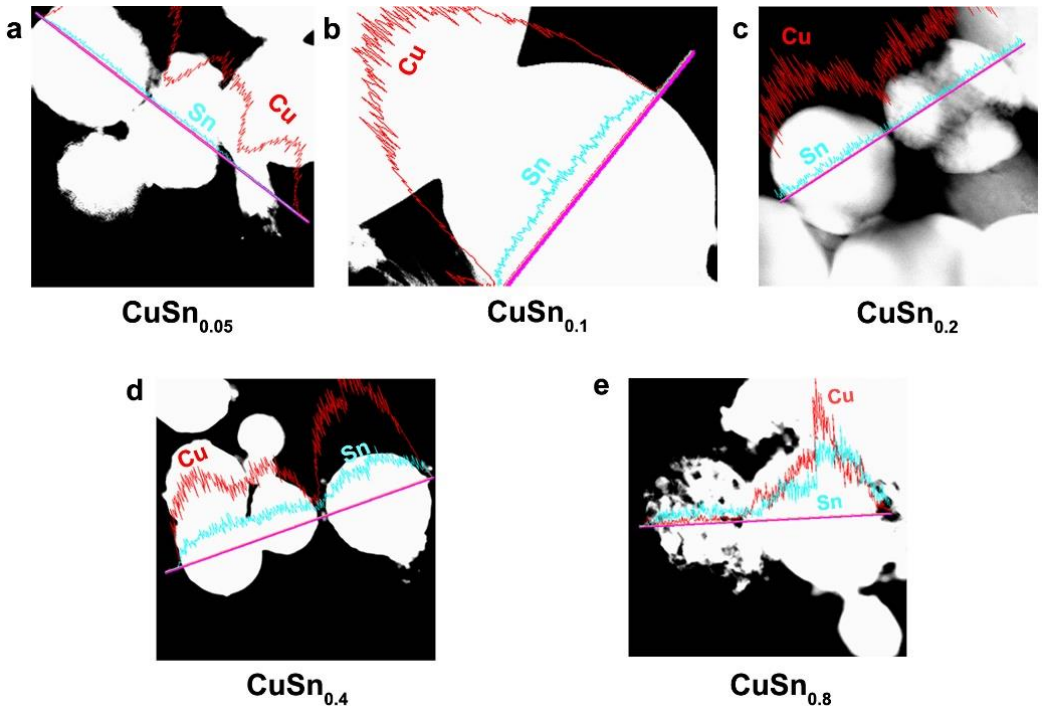

Figure 4.8. Line scans of Cu and Sn elemental profiles of $CuSn_{0.05}$ (a), $CuSn_{0.1}$ (b), $CuSn_{0.2}$ (c), $CuSn_{0.4}$ (d), and $CuSn_{0.8}$ (e).

4.4.2 Oxidation behavior of $CuSn_y$ particles

After the as-prepared $CuSn_y$ ($y \leq 0.1$) powders were oxidized at 150 ^oC for 10 min in ambient air, no detectable oxide peaks can be seen in the XRD patterns (Figure 4.3). Since the low temperature oxidation normally results in the formation of amorphous oxides or oxide crystals with low crystallinity (Kim et al. 2004), peaks from the oxides are negligible, compared to those from metals. We also observed the oxide layers at the edges of both Cu and $CuSn_{0.1}$ particles (Figure 4.9) after powder was oxidized at 100 ^oC for 60 min. However, the low degree of crystallinity of the oxide layer resulted in negligible peaks in the XRD spectrum. Therefore, the oxidation of $CuSn_y$ particles at this conditions is insignificant.

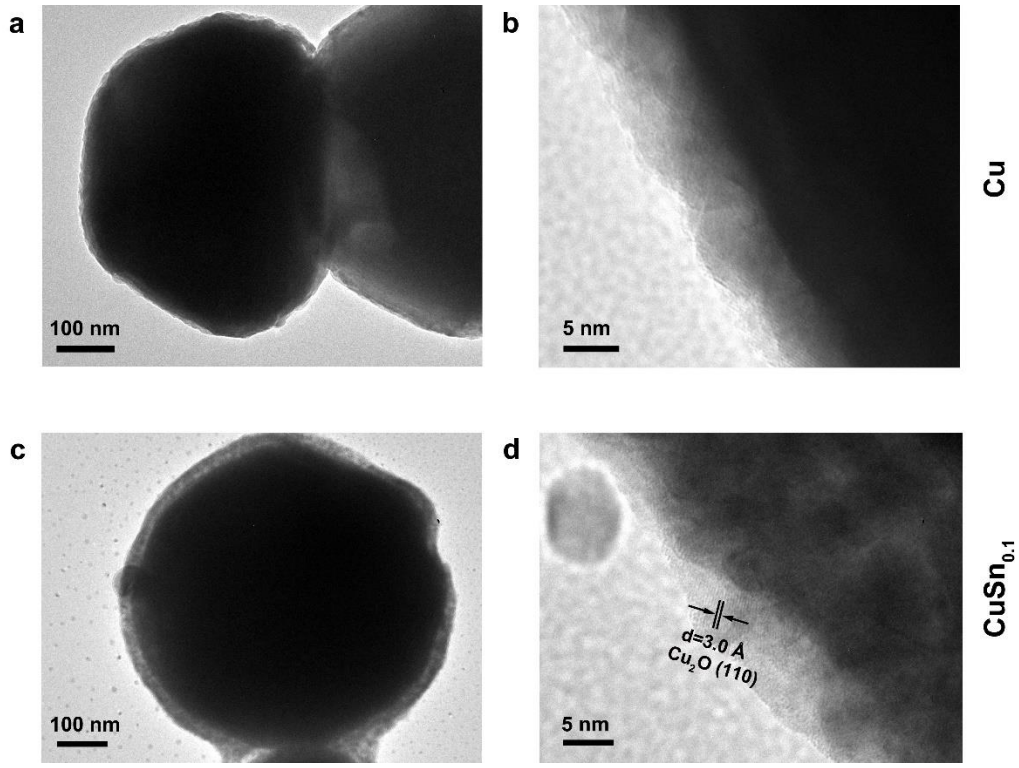

Figure 4.9. TEM images of the Cu (a-b) and $CuSn_{0.1}$ (c-d) particles after being oxidized in ambient for 60 min at 100 ^{o}C. Oxide layers were formed on the particle surfaces as shown by the lattice fringe in (d), which is attributed to the (110) plane of Cu_2O (PDF No. 01-071-3645).

More pronounced peaks attributed to oxides began to appear in Cu particles, after the as-prepared powders were heated at 300 ^{o}C for 10 min in ambient air, while observable peaks belonging to Cu_2O were exhibited in $CuSn_{0.01}$, $CuSn_{0.05}$, and $CuSn_{0.1}$ particles (Figure 4.10a-d). Therefore, Cu, $CuSn_{0.01}$, $CuSn_{0.05}$, and $CuSn_{0.1}$ powders are oxidized more significantly at 300 ^{o}C than at 150 ^{o}C. To understand the phase composition in these powders, Rietveld refinement was applied to analyze the XRD patterns. The Cu particles exhibit the lowest oxidation resistance at 300 ^{o}C with only 18 wt % of post-oxidation

powders remaining as Cu (Figure 4.10e). $CuSn_{0.01}$ powders display a sharp increase in the relative metallic amount (including Cu and Cu-Sn solid solution) in the post-oxidation products, from 18 wt % to 72 wt %, compared to that of Cu particles. However, CuO is still observable in the post-oxidation product of both Cu and $CuSn_{0.01}$ powders. Further increase of the Sn loading in the particles led to a higher relative amount of metallic products after oxidation, namely 92 wt % in $CuSn_{0.05}$ and 93 wt % in $CuSn_{0.1}$ powders. The oxidation resistance of $CuSn_{0.01}$ particles is close to that of Cu powders and significantly lower than $CuSn_{0.05}$ and $CuSn_{0.1}$ powders. This is possibly caused by the $CuSn_{0.01}$ particles not having enough Sn compared to the $CuSn_{0.05}$ and $CuSn_{0.1}$ powders. As shown in Figure 4.10f, the lattice parameter of Cu-Sn solid solution phases in the post-oxidation products of $CuSn_{0.01}$, $CuSn_{0.05}$, and $CuSn_{0.1}$ particles increases with the relative amount of Sn in the as-prepared particles, and larger than the lattice parameter of Cu. This indicates the increasing Sn relative amount in the post-oxidation products, since dissolving Sn into Cu matrix can increase the lattice parameter of Cu-Sn solid solution (Saunders and Miodownik 1990), which is consistent with the results in Figure 4.3. The lattice parameter of Cu-Sn solution in the post-oxidation product of $CuSn_{0.01}$ powders is close to that of Cu phase in the post-oxidation product of Cu particles. This further verifies that the insufficient Sn loading in the as-prepared $CuSn_{0.01}$ powders results in the similar oxidation resistance as that of Cu particles. Thus, the oxidation behavior of $CuSn_{0.05}$ and $CuSn_{0.1}$ particles was further investigated to find the optimal oxidation resistant composition, while Cu particles were utilized as the reference.

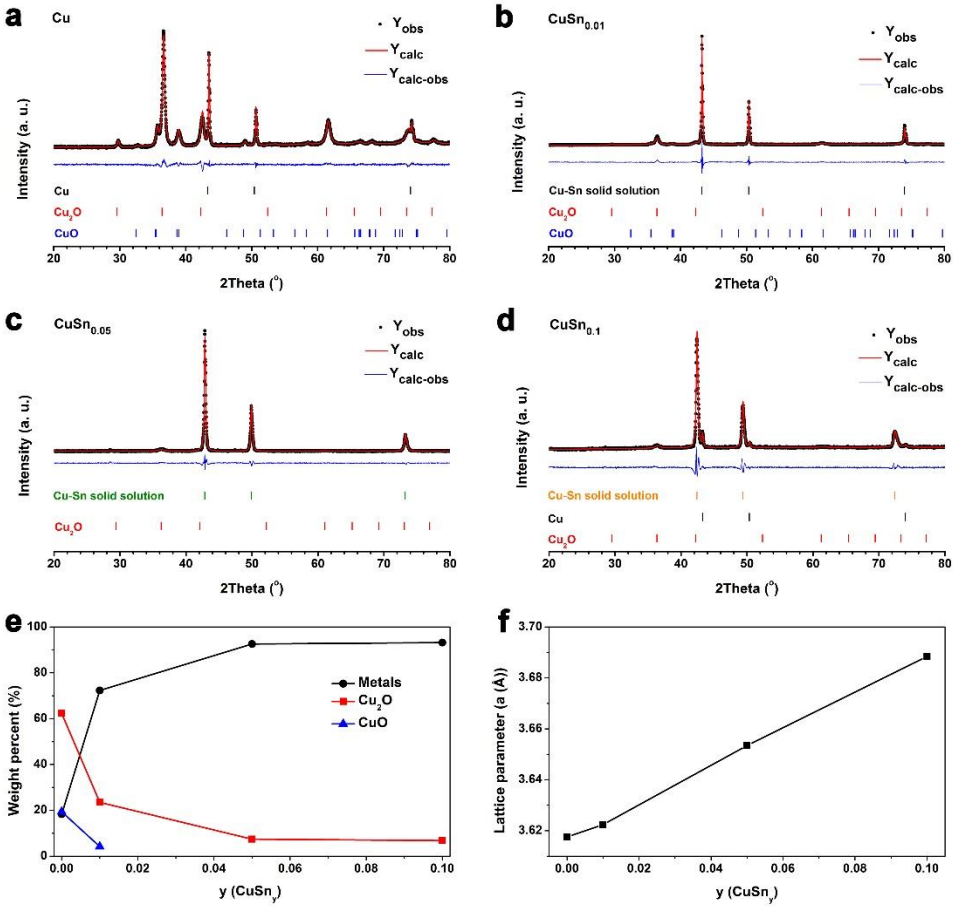

Figure 4.10. XRD patterns (Y_{obs}, black dots) of Cu (a), $CuSn_{0.01}$ (b), $CuSn_{0.05}$ (c), and $CuSn_{0.1}$ (d) powders, after they were oxidized at 300 °C for 10 min in ambient air analyzed by Rietveld refinement. XRD patterns were analyzed by Rietveld refinement (Y_{calc}, red curves) with the difference between the observed and calculated values ($Y_{calc-obs}$, blue curves). Tick marks represent the phases utilized in refinements, including Cu (black, PDF No. 00-004-0836), Cu_2O (red, PDF No. 01-071-3645), CuO (blue, PDF No. 01-073-6023), and Cu-Sn solid solutions. Cu-Sn solid solutions are Cu (black) in (b), $(Cu_{32}Sn)_{0.12}$ (green, PDF No. 01-077-7742) in (c), and $(Cu_{13.7}Sn)_{0.068}$ (yellow, PDF No. 01-071-7874) in (d). (e) Detailed results of the weight percent of crystal phases in post-oxidation products. (f) The evolution of lattice parameter from Cu in (a) to Cu-Sn solid solutions in (b-d). The Cu-Sn solid solution phases and Cu phase share the same space group of Fm-3m.

To further explore the phase evolution of the $CuSn_y$ powders, *in-situ* XRD measurements during oxidation were conducted with the temperature profile illustrated in Figure 4.11b. When temperature is below 200 ^oC and the oxidation duration is 62 min, no significant oxide peaks can be seen in all XRD patterns of the $CuSn_y$ (y = 0, 0.05, and 0.1) powders (Figure 4.11a). Peaks attributed to Cu_2O appear in all samples after being oxidized at 300 ^oC and the oxidation duration is 87 min. CuO phase is observed in $CuSn_y$ powders when the temperature is increased to 400 ^oC and the oxidation duration is up to 112 min. Therefore, the onset temperature of significant oxidation of $CuSn_y$ (y = 0, 0.05, and 0.1) powders is between 200 ^oC and 300 ^oC. To test this hypothesis, an oxidation experiment of long-time duration (up to 242 min) was conducted, keeping the temperature of powders at 200 ^oC during the *in-situ* XRD measurements, as shown in Figure 4.12. The CuO phase does not appear even after the $CuSn_y$ powders are heated for 227 min at 200 ^oC. Moreover, peaks of Cu_2O are observed after the powders are heated for 17 min, though the intensities of its peaks were low. The continuous oxidation of Cu, $CuSn_{0.05}$, and $CuSn_{0.1}$ powders leads to the increasing intensities of Cu_2O peaks. However, their intensities are still not comparable with those of metal peaks, even after being oxidized for 227 min, especially for the oxidation of $CuSn_{0.05}$ and $CuSn_{0.1}$. These results show that the $CuSn_{0.05}$ and $CuSn_{0.1}$ powders are more oxidation resistant than Cu particles.

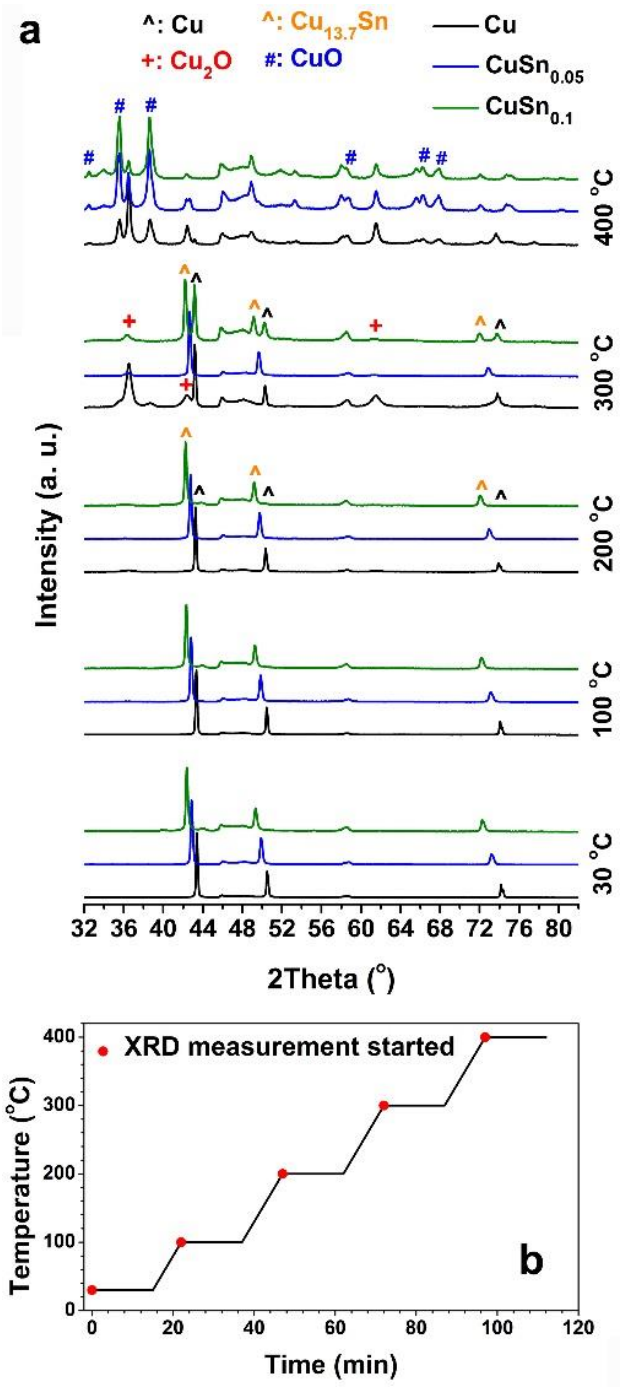

Figure 4.11. *In-situ* XRD measurements of pure Cu, $CuSn_{0.05}$, and $CuSn_{0.1}$ powders in ambient air at increasing temperature from 30 °C to 400 °C (a) with corresponding temperature profile during the oxidation (b). The red dots correspond to initiation of XRD scans. Every XRD measurement lasts 15 min.

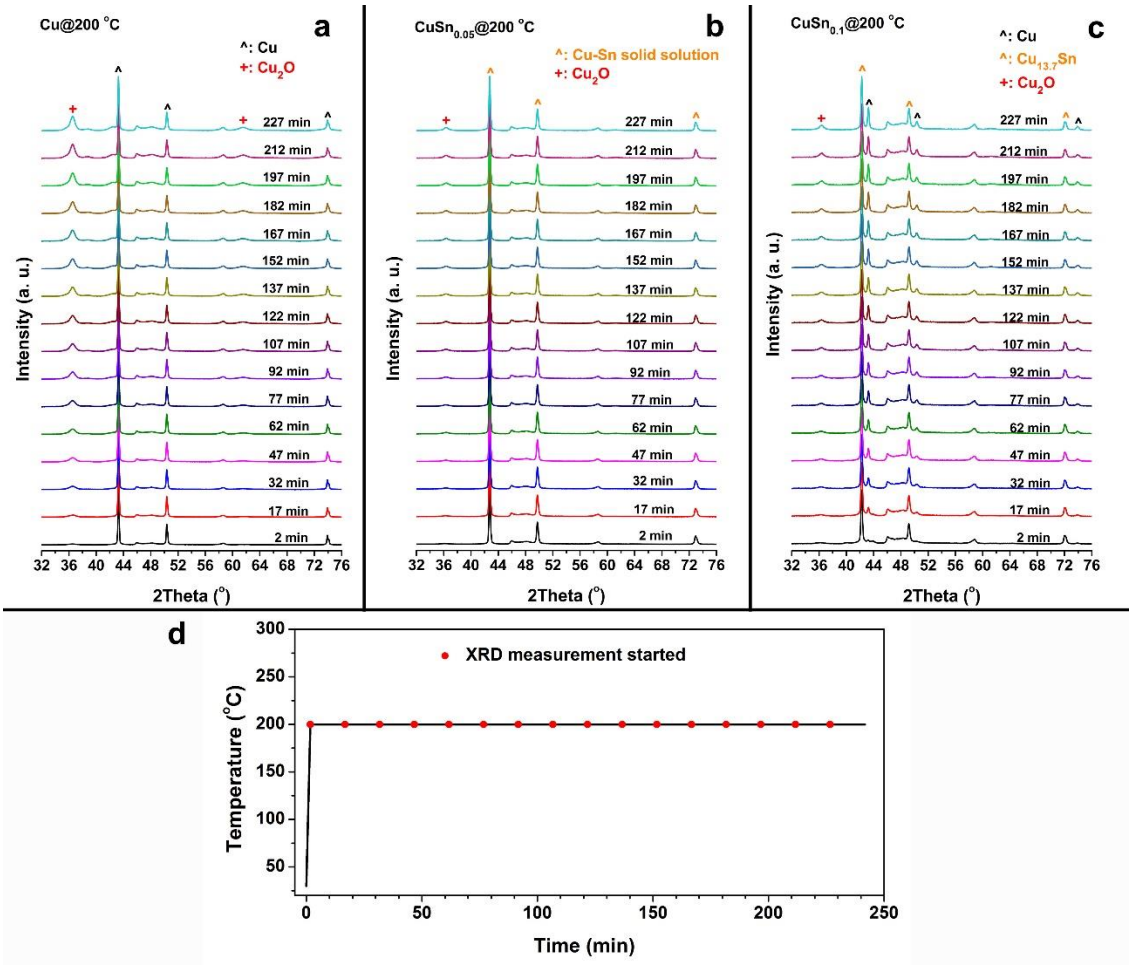

Figure 4.12. *In-situ* XRD measurements of pure Cu (a), $CuSn_{0.05}$ (b), and $CuSn_0.1$ (c) when the sample temperature was held at 200 °C in ambient air subject to heating. (d) The temperature profile of the sample during the oxidation. In (d), the red dots correspond to initiation of XRD scans.

4.4.3 Oxidation kinetics of $CuSn_y$ powders

To quantitatively understand the oxidation kinetics of $CuSn_y$ particles, the oxidation experiments were conducted in a packed-bed reactor by flowing a diluted O_2 gas through the $CuSn_y$ particles at different reaction temperatures. The difference of O_2 flow rates

between the feed and product streams represents the O_2 gas consumption due to the oxidation of $CuSn_y$ particles in the packed-bed reactor.

The $CuSn_y$ powders (y = 0, 0.05, and 0.1) were oxidized at 300 ^oC and 500 ^oC, respectively. Both oxidation temperatures were chosen based on the melting point of Sn (230 ^oC) (Ju et al. 2015), onset temperature of significant oxidation of $CuSn_y$ powders (200 – 300 ^oC, discussed in above), and the oxidation rate. The O_2 partial pressure was measured in the product stream (Figure 4.13) and then converted into O_2 gas flow rate (Figure 4.14a). To better understand the oxidation extent of the powders with time, we assume all the consumption of O_2 contributes to the weight gain of the powders. Therefore, the area enclosed by the line that represents the O_2 flow rate in the feed stream at the top and the line which represents the O_2 flow rate in the product stream at the bottom (Figure 4.14a) is regarded as the consumption of O_2 in the packed-bed or the weight gain of the powders. For example, the weight gain of $CuSn_{0.1}$ particles being oxidized at 300 ^oC can be demonstrated by the area marked as "1" in Figure 4.14a. By applying the trapezoidal rule, the relationships between the relative weight gain ($\Delta m/m$) and the oxidation time (t) at 300 ^oC and 500 ^oC are shown in Figure 4.14b,d, respectively.

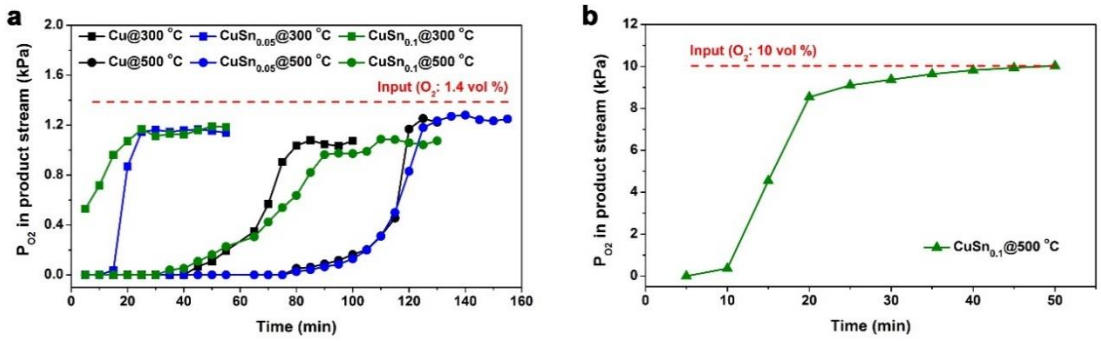

Figure 4.13. O_2 partial pressures in the product streams of the packed-bed reactor when the volume percents of O_2 in feed stream are 1.4 % (a) and 10 % (b).

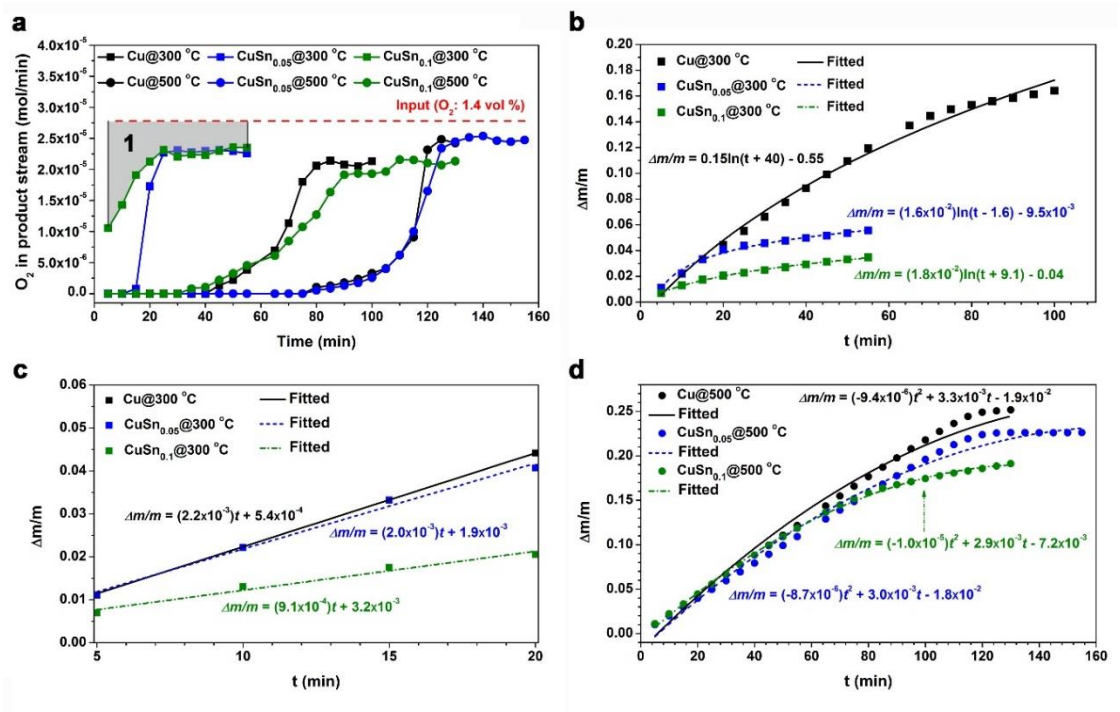

Figure 4.14. (a) O_2 flow rates in the product streams of the packed-bed reactors when the volume percent of O_2 in feed stream is 1.4 %. (b) and (d) The weight gains of the powder during the oxidation at 300 ^oC (b) and 500 ^oC (d). They are calculated by applying the trapezoidal method on the results as shown in (a), for example the area marked by "1" for the $CuSn_{0.1}$ sample at 300 ^oC. (c) The initial 20 min of the oxidation process at 300 ^oC.

Low temperature oxidation mechanism

At 300 ^oC, O_2 was observed earlier in product stream of $CuSn_{0.05}$ and $CuSn_{0.1}$ particle-packed reactors than Cu particle-packed reactor. The subsequent plateaus of the O_2 flow rate in the product streams suggest the slow oxidation rates after the significant oxidation in the initial 20 min. The oxidation of Cu particles lasts longer than $CuSn_{0.05}$ and $CuSn_{0.1}$ powders. As shown in Figure 4.15, after being oxidized, a trace amount of Cu remained in

the Cu powders with low intensity peaks. However, peaks attributed to CuO and Cu_2O phases are pronounced in the post-oxidation powders of Cu, which is consistent with the results in Figure 4.10 and the reported oxidation products of 1 μm Cu particles at 300 °C (Feng et al. 2003). For the post-oxidation powders of $CuSn_{0.05}$ and $CuSn_{0.1}$, distinct peaks belonging to metals (Cu and $Cu_{13.7}Sn$) are observed, compared to those attributed to Cu_2O and SnO_2 phases. SnO_2 instead of SnO is seen because SnO_2 is more stable than SnO in the presence of O_2 gas (Dai et al. 2002; Duan 2008). The CuO phase is negligible in the post-oxidation powders of $CuSn_{0.05}$ and $CuSn_{0.1}$.

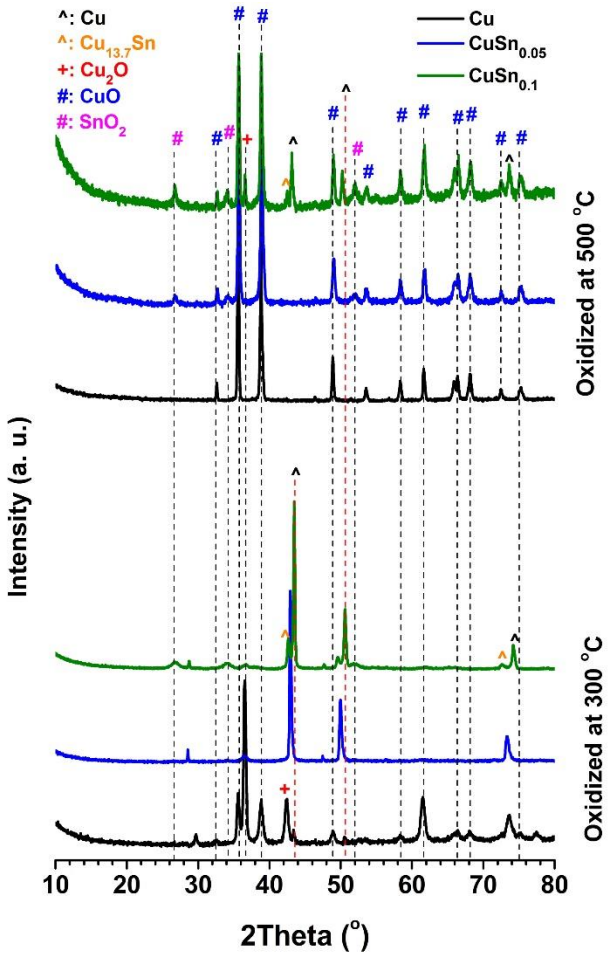

Figure 4.15. XRD patterns of powders after being oxidized in a packed-bed reactor at 300 °C (bottom) and 500 °C (top). The volume percent of O_2 in the feed stream is 1.4 %.

The kinetic equations to describe the relative weight gains of Cu, $CuSn_{0.05}$, and $CuSn_{0.1}$ powders with the oxidation time are obtained by fitting the curves in Figure 4.14b. $CuSn_y$ (y = 0, 0.05, and 0.1) powders underwent rapid oxidation until 20 min. The rapidly formed oxide layer, consisting of both copper and tin oxides, may reduce the oxidation rates of these particles after 20 min. Thus, the relative weight gains with oxidation time can be described by logarithmic equations. The higher reactivity of Sn towards O_2 than Cu causes the faster formation of oxide layer (Liu et al. 2005; Liu et al. 2007a), which may lead to the relative weight gains of powders in the following sequence: $Cu>CuSn_{0.05}>CuSn_{0.1}$.

As shown in Figure 4.14c, in the first 20 min of oxidation, the oxidation rates of these particles are observed to obey the linear equations. The apparent rate constants of the oxidation rate in the initial 20 min can be obtained by:

$$k_{app} = \frac{d(\frac{\Delta m}{m})}{dt} \quad (4.1)$$

$k_{app,Cu}$ = 2.2×10^{-3} min^{-1} and $k_{app,CuSn0.05}$ = 2.0×10^{-3} min^{-1} are significantly higher than $k_{app,CuSn0.1}$ = 9.1×10^{-4} min^{-1}. Thus, higher reactivity of Sn towards O_2 than Cu may contribute to the faster formation of oxide layer on the particle surface and lower oxidation rates of $CuSn_{0.1}$ and $CuSn_{0.05}$ than Cu particles in the initial 20 min.

According to classic oxidation theory, the fast formation of the oxide layer in the initial oxidation step will set up a strong electric field in the oxide layer, creating an obstacle to diffusion of O^{2-}, and resulting in the logarithmic growth of oxide layer (Cabrera and Mott 1949). Therefore, we believe that the oxidation of Cu, $CuSn_{0.05}$, and $CuSn_{0.1}$ powders at 300 ^oC is controlled by the migration of absorbed O^{2-} through the oxide layer.

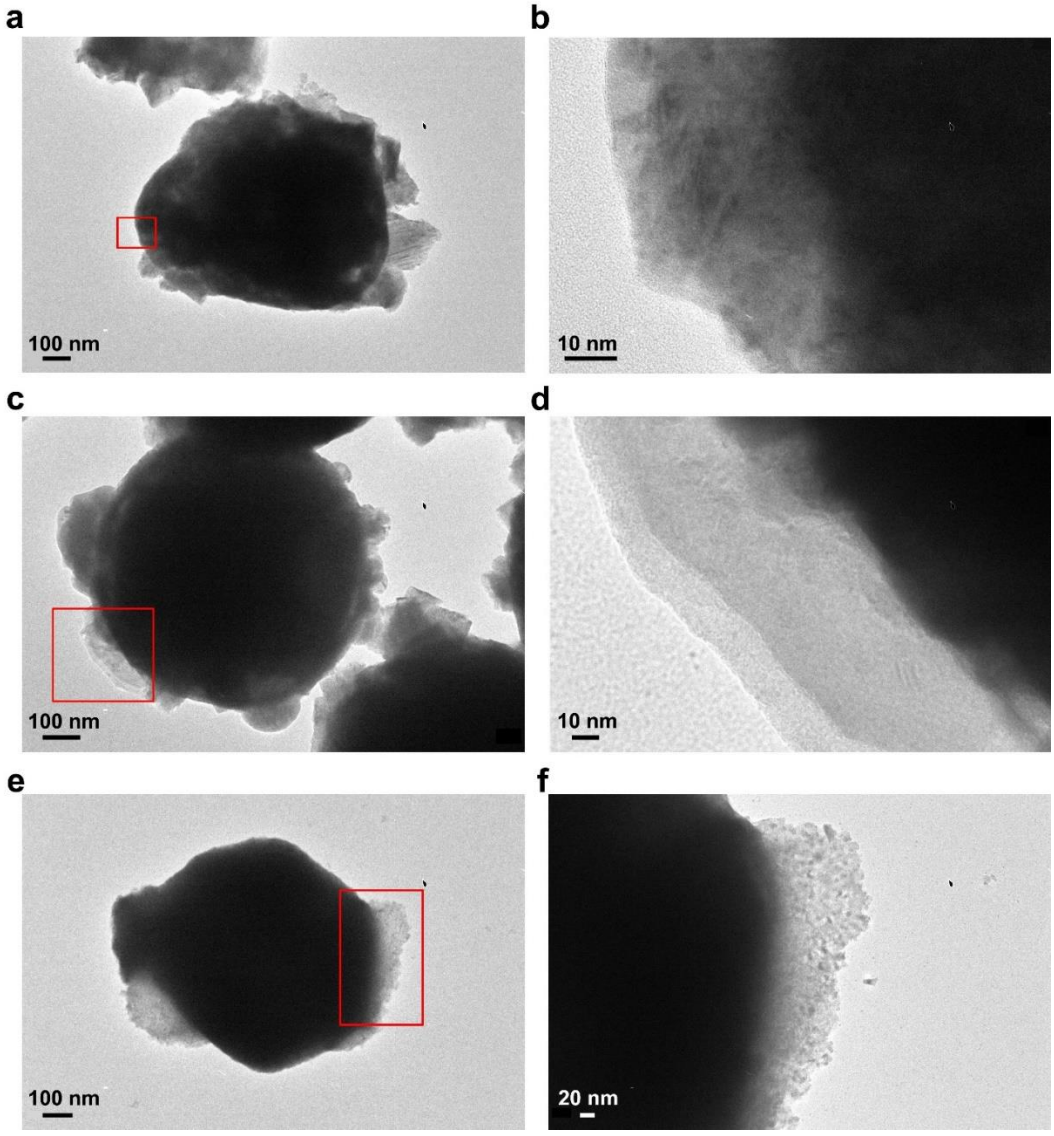

Figure 4.16 TEM images of Cu (a)-(b), $CuSn_{0.05}$ (c)-(d), and $CuSn_{0.1}$ (e)-(f) particles after being oxidized in packed-bed reactor under 300 ^{o}C. The volume percent of O_2 in feed stream is 1.4 %. (b), (d), and (f) are the higher magnification images of the areas marked by red boxes in (a), (c), and (e), respectively.

Some researchers also claimed that the oxidation of Cu-based composite particles was controlled by the internal diffusion of O_2 through the oxide ash layer on the particle surface

by analyzing their experimental results using a shrinking-core model (SCM) (Chuang et al. 2010). As detailed in Section A1 of Appendices, SCM was used to analyze the experimental data in Figure 4.14b. This model does not clearly explain the experimental observations for the following reasons: 1) the diffusivities of O_2 through oxide ash layer either cannot be obtained (for Cu particles) or are 10^4 higher than the reported values for the diffusion coefficients at the same temperature (for $CuSn_{0.05}$ and $CuSn_{0.1}$ particles), as shown in Figure A.1.2 (Appendices). This phenomena may be attributed to the different experimental conditions between the reported work and ours. In the reported work, the oxidation of Cu-Al_2O_3 composite particles was conducted in a fluidized-bed (Chuang et al. 2010), which has different mass transport phenomena than that in a packed-bed of $CuSn_y$ solid particles. 2) the key assumption in the SCM of an oxide layer of uniform thickness (Levenspiel 1999) may not be appropriate for $CuSn_y$ powders, which have oxide layers that vary in thickness as shown in Figure 4.16. Therefore, we believe the O^{2-} migration through the oxide layer instead of the internal diffusion of O_2 through the oxide ash layer controls the oxidation of $CuSn_y$ particles at 300 ^oC.

High temperature oxidation mechanism

O_2 appeared later in the product streams at 500 ^oC than 300 ^oC, implying longer and more significant oxidation of the $CuSn_y$ powders at 500 ^oC than that at 300 ^oC (Figure 4.14a). In addition, the O_2 concentration in the product stream of $CuSn_{0.1}$ powders reached a plateau faster in than those in $CuSn_{0.05}$ and Cu particles. The disappearance of peaks attributed to metals in the post-oxidation particles of Cu and $CuSn_{0.05}$ also indicates the higher oxidation extent at 500 ^oC than 300 ^oC (Figure 4.15). CuO is the main oxidation product of Cu and $CuSn_{0.05}$ powders. Cu_2O phase is still observable in the post-oxidation

products of $CuSn_{0.1}$ than Cu or $CuSn_{0.05}$ powders. This result implies that the existence of sufficient Sn increases the particle oxidation resistance. SnO_2 is the product of the Sn oxidation in both $CuSn_{0.05}$ and $CuSn_{0.1}$ powders.

The kinetic equations to describe the weight gains of Cu, $CuSn_{0.05}$, and $CuSn_{0.1}$ powders with the oxidation time are obtained by fitting the plots in Figure 4.14d. The relative weight gains of these particles with the oxidation time can be described by parabolic formula. The oxidation mechanism could change dramatically by elevating the oxidation temperature and this results in the change in oxidation behavior of the materials, as evidenced by the shifting of oxidation equations from logarithmic to parabolic or cubic (Cabrera and Mott 1949; Feng et al. 2003; Fujita et al. 2013).

For $CuSn_{0.1}$ particles, the sufficient Sn loading may greatly increase the their oxidation resistance by fast formation of a self-limiting oxide layer in the initial stage of oxidation, due to the higher activity of Sn towards O_2 than Cu (Cabrera and Mott 1949; Feng et al. 2003; Liu et al. 2005; Liu et al. 2007a). The rapid growth of the SnO_2 layer has been reported that it can block further incorporation of oxygen into the bulk (Korber et al. 2011), which can prevent further bulk oxidation. In addition, grain growth of oxides is observed in the post-oxidation powders of $CuSn_{0.1}$ at 500 ^oC. The full width at half maximum (FWHM) of the SnO_2 peak at 26.7^o decreases from 1.056 (oxidized at 300 ^oC) to 0.441 (oxidized at 500 ^oC), as shown in Figure 4.15. The FWHM of the Cu_2O peak at 36.6^o decreases from 0.611 (oxidized at 300 ^oC) to 0.254 (oxidized at 500 ^oC). The CuO phase does not appear in the post-oxidation sample at 300 ^oC. In the sample at 500 ^oC, the FWHM of the CuO peak at 35.8^o is 0.312. Therefore, after being oxidized at 500 ^oC, the oxides in $CuSn_{0.1}$ powders display a higher degree of crystallinity, because the smaller FWHM

represents larger size of crystalline domains based on Scherrer equation. Therefore, the decrease of FWHM of XRD peaks implies the grain growth in the powders. Grain growth was also observed in the post-oxidation products of Cu and $CuSn_{0.05}$ particles. The FWHMs of the CuO peak at 35.8^{o} are 0.233 for $CuSn_{0.05}$ particles and 0.308 for Cu particles at 500 ^{o}C. Furthermore, the TEM images of the post-oxidation products of 500 ^{o}C also display higher degree of crystallinity than at 300 ^{o}C (Figures 4.17, 4.16, respectively). Thus, compared to the post-oxidation sample of 300 ^{o}C, results suggest the oxides undergo grain growth during the oxidation of 500 ^{o}C. The grain growth of the oxide may be the rate-limiting step for the oxidation of Cu, $CuSn_{0.05}$, and $CuSn_{0.1}$ particles at 500 ^{o}C, with the relative weight gain with oxidation time following a parabolic equation, which is consistent with similar phenomena observed by other researchers in Cu oxidation (Fujita et al. 2013; Matsnnaga and Homma 1976).

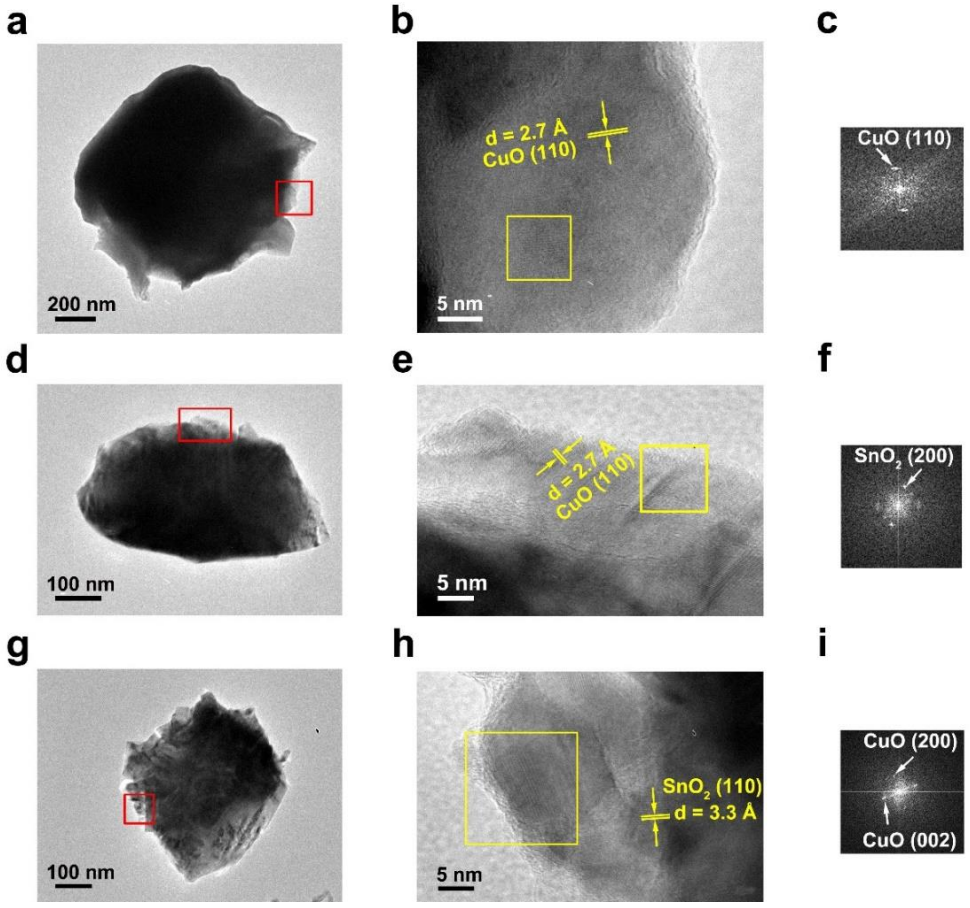

Figure 4.17. TEM images of Cu (a)-(c), $CuSn_{0.05}$ (d)-(f), and $CuSn_{0.1}$ (g)-(i) particles after being oxidized in packed-bed reactor under 500 ^{o}C. The volume percent of O_2 in feed stream is 1.4 %. (b), (e), and (h) are the higher magnification images of the areas marked by red boxes in (a), (d), and (g), respectively. (c), (f), and (i) are the selected area electron diffraction (SAED) patterns of areas highlighted by yellow boxes in (b), (e), and (h), respectively. SAED images are obtained by performing the fast Fourier transform (FFT). The identified phases are CuO (PDF No. 01-073-6023) and SnO_2 (PDF No. 01-072-1147).

The relative weight gain ($\Delta m/m$) of Cu particles also approaches the theoretical limit given by complete oxidation of Cu to CuO, which is 0.25. Based on the theoretical

calculation, the weight gains of $CuSn_y$ ($y \leq 0.1$) particles given by complete oxidation to CuO and SnO_2 are also 0.25. Therefore, the oxidation extent of $CuSn_{0.1}$ particles within 100 min during the packed-bed reaction, which is 0.19 (Figure 4.14d), is lower than the theoretical limit and the oxidation extent of Cu particles. This further validates that $CuSn_{0.1}$ powders have higher oxidation resistance than Cu particles.

To further examine the oxidation resistance of $CuSn_{0.1}$ powders, O_2 concentration in the feed stream was increased from 1.4 vol % to 10 vol %. As shown in Figure 4.18, even though the O_2 concentration in the feed stream increases by ~ 7 times, the relative weight gain of $CuSn_{0.1}$ powders only increases by 1.6 times. This suggests that the O_2 gas concentration may not be the rate-limiting step of the particle oxidation at 500 ^oC. The relative weight gain of $CuSn_{0.1}$ powders during the oxidation under 10 vol % O_2 is close to that of Cu particles during the oxidation under 1.4 vol % O_2 at 500 ^oC. This also implies the existence of Sn-enriched layer on the $CuSn_{0.1}$ particles greatly improves the oxidation resistance compared to Cu particles. In TGA measurements, significant weight gain can be observed from 133 ^oC for Cu particles, which is 44 ^oC lower than that of $CuSn_{0.1}$ particles (Figure 4.19). In addition, the relative weight gain of Cu is 4 % higher than that of $CuSn_{0.1}$ at 233 ^oC.

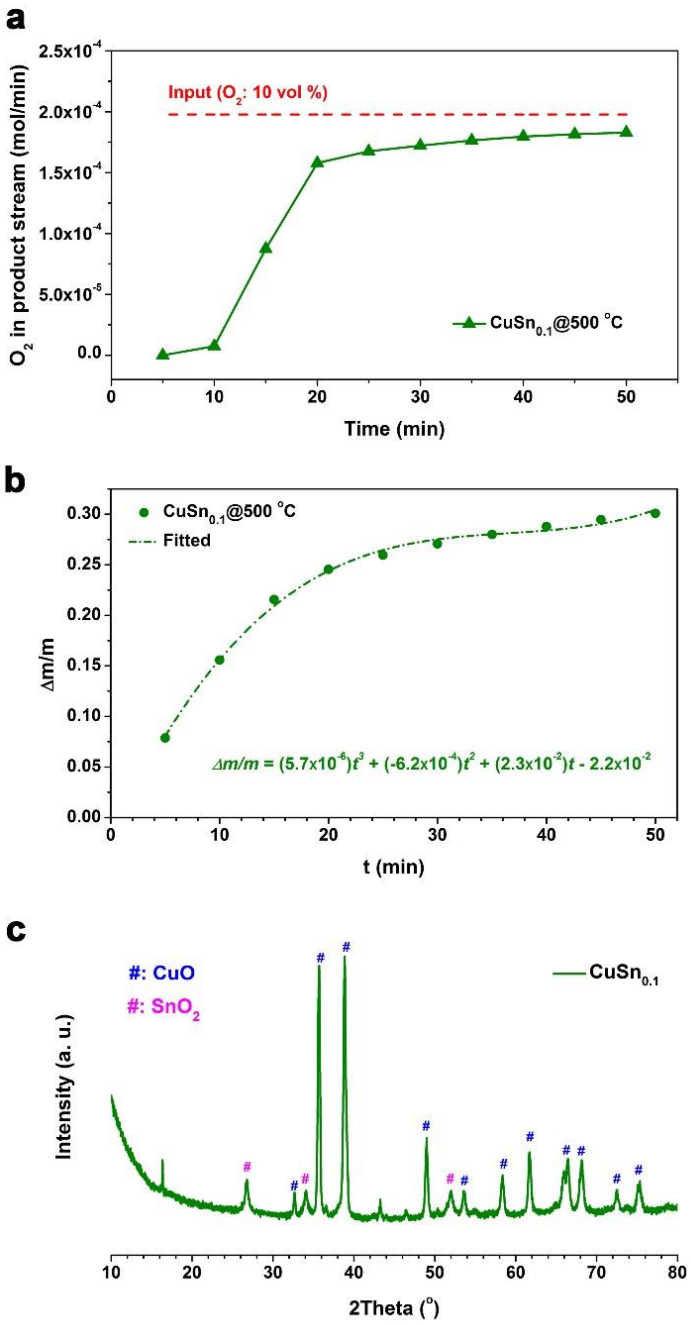

Figure 4.18. (a) O_2 flow rate in the product stream of the packed-bed reactor when the volume percent of O_2 in feed stream is 10 %. (b) The relative weight gains of the powder during the oxidation. The weight gain is calculated by applying the trapezoidal method on the results shown in (a). (c) XRD pattern of powders after being oxidized in a packed-bed reactor at 500 °C under 10 vol % O_2 stream.

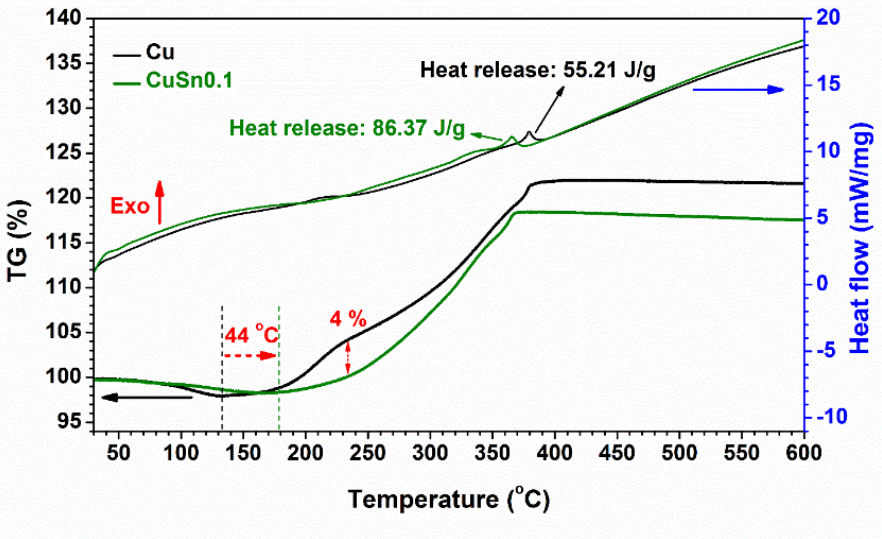

Figure 4.19. TGA (left axis) and DSC (right axis) measurements on Cu particles (black curves) and $CuSn_{0.1}$ particles (green curves). The initial oxidation temperature of $CuSn_{0.1}$ (vertical green dashed line) is ~ 44 °C higher than Cu (black dashed line). There are two distinct exotherms in both heat flow curves at 380 °C (Cu) and 365 °C ($CuSn_{0.1}$) corresponding to the weight losses.

As discussed, spherical solid $CuSn_y$ particles are generated when the Sn/Cu atom ratio is below 0.1. The thickness of the Sn-enriched layer on the spherical particle surface increases with Sn loading in the particles, which is supported by SEM (Figure 4.1), TEM with elemental mappings (Figure 4.2), XPS (Figure 4.6), and mass balance calculations (Table 4.1). Our engineering of $CuSn_y$ particles with a Sn-enriched layer on the surface can increase the oxidation resistance of powders, as shown in the XRD with refinement (Figure 4.10), *in-situ* XRD (Figure 4.11), and packed-bed oxidation (Figure 4.14). Furthermore. $CuSn_{0.1}$ particles exhibited highest oxidation resistance among all the $CuSn_y$ ($y \leq 0.1$) particles with desired spherical morphology at both 300 °C and 500 °C.

4.5 Summary of this chapter

Spray pyrolysis has been utilized to fabricated $CuSn_y$ products with Sn/Cu atomic ratio ranging from 0 to 1. Spherical micron-sized $CuSn_y$ solid particles are obtained when the Sn/Cu atomic ratio is below 0.1. $CuSn_y$ ($y \leq 0.1$) particles with a Sn-enriched layer on the particle surface exhibited better oxidation resistance than Cu particles, as confirmed by XRD with Rietveld refinement analysis, *in-situ* XRD, and oxidation kinetics studies. Based on theoretical analysis of the oxidation, the migration of O^{2-} through the oxide layer is a possible rate-limiting step when $CuSn_y$ powders are oxidized at 300 ^oC. For oxidation at 500 ^oC, grain growth of the oxide likely controls the oxidation process.

Micron-sized $CuSn_y$ solid powders with high oxidation resistance and conductivity are a promising alternative material to replace noble metal-based conductive powders, such as Ag and Au, in the fields of printed electronics, interference packaging, and solar cells metallization. $CuSn_{0.1}$ powders displayed the highest oxidation resistance with best spherical morphology among the $CuSn_y$ powders. In addition, the scalable particle fabrication process provides an extra benefit for industrial-scale manufacturing. However, to evaluate the utility of these powders for applications requires high conductivity. Further characterization of their electrical properties is still demanded, and is the subject of ongoing investigation in our group.

Chapter 5: Conductive one-dimensional and two-dimensional structures fabricated by Cu-Sn binary particles

5.1 Abstract

Cu-Sn powders are promising alternatives to Ag and Au in applications including printed electronics because of their low cost and high oxidation-resistance. Further development requires the knowledge of the conductivity of their corresponding one-dimensional and two-dimensional structures. Herein, $CuSn_y$ (y=atom ratio of Sn/Cu) wires and films were produced by direct printing. *In-situ* measurements of structural resistivities while varying the temperature from 2 K to 400 K in oxygen-free conditions revealed that $CuSn_{0.1}$ wires have comparable resistivities to Cu wires. Furthermore, $CuSn_{0.1}$ films exhibited significantly lower resistivity increase after being heated at 573 K in ambient air, compared with Cu films, indicating the $CuSn_{0.1}$ film are higher oxidation-resistant than Cu film.

5.2 Introduction

Cu particles are potential alternatives to replace Ag and Au powders in printed electronics, solar cell metallization, and interference packaging, because of their low cost and relatively low resistivity (Jeong et al. 2008; Li et al. 2017; Liu et al. 2016; Wu et al. 2016). However, Cu particles are easily oxidized even at room temperature (Jeong et al. 2013; Kim et al. 2004), resulting in increased resistivity, which greatly restricts their application. To prevent the formation of the oxide layer, approaches such as introducing secondary metals (Au and Ag) or organic molecules to coat the surface of Cu particle have

been proposed (Jianfeng et al. 2011; Jung et al. 2011; Sharma et al. 2014). However, neither noble metals nor organic molecules are ideal because of their high material cost or high resistivity, respectively. In Chapter 3, micron-sized solid $CuSn_y$ particles with a Sn-enriched surface layer have been developed to address these issues. The Sn-enriched layer can form a sacrificial oxide on the surface to prevent further oxidation of the particles, as discussed in Chapter 4. Although $CuSn_y$ particles are still expected to maintain low resistivity as a result of the relatively low resistivities of tin and tin oxides, introducing Sn into Cu solid solutions can still deteriorate particle conductivity since tin and tin oxides have higher resistivities than copper (Liu et al. 2007a; Shirai et al. 2016; Smithells et al. 2004). Therefore, further investigation is required on the resistivities of structures fabricated using oxidation-resistant $CuSn_y$ particles to evaluate the prospect of applying these particles.

Among the methods for converting metal particles into electronic patterns, the direct printing process has unique advantages, such as low cost, scalability to mass-production, and flexibility in designing patterns (Cao et al. 2008; Shen et al. 2014a). This process has been successfully applied to print conductive wires from inks containing Ag, Au, or Cu particles (Moonen et al. 2013; Schirmer et al. 2011; Shen et al. 2014a). These wires displayed resistivities comparable to their corresponding bulk materials. However, the previous investigations mainly focused on measuring the resistivities at/above the room temperature (Jeong et al. 2013; Jeong et al. 2008; Li et al. 2017; Liu et al. 2016; Wu et al. 2016). Moreover, for Cu-based materials, the influence of oxidation on the pattern resistivity is a crucial factor compared to Ag and Au-based materials.

Herein, we assessed the prospect of applying Cu-Sn powders in the aforementioned areas by *in-situ* measurement of the resistivities of one-dimensional and two-dimensional $CuSn_y$ structures fabricated by direct printing inks containing $CuSn_y$ powders. The resistivity measurements were conducted under various conditions including continuously changing the measurement temperature from 2 K to 400 K in oxygen-free environment and heating $CuSn_y$ patterns at 573 K in ambient air for 90 min, enabling a systematic study of the effects of temperature and oxidation on the resistivities of $CuSn_y$ structures.

5.3 Experimental

Materials

Ethylene glycol (EG, ≥99%) and nitric acid (HNO_3, 70%) were purchased from Sigma-Aldrich. $Cu(NO_3)_2{\cdot}3H_2O$ (99.5% purity) was purchased from Strem Chemicals. $SnCl_2{\cdot}2H_2O$ (>95%) was bought from Fisher Scientific. All chemicals were used without further purification. N_2 gas (99.5%) and mixture gas (5% H_2-95% N_2) were obtained from Airgas. Quartz substrates with dimensions of 5 mm×5 mm×1 mm were purchased from MTI Corporation.

Cu and $CuSn_y$ particles synthesis

Cu and $CuSn_y$ particles were produced by spray pyrolysis with a 1.7 MHz ultrasonic atomizer (Chapters 3-4). Aqueous precursor solutions contained 1.0 M $Cu(NO_3)_2$, *y* M $SnCl_2$ (*y* based on the designed atomic ratio of Sn/Cu in $CuSn_y$ particles), 0.1 M HNO_3, and 4.8 M EG. After the precursors were atomized into droplets, the droplets were carried by N_2 gas through two furnaces (both set at 1000 ^oC) in series. The residence time of the

process is 1.2 s, which was calculated based on the plug-flow reactor with the temperature profile measured along the axial direction (Chapter 3). The product particles were then cooled by quench gas (N_2) and collected by a polytetrafluoroethylene (PTFE) filter.

One-dimensional and two-dimensional structures fabrication by direct printing

Ink with a concentration of (1 g powder)/(1 ml EG) was prepared by dispersing metal particles into EG and then sonicating the mixture for 1 h. A 5-ml syringe with needle (ID=0.2 mm) was utilized to print liquid lines on the quartz substrates. One drop of the ink (~0.025 ml) was added onto the substrate through pipette to form a liquid film. Structures were sintered at 573 K, 673 K, or 773 K in H_2-N_2 mixture gas for 2 h to form wires and films.

Characterization

Particle morphology and structure were determined by scanning electron microscopy (SEM, Hitachi SU-70) with energy-dispersive X-ray spectroscopy (EDS) and transmission electron microscopy (TEM, Jeol Jem 2100 LaB6). Powders were sonicated in ethanol for 1 min and then added onto silicon wafers (for SEM) and TEM grids (for TEM). X-ray diffractometer (XRD, Bruker D8 advance) was applied to understand the crystal phases in the samples. The temperature-dependent resistances of wires were measured by four-point-probe method from 2 K to 400 K with 0.01 K step in helium. The setup of the experiments is shown in the inset of Figure 5.5a. The area of the cross-section of wire was obtained by profilometry (New View 6000), as shown in Figure 5.6. The effect of oxidation on the film resistance was determined using the four-point-probe method in a probe station (WL250, Signatone, Inc) equipped with a hot chuck system. The hot chuck system was stabilized at

a set temperature within ±4 K. The oxidation was operated at 573 K in ambient air. It took 5 min for the chuck to reach 573 K from room temperature.

5.4 Results and discussions

The one-dimensional and two-dimensional structures were fabricated by direct printing inks that are suspensions of $CuSn_y$ powders in ethylene glycol (EG). The metal powders were obtained by spray pyrolysis. Aqueous precursor solutions containing $Cu(NO_3)_2$, $SnCl_2$, and EG were ultrasonically atomized into droplets. The droplets were then transported by the carrier gas (N_2) into a heating unit, where a series of processes happened, including droplet solvent evaporation, chemical reaction, nucleation, and crystal growth. In the end of this continuous process, the powders were collected by filtration.

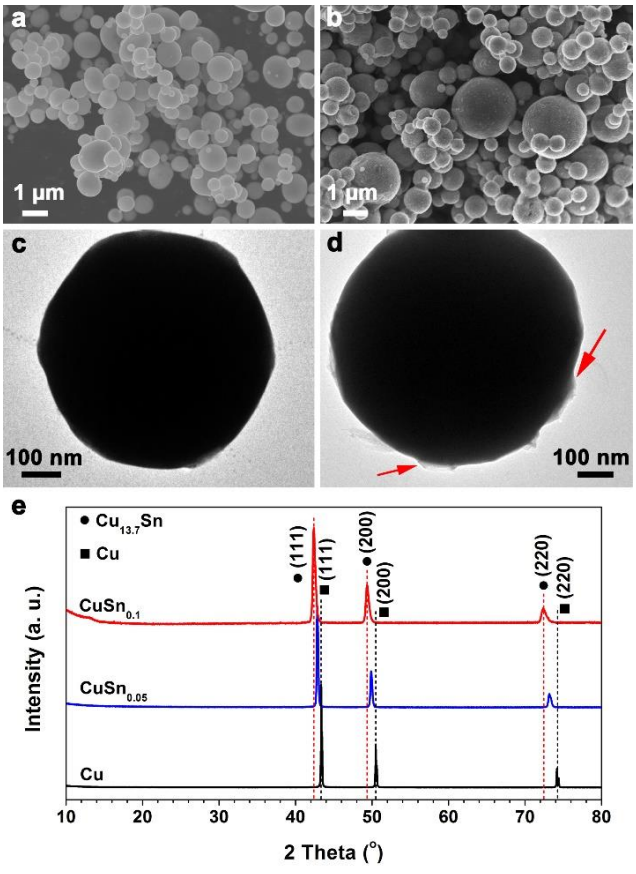

Figure 5.1. Powders used in the inks. (a-b) SEM images of Cu (a) and $CuSn_{0.1}$ (b) particles. (c-d) TEM images of Cu (c) and $CuSn_{0.1}$ (d) particles. (e) XRD diagram of Cu, $CuSn_{0.05}$, and $CuSn_{0.1}$ particles. Solid black circles and squares represent $Cu_{13.7}Sn$ (PDF No. 03-065-6821) and Cu (PDF No. 01-070-3038), respectively.

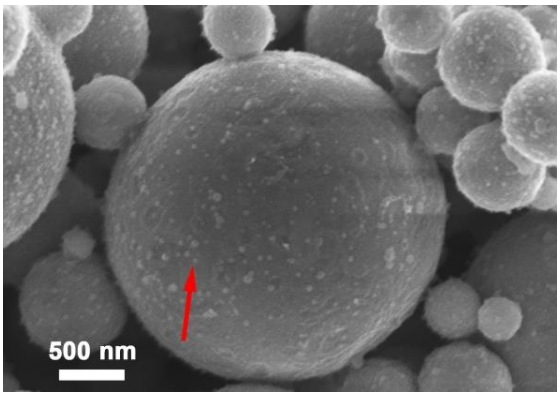

Figure 5.2. SEM image of $CuSn_{0.1}$ particles. The small particles on the particle surface, indicated by the red arrow, are believed to be Sn particles.

The prepared Cu particles exhibit solid and spherical morphology with a smooth particle surface, as shown in scanning electron microscopy (SEM) and transmission electron microscopy (TEM) images (Figure 5.1a,c), while small particles are observable on the surface of $CuSn_{0.1}$ particles (Figures 5.1b,d and 5.2). These small particles (denoted by red arrows in Figures 5.1d,5.2) are believed to be Sn particles, attributed to evaporation of Sn and subsequent gas-to-particle conversion during spray pyrolysis, as discussed in Chapter 4. In addition, $SnCl_2$ is easily hydrolyzed in aqueous solution (Perry 2011). During the solvent evaporation, granular precipitates could concentrate on the droplet surface, where the droplet is supersaturated, promoting the formation of Sn-enriched surface layers on the $CuSn_y$ particles. The as-prepared metal particles show a high degree of crystallinity

with pronounced peaks in X-ray diffractometer (XRD) diagram without observation of oxide phases (Figure 5.1e). A blue shift of the peaks with the increase of Sn concentration in the product is caused by dissolving Sn atoms into Cu matrix, same phenomenon was observed in Chapter 4. The full width at half maximum (FWHM) of each XRD curve is 0.125 at 43.4^{o} for Cu, 0.203 at 42.9^{o} for $CuSn_{0.05}$, and 0.378 at 42.5^{o} for $CuSn_{0.1}$. The increasing FWHM indicates the decreasing grain size based on Scherrer equation. The smaller grain size results in a higher fraction of atoms on the grain boundaries (Schiotz et al. 1998), which may lead to an increased electrical resistivity after converting these powders into electronic patterns (Mayadas and Shatzkes 1970; Sharma et al. 2014). The $CuSn_y$ particles have a number mean diameter of 710 nm with a standard deviation of 300 nm, consistent with Chapter 3. Based on mass balance calculations between the precursors and product particles presented in Chapter 4, the configuration of $CuSn_{0.1}$ particles is 3-nm-Sn surface layers on the $Cu_{13.7}Sn$ cores assuming the Sn enriched layer are pure Sn and no quantity loss of Cu and Sn caused by the evaporation during the spray pyrolysis. For $CuSn_{0.05}$ particles, the $Cu_{32}Sn$ cores are estimated covered by Sn layers of 2.1 nm.

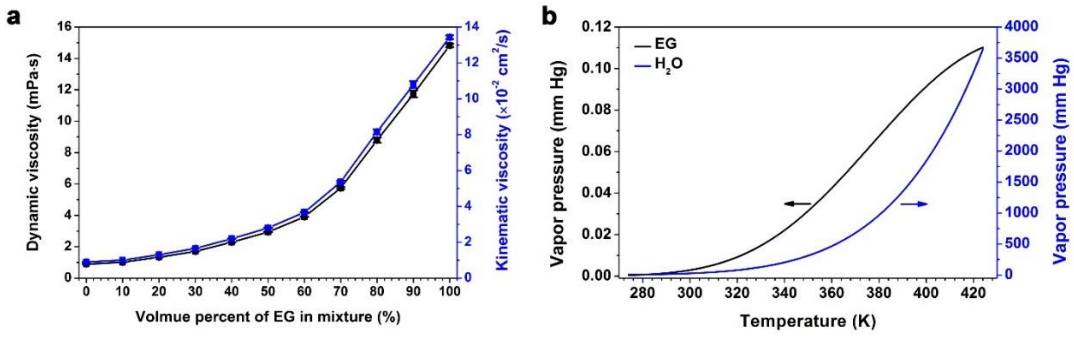

Figure 5.3. (a) Measured viscosity of H_2O-EG mixture solutions with varying volume percent of EG determined using a viscometer. (b) Vapor pressures of H_2O and EG as a function of temperature, adapted from (Yaws 1999).

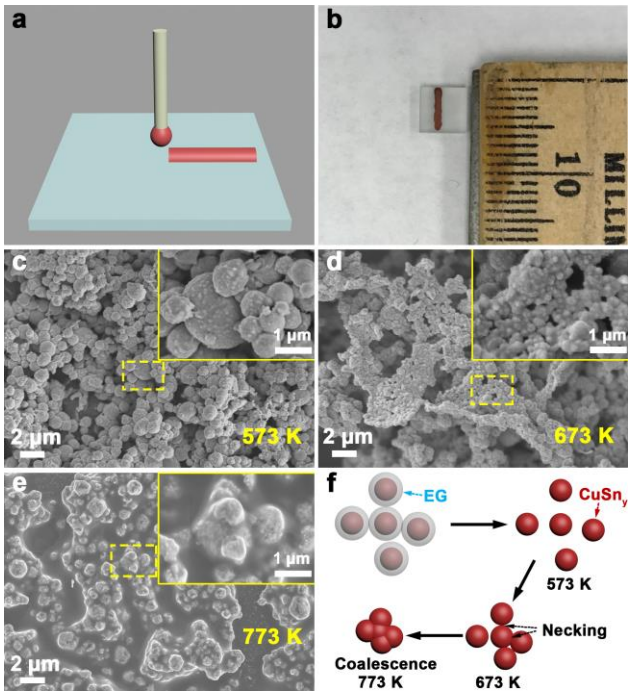

Figure 5.4. Microstructural evolution caused by increasing sintering temperature. (a) Schematic of direct printing ink on a 5 mm×5 mm quartz substrate. (b) An image of the wire after being sintered. (c-e) SEM images of wires after being sintered at 573 K (c), 673 K (d), and 773 K (e). (f) Schematic summary of microstructural evolution during sintering (f).

EG was used as the ink solvent because its high viscosity and low vapor pressure (Figure 5.3) can prevent the formation of a ring stain on the contact line (Talbot et al. 2014), contributing to a relatively uniform particle distribution after the solvent dries. The inks were sonicated for 1 h, then printed on 5 mm×5 mm quartz substrates, as shown in Figure 5.4a-b. The printed patterns were sintered under H_2-N_2 gas at 573 K, 673 K, and 773 K for 2 h. The minimum sintering temperature (573 K) was selected based on the initial decomposition temperature of EG which is 513 K (Yue et al. 2012). The post-printing

process is important for removing the solvent and decreasing the porosity of wires in order to decrease the resistivity (Ma et al. 2014). At low sintering temperature (573 K), the $CuSn_{0.1}$ particles largely retained spherical and intact morphology (Figure 5.4c), similar to that of freshly fabricated particles (Figure 5.1b,d). This phenomenon could be ascribed to the low input of thermal energy. Increasing the sintering temperature to 673 K leads to significant inter-particle necking, as shown in Figure 5.4d, contributing to the formation of conduction pathways. When the sintering temperature is 773 K, it is hard to observe distinct particle shapes in the microstructure of wire (Figure 5.4e). The microstructural evolution of the wires with the increasing sintering temperature is summarized in Figure 5.4f, which is consistent with the reported phenomena of sintering Cu and Ag patterns (Jeong et al. 2013; Shen et al. 2014a; Yong et al. 2015). Large quantity of conduction pathways are created at elevated temperature as a result of high input of thermal energy (Jeong et al. 2013; Shen et al. 2014a; Yong et al. 2015), which may lead to a low pattern resistivity.

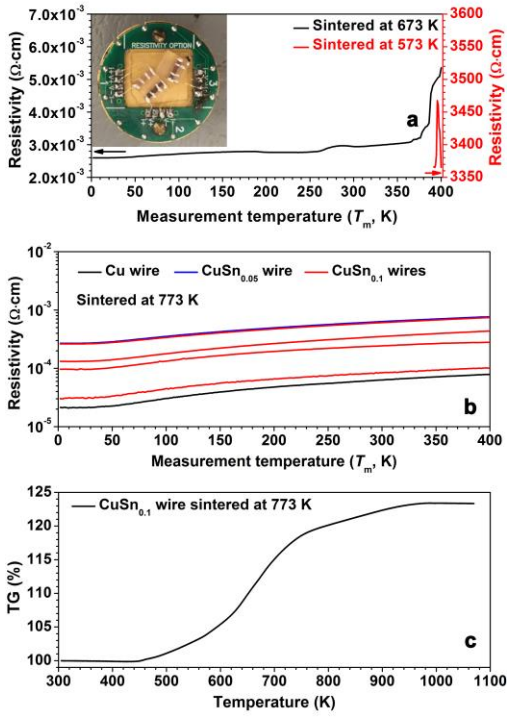

Figure 5.5. *In-situ* resistivity measurements of the wires from 2 K to 400 K. (a) Resistivities of $CuSn_{0.1}$ wires being sintered at 573 K (red) and 673 K (black). Inset is the image of the experimental setup. (b) Resistivity-temperature profiles of Cu (black), $CuSn_{0.05}$ (blue), and $CuSn_{0.1}$ (red) wires. These wires were sintered at 773 K after direct printing. $CuSn_{0.1}$ wires were fabricated from different batches. (c) Thermogravimetric analysis (TGA) of $CuSn_{0.1}$ wire.

Table 5.1. Dimensions of the wires fabricated by direct printing

	$CuSn_{0.1}$						$CuSn_{0.05}$	Cu
Sintering temperature (K)	773				673	573	773	773
Average cross-section area (cm^2)	1.2×10^{-4}	2.7×10^{-4}	1.7×10^{-4}	4.0×10^{-4}	1.1×10^{-4}	2.2×10^{-4}	8.0×10^{-5}	1.2×10^{-4}
Length (cm)	0.45	0.46	0.42	0.45	0.42	0.41	0.46	0.43

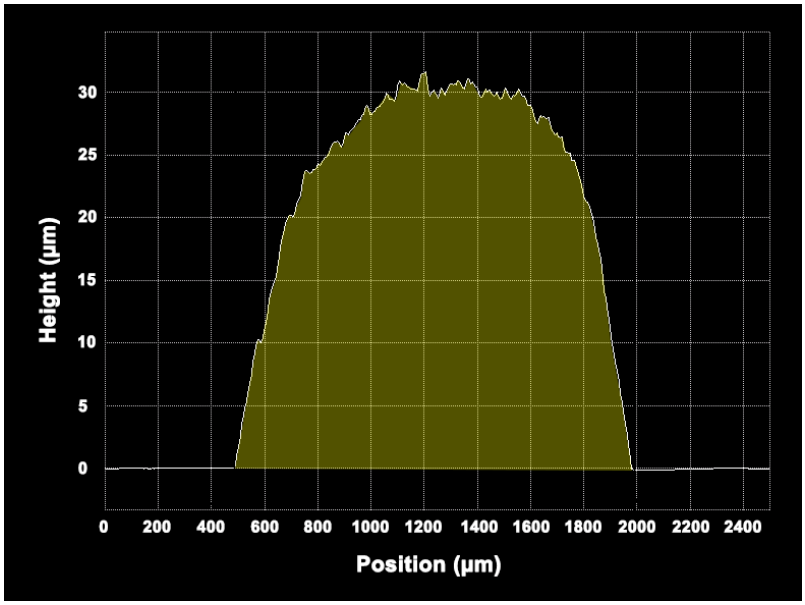

Figure 5.6. Typical cross-section profile of wire after sintering. Based on the average dimensions of the wire (Table 5.1), the expected maximum errors are 133 nm in width and

1 nm in height. Therefore, the maximum deviation of the measured resistivity caused by the uncertainty of profilometry is 2×10^{-4} of the measured values.

To validate this hypothesis, the resistances of these wires were measured by the four-point-probe method from 2 K to 400 K with 0.01 K steps in an oxygen-free environment. The four-point-probe method has been widely utilized as a tool to measure the resistivities of materials in various geometries (Smits 1958). The experimental setup is shown in the inset of Figure 5.5a. The obtained resistance (R) was converted into resistivity (ρ) by:

$$\rho = \frac{A}{l}R \quad (5.1)$$

where A is the area of the cross-section of wire, which is obtained by profilometry, as shown in Figure 5.6. l is the length of the wire. The detailed dimensions of each wire are presented in Table 5.1. On average, $A = 2\times10^{-4}$ cm^2, $l = 0.44$ cm.

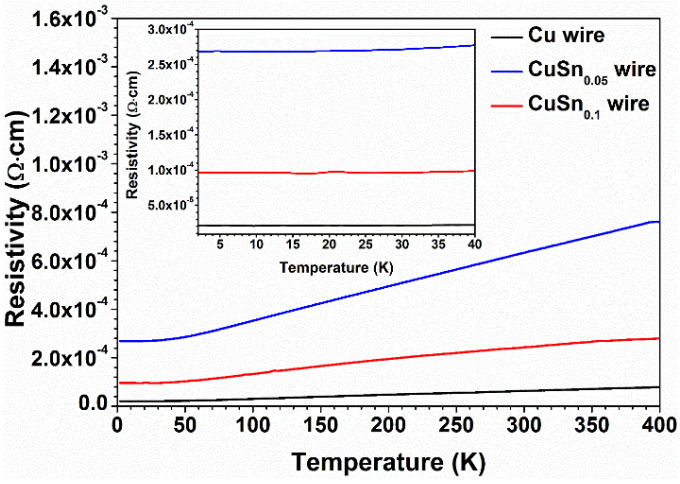

Figure 5.7. Temperature dependent resistivities of Cu, $CuSn_{0.05}$, and $CuSn_{0.1}$ wires with y-axis in linear scale. Inset is the resistivities when the measurement temperature was below 40 K.

The low sintering temperature leads to high porosity, resulting in a high resistivity (Jeong et al. 2013; Shen et al. 2014a; Yong et al. 2015). The fabricated structures may be regarded as insulators because of the limited conductive paths. The $CuSn_{0.1}$ wire sintered at 573 K exhibits a resistivity around 10^3 Ω·cm when the measurement temperature (T_m) is above 390 K (Figure 5.5a), which is remarkably higher than that of bulk Cu (1.7×10^{-6} Ω·cm) and Sn (1.0×10^{-5} Ω·cm) (Smithells et al. 2004). In addition, when T_m < 390 K, negligible current goes through the electrodes. This is believed to be caused by poor inter-particle connections when sintered at 573 K. Therefore, as the sintering temperature increases to 673 K, the intensified coagulation between particles creates paths to transfer electrons, contributing to the reduction of resistivities (Figure 5.5a). However, the measured resistivities over 2 K ≤ T_m ≤ 400 K are higher than 2.6×10^{-3} Ω·cm, implying that further increase of the sintering temperature is still required. When sintered at 773 K, the significant fusing between the $CuSn_{0.1}$ particles contributes to the lowest resistivity (around 10^{-4} Ω·cm, 2 K ≤ T_m ≤ 400 K, Figure 5.5b, red curves) among the examined sintering temperatures. In addition, the resistivity-temperature curves (Figures 5.5b,5.7) are observed to follow the classic resistivity-temperature relationship, which can be described as (Kittel 2005),

$$\rho = \rho_0 + \rho(T_m) \quad (5.2)$$

where ρ_0 is the resistivity ascribed to the scattering of the electron waves, which is caused by the static defects in the lattice. ρ_0 is independent of temperature. $\rho(T_m)$ represents the resistivity resulted from the thermal photons. Consequently, $\rho(T_m)$ is temperature-dependent and vanishes when T_m approaches 0 K (Kittel 2005). At low temperatures, the resistivity is dominated by the scattering of the electron waves, supported by the plateaus

in Figure 5.7 ($T_m \leq 30$ K). $\rho(T_m)$ becomes pronounced at high temperatures because the rate of collision between the electron and thermal photons/electrons is intensified. The collision rate is proportional to thermal photons and can be assumed to be proportional to temperature at high temperatures (Kittel 2005). Therefore, the resistivity increases linearly with temperature when the temperature exceeds a threshold ($T_m \geq 50$ K in Figure 5.7).

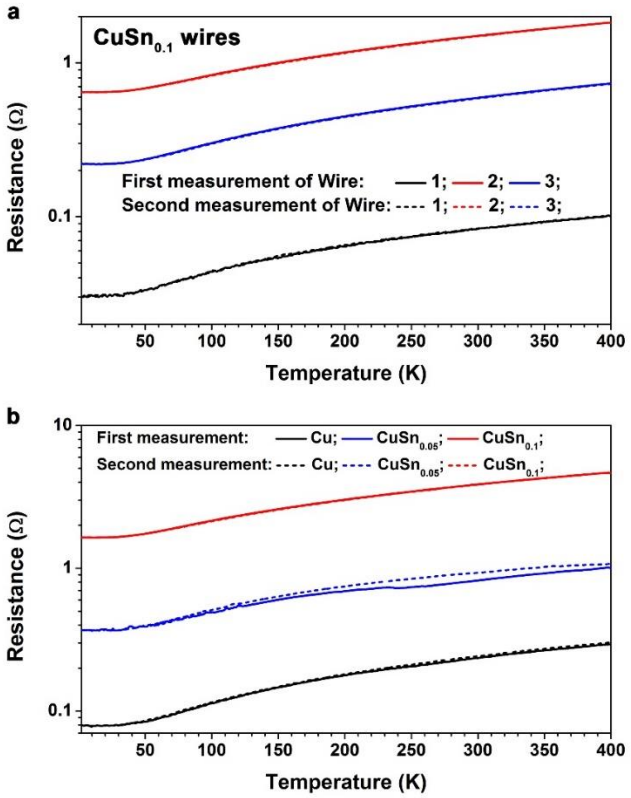

Figure 5.8. Temperature dependent resistances obtained by measuring the same wires twice. (a) Three $CuSn_{0.1}$ wires. (b) Cu, $CuSn_{0.05}$, and $CuSn_{0.1}$ wires. All the wires were sintered at 773 K.

$CuSn_{0.1}$ particles produced from different batches were used to fabricate four $CuSn_{0.1}$ wires for the resistivity measurements to understand the repeatability of this method. The fabricated $CuSn_{0.1}$ wire exhibits a weight gain of 23 % (Figure 5.5c), validating the

composition of wire is $CuSn_{0.1}$. As shown in Figure 5.5b (red curves), the resistivities of $CuSn_{0.1}$ wires are all smaller than 7.5×10^{-4} Ω·cm with a narrow deviation over the wide temperature range (2 K ≤ T_m ≤ 400 K). When T_m = 2 K, the mean value and standard deviation are 1.3×10^{-4} Ω·cm and 9.7×10^{-5} Ω·cm, respectively. When T_m = 400 K, the $CuSn_{0.1}$ wires have a mean resistivity of 3.9×10^{-4} Ω·cm and a standard deviation of 2.7×10^{-4} Ω·cm. Moreover, the resistivity of each wire was measured twice to further understand the possible uncertainty. As shown in Figure 5.8, the resistivities of each wire show consistency without significant deviation.

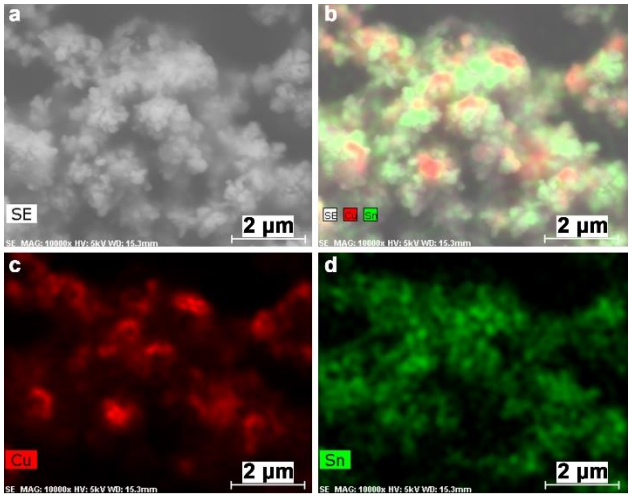

Figure 5.9. SEM images of $CuSn_{0.1}$ wire after being sintered at 773 K (a) with EDS mappings of overlap mapping (b), Cu (c) and Sn (d) elements.

Introducing Sn into Cu particles can increase the oxidation resistance of Cu particles as well as the electrical resistivity, attributed to the higher resistivity of tin than copper and possible grain boundaries in solid solutions (Mayadas and Shatzkes 1970; Sharma et al. 2014; Smithells et al. 2004). As shown in Figure 5.9, strong signals from both Cu and Sn elemental mapping validate the coexistence of Cu and Sn in the wire after being sintered. The resistivity of Cu wire ranges from 2.1×10^{-5} Ω·cm (T_m = 2 K) to 7.9×10^{-5} Ω·cm (T_m =

400 K), as shown in Figure 5.5b (black curve). Cu wire has lower resistivities than $CuSn_{0.05}$ (blue curve) and $CuSn_{0.1}$ (red curves) wires. However, $CuSn_{0.1}$, $CuSn_{0.05}$, and Cu wires still display low resistivities. For comparison, Cu-Au wires fabricated from similar sized $Cu_{core}Ag_{shell}$ particles (1.7 μm) by the same method (direct printing) show a resistivity of ~5×10^{-3} Ω·cm at room temperature (Li et al. 2016c), which is higher than the resistivities of our $CuSn_y$ wires.

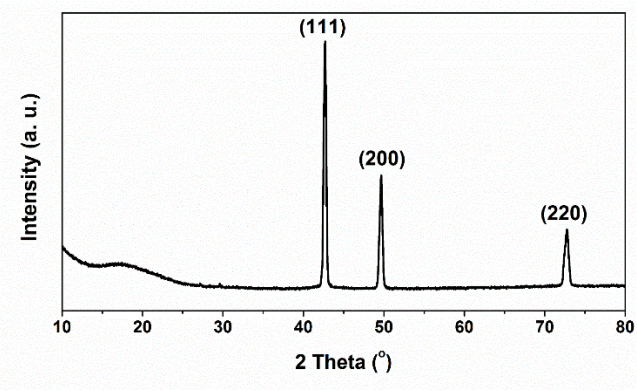

Figure 5.10. XRD pattern of the $CuSn_{0.1}$ film after being sintered at 773 K in H_2-N_2 gas for 2 h. The peaks are attributed to $Cu_{13.7}Sn$ phase with PDF No. 03-065-6821.

The Sn-enriched surface layer of $CuSn_y$ particles can prevent particle oxidation by forming a sacrificial oxide layer, as discussed in Chapter 4. Thus, we investigated the effect of oxidation on the structural resistivity by *in-situ* monitoring the relative resistivity increases of $CuSn_y$ and Cu films at 573 K in ambient air. The metal films were also fabricated by direct printing inks on 5 mm×5 mm quartz substrates and subsequent sintering at 773 K in H_2-N_2 gas for 2 h. The as-prepared metal films are oxide-free, supported by the XRD results. For example, only $Cu_{13.7}Sn$ phase are observed in $CuSn_{0.1}$ film (Figure 5.10), same as the XRD pattern of $CuSn_{0.1}$ powders (Figure 5.1e). The

resistances of the films were also measured by the four-point-probe method, as shown in the inset of Figure 5.11. The resistances of the metal films range from 10^{-3} to 10^{-2} Ω before oxidation (Figure 5.12). However, the resistance of Cu film increases remarkably after the onset of oxidation, while the resistances of $CuSn_y$ films remain below 0.1 Ω, even after being oxidized for 90 min.

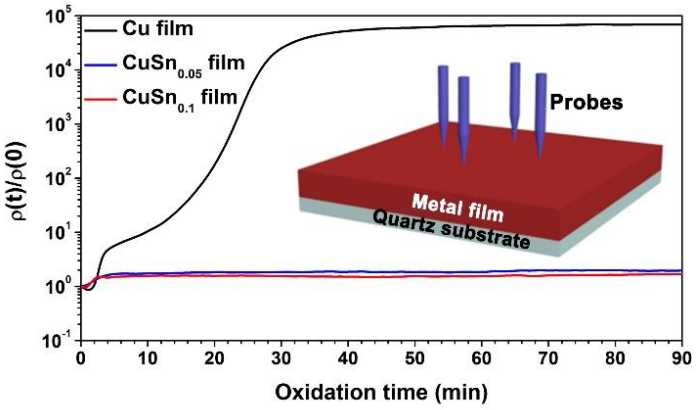

Figure 5.11. Resistivity ratios of film resistivities at given time (*t*) during oxidation at 573 K in ambient air to the resistivities before the oxidation. The films were sintered at 773 K after direct printing. The inset is the schematic illustration of the measurement.

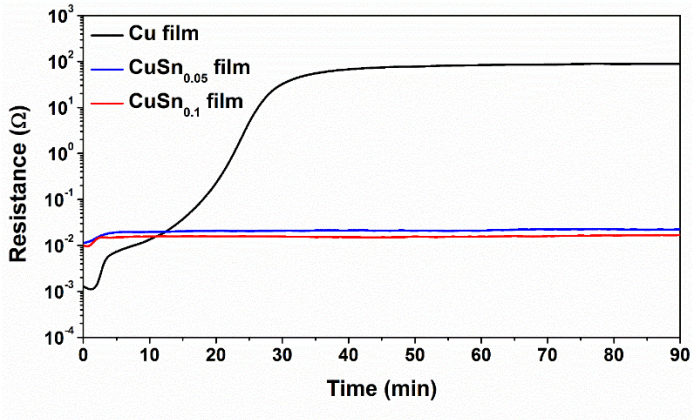

Figure 5.12. *In-situ* resistance measurements of Cu, $CuSn_{0.05}$, and $CuSn_{0.1}$ films during oxidation at 573 K in ambient air.

To demonstrate the oxidation effect on the film resistivity, Figure 5.11 presents the ratio of resistivity at any given time to the resistivity before oxidation ($\rho(t)/\rho(0)$) with the oxidation time. The resistivity ratios ($\rho(t)/\rho(0)$) of Cu and $CuSn_y$ films with the oxidation time at 573 K are similar to the reported weight gains ($\Delta m/m$) of Cu and $CuSn_y$ particles with oxidization time at 573 K, presented in Chapter 4. The resistivity ratios increase rapidly for Cu and $CuSn_y$ films in the initial 3 min. After that, the resistivities of $CuSn_{0.05}$ and $CuSn_{0.1}$ films are less than two times of their resistivities before oxidation. In the meantime, $\rho(t)/\rho(0)$ of Cu film continuously increases to 6×10^4 until being oxidized for 40 min, and then remains around that value. As reported, a 1.1-nm-thick oxide layer can be expected to form on the surface of 140-nm-diameter Cu particles for one year in ambient air at room temperature (Kim et al. 2004), resulting in an increased resistivity of Cu particles. Similar to the particle oxidation, the oxidation of Cu-based films also progresses from the surface towards the bulk. The formation of a sacrificial tin oxide layer has been reported to block the further incorporation of oxygen into the bulk (Korber et al. 2011), preventing the further oxidation of $CuSn_y$ particles. Thus, the conductive pathways beneath the surface of $CuSn_y$ wires are still able to transfer electrons even though oxidation happens on the surface. Contrarily, the significant oxidation of Cu results in remarkably less conductive paths, causing the highest increase of relative resistivity. Thus, the higher oxidation-resistance of $CuSn_y$ particles than Cu particles is substantiated again by *in-situ* resistance measurements of their corresponding films. This is consistent with the results obtained from measuring the O_2 consumptions during oxidizing Cu and $CuSn_y$ particles (Chapter 4).

5.5 Summary of this chapter

We successfully fabricated $CuSn_y$ wires and films via direct printing inks containing oxidation-resistant $CuSn_y$ particles and ethylene glycol. Regardless of higher resistivity of tin than copper, the $CuSn_{0.05}$ and $CuSn_{0.1}$ wires exhibited low resistivities ~10^{-4} Ω·cm (2 K ≤ T_m ≤ 400 K), which is comparable with that of Cu wires. $CuSn_{0.1}$ wires displayed a lower resistivity than the reported resistivity of wires produced from $Cu_{core}Ag_{shell}$ powders. $CuSn_{0.05}$ and $CuSn_{0.1}$ films have significantly less resistivity increases than Cu films when being oxidized at 573 K in ambient air. Together with our reported discovery in Chapter 4 that $CuSn_{0.1}$ powders have the best overall properties, including spherical structure and high oxidation resistance among the $CuSn_y$ particles, this work further demonstrates that one-dimensional and two-dimensional structures fabricated from $CuSn_{0.1}$ particles have low resistivities and high oxidation-resistance. Therefore, $CuSn_{0.1}$ particles are promising materials to replace Au and Ag in applications, including printed electronics, solar cell metallization, and interference packaging.

Chapter 6: Colloidal spray pyrolysis approach to engineer hierarchical tin@carbon particles as anode materials

6.1 Abstract

Spray pyrolysis is a scalable process to fabricate functional particles as cathode/anode materials in rechargeable batteries from precursor solutions. However, one prerequisite of spray pyrolysis to achieve uniform particle-to-particle composition and structure is a stable precursor solution, restricting its usage to highly soluble salts. Otherwise, extremely acidic precursors are necessary to ease the uncontrollable hydrolysis of the salts and the subsequent precipitation. Moreover, strong reduction agents such as H_2 are also needed for complete solid-state reactions, introducing potential safety concerns. Herein, we develop a novel process, colloidal spray pyrolysis (CSP), which can eliminate all the prerequisites simultaneously. Our process can generate particles directly from a multiphase precursor in mild processing conditions through *in-situ* solid-state reactions. The product structure and composition can be precisely designed based on aerosol dynamics and reaction kinetics. By applying CSP, Sn@C particles with three distinct interior nanostructures have been synthesized and evaluated as anodes for lithium-ion batteries (LIBs) and sodium-ion batteries (SIBs). The best performing Sn@C anode delivers 627.9 mAh/g at 2C with capacity retention of 88.5% after 1500 cycles in LIBs and demonstrates superior rate capability for SIBs. This novel CSP process is promising in preparing electrode materials in LIBs and SIBs for future practical applications.

6.2 Introduction

Spray pyrolysis is a scalable process with low operating cost, high process throughput, and minimal waste production (Jung et al. 2014; Lin et al. 2016; Zhu et al. 2017). It has been widely used to fabricate functional particles for many applications, including catalysts (Koirala et al. 2016), lithium-ion batteries (LIBs) and sodium-ion batteries (SIBs) (Choi et al. 2015; Reddy et al. 2013), and superconductors (Bang and Suslick 2010). A stable precursor solution with all salts dissolved is a necessity, or the precipitation in the precursor solution during spray pyrolysis can lead to non-uniform droplet-to-droplet concentration. This could cause product particles with non-uniform particle-to-particle composition and structure (Gurav et al. 1993). Therefore, it is challenging to synthesize functional particles from aqueous solutions containing poorly-soluble or easily-hydrolyzed salts. To resist precipitation, metal salts with strong acids and pure organic solvents are normally used to form stable precursor solutions (Route (I), Figure 6.1a) (Xu et al. 2013a; Zhang et al. 2014a). H_2 is typically introduced into the carrier gas to promote the complete reduction of the salts (Xu et al. 2013a), or residual oxides could be formed in the product (Hong and Kang 2015; Joshi et al. 2017). However, potential safety concerns accompanied with the usage of low flash point organic solvents (*e.g.*, ethanol, 13 ^{o}C), an acidic precursor, and explosive gas (H_2) make industrial scale production difficult (Yaws 1999).

Here, we present colloidal spray pyrolysis (CSP) for the first time, a process that can generate functional particles with uniform particle-to-particle composition and structure from stable multiphase precursor solutions (Route (II), Figure 6.1a), which could be a promising strategy to prepare uniform electrode materials in LIBs and SIBs. The structure and composition of particles are pre-designable based on our models. Several

distinguishable advantages of CSP make it unique when compared to conventional aerosol processes. Unlike spray pyrolysis, CSP can process low solubility salts, expanding the application of spray pyrolysis to a wider range of functional materials. CSP uses an aqueous precursor solution, with no direct addition of H_2 gas or pure organic solvents, which makes CSP safer and simpler for scale-up manufacturing. CSP is also different from multi-step spray drying, where colloids are used as templates to be etched away in the end (Boissiere et al. 2011; Jung et al. 2013). CSP is a one-step process with a short residence time where colloids are involved in *in-situ* solid-state reactions and structural evolution.

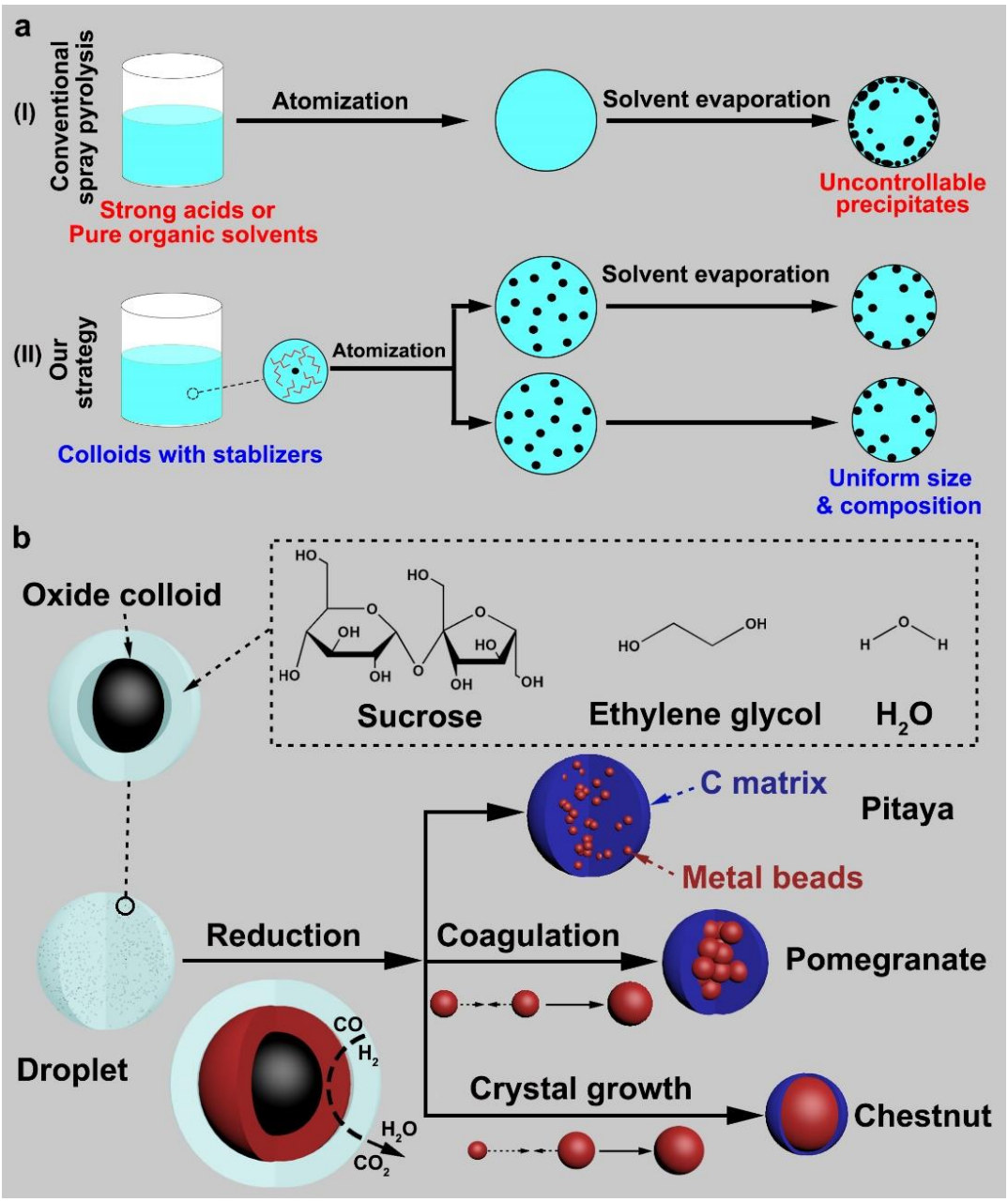

Figure 6.1. Schematic drawings of conventional spray pyrolysis and colloidal spray pyrolysis. (a) A comparison of conventional spray pyrolysis (Route I) and our strategy (Route II) with their advantages (in blue) and disadvantages (in red). (b) Schematic of colloidal spray pyrolysis to fabricate pitaya-structured, pomegranate-structured, and chestnut-structured particles.

To evaluate the robustness of CSP, we targeted tin@carbon (Sn@C) nanocomposite particles that are difficult to synthesize by conventional spray pyrolysis because Sn salts are easily hydrolyzed in aqueous solutions (Perry 2011). Sn@C nanoparticles are also promising anode materials for LIBs and SIBs due to their high theoretical capacities (993 mAh/g for $Li_{4.4}Sn$ and 847 mAh/g for $Na_{15}Sn_4$) and suitable working potentials (<0.5V) (Chen and Sieradzki 2013; Im et al. 2013; Tian et al. 2015; Xu et al. 2013a). Guided by theoretical analysis of the aerosol dynamics and reaction kinetics, Sn@C with different interior nanostructures of Sn in carbon matrices, similar to pitayas, pomegranates, and chestnuts, were synthesized by tuning the process parameters (Figure 6.1b, Table 6.1). The pomegranate-structured Sn@C powders exhibit superior electrochemical performance as anode materials in LIBs and SIBs. CSP with *in-situ* solid-state reactions opens up new opportunities to produce uniform composition particles with complex structures from precursors without solubility limitations.

Table 6.1. Precursors to fabricate different structures of Sn@C particles

		Pitaya	Pomegranate	Chestnut
Sucrose	[Sucrose] (mol/L)	2.0×10^{-1}	2.0×10^{-1}	1.0×10^{-2}
	Mass loading (kg/L)	7.0×10^{-2}	7.0×10^{-2}	3.5×10^{-3}
SnO_2	[SnO_2] (mol/L)	2.3×10^{-2}	3.8×10^{-2}	7.6×10^{-2}
	Mass loading (kg/L)	3.5×10^{-3}	5.8×10^{-3}	1.2×10^{-2}
	[SnO_2 colloid] (#/L)	1.1×10^{19}	1.9×10^{19}	3.8×10^{19}
Sucrose/SnO_2	Molar ratio	8.9	5.2	0.13
	Mass ratio	20.2	12.1	0.3
Viscosity of precursor (mPa·s)		2.24	2.14	1.63
Concentration of ethylene glycol (M)		4.8		

6.3 Experimental

6.3.1 Sn@C fabrication by CSP

In the precursor, SnO_2 colloids (Nyacol, SN15ES) were added to an aqueous solution containing sucrose (FISHER CHEMICAL), and then mixed with ethylene glycol (EG, SIGMA-ALDRICH, ≥ 99 %) to form a 150-ml-precursor solution. The mass ratio of sucrose to SnO_2 colloids in the precursor was 20.2 (Sn@C pitaya), 12.1 (Sn@C pomegranate), and 0.3 (Sn@C chestnut), as shown in Table 6.1. Detailed calculation procedures to obtain the colloid concentration are presented in Section A3 of Appendices.

The prepared precursor was then atomized into droplets by a home built ultrasonic atomizer with a 1.7 MHz transducer. The droplets were transported by N_2 gas through a quartz tube heated by a double furnace system (two furnaces connected in series, 81.3 cm in length). The set points of both furnaces were 750 ^oC. The residence time of the reactor was 1.5 s for experiments to obtain Sn@C pitaya particles and 4.5 s for the fabrication of Sn@C pomegranate and chestnut particles. The residence time was tuned by changing the carrier gas flow rate into the system. At the end of the tube, the powders were cooled to 57 ^oC by quench gas (N_2) and collected on a polytetrafluoroethylene (PTFE) filter (with a diameter of ~ 9.5 cm).

The residence time of our process was calculated by assuming our reactor is a plug-flow reactor, consisting 32 sub-units of identical length. By measuring the temperature in each sub-unit, the residence time of the process can be calculated as:

$$\tau = \sum_1^{32} \frac{A \times l}{F} \times \frac{T_{room}}{T_i} \quad (6.1)$$

Here, A is the cross sectional area of the tube, l is the length of the calculation element, F is the carrier gas flow rate, T_{room} is the room temperature, and T_i is the temperature in each element which has been presented in Chapter 3.

6.3.2 Characterization

TEM was carried out using a JEOL 2100 LaB_6 TEM and a JEOL 2100F FEG TEM equipped with Gatan image filter (GIF, Tridiem 863). The collected powders were dispersed into ethanol and sonicated for ~ 1 min. Then the mixture was added dropwise onto a lacey carbon film coated Cu grid in order to avoid the interference of C signal from the carbon film itself. SEM images were taken by a Hitachi SU-70 SEM. Similar to the TEM sample preparation, the ethanol particle mixture was added dropwise onto a silicon wafer. In addition, a BRUKER D8 advance XRD was used to determine crystallographic information.

6.3.3 Electrode preparation and electrochemical measurement

Electrochemical measurements were performed using coin cells (CR2032) assembled in an argon-filled glove box (<1 ppm of water and oxygen). To prepare the Sn@C electrode, Sn@C powders, carboxyl methyl cellulose (CMC), and carbon black with a mass ratio of 70: 20: 10 were magnetically stirred for over 5 h to ensure thorough mixing. The slurry was cast onto a thin copper foil and dried. Prior to cell fabrication, the electrodes were dried overnight at 80 °C in a vacuum. The coin cells were assembled with lithium foil as the counter electrode, 1.0 M $LiPF_6$ solution in a mixture of dimethyl carbonate (DMC) and ethyl methyl carbonate (EMC) (1:1 volume ratio) with 10% fluoroethylene carbonate (FEC) for LIBs or 1.0 M $NaClO_4$ solution in a mixture of ethylene carbonate/dimethyl carbonate (EC/DMC, 1:1 by volume) for SIBs as the electrolyte, and a polypropylene film

(Celgard3501, LLC Corp., USA) as the separator. The electrochemical properties of the Sn@C particles were studied with a multichannel battery-testing system (Arbin Instruments, TX, US), using charge/discharge galvanostatic cycling from 2.0 V to 0.01 V with the loading mass of ~ 1.0 $mg \cdot cm^{-2}$. The specific capacity was calculated based on the mass of Sn@C powders. The electrochemical impedance spectrum and cyclic voltammetry measurements were carried out on an electrochemistry workstation (Solartron 1287/1260) at room temperature.

6.4 Results and discussion

6.4.1 Aerosol dynamics and reaction kinetics in colloidal spray pyrolysis

In CSP, the aqueous precursor solution containing colloids, co-solvent, and stabilizer for colloids is first atomized into droplets. The droplets go through a series of processes including solvent evaporation, colloid reduction, and inter-colloid collision, forming product particles. The particle engineering of CSP involves both the oxide-colloid reduction and inter-colloid collision/coagulation processes (Figure 6.1b). The product composition is controlled by colloid reduction. The inter-colloid collision/coagulation determines the interior nanostructure of the product particles. Although both processes happen simultaneously during CSP, we can still model CSP in the ideal case in which the two processes are isolated.

For the colloid reduction, the co-solvent is the main reducing agent in CSP during its decomposition. In a multiphase system, the diffusion of reactant gases through the colloids (Figure 6.1b) may be difficult because of the mass transport resistance. For example, $D_{gas\text{-}in\text{-}solid}/D_{liquid\text{-}in\text{-}liquid}$ (diffusivity ratio) is as low as 10^{-5} at 25 ^{o}C (Deen 1998; Nowick 2012).

In many cases, the densities of metals and their oxides are comparable. Therefore, the colloid reduction process can be simulated by the shrinking-core model (Levenspiel 1999). In CSP, H_2 is mainly generated from co-solvent, which are uniformly dispersed in the droplets. The concentration of H_2 ($C_{s,H2}$) was assumed to be uniform. The reduction process consists of mass transport of reactants and the chemical reaction.

Corresponding equations to calculate the time of the colloid reduction process were derived with detail procedures in A2.1 (Appendices). The chemical formula of the oxide (MO_x) reduction into metal (M) can be described as:

$$xH_2 + MO_x \rightleftharpoons M + xH_2O \quad (6.2)$$

When the reduction is controlled by diffusion of H_2 through the metal ash outside the oxide core, the colloid reduction time is:

$$\tau = \frac{\rho_{MOx} R^2}{6 x D_e C_{s,H2}} \quad \text{(diffusion controls)} \quad (6.3)$$

If chemical reaction between H_2 and the oxide core controls the CSP process, the colloid reduction time can be calculated as:

$$\tau = \frac{\rho_{MOx} R}{x k_r C_{s,H2}^n} \quad \text{(reaction controls)} \quad (6.4)$$

Here, D_e is diffusivity of H_2 in the metal layer. k_r is rate constant. n is reaction order. ρ_{MOx} is density of metal oxides. R is colloid radius. Based on Equations (6.3,6.4), the composition of product particles can be controlled. When the residence time of CSP process is larger than the time required for colloid reduction, the oxide colloids can be reduced completely into metal.

In aerosol dynamics, the colloid collision frequency within individual droplets is a critical factor influencing the interior structure of the product particles (Nandiyanto and Okuyama 2011). The collision frequency (*f*) of colloids in the droplets can be expressed as (Levich 1962):

$$f = 8\pi DRN_{\infty}(t)^2 \quad (6.5)$$

where *D* is the viscosity of the media which can be estimated by Stokes-Einstein formula (Equation 6.6). Equation 6.5 can be expanded into Equation 6.7:

$$D = \frac{kT}{6\pi R\mu} \quad (6.6)$$

$$f = \frac{4}{3} \cdot \frac{kT}{\mu} \cdot N_{\infty}(t)^2 \quad (6.7)$$

k is Boltzmann constant. *T* is temperature. μ is the viscosity of the precursor. *t* is the time elapsed after the droplets enter the reactor. The collision frequency of colloids significantly depends on the initial colloid loading in the droplet ($N_{\infty}(0)$). A high colloid loading results in a high collision frequency, promoting the formation of large interior structures. Thus, precursor solutions with higher initial colloid loading favor denser particles, while lower colloid loading results in more porous particles composed of smaller beads as the interior structures (Bahadur et al. 2010; Iskandar et al. 2009; Wang et al. 2007b). Based on the analysis and Equations (6.5-6.7), we predict that the increasing colloid loading in the precursor solution may result in a growth of interior structure of the product particles, from dispersed small beads to large core, making the structure of product particles similar to pitaya, pomegranate, and chestnut in sequence, as illustrated in Figure 6.1b.

6.4.2 Application of colloidal spray pyrolysis in fabricating Sn@C particles.

To test the feasibility of CSP, it was applied to produce Sn@C particles from an aqueous precursor solution, containing SnO_2 colloids, ethylene glycol (EG) as the co-solvent and sucrose as the stabilizer (Figure 6.1b). The decomposition of EG can generate H_2 and CO gases during the processing (Yue et al. 2012; Zhong et al. 2013b). Sucrose acts as a stabilizer for colloids in precursor, carbon source, and reducing agent during its decomposition to carbon (Cho et al. 2013; Wang et al. 2009). Therefore, both EG and sucrose provide H_2. The precursor was atomized into 5 μm droplets (a volume mean diameter) by a 1.7 MHz ultrasonic generator (Zhong et al. 2013b). The droplets were then transported by N_2 gas into two tube furnaces in series, both set at 750 ^oC. The SnO_2 colloids used in precursor solution have high crystallinity with lattice fringes attributed to the (200) plane of SnO_2 and narrow size distribution (number mean = 4.4 nm; standard deviation = 1.3 nm, Figure 6.2a-c). The SnO_2 colloids-sucrose-EG aqueous precursor displayed stability with respect to precipitation for at least 2 h (Figure 6.3), which is the prerequisite condition for uniform particle-to-particle composition and structure in products (Gurav et al. 1993).

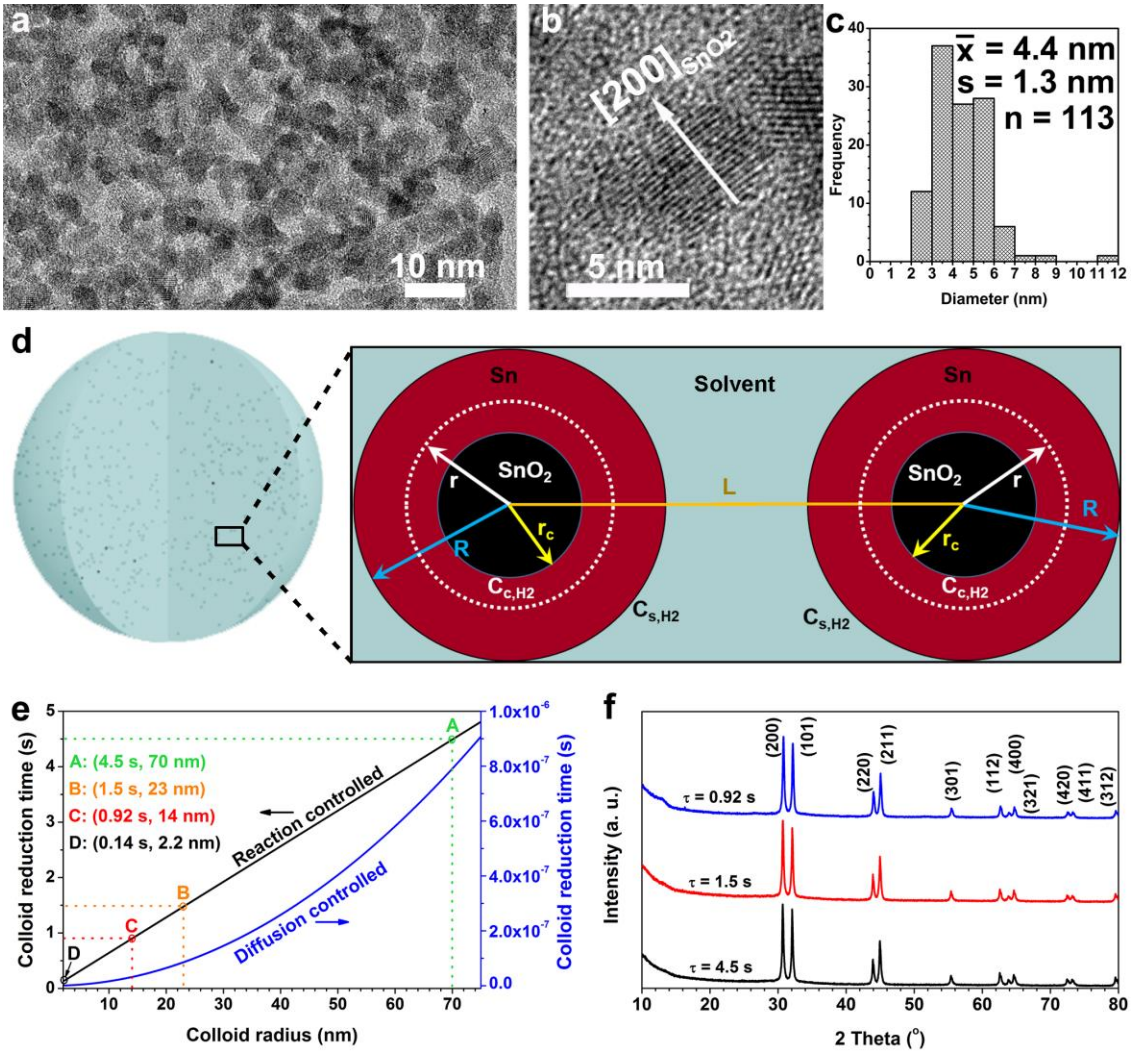

Figure 6.2. Composition control of the product particles by colloidal spray pyrolysis. (a-b) TEM image of the SnO_2 colloids used in the precursor (a) with HRTEM image (b). (c) Diameter distribution of SnO_2 colloids with mean diameter, standard deviation, and sample size. (d) Schematic of parameters used in calculating the time of colloid reduction in colloidal spray pyrolysis. (e) Time required to reduce a SnO_2 colloid as a function of initial colloid diameter, based on reaction-controlled model (left y-axis) and diffusion-controlled model (right y-axis). (f) XRD diagram of powders obtained at 750 ^{o}C when the residence time of the process is 4.5 s (black curve), 1.5 s (red curve), and 0.92 s (blue curve).

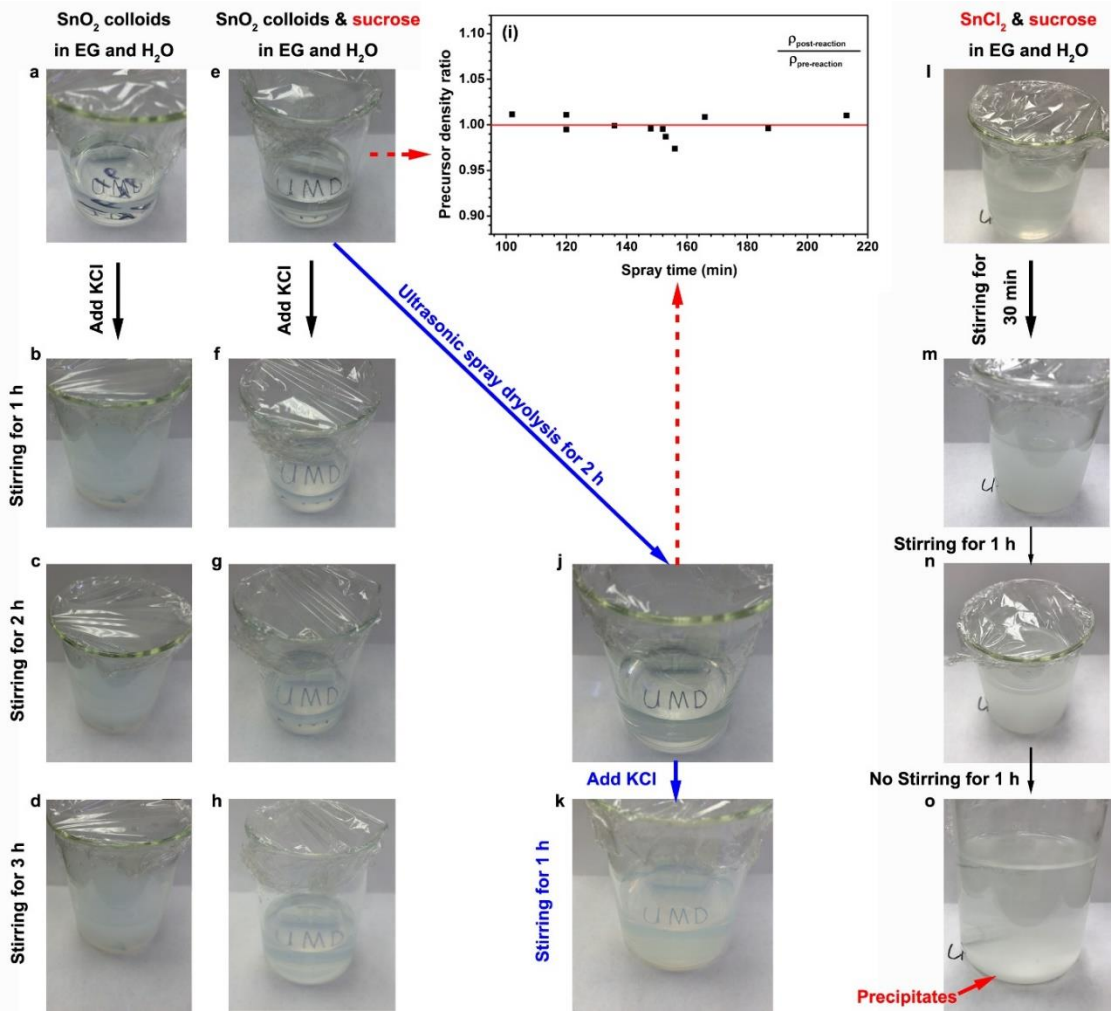

Figure 6.3. (a) is a beaker containing an aqueous solution with 3.8×10^{-2} M SnO_2 and 4.8 M EG. After adding 0.11 M KCl into (a), the solution was stirred for 1 h (b), 2 h (c), and 3 h (d) consecutively. (e) is a beaker containing the precursor for the generation of Sn@C pomegranate particles. The precursor composed of 0.2 M sucrose, 3.8×10^{-2} M SnO_2, and 4.8 M EG. After adding 0.11 M KCl into (e), the solution was stirred for 1 h (f), 2 h (g), and 3 h (h) consecutively. (j) is the image of (e) after being ultrasonically sprayed for 2 h. After adding 0.11 M KCl into (j), the solution was stirred for 1 h shown in (k). Density measurements were taken for the precursor before (e) and after (j) the reaction. When taking the photos, beakers were placed on the marked area of paper with letters of "UMD".

Without adding sucrose, SnO_2 colloids precipitated within 1 h after adding KCl into the solution. As shown in (b), "UMD" was hard to see. With sucrose, the SnO_2 colloids remained stable and dispersed in the precursor shown in (f)-(h). After adding KCl into the solution (f), "UMD" can still be seen at least for 3 h as shown in (h). For the precursor after being sonicated for 2 h (j), "UMD" can be seen after adding KCl and stirring for 1 h as illustrated in (k). Since the size of SnO_2 colloids is small (mean diameter = 4.4 nm), we cannot separate them from precursor via filtration and high-speed centrifuging. This is the best method to demonstrate the high uniformity and the high stability of our precursor. (l) is an aqueous solution with 0.1 M $SnCl_2$, 0.4 M sucrose, and 4.8 M EG. The molar ratio of sucrose to $SnCl_2$ is 4. "UMD" is hard to be observed due to the hydrolysis of $SnCl_2$. (m) is an image of the solution in (l) after being stirred for 1 h. The solution is cloudy. We cannot see the "UMD" through the solution. (n) shows the solution in (m) after being placed for 1 h without stirring. The precipitates concentrate at the bottom of the beaker.

Firstly, the reduction time of SnO_2 colloids was calculated to understand the practicability of this process. The densities of Sn (ρ_{Sn}=7.31 g/cm^3, 20 ^{o}C) and SnO_2 (ρ_{SnO2}=6.95 g/cm^3, 20 ^{o}C) are comparable (Perry 2011). Hence, the reduction time was determined based on Equations (6.3-6.4) using shrinking-core model, as shown in Figure 6.2d. The detailed simulation procedures are presented in A2.2 (Appendices). The precursor composition is listed in the Column Pomegranate of Table 6.1. The calculated results are summarized and plotted in Figure 6.2e. The ratio of calculated colloid reduction time based on diffusion-controlled model to that based on reaction-controlled model is ~10^{-7}, when colloid radius is smaller than 75 nm. Therefore, chemical reaction is determined to

be the rate-limiting step. In addition, when the residence times are 4.5 s, 1.5 s, or 0.92 s, the maximum radii of the SnO_2 colloids that can be completely reduced are 70 nm, 23 nm or 14 nm, respectively (Figure 6.2e). These estimated radii are all larger than that of the SnO_2 colloids we used (2.2 nm), which means theoretically SnO_2 colloids can be completely converted to Sn by CSP.

Experimentally, the SnO_2 colloids have been successfully reduced in CSP with the conditions we used in the simulation mentioned above, as shown in Figure 6.2f. All the peaks in the XRD diagram are pronounced and attributed to Sn (PDF No. 01-075-9188) without the existence of oxide phases. When the process residence time is 4.5 s, the product particles exhibit pomegranate-like structure with beads inside the particles (Figures 6.4-6.5). The product particles change from spherical to fragmental structures with decreasing residence time, which is commonly observed in products by tuning the residence time of aerosol processes (Nandiyanto and Okuyama 2011).

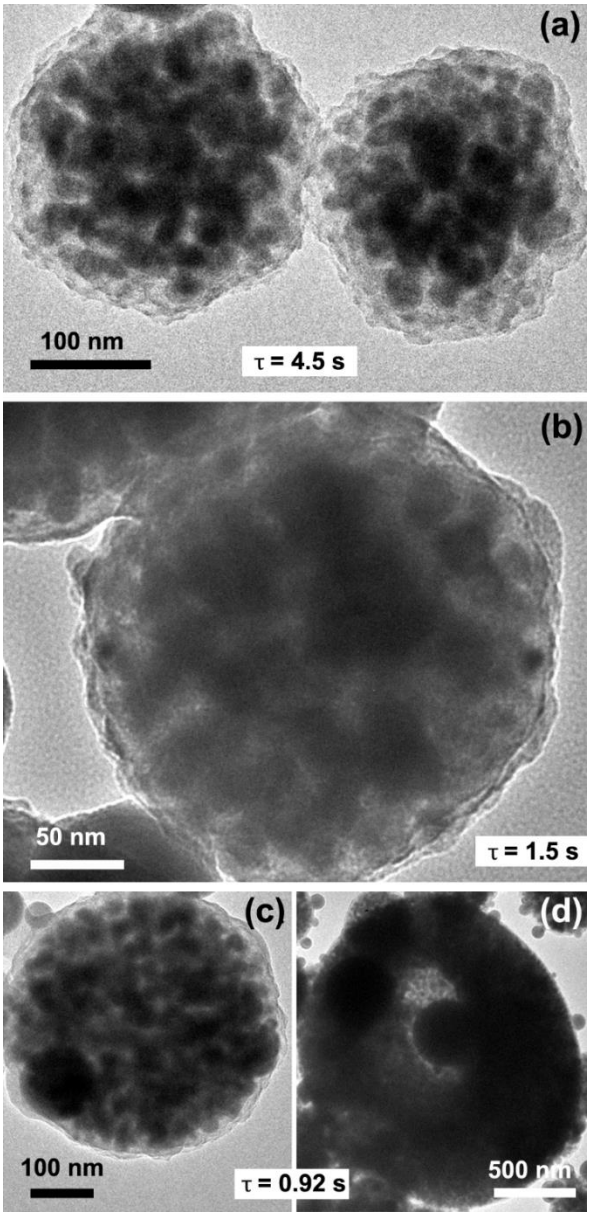

Figure 6.4. TEM images of powders obtained at 750 ^{o}C with the same precursor solution used to generate Sn@C pomegranate particles. The residence times for the fabricated process are 4.5 s (a), 1.5 s (b), and 0.92 s (c)-(d). The fragmented particles shown in (d) together with Figure 6.5c are believed to stem from the burst of the droplets caused by build-up pressure inside the droplet during solvent evaporation, as discussed in Chapter 3.

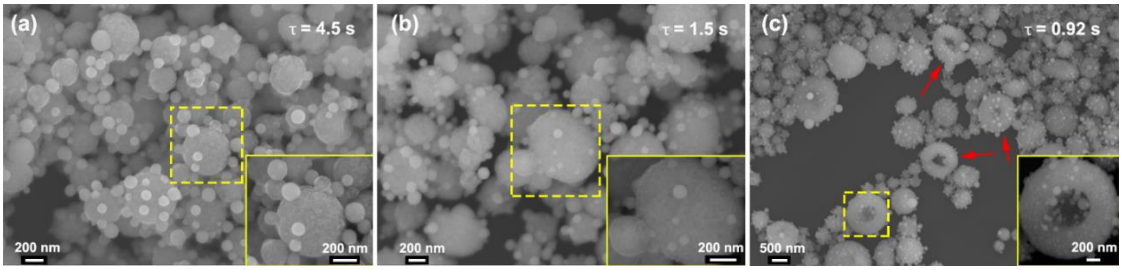

Figure 6.5. SEM images of powders obtained at 750 ^{o}C with the same precursor solution used to generate Sn@C pomegranate particles. The residence times for the fabrication process are 4.5 s (a), 1.5 s (b), and 0.92 s (c). The insets are the high magnification images of the corresponding areas marked by dashed boxes. Fragmented particles are marked by red arrows in (c). The fragmented particles shown in (c) are believed to stem from the burst of the droplets caused by build-up pressure inside the droplet during solvent evaporation, as discussed in Chapter 3.

Guided by aerosol dynamics and Equations (6.5-6.7), we have also successfully controlled the interior structure of Sn@C particles by adjusting the initial colloid loading in precursor (Table 6.1). Consistent with the theoretical prediction, when the initial SnO_2-colloid loading increases from 1.1×10^{19} to 3.8×10^{19} colloids/L, the interior nanostructure in the carbon matrix shifts from small beads (pitaya-structure in Figure 6.6a,d-g), through more coagulated beads (pomegranate-structure in Figure 6.6b,h-k), to large cores (chestnut-structure in Figure 6.6c,l-o), as clearly demonstrated in HRTEM images and their corresponding elemental mappings. From both TEM and SEM images (Figure 6.7), particle size distributions are summarized in Figure 6.6p-v. The average size of Sn beads in C matrix are 16 nm (pitaya-structured), 24 nm (pomegranate-structured), and 139 nm (chestnut-structured). The increasing average size of Sn beads with colloid loading

confirms that inter-colloid collision frequency increased with initial colloid loading. Sn@C particles show spherical morphology with average particle diameter decreasing from 340 nm (pitaya-structured), through 301 nm (pomegranate-structured), to 139 nm (chestnut-structured). The mass fraction of Sn in the Sn@C particles increases from 77% (pitaya-structured), through 83% (pomegranate-structured), to 89% (chestnut-structured) with decreasing mass ratio of sucrose to SnO_2 in precursor, as shown in Figure 6.8.

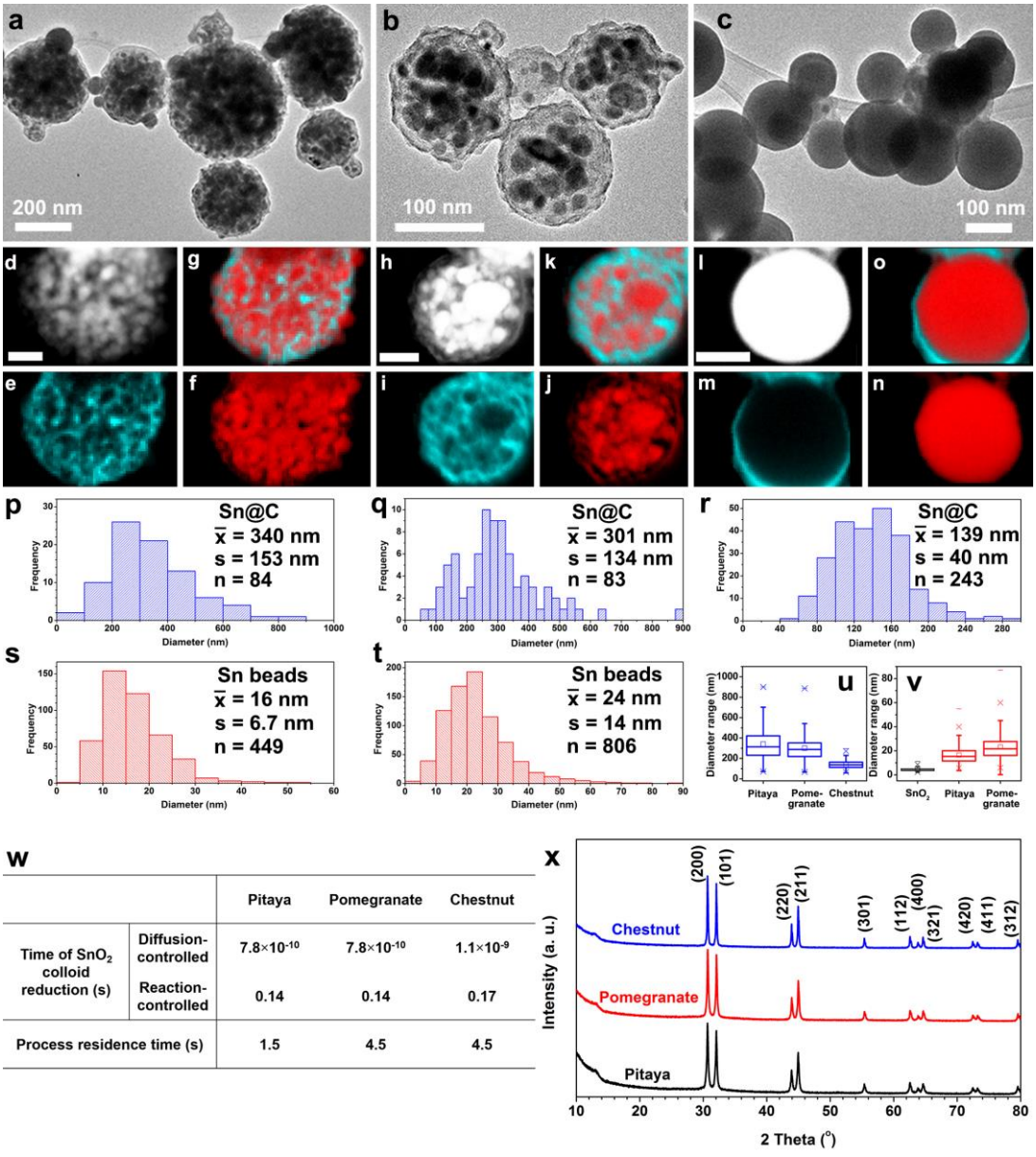

		Pitaya	Pomegranate	Chestnut
Time of SnO_2 colloid reduction (s)	Diffusion-controlled	7.8×10^{-10}	7.8×10^{-10}	1.1×10^{-9}
	Reaction-controlled	0.14	0.14	0.17
Process residence time (s)		1.5	4.5	4.5

Figure 6.6. Structure and composition control of the product particles by colloidal spray pyrolysis. (a-c) TEM images of pitaya-structured (a), pomegranate-structured (b), and chestnut-structured (c) particles. (d-n) STEM-HAADF image and EELS elemental mappings of C signal, Sn signal, and overlap result of Sn@C pitaya (d-f, respectively), pomegranate (h-k, respectively), and chestnut (l-o, respectively) particles. The scale bars in STEM-HAADF images are 50 nm. (p-t) Statistical summaries of Sn@C particle and interior Sn bead diameters of pitaya-structured (p,s, respectively), pomegranate-structured (q,t, respectively), and chestnut-structured (r) particles with mean values, standard deviations, and sample sizes. (u-v) Box plots to summarize the size distributions of Sn@C particles (u) and Sn beads (v). (w) Calculations of the colloid reduction time on conditions to generate Sn@C pitaya, pomegranate, and chestnut particles. (x) XRD patterns of the generated Sn@C pitaya, pomegranate, and chestnut particles.

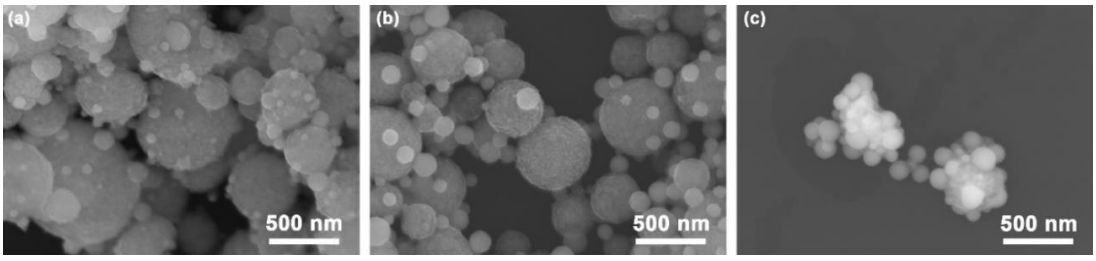

Figure 6.7. SEM images of Sn@C pitaya (a), pomegranate (b), and chestnut (c) particles.

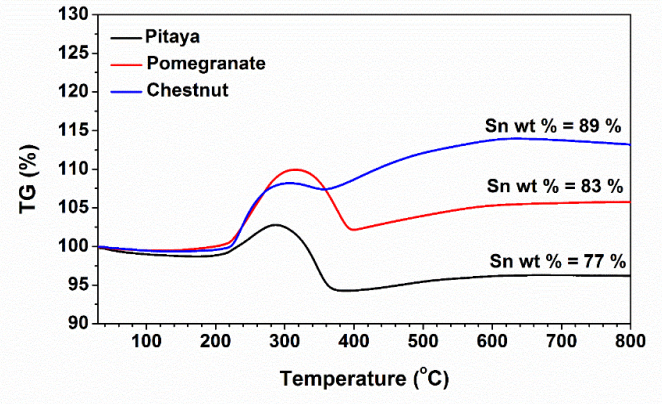

Figure 6.8. TGA results of the Sn@C pitaya (black), pomegranate (red), and chestnut (blue) powders. The relative weight percentages of Sn were calculated based on following equation (Xu et al. 2013a):

$$Sn\ wt\ \% = \frac{\frac{W_{Final,SnO2}}{Mw_{SnO2}} \cdot Mw_{Sn}}{W_{Initial,Sn@C}} \cdot 100\ \% \qquad (6.8)$$

The formation of crystal Sn and amorphous carbon in all three types of Sn@C particles is supported by the theoretical analysis on the colloid-reduction and confirmed by the XRD measurement (Figure 6.6w-x). Although the colloid loading varies between the three conditions to obtain different structured Sn@C particles, as shown in Table 6.1, the colloid reduction time is also controlled by chemical reaction based on the calculated results (Figure 6.6w). The theoretical colloid reduction times are all smaller than the process residence times, suggesting the colloids can be completely reduced by the CSP. The XRD patterns further validate this hypothesis with noticeable peaks from Sn phase (PDF No. 01-075-9188) and the absent of oxide phases. The full-width at half-maximum (FWHM) of the main peak at 30.8^o decreased from 0.27 (pitaya-structured), through 0.25 (pomegranate-structured), to 0.18 (chestnut-structured), indicating that the Sn@C chestnut particles have the largest Sn crystalline domain based on Scherrer equation. Sn@C chestnut has the greatest degree of crystallinity, which is attributed to the fastest nucleation and crystal growth among the Sn@C particle production processes. This is also consistent with the aerosol dynamic analysis that the high initial colloid loading contributes to the high frequency of inter-colloid collision.

To validate this aerosol dynamic analysis, we further changed the initial SnO_2 colloid loading to 6.1 (mass ratio of sucrose to SnO_2 colloids, Table 6.2), a condition between

those to obtain Sn@C pomegranate (12.1) and chestnut (0.3) particles. The Sn@C particles fabricated at this condition (termed as intermediate) display a mix of pomegranate-structured and chestnut-structured particles (Figure 6.9), which is consistent with our theoretical analysis. In the XRD pattern of Sn@C intermediate particles (Figure 6.10), the FWHM of the main peak at 30.8^o is 0.24, which is also between those of the Sn@C pomegranate and chestnut powders, consistent with the SnO_2 loading in the precursor.

Table 6.2. Precursor to obtain Sn@C intermediate particles

		Intermediate
Sucrose	[Sucrose] (mol/L)	2.0×10^{-1}
	Mass loading (kg/L)	7.0×10^{-2}
SnO_2	[SnO_2] (mol/L)	7.6×10^{-2}
	Mass loading (kg/L)	1.2×10^{-2}
	[SnO_2 colloid] (#/L)	3.8×10^{19}
Sucrose/SnO_2	Molar ratio	2.7
	Mass ratio	6.1
Concentration of ethylene glycol (M)		4.8

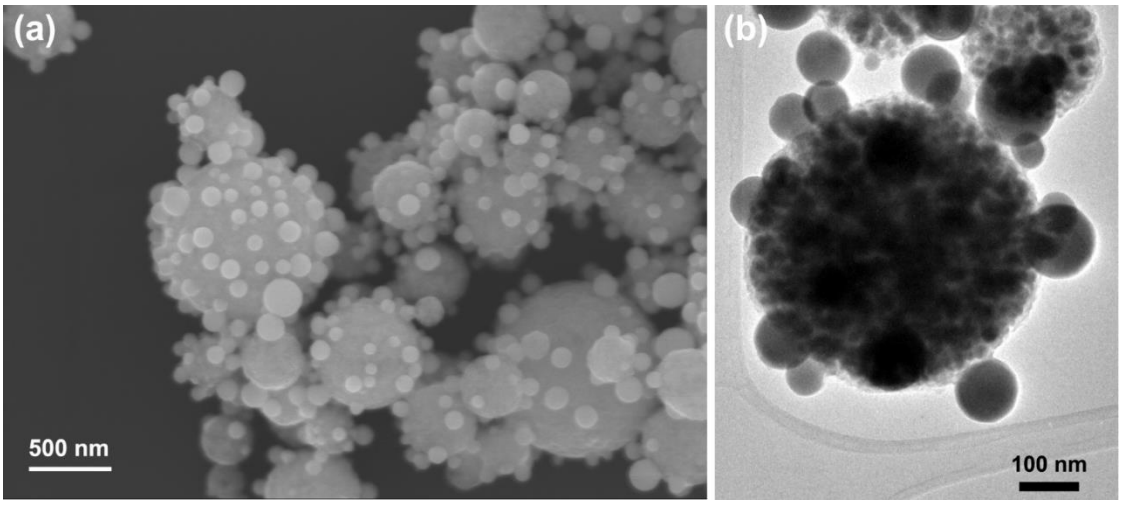

Figure 6.9. SEM (a) and TEM (b) images of Sn@C intermediate powders fabricated from a precursor with sucrose/SnO_2 (mass ratio) = 6.1, which is between that of Sn@C pomegranate and chestnut particles.

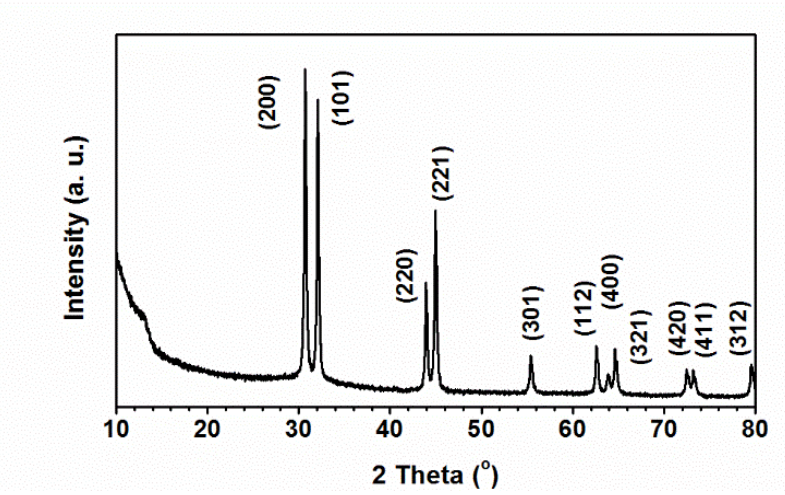

Figure 6.10. XRD diagram of Sn@C intermediate powders fabricated from a precursor with [sucrose]/[SnO_2] = 2.7, which is between that of Sn@C pomegranate and chestnut particles. All the peaks are attributed to the Sn phase (PDF No. 01-075-9188).

It is worth mentioning that the model in the above discussion is based on the ideal situation where the colloid reduction and inter-colloid collision/coagulation are isolated procedures. In reality, these steps happen simultaneously, which means the size of colloids is increasing due to coagulation during the reduction. Therefore, the actual radius of the colloids that needs to be reduced is larger than the radius of the colloids added into the precursors. A precursor solution was also processed at the same conditions to obtain Sn@C pomegranate-structured particles but without the addition of EG ($C_{s,H2}$=1.5 M). Based on the reaction kinetics, the colloid reduction time is 0.3 s, which is smaller than the process residence time (4.5 s). Thus, theoretically, SnO_2 colloids should be completely reduced. However, residual SnO_2 exists in Sn@C particles synthesized from the EG-free precursor, as demonstrated by a weak SnO_2 peak in the XRD diagram (Figure 6.11). This

phenomenon implies that EG is the main reducing agent in the CSP process and is crucial in tuning the composition of the products. Furthermore, the coagulation of the colloids increases the difficulty of complete reduction of the colloids. However, our model can still be applied to screen the colloids that can be processed by CSP and pre-design product structures.

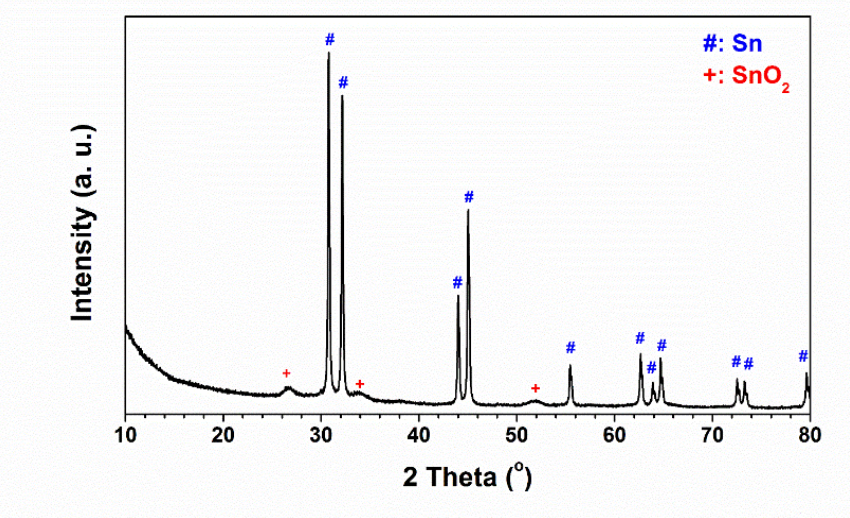

Figure 6.11. XRD diagram of powders fabricated with the same [sucrose]/[SnO_2], reaction temperature, and residence time to obtain Sn@C pomegranate structured particles without the addition of EG to the precursor. The peaks are indexed to SnO_2 (PDF No. 00-041-1445) and Sn (PDF No. 01-075-9188).

The possibility of collision between the product particles should also be considered. Both conventional spray pyrolysis and spray drying have long been considered as one-droplet-one-particle processes (Gürmen et al. 2006; Lengsfeld et al. 2000; Zhao et al. 1998). Therefore, we believe the multiphase spray pyrolysis also shares the same basis. To verify this hypothesis, the collision half-life of the Sn@C particles, defined as the time

necessary for the number concentration to fall to one half the value because of collisions, was calculated. Since the average diameters of all the three kinds of the Sn@C particles are less than 340 nm, the collision between the particles depends on the Brownian motion (Friedlander 2000).

With the initial colloid loading ($N_{p,\infty}(0)$), viscosity (μ), temperature (T) of the system, and target particle concentration ($N_{p,\infty}$), the characteristic time (t) can be calculated as (Friedlander 2000):

$$t = \frac{\frac{N_{p,\infty}(0)}{N_{p,\infty}} - 1}{\frac{8kT}{3\mu}\frac{N_{p,\infty}(0)}{2}} \quad (6.9)$$

Here, k is the Boltzmann constant. To compare the collision time in a quantitative manner, we calculate the half-life of the colloids during the process, where $N_{p,\infty}(0)/N_{p,\infty} = 2$. Then,

$$\tau_{1/2} = \frac{3\mu}{4kT \cdot N_{p,\infty}(0)} \quad (6.10)$$

To obtain the collision time by Equations (6.9-6.10), μ was calculated as the viscosity of N_2 gas. The viscosity of the N_2 at 750 ^oC can be obtained as (Yaws 1999):

$$\mu = 42.606 + 0.475T - 9.88 \times 10^{-5}T^2 \ [\mu P] \quad (6.11)$$

At 750 ^oC, μ = 425 μP, which is 4.25×10^{-5} Pa·s. The $N_{p,\infty}(0)$ was obtained by the assumption that our process is a plug-flow reactor. Therefore, collisions could only happen laterally, and not along the flow path (Levenspiel 1999). The average consumption rate of the precursors was determined experimentally as 5.5×10^{-3} ml/s. Accounting for the average diameter of our droplets (5 μm) (Zhong et al. 2013b), reactor volume (3.0×10^{-4} m^3), and

residence times, $N_{p,\infty}(0)$ and $\tau_{1/2}$ were calculated and listed in Table 6.3. Therefore, considering the residence times of the conditions, no inter-particle collision would be expected, which validates the one-droplet-one-particle mechanism.

Table 6.3. The half-time of inter-particle collision between Sn@C particles

	Sn@C pitaya	Sn@C pomegranate	Sn@C chestnut
Residence time (s)	1.5	4.5	4.5
$N_{p,\infty}(0)$ (#/m^3)	4.2×10^{11}	1.3×10^{12}	1.3×10^{12}
$\tau_{1/2}$ (s)	5.4×10^{3}	1.8×10^{3}	1.8×10^{3}

The collision rates between Sn@C particles in all three scenarios were also calculated and shown in Table 6.3. Significantly longer collision/coagulation half-lives than process residence times indicate negligible collision between Sn@C particles, verifying the one-droplet-one-particle model (Lengyel et al. 2014).

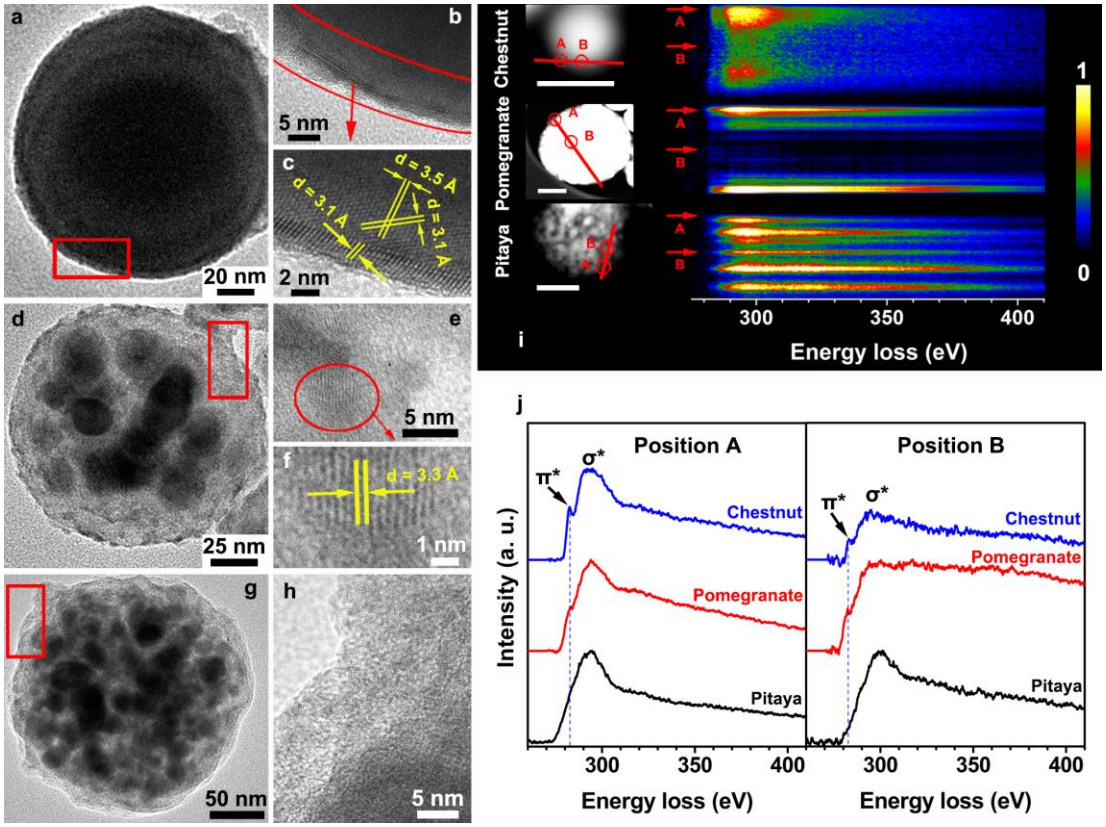

Figure 6.12. Carbon frames in Sn@C particles. (a-h) TEM images of chestnut-structured (a), pomegranate-structured (d), and pitaya-structured (g) particles with its corresponding HRTEM images (b)-(c), (e)-(f), and (h), respectively. The HRTEM images were taken from the areas marked by red color boxes. (c,f) Higher magnification images of areas in (b) and (e), respectively. (i) STEM-HAADF images (left) and EELS line scan results (right) of chestnut-, pomegranate-, and pitaya-structured particles (from top to bottom). The scale bars in HADDF images are 100 nm. (j) EELS spectra of C K-edge extracted from position A (left) and B (right) of (i).

In addition to the interior nanostructure and composition of Sn@C particles, carbon can also be controlled by varying the process parameters. As discussed in above, sucrose produces reducing gases during its decomposition and also results in the formation of

carbon (Cho et al. 2013), which serves as frame in Sn@C particles. As shown in Figure 6.12a-h, the edge of the chestnut-structured particles is encapsulated by crystalline carbon layers, revealing long-range ordered lattice fringes with spacing of 3.1~3.3 Å (Figure 6.12a-c). It is consistent with the results that the inter-layer distance in the stacked carbon layers is around 3.3 Å (de Andres et al. 2008; Lee et al. 2013). The strong C signal in electron energy loss spectroscopy (EELS) spectra (Figure 6.12i-j) validates the $Sn_{core}C_{shell}$ structure of chestnut-like particles. The EELS spectral feature of C *K*-edge from both the edge and center of the chestnut particle displays clear π* peaks at ~ 284 eV (Figure 6.12i-j), which are excited from C atoms with the sp^2 coordination environment (Suenaga and Koshino 2010). The nature of π bonding prohibits its formation on structures with sharp arches or small radii, because the p-orbital electrons can only delocalize sideways in a planar formation. Therefore, neither long-range stacking of crystalline carbon layers is observed in TEM images (Figure 6.12g-h) nor significant π* peaks appear in the EELS spectra (Figure 6.12i-j) in Sn@C pitaya particles, because the diameters of the Sn beads of pitaya-structured particles are remarkably smaller than those of Sn@C chestnut particles (Figure 6.6). For the Sn@C pomegranate, the stacking of C layers can only be found in the localized region (Figure 6.12d-f). Therefore, the difference of crystallinity of carbon also verifies the size difference of Sn beads in carbon frame. Raman spectra of Sn@C pitaya, pomegranate, and chestnut are consistent with TEM and EELS observations with Sn@C chestnut showing the highest D/G peak ratio and most pronounced 2D peak (Figure 6.13). Contrarily, Sn@C pitaya exhibits the lowest D/G peak ratio and negligible 2D peak.

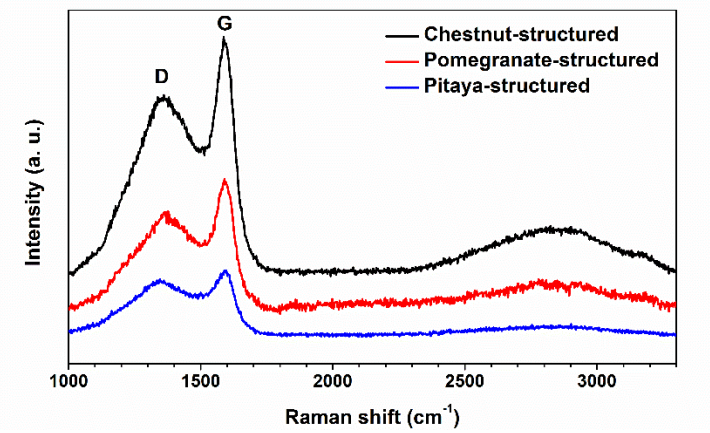

Figure 6.13. Raman spectra of the Sn@C pitaya (blue), pomegranate (red), and chestnut (black) powders. It was recorded by a Raman spectrometer, equipped with a 532 nm laser.

Compared to reported Sn-based functional particle engineering, CSP exhibits distinguished advantages including simple operating procedures, short processing time, mild reducing conditions, and better control of product structure and composition (The reported methods are summarized in Section 2.2 in Chapter 2). The increasing concentration of co-solvent in the precursor solution can tune the product from oxides to metals. Moreover, the desired product structure (pitaya-like, pomegranate-like, or chestnut-like) can be achieved by adjusting the colloid loading in precursor solution.

6.4.3 Electrochemical performance of Sn@C anodes in LIBs and SIBs.

The Sn@C particles are promising anode materials for LIBs because Sn is an electrochemically active component with a high capacity (The theoretical specific capacity of Sn is 993 $mAhg^{-1}$ for LIBs) (Huang et al. 2015; Winter and Besenhard 1999) and the elastic carbon matrix can effectively act as a sponge to alleviate the mechanical stress accompanying the volume change of Sn, which is a critical factor to influence the

electrochemical performance of Sn-based anodes (Huang et al. 2015; Kaspar et al. 2014; Ke et al. 2013; Ni et al. 2014).

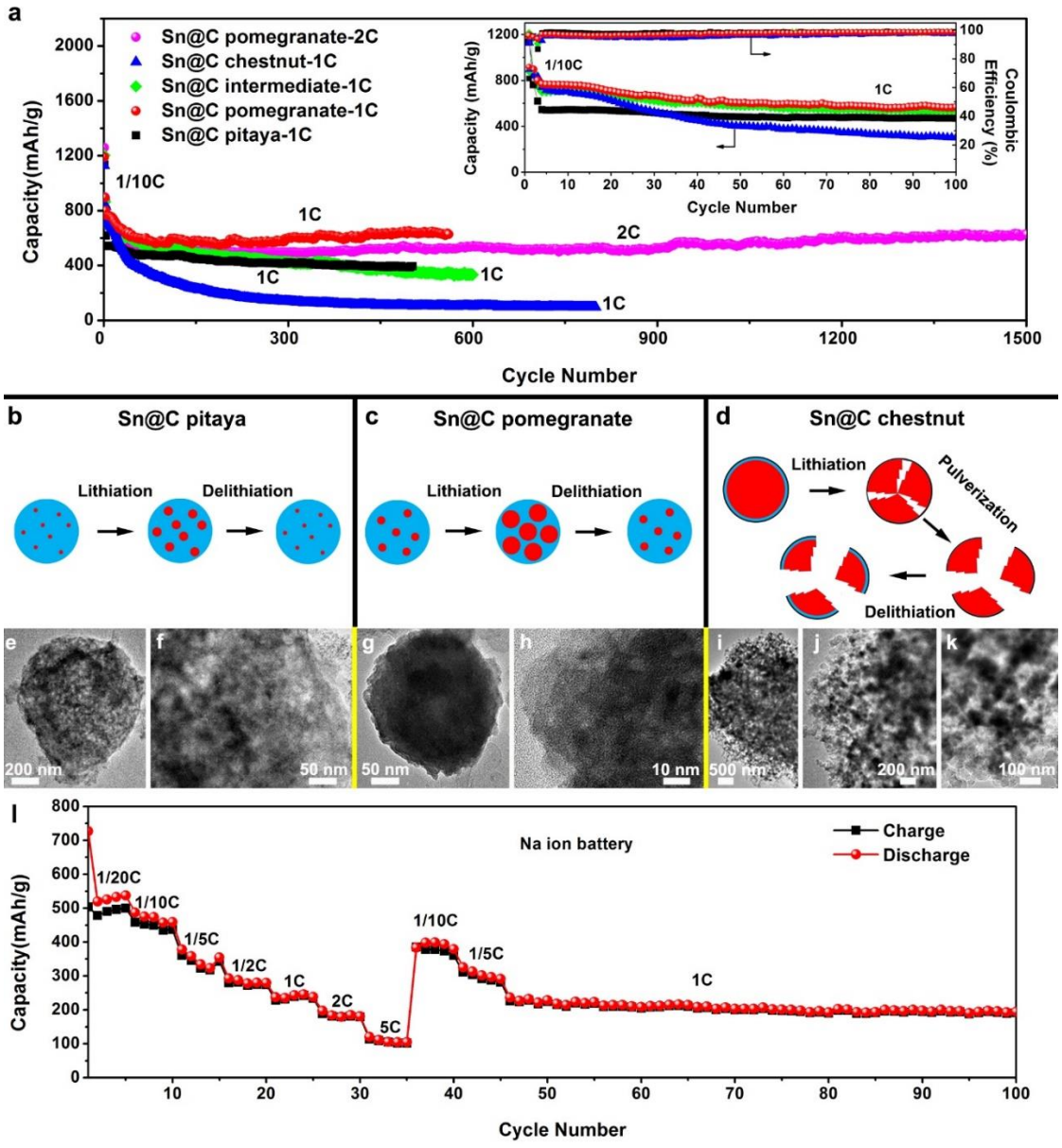

Figure 6.14 (a) Long-term cycling stability of the Sn@C electrodes at a current density of 1/10 C for the initial three cycles and at 1C for the following cycles. The inset is cycling performance of the Sn@C anodes for the initial 100 cycles at 1C. (b-k) Schematic summaries of structural evolution during lithiation/delithiation and TEM images of pitaya-

structured (b,e-f), pomegranate-structured (c,g-h), and chestnut-structured (d,i-k) particles in anodes after 100 cycles in rate performance test. (l) Rate capability of Sn@C pomegranate anode in SIB. Electrochemical experiments in (a) and (l) are conducted by collaborator (Huajun Tian).

The long-term cycling stability of three Sn@C anodes was evaluated at 1C after activation for the initial 3 cycles at 1/10C (inset of Figure 6.14a). The capacity of Sn@C chestnut anode endured the most significant capacity decay at the initial 100 cycles. In contrast, the Sn@C pitaya and pomegranate anodes retained highly stable electrochemical performance after 100 charge/discharge cycles. Similarly, the Sn@C pitaya also exhibited good cycling stability due to its nanostructured Sn and elastic carbon framework, which can support the large volume change during lithiation process, after capacity decay in first 5 cycles. Long-term cycling performance (Figure 6.14a) of the Sn@C electrodes were evaluated at a high rate of 1C and 2C. The capacity retention of Sn@C pomegranate anode can be maintained at 627.9 $mAhg^{-1}$ even after 1500 cycles, corresponding to 88.5% capacity retention at 2C, which is one of the best performance in Sn@C anode reported to date (Detailed comparison See Table 6.4 and Figure 6.15). The Sn@C pitaya anode also displayed a stable cycling performance, which could be maintained at 400 $mAhg^{-1}$ after 500 cycles, about 72.8% of initial capacity at 1C. Contrarily, for Sn@C chestnut anode, the capacity dropped rapidly after only 200 cycles to less than 200 $mAhg^{-1}$. Therefore, the electrochemical performance of Sn@C in LIBs could be effectively controlled by CSP.

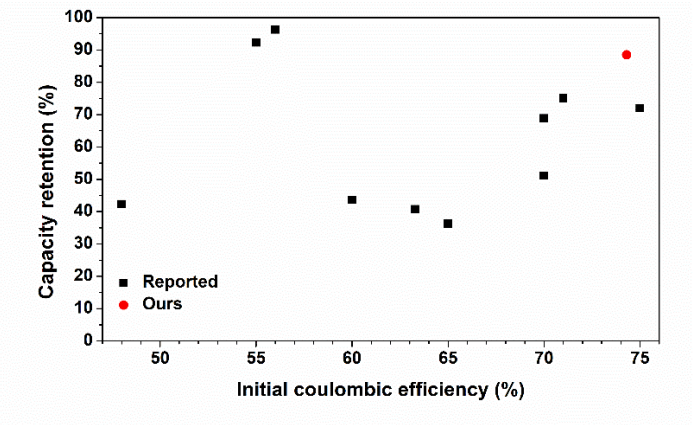

Figure 6.15 Comparison of electrochemical performance of our Sn@C anodes with references in Table 6.4.

Table 6.4. Comparison of electrochemical performance of our Sn@C anodes with references

Sn/C composite	Particle size	Initial Coulombic efficiency	Highest capacitances obtained (mAh g^{-1})	Properties degradation	Ref.
Sn/C composite	~300 nm	74.3%	952mAh/g @0.2Ag^{-1}	88.5% capacity retention over 1500 cycles	This work
Sn/C composite	Micro size	~56%	786.4 mAhg^{-1}@0.06Ag^{-1} (0.01~2.5V)	~96.3% capacity retention over 1000 cycles	(Huang et al. 2015)
Sn quantum dots in N-doped CNFs	~210 nm	71%	1176 mAh/g @0.1Ag^{-1} (0.01~3V)	75% capacity retention over 200 cycles	(Im et al. 2013)
TiO_2-Sn/C core-shell	12 µm ± 0.5 µm	~60%	769 mAh/g @0.0335Ag^{-1} (0.01~3V)	459 mAh/g after 16 cycles at 335 mAg^{-1}	(Liao and Manthiram 2014)
nano-Sn/C composite	>100 nm	69%	1029 mAh/g@0.2Ag^{-1} (0.02~3V)	~100% capacity retention over 130 cycles	(Xu et al. 2013b)
Sn in Carbon Spheres	~400 nm	<70%	> 800 mAh/g @0.2Ag^{-1} (0.005~3V)	> 550 mAh/g over 100 cycles	(Zhang et al. 2008)
porous Sn@C nanocomposite	100 ~ 300 nm	67.3%	865.3 mAh/g@0.2Ag^{-1} (0.01~3V)	N.A	(Zhang et al. 2015)

Sn in N-doped Carbon	~50 µm	48%	~1490mAh/g@~0.2 Ag^{-1} (0.01~3V)	630 mAh/g after 400 cycles	(Youn et al. 2016)
yolk-shell nanostructures Sn/C	~400 nm (average diameter)	~70%	979mAh/g@0.05Ag^{-1}(0.01~2V)	> 500 mAh/g after 10 cycles	(Ni et al. 2014)
Nano-Sn in expanded graphite	~210 nm(Sn)	~55%	650 mAh/g @ 0.13Ag^{-1} (0.01~2V)	~ 600 mAh/g after 350 cycles	(Yan et al. 2016)
Sn-carbon nanotube nanocapsules	40 nm in diameter and 200-300 nm in length	~75%	850 mAh/g @0.06Ag^{-1} (0.01~2.5V)	612 mAh/g after 10 cycles	(Liu et al. 2014)
Sn/graphene	200 nm (a side length)	~65%	1795 mAh/g @ 0.1Ag^{-1} (0.005~3V)	650 mAh/g after 100 cycles	(Li et al. 2014)
Sn@C nanocomposites	8 nm and 40nm (Sn)	63.3%	1007.1 mAh/g @ 0.2Ag^{-1}	410 mAh/g after 1000 cycles	(Zhang et al. 2014b)
Nano Sn in N-doped Carbon	~5 nm (Sn)	~75%	1014 mAh/g @ 0.2Ag^{-1}	71% capacity retention over 200 cycles	(Zhu et al. 2014b)

As reported, the volume expansion of Sn could be ~260 % (Huang et al. 2015; Kaspar et al. 2014; Ke et al. 2013; Ni et al. 2014), thus the superior cycling and rate performance of Sn@C pomegranate anodes are attributed to the excellent structural stability, originated from the well distributed Sn beads within relative small Sn@C particles. To effectively

accommodate for the volume change in Sn@C, both diameters of Sn@C particle and interior Sn bead should be small, while the Sn@C particle size is more crucial in cycling stability (Figure 6.14b-d). As demonstrated in Figure 6.6, the pomegranate-structured particles have smaller Sn@C particle size but larger interior Sn size (301 nm and 24 nm, respectively) than pitaya-structured particles (340 nm and 16 nm, respectively). The smaller pomegranate-structured particle in Sn@C pomegranate anode ensures better cycling stability than Sn@C pitaya anode. Although chestnut-structured particles have the smallest Sn@C particle size (139 nm), the significantly large Sn core (close to 139 nm) can seriously damage the Sn@C composite particles (Figure 6.14d), resulting in quick capacity decay. Therefore, the specifically designed structure of Sn@C pomegranate particles has sufficient and well-defined internal space to tolerate the expansion of Sn beads in the elastic carbon frames without deteriorating the structural integrity of the anode (Figure 6.14c). To test this hypothesis, the particle structures of Sn@C anodes were characterized by TEM (Figure 6.14) and SEM (Figure 6.16) after 100 cycles in rate performance tests. The Sn@C pitaya and pomegranate anodes maintained stable structures with spherical shape of Sn@C particles, which are similar to those before the electrochemical test (Figure 6.14e-f and g-h, respectively). However, cracking or fracture in the Sn@C chestnut anode was observed as shown in Figure 6.14i-k.

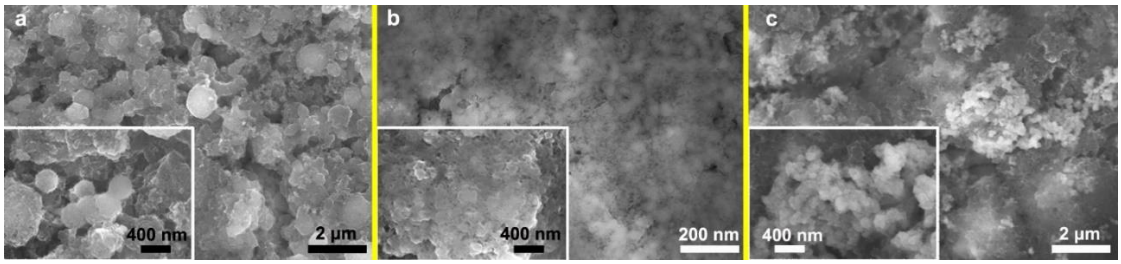

Figure 6.16. Post-cycling characterization of Sn@C pitaya (a), pomegranate (b), and chestnut (c) anodes.

To further validate our theory, the Sn@C intermediate anode was tested for electrochemical performance. Since Sn@C intermediate particles are comprised of structures between pomegranate-structured and chestnut-structured particles, Sn@C intermediate anode in theory should have a structural and cycling stability between Sn@C pomegranate and chestnut anodes, which was verified experimentally in the electrochemical performance testing (Figure 6.14a) and the structure characterization of the anode after the electrochemical test (Figure 6.17).

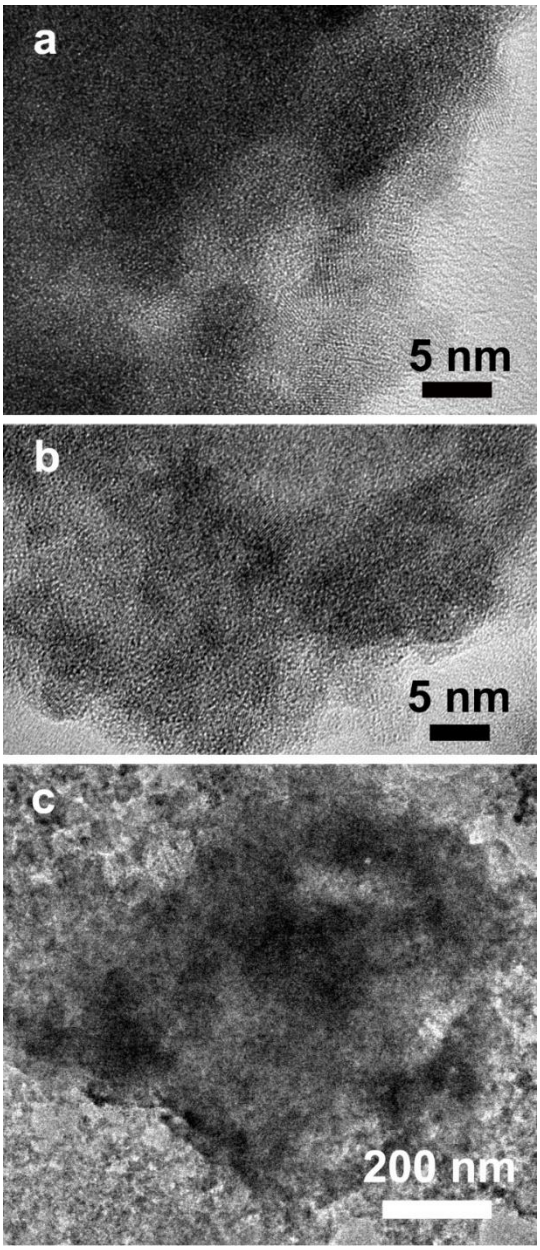

Figure 6.17. Post-cycling characterization of Sn@C intermediate anode.

Although the volume expansion of Sn-based anodes in SIBs is 420% (Zhu et al. 2013), the Sn@C pomegranate anodes for SIBs present excellent electrochemical performance, as shown in Figure 5.14l. Sn@C pomegranate anode in SIBs was galvanostatically discharged

and charged at different current densities from 0.05C to 5C. The cell could deliver 487.3, 378.0, 293, 237.6, 197.2, 120.4 $mAhg^{-1}$ at 0.1C, 0.2C, 0.5C, 1C, 2C and 5C, respectively. In particular, the capacity could be recovered to its original value when the rates were set back to 0.1 C, 0.2C and even 1C after 100 cycles, respectively. This clearly substantiates that the sodiation reaction in Sn@C pomegranate anode is highly reversible.

6.5 Summary of this chapter

We have successfully developed a general strategy to synthesize multicomponent particles by CSP. This process is fundamentally different from the conventional aerosol processes where only highly soluble salts, pure organic solvents, and extreme reducing conditions are favored. By applying CSP, a wider range of functional materials can be produced at low cost, with safer process conditions, and facile operating procedures. A specific example of the application of CSP was presented to generate Sn@C particles for LIBs and SIBs anodes, which is difficult to obtain by conventional methods. Although this work only utilized Sn as the example, CSP is applicable to other elements. Furthermore, the model we developed provides a better understanding of the particle formation mechanism in the aerosol processes. Meanwhile, this model can also be utilized to prescreen the colloids that can be processed by CSP and design the process variables to obtain desired products. With the guidance of theoretical analysis of the colloid-reduction kinetics and aerosol dynamics, Sn@C particles with controllable interior structures (pitaya, pomegranate and chestnut-structured) were produced through complete reduction of the SnO_2 colloids by *in-situ* solid-state reaction. The Sn@C pomegranate anodes displayed excellent battery performance with 88.5% (1500 cycles; 2C) capacity retention for LIBs

and exhibited superior rate capability for SIBs, which are among the best performance for Sn-based anodes reported to date.

Chapter 7: Fabrication of nanocomposite particles containing SnO_2 colloids and edge-oxidized graphene oxide sheets as photocatalysts

7.1 Abstract

Artificial photosynthesis requires the usage of catalysts to cleave the C=O bond of CO_2 and convert it into valuable hydrocarbon products. However, this technology is strongly restricted by two issues: insufficient catalytic efficiency and complicated processes of catalyst fabrication. Herein, a novel photocatalyst engineering process, spray drying, has been developed to address these two issues. Through one-step spray drying with a residence time of 1.5 s, nanocomposites containing tin oxide (SnO_2) nanoparticles and edge-oxidized graphene oxide (eo-GO) sheets were fabricated without post-treatment. After 4 h irradiation of simulated sunlight, the nanocomposites exhibited 28-fold and 5-fold enhancements in photocatalytic efficiency in CO_2 reduction compared to SnO_2 and commercialized TiO_2 (P25), respectively. Our approach is scalable with short residence time and simple equipment required, which can promote the practical application of artificial photosynthesis by realizing mass-production of efficient photocatalysts.

7.2 Introduction

Advancement of society has greatly relied on the consumption of fossil fuels, which results in the accumulation of greenhouse gases such as carbon dioxide (CO_2) and the depletion of non-renewable fossil resources. A promising strategy to address these concerns simultaneously is artificial photosynthesis, in which CO_2 is converted into hydrocarbons with the assistance of biomimetic catalysts. In consequence of the large dissociation energy of C=O bond (750 kJ/mol) (Chang et al. 2016), advanced catalysts are

required to enhance the efficiency in artificial photosynthesis. Unfortunately, photocatalyst engineering is greatly restricted by the complexity in catalyst development and fabrication. It is even more challenging to develop high-performance photocatalysts that can be produced via a simple, scalable, and commercially applicable approach.

Titania (TiO_2) has been intensively studied as a catalyst for artificial photosynthesis since the pioneering work of Inoue *et al*. (Inoue et al. 1979). However, it exhibits low catalytic efficiency that can be ascribed to three factors: 1) the low CO_2 adsorption on the surface, 2) rapid recombination of the photo-generated electrons and holes, and 3) catalyst deactivation due to adsorption of less reactive intermediates (Chang et al. 2016; Habisreutinger et al. 2013). Various strategies have been attempted to resolves these issues including modification of TiO_2 and development of alternative photocatalysts. For example, TiO_2 with particle sizes in the nanometer regime shows enhanced CO_2 adsorption due to increased surface area (Fang et al. 2014). The inclusion of noble metals as the electron sink in TiO_2 retards the recombination between electrons and holes (Jiao et al. 2017). Alternative photocatalysts with narrow band gap and better separation of the charges, such as CeO_2 (Li et al. 2016b; Ye et al. 2017), C_3N_4 (Li et al. 2015a; Li et al. 2016b), $BiVO_4$ (Mao et al. 2012; Murcia-López et al. 2017), and graphene oxide (GO) (Hsu et al. 2013; Lin et al. 2017; Shown et al. 2014) can outperform TiO_2 in artificial photosynthesis applications.

Among the alternative photocatalysts that have been developed to date, GO is an efficient hole-collector with semiconductor-like band gap, large specific surface area, and negatively charged O atoms to adsorb and activate CO_2 in artificial photosynthesis (Hsu et al. 2013; Lin et al. 2017; Shown et al. 2014). However, the wide band gap and the

interruptions in π bond in the aromatic rings can deteriorate light absorption and electron transfer capability of GO (Hsu et al. 2013; Zerjav et al. 2017). On the other hand, an electron trapper together with GO is favored to further retard the recombination of electrons and holes. SnO_2 is a better electron acceptor than TiO_2, because of its more positive conduction band (CB) edge. Moreover, SnO_2 is an effective photocatalyst to degrade dye molecules (Liu et al. 2007b). Nevertheless, the wide bandgap of SnO_2 (3.8 eV) (Inoue et al. 1979) is an obstacle to promote its application in artificial photosynthesis. The combination of GO and SiO_2 to develop a composite may result in a more efficient catalyst that can outperform each of the individual components in CO_2 reduction in artificial photosynthesis.

The synthesis of photocatalysts often involves multiple synthesis steps or sophisticate equipment (see Section 2.3 of Chapter 2). This has constrained the scale-up of the photocatalyst synthesis for widespread applications. For example, hydrothermal process has been often employed for preparation of a variety of photocatalysts, but unfortunately, it requires long processing time and sophisticated post-treatment steps, and it raises safety concerns because of the autogenous pressure in the reactor (Hsieh et al. 2014; Ide et al. 2016; Sun et al. 2015). Approaches such as molecular beam epitaxy (MBE), sol-gel, and ion-exchange, etc. have also been developed (AlOtaibi et al. 2015; Li et al. 2015a; Tahir and Amin 2015). Nevertheless, MBE requires significant equipment investment, while sol-gel or ion-exchange approaches have sophisticated operating procedures and long processing times. A simple, short processing time, low cost and scalable approach is desired to promote the practical application of artificial photosynthesis.

Herein, a novel photocatalyst engineering process has been developed to produce efficient SnO_2-GO nanocomposites as catalysts for artificial photosynthesis. Spray drying, a continuous and scalable process, is applied to fabricate nanocomposites that comprise of edge-oxidized graphene oxide (eo-GO) sheets and nano-sized SnO_2 colloids, as shown in Figure 7.1a. The obtained powders are termed TinGOx, where *x* equals to mass ratio of SnO_2 to eo-GO in the precursor mixture. The eo-GO sheets have large intact sp^2 carbon network to deliver large surface area, excellent electron transfer ability, sufficient active sites of negatively charged O atoms, and narrow band gap. The utilization of nano-sized SnO_2 can efficiently trap the photogenerated electron and create a defect state to narrow its wide bandgap. State-of-art techniques have been utilized to reveal the configuration of nanocomposites, including electron energy loss spectroscopy (EELS) in low-loss and core-level regions. A detailed investigation of the photoreduction of CO_2 has been conducted to understand the photocatalytic activity, optimal SnO_2/eo-GO mass ratio, and reaction mechanism. The best TinGOx photocatalyst exhibits superior performance in photoreducing CO_2 into CH_4 with high yield and selectivity compared to bare eo-GO, SnO_2, and the commercial TiO_2 (P25).

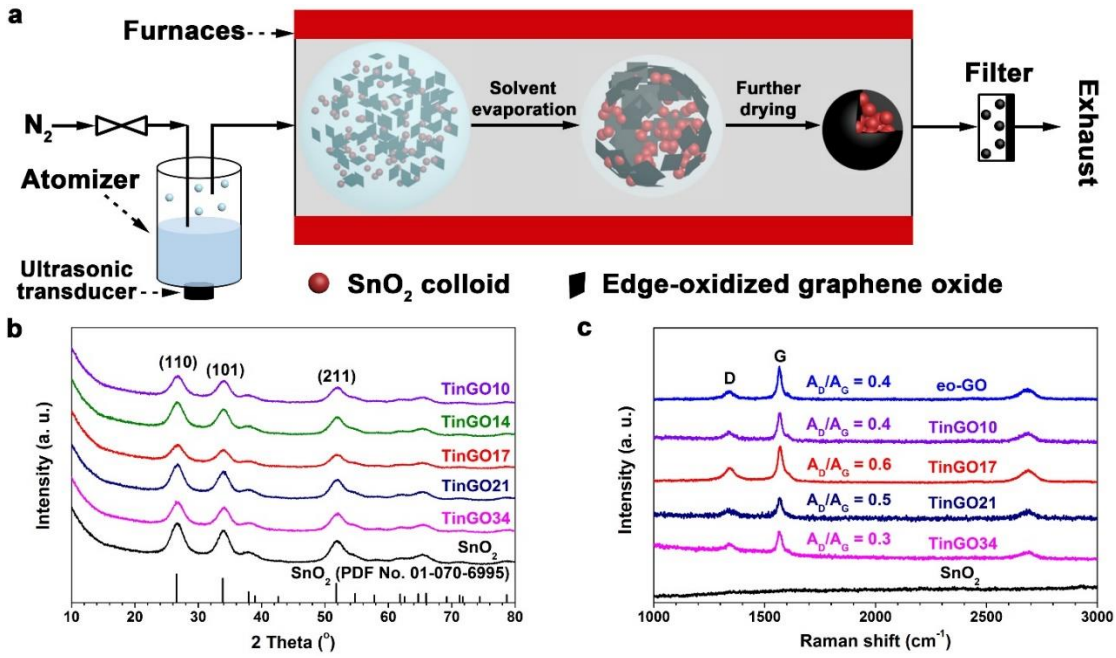

Figure 7.1. Particles synthesized by spray drying. (a) Schematic illustration of spray drying process. (b) XRD patterns of TinGOx powders obtained through spray drying. (c) Raman spectra of TinGOx powders.

7.3 Experimental

7.3.1 Materials

The SnO_2 colloid with particle diameters of 10-15 nm was received from NYACOL (SN15). The counter ion is K^+. The specific gravity (SG) is 1.15. The 4-10% edge-oxidized eo-GO powder was purchased from Sigma-Aldrich (product number: 796034, molecular weight = ~4200 g/mol, bulk density = ~1.8 g/cm^3). The molecular structure of eo-GO is schematically shown in Figure 7.2. It is noted that the eo-GO sheets are dispersible in water or other polar solvents. Ethanol (ethyl alcohol, 99.98 %) was bought from Pharmco-Aaper.

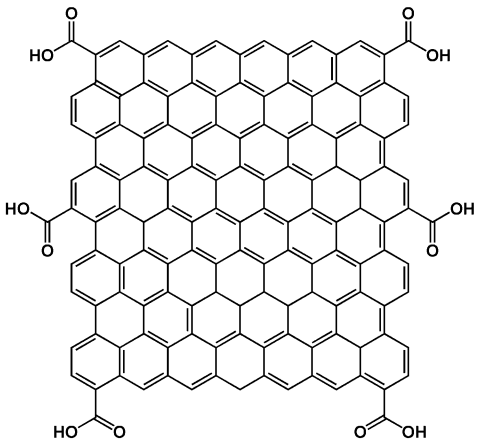

Figure 7.2. Molecular structure of 4-10% edge-oxidized graphene oxide sheet received from Sigma-Aldrich.

7.3.2 Photocatalyst fabrication by spray drying

A 150-mL-aqueous precursor containing SnO_2 colloids, eo-GO sheets, and ethanol were utilized to fabricate TinGOx phototcatalysts, where *x* is the mass ratio of SnO_2 to eo-GO in the precursor mixture. The concentration of SnO_2 colloids can be calculated as:

$$n_{SnO_2} = \frac{v \cdot SG \cdot w \cdot \rho_{H_2O}}{Mw} \cdot 10^{-3} \ [mol] \quad (7.1)$$

$$C_{SnO_2} = \frac{n_{SnO_2}}{V} \cdot 1000 \ [mol/L] \quad (7.2)$$

$$N_{colloid,SnO_2} = \frac{v \cdot SG \cdot w \cdot \rho_{H_2O}}{\frac{1}{6}\pi \cdot d_0^3 \cdot \rho_{SnO_2}} \cdot 10^{21} \quad (7.3)$$

$$\frac{\delta N_{colloid,SnO_2}}{\delta V} = \frac{N_{colloid,SnO_2}}{V} \cdot 1000 \ [\#/L] \quad (7.4)$$

where *v* [ml] is the volume of extracted SnO_2 colloid raw solution, specific gravity (*SG*) = 1.15 is the specific gravity of SnO_2 colloid solution at 25 ^oC, *w* (=0.15) is the mass fraction of SnO_2 in its colloid solution, *Mw* [g/mol] is the molecular weight of SnO_2, *V* =150 ml is

the volume of precursor, d_0 [nm] is particle size or particle diameter (=15 nm), ρ_{H2O} [kg/m^3] is the density of bulk H_2O (1.0×10^3), and ρ_{SnO2} [kg/m^3] is the density of bulk SnO_2 (6.85×10^3), respectively.

Based on Equations (7.1-7.4), the concentration of SnO_2 colloids and eo-GO in each experimental condition are summarized in Table 7.1.

Table 7.1. Composition of precursor solutions for fabrication of SnO_2/eo-GO photocatalysts.

	Product particle					
	TinGO10	TinGO14	TinGO17	TinGO21	TinGO34	SnO_2
[SnO_2] (kg/L)	5.2×10^{-4}	6.9×10^{-4}	8.6×10^{-4}	1.0×10^{-3}	1.7×10^{-3}	1.7×10^{-3}
[SnO_2] (mol/L)	0.022	0.030	0.037	0.044	0.072	0.072
SnO_2 colloid quantity (#)	4.3×10^{16}	5.7×10^{16}	7.1×10^{16}	8.6×10^{16}	1.4×10^{17}	1.4×10^{17}
[SnO_2 colloids] (#/L)	2.8×10^{17}	3.7×10^{17}	4.6×10^{17}	5.5×10^{17}	8.9×10^{17}	8.9×10^{17}
eo-GO (kg/L)	3.3×10^{-4}	3.2×10^{-4}	3.2×10^{-4}	3.2×10^{-4}	3.1×10^{-4}	0
SnO_2/GO (mass ratio)	10	14	17	21	34	∞
[Ethanol] (mol/L)	6.7	6.7	6.6	6.6	6.4	0

During the spray drying, the precursors were atomized by a 1.7 MHz transducer into droplets with a volume mean diameter of 5 μm (Zhong et al. 2012). The droplets were transported by the N_2 gas (99.5%, Airgas) into two furnaces connected in series, as shown in Figure 1a of main text. The furnaces were set at 500 ^{o}C and the product particles were collected on a PTFE filter. The residence time was controlled at ~1.5 s, which was calculated by using a plug-flow model, consisting 32 sub-units of identical length. Detailed calculation procedures are reported in Chapter 3. Ethanol was used to ease the oxidation of eo-GO sheets during the spray drying.

7.3.3 Materials characterization

Scanning electron microscopy (SEM, HITACHI SU-70) and transmission electron microscopy (TEM, JEOL 2100F field emission gun) with in Gatan image filter (GIF, Tridiem 863) were utilized to understand the particle morphology, structure, and chemical distributions. X-ray diffractometer (XRD, Bruker D8 advance) was used to determine the crystallographic information of the TinGOx powders. X-ray photoelectron spectroscopy (XPS, Kratos Axis 165) was performed to understand the valence band and chemical status of the elements. Raman signals were collected using a Horiba Jobin Yvon LabRAM Raman microscope with a 532 nm laser. N_2 adsorption-desorption isotherms of the samples were measured using an Autosorb-iQ analyzer (Quantachrome Instruments) at -196 ^{o}C. The samples were outgassed at 250 ^{o}C for 8 h and 1 mm Hg prior to measurements. Brunauer-Emmett-Teller (BET) method was used to determine the specific surface area of the sample. Barret-Hoyner-Halenda (BJH) method was utilized to analyze the pore size distribution in the particles. The UV-Vis-NIR spectrophotometer (Lambda 1050, PerkinElmer) equipped with an integrating sphere (Labsphere Model No. 150MM RSA ASSY) and an InGaAs detector was used for the measurement of the diffuse reflectance spectra (DRS) on the fabricated photocatalyst samples.

7.3.4 Photoreduction of CO_2

The photoreduction of CO_2 was performed in a cylindrical batch reactor under ambient condition. The batch reactor was custom-built with a stainless steel body and two quartz windows of 1.4 cm in diameter and 0.5 cm thick. The inner cavity of the batch reactor is 3.0 cm in diameter and 2.0 cm in depth. A xenon (Xe) arc lamp (450 W) was placed on the top of the reactor. The batch reactor is connected by two gas lines for inlet and outlet gases

of the reactor on the perimeter wall of the cylindrical reactor body. The outlet gas goes through an automated gas valve and a gas-chromatograph (Agilent Technologies, 6890N) in series for gaseous composition determination. The gas-chromatograph is equipped with a 3.0 m×0.0254 m packed column (Agilent HAYESEP DB) and a 30 m×0.25 mm capillary column (Supelco SP-2330), which are connected to a thermal conductivity detector (TCD), a flame ionization detector (FID), respectively.

Prior to each reaction, 20 mg catalyst and 0.05 mL water were manually loaded into the batch reactor. The reactor was then purged with a mixture of CO_2 (99.99%, Airgas, Inc.) and Argon (99.99%, Airgas, Inc.) at 42 mL/min and 9 mL/min, respectively, for 50 min. Then the batch reactor was enclosed by turning off gas valves next to the reactor body and the Xe lamp was turned on. After 4 h irradiation, the Xe lamp was turned off. CO_2 gas was introduced at 3 mL/min to the rector to flush the product gases into the gas-chromatograph for composition analysis.

7.4 Results and discussions

The nanocomposites were fabricated by a one-step and one-pot process, *i.e.*, spray drying. As illustrated in Figure 7.1a, aqueous precursor containing SnO_2 colloids (particle diameter: 10-15 nm) and eo-GO sheets was firstly ultrasonically atomized into droplets. Then the droplets were transported by the N_2 gas into the furnaces, in which solvent evaporation and structural progression lead to the formation of product particles. At the end of this continuous process, nanocomposite particles were collected on a polytetrafluoroethylene (PTFE) filter and can be immediately used as photocatalysts without any post-production treatments. As SnO_2 colloids are uniformly and stably

dispersed in the aqueous precursor and eo-GO is soluble in polarized solvents, the product particles have a uniform particle-to-particle composition and structure, as discussed in Chapter 3. By tuning the mass ratio of SnO_2 to eo-GO in the precursor (Table 7.1), TinGOx particles have been prepared over a range of 10 to 34. Compared with reported photocatalyst fabrication processes, including hydrothermal, MBE, sol-gel, and ion-exchange methods, our process is scalable and continuous with short processing time, facile equipment requirement, and simple operating procedures (detailed comparison is presented in Section 2.3 of Chapter 2). All these merits can promote future photocatalyst manufacturing at an industrial-scale.

In the TinGOx powders, SnO_2 is a main component, verified by XRD characterization (Figure 7.1b). The broad SnO_2 peaks indicate small particle sizes in the nanocomposites based on the Scherrer equation. Additionally, the short residence time, low processing temperature, and existence of eo-GO all inhibit the significant coagulation between SnO_2 colloids during spray drying. The existence of eo-GO in the nanocomposites is validated by the Raman spectroscopic study with three distinct peaks from the eo-GO in the spectrum (Figure 7.1c). The D band at ~1345 cm^{-1} represents the disorder in carbon materials while G band at ~1585 cm^{-1} is indicative of sp^2 graphitic carbon lattice. Another peak at ~2700 cm^{-1} is the second disorder-induced Raman signature, or 2D band (Eigler et al. 2012). The ratio of D band to G band peak areas (D/G ratio) is an indicator of the defect density (Eigler et al. 2012). Since the D/G ratios in Figure 7.1c (including pure eo-GO) are all less than 1, the oxidized (or disorder) extent of eo-GO is less than GO (Eigler et al. 2012). The eo-GO is 4-10% edge oxidized, as shown in Figure 7.2, compared with GO (Figure 7.3c). The Raman signals from TinGO17 powder exhibit the highest D/G ratio among all the TinGOx

nanocomposite particles. Together with a red shift of D band and a blue shift of G band in Raman spectrum of TinGO17 (Figure 7.1c and Table 7.2), the carbon materials in TinGO17 particles have the highest defect density. This could be attributed to the modification of planer structured eo-GO by spherical structured SnO_2 colloids. Similar phenomena have also been observed by Shown *et al* in the system of Cu nanoparticles decorated GO sheets (Shown et al. 2014). The highest defect density of eo-GO in TinGO17 can promote the collection of photogenerated holes (Yang et al. 2017), increasing the efficiency in CO_2 reduction.

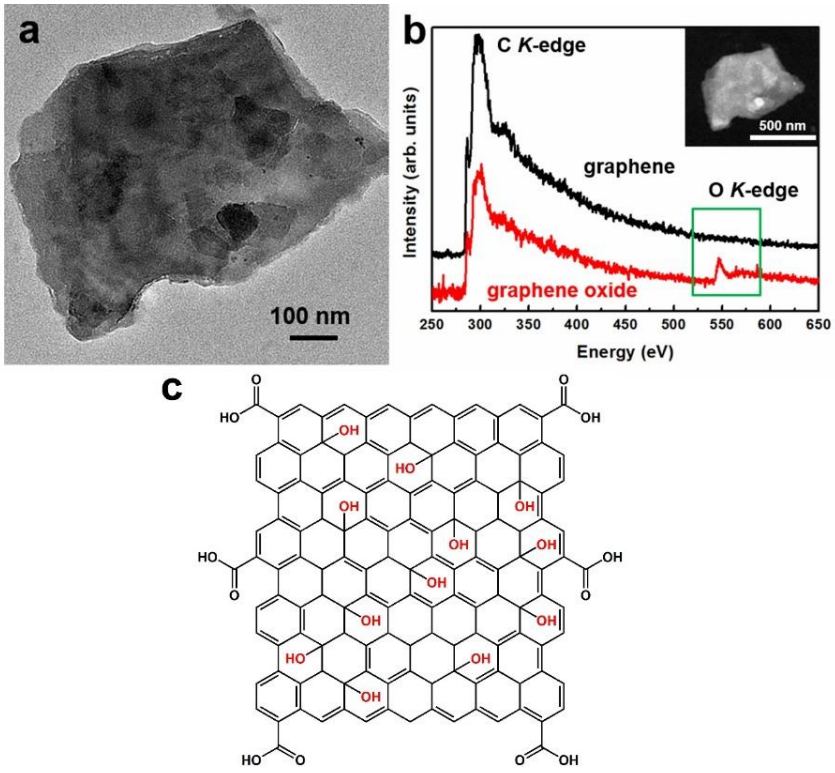

Figure 7.3. Image of GO (a) and EELS core loss spectra of graphene (black) and GO (red) (b). (c) is the molecular structure of the GO sheet. The red groups in (c) highlight the difference from eo-GO sheet, as shown in Figure 7.2.

Table 7.2. D and G band positions and D/G ratio of Raman spectra

	D band (cm^{-1})	G band (cm^{-1})	D/G
eo-GO	1337.27	1564.35	0.4
TinGO10	1336.33	1564.63	0.4
TinGO17	1341.85	1569.46	0.6
TinGO21	1337.03	1567.39	0.5
TinGO34	1339.09	1565.32	0.3

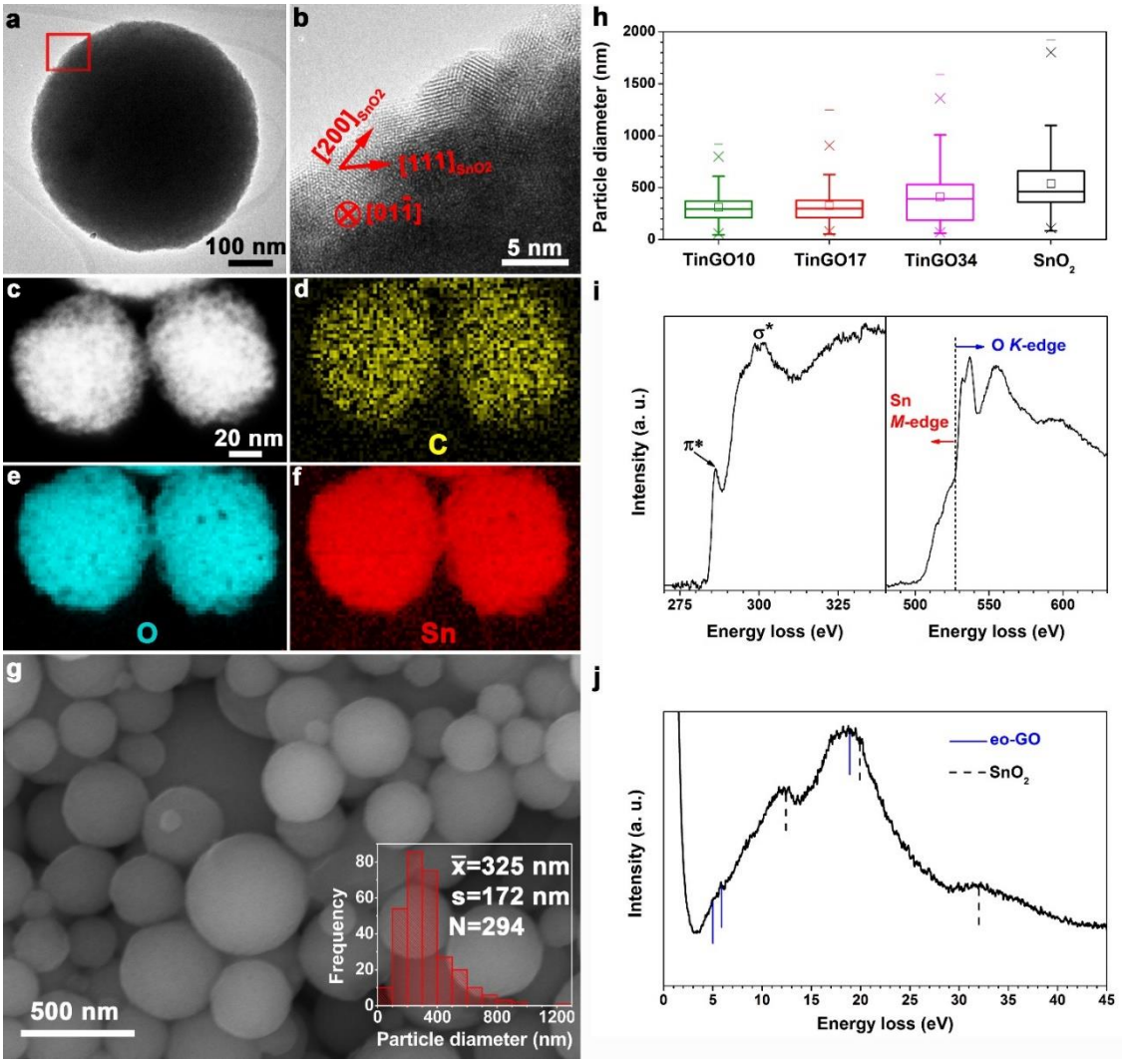

Figure 7.4. Typical morphologies and structures of SnO_2/eo-GO powders. (a-b) TEM image of a TinGO17 particle (a) with corresponding HRTEM image (b). (c-f) HAADF

image (c) together with C (d), O (e), and Sn (f) elemental mappings. (g) SEM image of the TinGO17 particles with a statistical summary of the particle size distribution. The number mean diameter, standard deviation, and sample size are presented. (h) Box plots of size distributions of TinGOx powders. (i) EELS spectra of C *K*-edge (left) and Sn $M_{4,5}$-edge (right) in core-loss level region. (j) Low-loss EELS spectrum of TinGO17 particles.

A representative TEM image of TinGOx (e.g. TinGO17 sample) is shown in Figure 7.4a with particle-like morphology. An enlarged high resolution TEM (HRTEM) image of the red squared area in Figure 7.4a is shown in Figure 7.4b. Distinct lattice fringes indexed to the [200] and [111] orientations of SnO_2 can be observed through the incident e-beam direction of [01-1], substantiating that SnO_2 is one constituent component. SnO_2 and eo-GO distribute uniformly over the product particles, validated by the EELS elemental mapping of C ***K***-edge, O ***K***-edge, and Sn $\boldsymbol{M}_{4,5}$-edge of TinGO17 particles (Figure 7.4d-f, respectively). During the spray drying process, eo-GO sheets in the vicinity of SnO_2 colloids preferentially adsorb on the colloid surface, because the oxygenated groups in eo-GO have high affinity to the SnO_2 colloids through the hydrogen bonding and electrostatic attraction (Song et al. 2011). The full coverage of SnO_2 colloids by eo-GO sheets has been estimated on the basis of simple calculation by considering an extreme scenario (TinGO34 particles), in which eo-GO relative amount is the lowest in the TinGOx particles.

Based on Figures 7.1,7.4, we assume the configuration of TinGOx particles are eo-GO covered on the surface of SnO_2 colloids. In one extreme condition, the SnO_2 colloids are assumed to be isolated without coagulation in the product particles to deliver the largest surface area of SnO_2 colloids.

The atomized droplets have a mean volume diameter of 5 μm (Zhong et al. 2013b). Therefore, based on the one-droplet-one particle model, the TinGO34 powders contain many SnO_2 colloids in one single particle, which is N=5.8×10^4. By assuming the thickness of eo-GO layer on SnO_2 particle surface is t (nm), the mass of eo-GO in one single TinGO34 particle ($m_{GO,req}$) is required to be:

$$m_{GO,req} = N \times \frac{4}{3}\pi\left[\left(\frac{d_0}{2}+t\right)^3 - \left(\frac{d_0}{2}\right)^3\right]\rho_{GO} \times 10^{-24}\ [kg] \quad (7.5)$$

where ρ_{GO} is the density of eo-GO, which is 1.8 g/cm^3. The mass of eo-GO in each product particle is 2.0×10^{-17} kg, which equals $m_{GO,req}$. Thus, t is 132 nm, significantly thicker than the thickness of single sheet of eo-GO. As other TinGOx particles have less SnO_2 colloids but same amount of eo-GO as TinGO34 powders, our theoretical analysis indicates the SnO_2 colloids are covered by eo-GO in the product powders.

This implies excellent affiliation could be realized between the SnO_2 and eo-GO components. SEM observation of the TinGOx powders further verifies their spherical structure, as shown in Figure 7.4g for TinGO17 and Figure 7.5 for all other TinGOx samples. The number mean diameter of TinGO17 particles is 325 nm with a standard deviation of 172 nm, statistically summarized from 294 particles, as depicted in the inset of Figure 7.4g. Same statistical analysis has also been conducted on other TinGOx powders, as shown in Figure 7.5. Apparently, the increasing SnO_2 amount in the precursor solution leads to an increased size of product particles (Figure 7.4h), which is consistent with reported results in other aerosol process (Nandiyanto and Okuyama 2011).

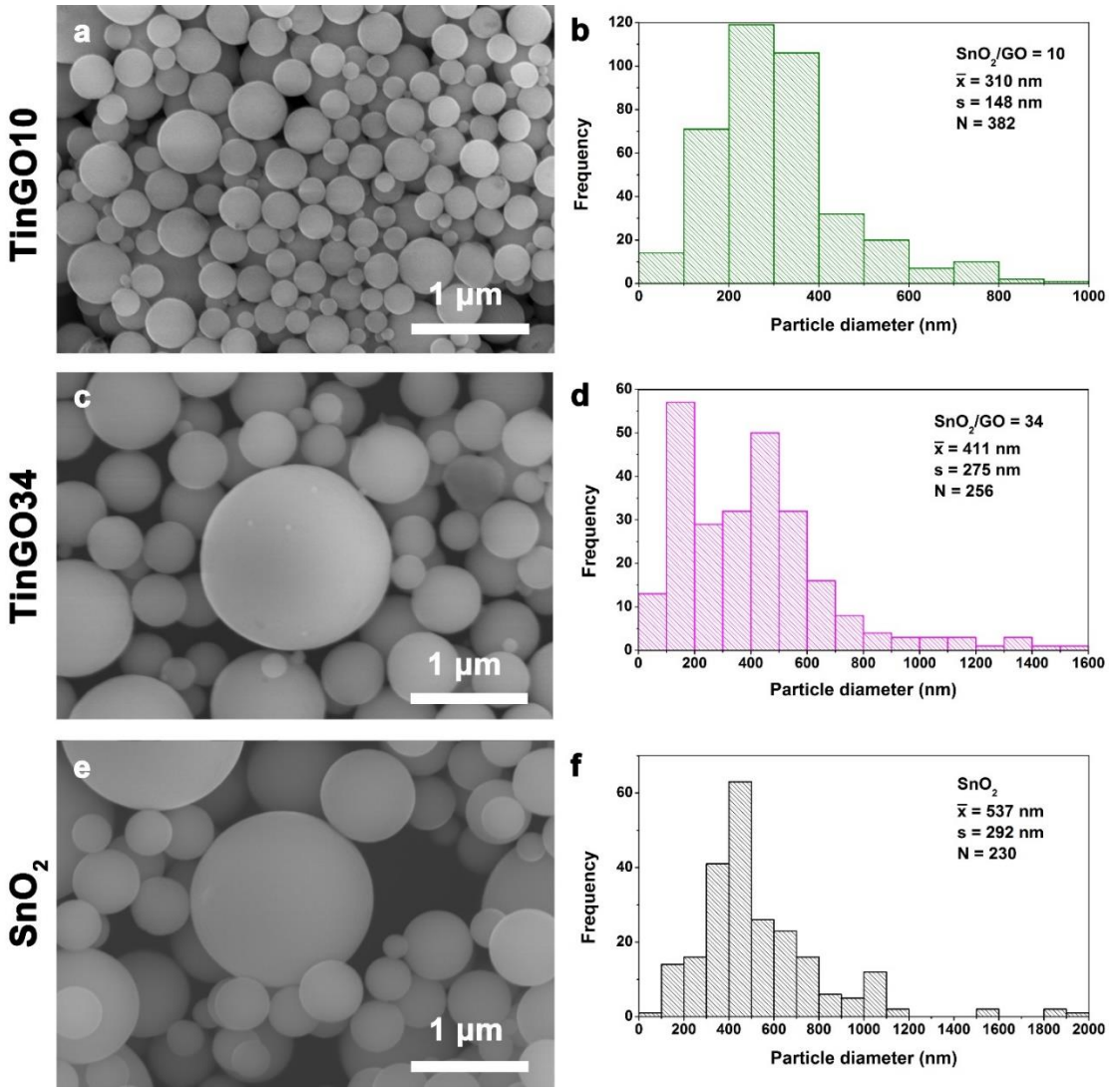

Figure 7.5. SEM images and size distributions of particles fabricated from different precursor solutions. SEM images of particles produced from precursor solutions with SnO_2/eo-GO ratios (mass) are 10 (a), 34 (c), and SnO_2 only (e). Particle size-distributions when SnO_2/eo-GO ratios (mass) are 10 (b), 34 (d), and SnO_2 only (f) in precursor solutions. Statistical summaries include number means, standard deviations, and sample sizes.

To better understand the chemical bonding, electronic excitations between valence band (VB) and CB, EELS was performed on TinGO17 particles, and results are shown in

Figure 7.4i-j. The EELS spectra of C ***K***-edge and O ***K***-edge with background subtracted are shown in Figure 7.4i. The spectral peaks at ~ 285 eV and ~ 300 eV in C ***K***-edge spectrum represent the sp^2 (π^* bond) and the sp^3 (σ^* bond) in carbon, respectively, verifying the existence of eo-GO (Mkhoyan et al. 2009). The shoulder spectral features (~515 eV and 524 eV) and spectral peak (~532 eV) correspond to Sn $\boldsymbol{M}_{4,5}$-edge and O ***K***-edge of SnO_2, respectively (Huang et al. 2010). The spectral peak at ~538 eV is O ***K***-edge ascribed to both eo-GO and SnO_2 (Huang et al. 2010; Mkhoyan et al. 2009). For comparison, the core-level EELS spectra of graphite, graphene, and GO are depicted in Figures 7.3,7.6. Only in the C ***K***-edge spectrum of graphite, there are three spectral peaks between 300 to 310 eV (Figure 7.6). In addition, the spectral peak at ~538 eV can be found in the O ***K***-edge spectra of eo-GO and GO (Figure 7.3i,7.4) instead of graphene (Figures 7.3,7.6). In the low-loss EELS spectrum (Figure 7.4j), the spectral peaks at 13 eV, 20 eV and 32 eV are the surface plasmon, volume plasmon, and Sn $\boldsymbol{M}_{4,5}$-edge of SnO_2 (Huang et al. 2010). For the eo-GO, the $\pi+\sigma$ plasmon peak occurs at ~19 eV, similar to the low-loss spectrum of GO (Johari and Shenoy 2011; Mkhoyan et al. 2009). Weak peaks at ~5 eV and 6 eV are observable possible because the scattering vector **q** is parallel to the basal plane of eo-GO (**q**||**a**) (Johari and Shenoy 2011). In addition, low-loss EELS observation indicates the absorption edge of TinGO17 is ~3.7 eV, substantiating the semiconductor-like property of eo-GO.

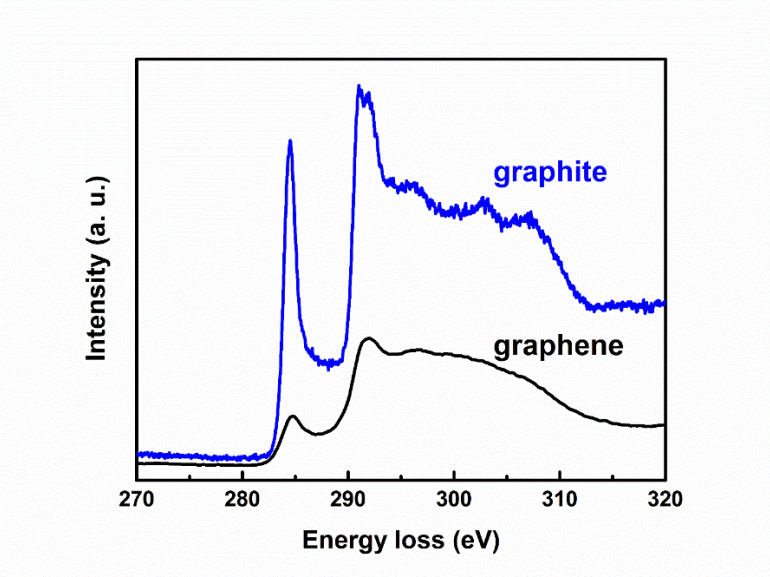

Figure 7.6. EELS core loss spectra of graphite (blue) and monolayer graphene (black).

The wide-range XPS measurements were performed to further understand the electronic structures of SnO_2, TinGO17, and eo-GO. As shown in Figure 7.7a-b, C and Sn are the main components of the TinGO17 powders, which are stemmed from eo-GO and SnO_2, respectively. The C 1s spectrum of TinGO17 displays three features of eo-GO at 284.4, 286.0, 288.4 eV attributed to the sp^2 C (C-C/C=C) in the aromatic rings, sp^3 C, and O-C=O, respectively. For reference, the XPS C 1s spectrum of eo-GO is also presented, as shown in the bottom of Figure 7.7a. It can be deconvoluted into five peaks at 284.4, 286.1, 287.3, 288.5, and 290.5 eV, corresponding to the sp^2 C, C-O, C=O, O-C=O, and π-π plasmonic, respectively. This is consistent with the molecular structure of eo-GO (Figure 7.2). The pronounced sp^2 C peak in C 1s spectrum of eo-GO supports that the defect density of eo-GO sheets is low, in agreement with D/G ratio in Raman observation. However, when eo-GO sheets couple with SnO_2 colloids to form TinGO17, the small radii of SnO_2 colloids (10-15 nm) may bend the aromatic ring of eo-GO sheets, resulting in more discorded

structures, which is consistent with our Raman observation of TinGO17 and the reported phenomena in GO-nanoparticle system (Shown et al. 2014). Therefore, the intensities of O-C=O peak and sp^3 C increase significantly in C 1s spectrum of TinGO17 compared with eo-GO. The K 2p peaks are observed in both TinGO17 and SnO_2 spectra (Figures 7.7a,7.8, respectively), substantiating that K^+ is the counter-ion in the received SnO_2 colloid dispersion solution. In Figure 7.7b, two peaks are displayed in the Sn 3d XPS spectrum of TinGO17 particles at 486.2 and 494.7 eV, corresponding to the $3d_{5/2}$ and $3d_{3/2}$ levels, respectively. The area ratio of $3d_{5/2}$ peak to $3d_{3/2}$ peak (~1.5) and their peak positions all validate the existence of SnO_2 in TinGO17 particles according to our XPS characterization on SnO_2 (bottom of Figure 7.7b) and reported Sn 3d XPS spectrum of SnO_2 (Song et al. 2011). The VB maxima of SnO_2, eo-GO, and TinGO17 were also investigated by XPS and determined by extrapolating the peaks to baseline, as shown by inset plots in Figure 7.7c. SnO_2 has the band edge position of 3.2 eV. The band edge position of the eo-GO is 1.5 eV, which is significantly greater than the graphene (theoretical VB maxima=0 eV) but smaller than the reduced GO (3.05 eV) (Zerjav et al. 2017). When the SnO_2 colloids couple with the eo-GO sheets, the VB maxima of TinGO17 exhibits a binding energy of 2.7 eV.

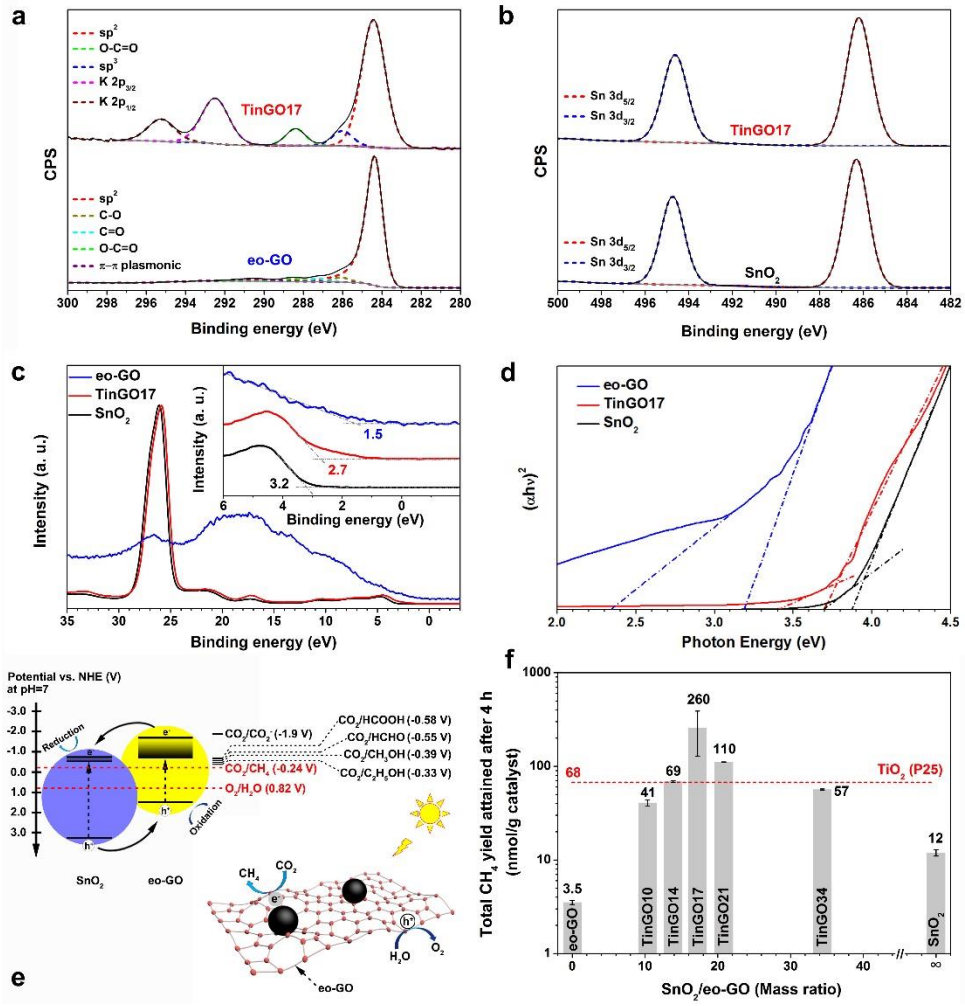

Figure 7.7. (a) C 1s and K 2p XPS spectra of TinGO17 and eo-GO. (b) Sn 3d XPS spectra of TinGO17 and SnO_2. Valence band spectra (c) and Tauc plots (d) of SnO_2, TinGO17, and eo-GO photocatalysts. (e) Schematic illustration of photocatalytic reactions and reduction potentials of possible CO_2 reduction pathways. (f) CH_4 yields over TinGOx photocatalysts under irradiation of a Xe lamp for 4 h.

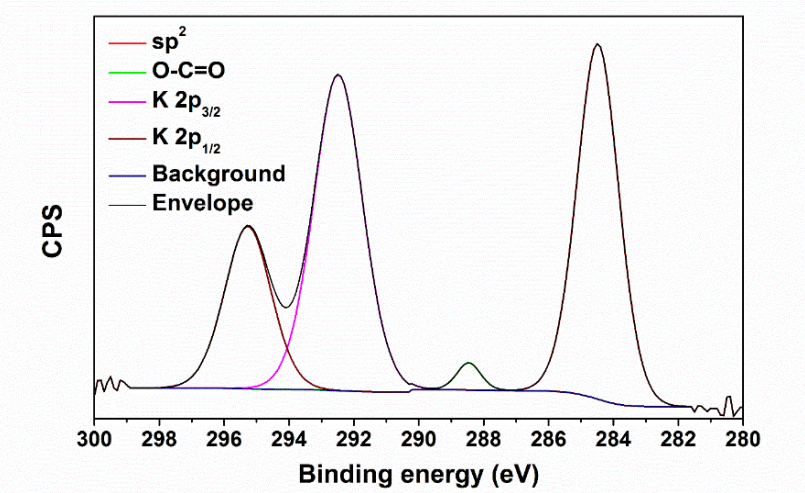

Figure 7.8. C 1s and K 2p XPS spectra of SnO_2.

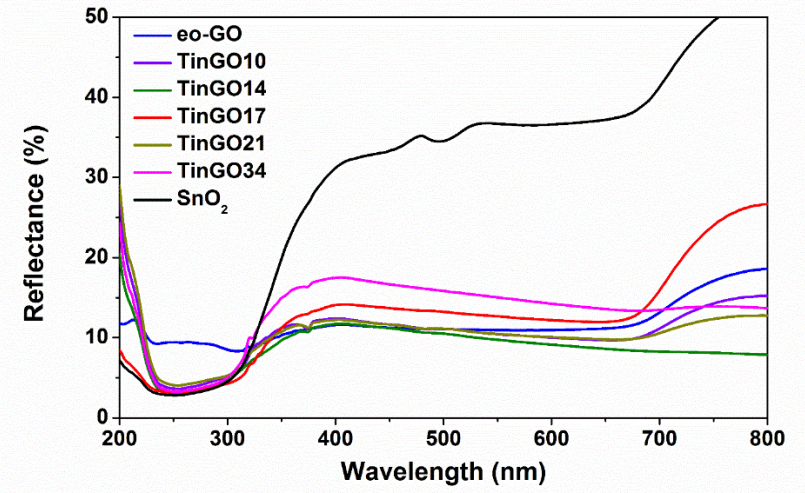

Figure 7.9. Diffuse reflectance spectra (DRS) of eo-GO, TinGO10, TinGO14, TinGO17, TinGO21, TinGO34, and SnO_2.

To better understand the band structures of the photocatalysts, the band gaps of SnO_2, TinGO17, and eo-GO are calculated using Tauc equations. The band gaps are determined in the Tauc plot of linear extrapolation of the edge to the *x*-axis (Figure 7.7d). The Tauc

plot is obtained from analyzing the DRS spectrum (Figure 7.9) through Kubelka–Munk function followed by the procedures provided in these references.(Ehsan and He 2015; Kumar et al. 2016)

$$(\alpha h\nu)^2 = [(\frac{1-R}{2R})h\nu]^2 \quad (7.6)$$

$$h\nu = h\frac{c}{\lambda} \quad (7.7)$$

where, R is the relative reflectance obtained from DRS (Figure 7.9), h is the Planck constant, which is 6.63×10^{-34} m^2·kg/s, c is the speed of light ($=3\times10^8$ m/s), and λ is the corresponding wavelength to detect R in DRS.

SnO_2 displays an E_g of 3.69 – 3.87 eV, which is similar to the results reported by Inoue *et al.*(Inoue et al. 1979). The E_g of eo-GO is 2.34 – 3.19 eV, narrower than those of GO sheets (Hsu et al. 2013). The TinGO17 photocatalysts have an absorption edge of 3.40 – 3.70 eV, between those of eo-GO and SnO_2 and consistent with the low-loss EELS result. A summary of the band structures of these photocatalysts is presented in Figure 7.7e and Table 7.3. Moreover, the absorption edges of TinGOx were calculated by converting the DRS spectra (Figure 7.9) into Tauc plots, as shown in Figure 7.10. The increasing SnO_2 concentration in TinGOx increases the absorption edge. All the results obtained from EELS, DRS, and XPS validate that TinGOx particles are promising photocatalyst with suitable electronic band structure and materials construction.

Table 7.3. Band structures of eo-GO, TinGO17, and SnO_2 as photocatalysts

	Band gap energies (eV)	**VB (eV)**	**CB (eV)**
eo-GO	2.34 – 3.19	1.5	-0.84 – -1.69
TinGO17	3.40 – 3.70	2.7	-0.70 – -1.00
SnO_2	3.69 – 3.87	3.2	-0.49 – -0.67

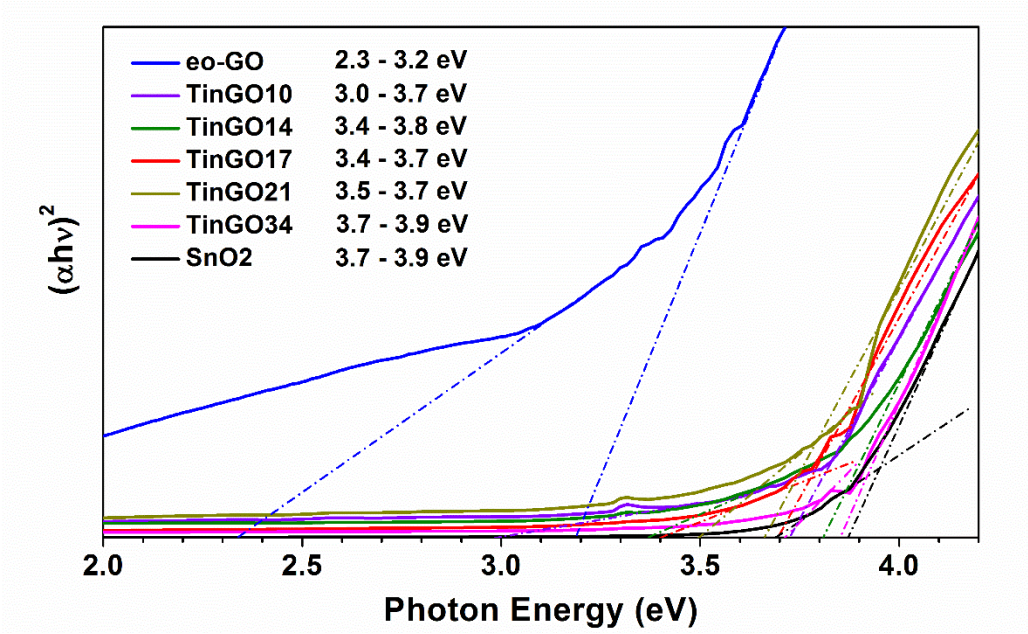

Figure 7.10 Absorption edges of TinGOx photocatalysts, eo-GO, and SnO_2 determined by Tauc plots.

Table 7.4. Detailed yields and selectivities of SnO_2/eo-GO photocatalysts

		Yield (nmol·h^{-1}·(g catalyst)$^{-1}$)					Selectivity (%)
		Methane	Formaldehyde	Methanol	Ethanol	Formic acid	
Photocatalysts	eo-GO	0.88	0.0065	0.04	0	0.22	76
	TinGO10	10	0.073	0.068	0.028	0.32	95
	TinGO14	17	0.065	0.058	0.018	0.36	97
	TinGO17	85	0.25	0.038	0.04	0.53	99
	TinGO21	28	0.045	0.058	0.010	0.33	98
	TinGO34	14	0	0	0	0	100
	SnO_2	3	0.023	0.065	0	0.55	82
	TiO_2 (P25)	17	0	0	0	0	100

The photocatalysts were irradiated by Xe lamp for 4 h.

The photocatalytic activities of the TinGOx, eo-GO sheets, and SnO_2 in reducing gaseous CO_2 were investigated under irradiation of a xenon (Xe) lamp for 4 h. The main product from this reaction was CH_4. Trace amounts of CHO, CH_3OH, C_2H_5OH, and HCOOH were also identified, as shown in Table 7.4. The yield of CH_4 is remarkably enhanced over TinGOx than either eo-GO or SnO_2 (Figure 7.7f). After 4 h reaction, the yield and selectivity of CH_4 over eo-GO photocatalyst are 3.5 nmol/(g catalyst) and 76%, respectively. The low photocatalytic conversion of CO_2 into CH_4 by eo-GO is possibly caused by the poor light absorption in the wavelength range of 222-316 nm, corresponding to photons with energies of 5.6-3.9 eV, as shown in Figure 7.9. The yield and selectivity of CH_4 are slightly increased to 57 nmol/(g catalyst) and 82%, respectively over SnO_2. However, the wide E_g deteriorates its efficiency in CO_2 photoreduction. Among the TinGOx photocatalysts, TinGO17 achieves the highest CH_4 yield (mean and maximum values of three experiments: 260 and 340 nmol/(g catalyst), respectively, Figure 7.7f), which is 5 times that of P25, 97 times that of eo-GO, and 28 times that of SnO_2 under the same experimental condition. Moreover, the TinGO14 and TinGO21 also depict higher CH_4 yields compared with P25, although less than that of TinGO17.

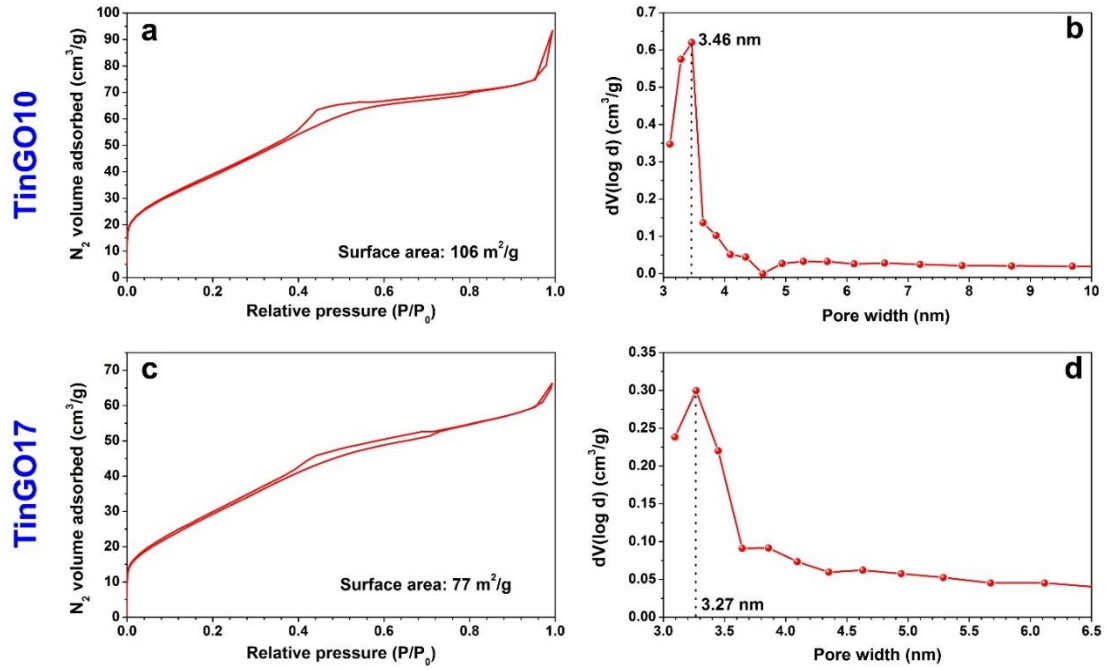

Figure 7.11. N_2 adsorption-desorption isotherm of TinGO10 (a) and TinGO17 (c) particles. The surface areas are 106 m^2/g (TinGO10) and 77 m^2/g (TinGO17) based on slit/cylindrical NLDFT model. (b) and (d) Pore size distributions derived from N_2 desorption branches of (a) and (c) according to the BJH method. The average pore sizes are 3.46 nm (TinGO10) and 3.27 nm (TinGO17), implying the average distance between the SnO_2 colloids.

By our particle engineering, the photogenerated holes and electrons could migrate independently and spatially separated, because eo-GO and SnO_2 are efficient collectors for holes and electrons, respectively. The strong affinities of SnO_2 to electrons and eo-GO to holes could further alleviate the recombination of electrons and holes. The utilization of eo-GO can also enhance the adsorption of CO_2 molecules on the photocatalysts, since GO is reported to have large surface area (Lin et al. 2017). Experimentally, both TinGO10 and TinGO17 photocatalyst have high surface areas, supported by the BET results (Figure

7.11). TinGO10 powders display larger surface area and inner pore size than TinGO17 due to the higher relative eo-GO amount. Moreover, the negatively charged O atoms in eo-GO can perform as the active sites during the catalysis (Yang et al. 2017), facilitating the CO_2 reduction. The higher VB maxima of TinGO17 than TiO_2 (=-0.5 V) implies a higher activity of the photogenerated holes in oxidation, because the greater overpotential between the VB maxima and the CO_2 reduction potentials is believed can enhance the photocatalytic efficiency (Habisreutinger et al. 2013). Therefore, the reductions mainly happen on SnO_2 with lower reduction potential and oxidation will proceed on eo-GO with lower oxidation potential (Low et al. 2017). This evidence validates that the coupling between SnO_2 colloids and eo-GO sheets is the key factor to improve the catalytic efficiency and explain the highest CH_4 yield and selectivity achieved over TinGO17 photocatalyst.

Theoretically, the CO_2 reduction over TinGOx photocatalysts can be completed in a single step by involving multiple electrons, since the lower edge of CB of TinGO17 is still higher than the reduction potentials of possible reduction products according to (Hong et al. 2013), as shown in Figure 7.7e. Unfortunately, limited evidence has been reported to validate that mechanism (Habisreutinger et al. 2013). Instead, the reduction of CO_2 over TinGOx photocatalysts is believed to follow the formaldehyde pathway by a series of one-electron steps (Habisreutinger et al. 2013; Koci et al. 2010). This is supported by the various reduction products (HCOOH, HCHO, CH_3OH, and CH_4) in our experiments, as presented in Table 7.4. In addition, the geometries of CO_2 molecule adsorption on the photocatalyst surface can also influence the chemical pathways (Tran et al. 2012). The anchoring of the C atom in the CO_2 molecule on the photocatalyst surface favors the formation of CO. The produced CO can be the final products or the intermediate for further

hydrogenation to various hydrocarbon products, including CH_4 (Tran et al. 2012). Based on these findings, the configuration of CO_2 molecular adsorption on the TinGOx photocatalyst surface is believed also through its C atom.

7.5 Summary of this chapter

Through fabrication of TinGOx nanocomposites by a spray drying process, innovations have been made to the artificial photosynthesis regarding both photocatalyst development and fabrication. The TinGOx photocatalysts exhibit a suitable electronic band structure and materials construction with SnO_2 colloids and eo-GO sheets uniformly distributed over the nanocomposites. The utilization of nano-sized SnO_2 colloids and eo-GO guarantees the TinGOx photocatalysts can efficiently photogenerate and separate the electrons and holes. The high surface area attributed to the eo-GO also promotes the adsorption of CO_2 gases. Among the TinGOx photocatalysts, TinGO17 displays the best catalytic performance. It delivers a CH_4 yield of 85 $nmol \cdot h^{-1} \cdot (g\ catalyst)^{-1}$ under irradiation of full-spectrum light for 4 h, which is five times that of P25 and 28 times that of SnO_2 under same reaction condition. Our catalyst engineering for artificial photosynthesis has successfully increased the efficiencies in both catalysis reaction and catalyst fabrication, which is scalable for the future mass-production.

Chapter 8: Conclusions and future work

8.1 Conclusions

Three different aerosol-assisted processes (spray pyrolysis, colloidal spray pyrolysis, and spray drying) were developed in this dissertation to fabricate functional particles as conductive pastes in solar cell metallization and interference packaging, anode and cathode materials in energy storage devices, and photocatalysts in energy conversion.

A spray pyrolysis process was developed to fabricate Cu-Sn particles from aqueous precursor solutions. The particle configuration is a Sn-enriched surface layer on the Cu-Sn solid solution core. In the precursor solution, EG was used as the co-solvent, because of its higher flash point (111 ^{o}C) than conventional reducing agents (formic acid: 69 ^{o}C and ethanol: 13 ^{o}C) (Yaws 1999; Zhong et al. 2013a; Zhong et al. 2012). This addresses the safety concerns during the potential scale-up manufacturing in the future. The formation mechanism of Cu-Sn binary particles was also studied. Substances in the precursor were first hydrolyzed into hydroxides. Then the hydroxides decomposed into metal oxides. Subsequently, the metal oxides were reduced to metals, and a solid solution formed. For the structural evolution, precipitation of the solutes occurred during solvent evaporation of the precursor droplets. Thus, hollow structures were also generated. Finally, the shrinking of the hollow particles continued until solid particles were formed. Therefore, high reaction temperature (in our experiments: 1000 ^{o}C) promoted the formation of solid dense particles of Cu-Sn particles. Low reaction temperature, 500 ^{o}C in our experiments, led to the formation of hollow porous particles of Cu-Sn. Further decreasing the reaction temperature (to 300 ^{o}C in our experiments), resulted in generating intermediate products. The residence time also exhibited significant influence on the product morphology. With low residence

time (0.92 s, 750 ^{o}C), fragmented particles or irregular morphologies were observed in the products. With long residence time (4.5 s, 750 ^{o}C), spherical particles with smooth surfaces were obtained. With intermediate residence time (1.5 s, 750 ^{o}C), small particles became distinct on the surface of product particles.

After I understood the formation mechanism of Cu-Sn particles in spray pyrolysis and successfully obtained solid dense particles, I investigated their oxidation resistance. Micron-sized solid particles are favored by industry for applications such as conductive pastes and interference packaging (Deshpande et al. 2005; Wu et al. 2009). Therefore, Cu-Sn solid particles fabricated at 1000 ^{o}C were used. The Sn-enriched surface layer guarantees the Cu-Sn particles exhibit better oxidation resistance than Cu particles, as confirmed by XRD with Rietveld refinement analysis, *in situ* XRD, and oxidation kinetics studies. Among the $CuSn_y$ particles, $CuSn_{0.1}$ powders displayed the highest oxidation resistance with best spherical morphology among the $CuSn_y$ powders. Therefore, $CuSn_{0.1}$ particles are promising alternative materials to replace noble metal-based conductive powders, such as Ag and Au, in the fields of printed electronics, interference packaging, and solar cells metallization. Moreover, based on theoretical analysis of the oxidation, the migration of O^{2-} through the oxide layer is a possible rate-limiting step when $CuSn_y$ powders are oxidized at 300 ^{o}C. For oxidation at 500 ^{o}C, grain growth of the oxide likely controls the oxidation process.

Next, investigation was performed on the resistivities of structures fabricated using oxidation-resistant $CuSn_y$ particles to evaluate the prospect of applying these particles. We successfully fabricated $CuSn_y$ wires and films via the direct printing of inks containing oxidation-resistant $CuSn_y$ particles and EG. The $CuSn_{0.1}$ wires exhibited comparable

resistivities with those of Cu wires, and lower than the reported resistivities of wires produced from $Cu_{core}Ag_{shell}$ powders. In addition, $CuSn_{0.1}$ films have significantly less resistivity increases than Cu films when being oxidized at 573 K in ambient air. Therefore, based on the above discussions, $CuSn_{0.1}$ particles are promising materials to replace Au and Ag in applications, including printed electronics, solar cell metallization, and interference packaging.

Colloidal spray pyrolysis has also been developed to addresses issues of conventional spray pyrolysis. For example, conventional spray pyrolysis requires a stable precursor solution to achieve uniform particle-to-particle composition and structure, restricting its usage to highly soluble salts. Moreover, extremely acidic precursors are necessary to ease the uncontrollable hydrolysis of the salts and the subsequent precipitation. By using colloidal spray pyrolysis, all the prerequisites are eliminated simultaneously. A specific example of the application of colloidal spray pyrolysis was presented to generate Sn@C particles for anodes of LIBs and SIBs, which is difficult to obtain by conventional methods. With the guidance of theoretical analysis of the colloid-reduction kinetics and aerosol dynamics, Sn@C particles with controllable interior structures (pitaya, pomegranate and chestnut-structured) were produced. The Sn@C pomegranate anodes displayed excellent battery performance with 88.5% (1500 cycles; 2C) capacity retention for LIBs and superior rate capability for SIBs.

Spray drying process was developed to fabricate nanocomposites (TinGOx) comprising of tin oxide (SnO_2) nanoparticles and edge-oxidized graphene oxide (eo-GO) sheets as photocatalysts in CO_2 reduction. This approach addressed the issues in conventional methods for generating photocatalysts, such as sophisticated experimental

procedures, long processing time, and high investment on instruments. TinGO17 displays the best catalytic performance. It delivers a CH_4 yield of 85 $nmol \cdot h^{-1} \cdot (g\ catalyst)^{-1}$ under irradiation of full-spectrum light for 4 h, which is 5 times that of P25 and 28 times that of SnO_2 under same reaction condition. State-of-art tools, including EELS, have been utilized to validate the TinGOx photocatalysts have a suitable electronic band structure and particle configuration with SnO_2 colloids and eo-GO sheets uniformly distributed over the nanocomposites.

8.2 Future work

This dissertation not only develops three specific processes and applies them in fabrication various functional particles, but also investigates the underlying mechanisms, for example, those controlling the CSP process. Based on the experimental and theoretical analyzing results, I will propose several research projects that can be conducted in the future.

8.2.1 Alternative materials in applications, including printed electronics

In this dissertation, we investigated the prospect of applying Cu-Sn particles as the alternative materials in applications, including printed electronics. In one research article published by (Chen et al. 2014), Cu wires were coated by second metals (Sn, Zn, and In) by electroplating. All these Cu-based wires exhibited significantly higher oxidation-resistance than Cu wire. I have validated that Cu-Sn particles are promising materials. For the other two metals, they are also worth exploring.

Challenges also exist in these two approaches. For example, the reduction of Zn and In ions to metals are more difficult than that of Sn ions, based on the Ellingham diagrams and reported article (Ellingham 1944; Schoeller and Cho 2011). Oxides are expected in the product particles. Moreover, it will be difficult to obtain spherical solid particles because the oxides and metals are not miscible to form solid solutions. Phase segregation may be observed in the product particles, in which Cu will expose directly to air without the protection from the secondary materials (Zn and In). Another obstacle may be expected is during converting the Cu-Zn and Cu-In particles into one- and two-dimensional structures. Since Zn and In ions are difficult to be reduced, their oxides may remain in the product particles. After the one- and two-dimensional structures are printed by inks containing these particles, more reductive condition is required during the sintering step than that to fabricate Cu-Sn structures. Therefore, higher sintering temperature, longer sintering time, and higher H_2 concentration are expected to form the metallic Cu-Zn and Cu-In structures, which may bring additional safety concerns.

8.2.2 Further investigation on CSP

In Chapter 6, I have mentioned that the inter-colloid collision and colloid reduction happen simultaneously during the CSP. I have explored the particle formation at 750 ^{o}C. However, when the reaction temperature further increased to 1000 ^{o}C, the inter-colloid coagulation is expected to be completed faster than colloid reduction, as shown in Figure 8.1.

One major obstacle in this process is the difficulty in completely reducing colloids. As the inter-colloid coagulation is expected to be completed faster than colloid reduction, the

radius of actual colloids need to be reduced is significantly larger than that of the input colloids. Therefore, oxides or reaction intermediates may remain in the product particles. For anode materials, the metals and alloy are more favorable than the oxides due to higher capacities (Goriparti et al. 2014).

On the other hand, the fabricated particles are expected to have core-shell structures, since the faster inter-colloid coagulation has high possibility of resulting in a core covered by another component. The core-shell structure may be promising to be applied as battery materials because it can tolerate large volume expansion.

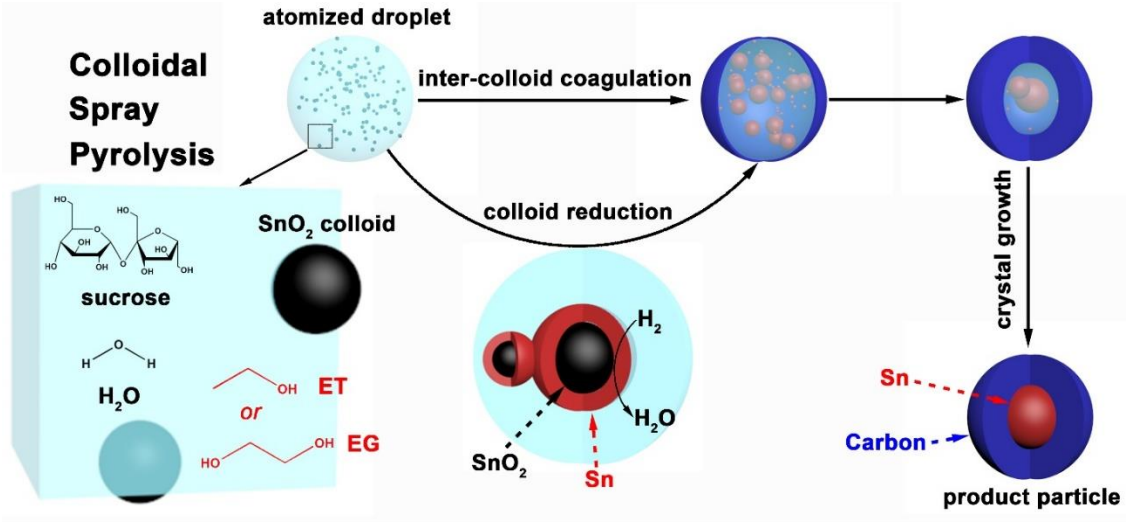

Figure 8.1 Schematic illustration of colloidal spray pyrolysis at high temperature.

Another possible project that worth investigating is applying CSP to produce other battery materials listed in Figure 2.1 and Table 2.1. Based on the procedures presented in Chapter 6 and in Appendices, the possible materials that can be obtained from aqueous

solutions containing their corresponding colloids can be determined. This can further expand the application of CSP.

One difficulty in this approach is to find the values of variables in the equations shown in Chapter 6 and Appendices. For example, the k_r in Equation (A.2.19) is approximated by the equation to calculate the k_r of CuO reduction. In this dissertation, this approximation is valid because our experimental results are consistent with the theoretical analysis. Nevertheless, for other metal oxide colloids, the approximation may not be valid. In the worst case, the values of other variables may have not be reported and are difficult to be determined by experiments. For example, Equations (6.6-6.7) contain μ, which is the viscosity of the precursor solution. In this dissertation, it is measured by using a viscometer with a capillary tube. Since the diameter of the SnO_2 colloids used is 4.4 nm, the viscosity of precursor solution is still measurable by this viscometer. Unfortunately, for other colloids with larger size, clots may be formed in the capillary tube during the viscosity measurement. Then alternative approaches may be required. Nevertheless, the procedures I presented in this dissertation are still applicable to determine the possible metal colloids that can be processed by CSP.

Appendices

A1. Detailed procedures and equations to understand oxidation of Cu-Sn particles by shrinking-core model (SCM) in Chapter 4

SCM was utilized to simulate the oxidation process and to investigate the chemical kinetics and material transport (Chuang et al. 2010; Levenspiel 1999). The densities of Cu (8.9 g/cm^3) and Sn (7.3 g/cm^3) are comparable to their corresponding oxides, such as Cu_2O (6.0 g/cm^3), CuO (6.3 g/cm^3), SnO (6.5 g/cm^3), and SnO_2 (7.0 g/cm^3) (Perry 2011). Therefore, the particle diameter was assumed to be constant during the oxidation process at 300 ^{o}C, which is also validated by the SEM images of the post-oxidation particles, as shown in Figure A.1.1a-c. For oxidation at 500 ^{o}C, SCM is not applicable because of significant coagulation between particles and the resulting particle size change (Figure A.1.1d-f).

The oxidation process can be divided into three steps: (i) migration of O_2 gas through the gas film around the particle to the particle surface; (ii) diffusion of O_2 gas through the porous oxide ash layer to the inner metal core; (iii) reaction of O_2 gas with metal core (Chuang et al. 2010; Levenspiel 1999). If Step (i) controls the process the radius of the unreacted core, r_c, can be related to the oxidation time through (Levenspiel 1999):

$$t = \frac{\rho_p R}{3bk_g C_{O2,g}}\left[1 - \left(\frac{r_c}{R}\right)^3\right] \qquad \text{(A.1.1)}$$

$$\tau = \frac{\rho_p R}{3bk_g C_{O2,g}} \qquad \text{(A.1.2)}$$

where t is the oxidation time. τ is the time for a complete oxidation. ρ_p is the density of the particle. R is the radius of the particle, which is assumed to be 355 nm. b is the

stoichiometric coefficient in the oxidation. k_g is the mass transfer coefficient. $C_{O2,g}$ is the O_2 gas concentration in the main stream.

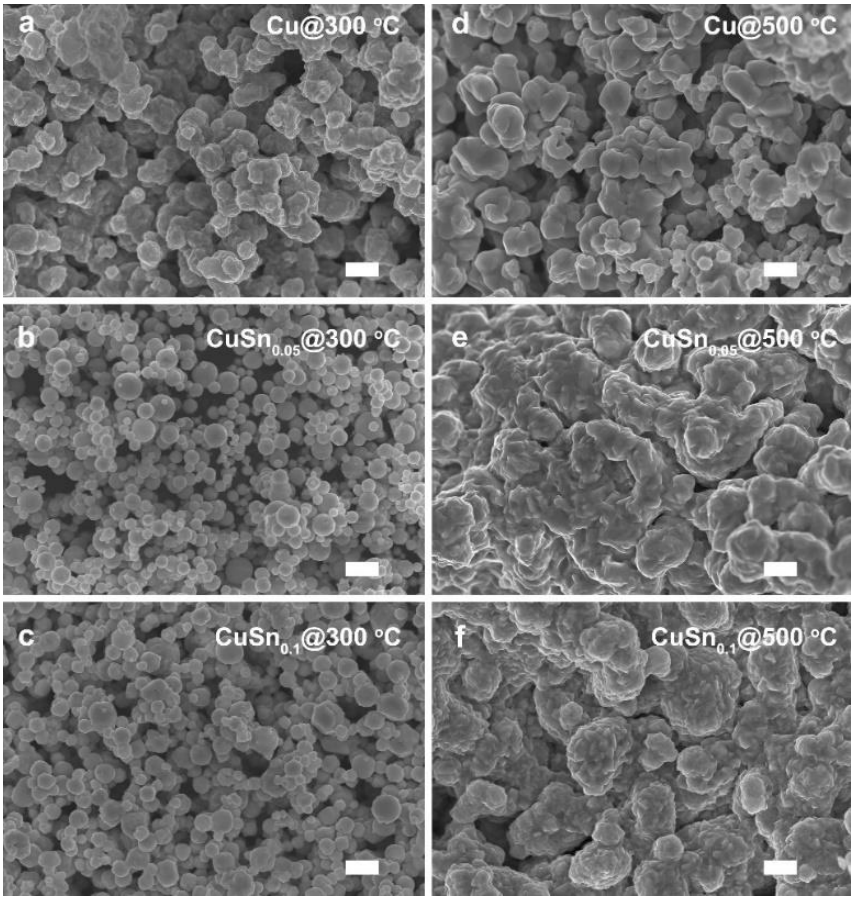

Figure A.1.1. SEM images of particles after being oxidized in a packed-bed reactor under 300 ^oC (a)-(c) and 500 ^oC (d)-(f). The volume percent of O_2 in the feed stream is 1.4 %. The scale bars in SEM images are 2 μm.

If Step (ii) controls the process (Levenspiel 1999):

$$t = \frac{\rho_p R^2}{6bD_e C_{O2,g}}[1 - 3(\frac{r_c}{R})^2 + 2(\frac{r_c}{R})^3] \quad \text{(A.1.3)}$$

$$\tau = \frac{\rho_p R^2}{6bD_e C_{O2,g}} \quad \text{(A.1.4)}$$

where D_e is the effective diffusion coefficient of O_2 in the ash layer.

If Step (iii) controls the process (Levenspiel 1999):

$$t = \frac{\rho_p}{bk_v C_{O2,g}}(R - r_c) \qquad \text{(A.1.5)}$$

$$\tau = \frac{\rho_p}{bk_v C_{O2,g}} R \qquad \text{(A.1.6)}$$

where k_v is the first-order rate constant of Cu oxidation.

k_g in Equations (A.1.1-A.1.2) can be obtained as follows (Fogler 1999):

$$k_g = \frac{1-\emptyset}{\emptyset}\left(\frac{D_{AB}}{d_p}\right)\text{Sh} \qquad \text{(A.1.7)}$$

$$Sh = Re^{1/2}Sc^{1/3} \qquad \text{(A.1.8)}$$

$$Re = \frac{Ud_p}{(1-\emptyset)\nu} \qquad \text{(A.1.9)}$$

$$U = \frac{u_0}{A_c} \qquad \text{(A.1.10)}$$

$$Sc = \frac{\nu}{D_{AB}} \qquad \text{(A.1.11)}$$

$$D_{AB} = 10^{-3}\frac{T^{1.75}\left(\frac{1}{M_{O2}}+\frac{1}{M_{N2}}\right)^{1/2}}{P\left[(V_{O2})^{\frac{1}{3}}+(V_{N2})^{\frac{1}{3}}\right]^2} \qquad \text{(A.1.12)}$$

All dimensionless numbers, *Sh*, *Re*, *Sc*, and symbols are defined in Tables A.1.1-A.1.2. The diffusivity of O_2 gas through the oxide ash layer (D_e) is first assumed to be 10^{-17} m^2/s at 300 ^oC based on the reported O_2 gas diffusion coefficient in Cu_2O (Li and Mayer 1992). After that, the actual D_e in our situation will be approximated by fitting to our experimental data.

Table A.1.1. Variables used in modeling with their definitions and values

Variables	Definition	Value
ρ_{Cu}	Density of Cu	8.9×10^3 kg/m^3 1.4×10^5 mol/m^3 [(Perry 2011)]
ρ_{Sn}	Density of Cu	7.3×10^3 kg/m^3 6.1×10^4 mol/m^3 [(Perry 2011)]
ρ_{Cu2O}	Density of Cu_2O	6.0×10^3 kg/m^3 4.2×10^4 mol/m^3 [(Perry 2011)]
R	Mean radius of particles	355 nm [(Chapter 3)]
d_p	Mean diameter of particles	710 nm [(Chapter 3)]
Φ	Porosity	0.4 [(Chuang et al. 2010)]
U	Superficial velocity	6.5×10^{-3} m/s
u_0	inlet gas flow rate	50 ml/min
v	kinematic viscosity	3.6×10^{-4} m^2/s at 300 ºC 6.1×10^{-4} m^2/s at 500 ºC [(Yaws 1999)]
D_{AB}	Gas-phase diffusivity	0.65 cm^2/s at 300 ºC 1.1 cm^2/s at 300 ºC
A_c	Cross-sectional area of pipe	1.3×10^{-4} m^2
M_{O2}	Molecular weight of O_2	32 g/mol
M_{N2}	Molecular weight of N_2	28 g/mol
P	Pressure	1 atm
V_{O2}	Diffusion volume for O_2	16.6 [(Cussler 2009)]
V_{N2}	Diffusion volume for N_2	17.9 [(Cussler 2009)]

Table A.1.2. Parameters used in modeling with definitions

Parameter	Definition	Unit
t	Oxidation time	s or min
τ	Time for complete oxidation	s
b	Stoichiometry of particle oxidation	dimensionless
k_g	Mass transfer coefficient between fluid and particle	m/s
$C_{O2,g}$	O_2 gas concentration in the main stream	mol/m^3
r_c	Radius of metal core	nm
D_e	Effective diffusion coefficient of O_2 in the ash layer	m^2/s
k_v	The first-order rate constant	s^{-1}
Sh	Sherwood number	dimensionless
Re	Reynolds number	dimensionless
Sc	Schmidt number	dimensionless
k_{app}	First order apparent rate coefficient	min^{-1}

For Equations (A.1.5-A.1.6), as the products of Cu oxidation are Cu_2O and CuO, the rate constants representing the processes of converting Cu to Cu_2O ($k_{v,1}$) and Cu_2O to CuO ($k_{v,2}$) are described as (Chuang et al. 2010):

$$k_{v,1} = 8.2 \times 10^6 \exp\left(\frac{-44 \pm 15 \frac{kJ}{mol}}{RT}\right) (s^{-1}) \text{(A.1.13)}$$

$$k_{v,2} = 1.0 \times 10^7 \exp\left(\frac{-55 \pm 15 \frac{kJ}{mol}}{RT}\right) (s^{-1}) \text{(A.1.14)}$$

The carrier gas was assumed to be pure N_2 gas when calculating the kinematic viscosity (v), which is 4.8×10^{-5} m^2/s based on the dynamic viscosity of N_2 gas at 300 ^oC and 1.01×10^5 Pa (Yaws 1999).

For Cu particles, the oxidation products include CuO and Cu_2O (Figure 4.15 in Chapter 4). As shown in Table A.1.3, Step (ii), internal diffusion of O_2 gas through porous oxide ash layer controls the process in both scenarios.

For $CuSn_{0.05}$ particles, the oxidation products are Cu_2O and SnO_2 (Figure 4.15). Step (ii) is the rate-limiting step. Detailed results are shown in Table A.1.3.

For $CuSn_{0.1}$ particles, the oxidation products are Cu_2O and SnO_2 (Figure 4.15). Step (ii) controls the process. Detailed results are shown in Table A.1.3.

Therefore, the oxidation of Cu, $CuSn_{0.05}$, and $CuSn_{0.1}$ particles are all controlled by internal diffusion of O_2 gas through the oxide ash layer based on SCM simulation.

Table A.1.3. Simulation results of Cu-Sn particle oxidation at 300 °C in a packed-bed reactor by SCM. The diffusion coefficients listed here are obtained by fitting the experimental results (Figure 4.16). The reported diffusion coefficients are 10^{-17} m^2/s for both situations of O_2 through Cu_2O and O_2 through SnO_2 and at 300 °C (Cussler 2009; Li and Mayer 1992).

			Particles		
			Cu	$CuSn_{0.05}$	$CuSn_{0.1}$
			300 °C	300 °C	300 °C
ρ_p			1.4×10^5 mol/m3	1.4×10^5 mol/m3	1.3×10^5 mol/m3
Mw			64 g/mol	66 g/mol	69 g/mol
Rate-limiting step	External diffusion of O_2 gas to particle surface	*Sc* *Re* *Sh* k_g	5.6 2.1×10^{-5} 8.1×10^{-3} 1.1 m/s	5.6 2.1×10^{-5} 8.1×10^{-3} 1.1 m/s	5.6 2.1×10^{-5} 8.1×10^{-3} 1.1 m/s
		τ	0.013 s, Cu_2O 0.025 s, CuO	0.013 s	0.013 s
	Internal diffusion of O_2 gas through oxide ash	D_e	2.2×10^{-13} m^2/s	8.2×10^{-14} m^2/s ($r_c/R \geq 0.9$) 3.5×10^{-14} m^2/s ($r_c/R \leq 0.9$)	1.4×10^{-14} m^2/s
		τ	4.2×10^6 min, Cu_2O **8.4×10^6 min, CuO**	**4.2×10^6 min**	**4.3×10^6 min**
	Chemical reaction of O_2 with metal core	k_v	800 s^{-1} Cu_2O 97 s^{-1} CuO	800 s^{-1}	800 s^{-1}
		τ	5.3×10^{-5} s Cu_2O 8.8×10^{-4} s CuO	5.4×10^{-5} s	5.4×10^{-5} s

Detailed procedures to obtain the D_e

In the SCM simulation, we utilized a diffusion coefficient of O_2 gas through Cu_2O layer at 300 °C obtained from the literature, 10^{-17} m^2/s at 300 °C (Li and Mayer 1992), which may not represent the internal diffusion of O_2 in our system. Thus, the actual diffusion coefficients in Equations (A.1.3-A.1.4) were fitted. To simplify the fitting model,

$$x = [1 - 3(\frac{r_c}{R})^2 + 2(\frac{r_c}{R})^3] \qquad \text{(A.1.15)}$$

Then Equation (A.1.3) becomes:

$$t = \frac{\rho_p R^2}{6bD_e C_{O2,g}} x \qquad \text{(A.1.16)}$$

To obtain the actual D_e, the results in Figure 4.14 need to be converted from ($\Delta m/m$ vs. t) to (t vs. x). The r_c/R in Equation (A.1.3) can be obtained by assuming the thickness of

the oxide layer was uniform on the particle surface (Kim et al. 2004). Therefore, the volume of oxide layer can be calculated as:

$$V = \frac{4}{3}\pi(R^3 - r_c^3) \qquad \text{(A.1.17)}$$

The relative weight gain caused by oxidation is:

$$\frac{\Delta m}{m} = \frac{\frac{V\rho_p}{Mw}\cdot\frac{2Mw_O}{b}}{V\rho_p} \qquad \text{(A.1.18)}$$

Cu particles:

To convert the results in Figure 4.14 ($\Delta m/m$ vs. t) into t vs. x, equations are also derived based on the two situations when Cu_2O and CuO were the oxidation products.

If Cu is oxidized to Cu_2O, b=4. Then Equation (A.1.18) can be converted into:

$$\frac{\Delta m}{m} = \frac{\frac{4}{3}\pi(R^3 - r_c^3)\rho_{Cu}\cdot\frac{Mw_O}{2}}{\frac{4}{3}\pi R^3\rho_{Cu}} = \frac{Mw_O}{2Mw_{Cu}}[1 - (\frac{r_c}{R})^3] \text{(A.1.19)}$$

When Cu is assumed to be directly oxidized into CuO, b=2. Then:

$$\frac{\Delta m}{m} = \frac{\frac{4}{3}\pi(R^3 - r_c^3)\rho_{Cu}}{\frac{4}{3}\pi R^3\rho_{Cu}}\frac{Mw_O}{Mw_{Cu}} = \frac{Mw_O}{Mw_{Cu}}[1 - (\frac{r_c}{R})^3] \text{(A.1.20)}$$

The curves representing the t vs. x are presented in Figure A.1.2a-b. In the case of Cu_2O as the main product, the results in Figure A.1.2a are not well explained by SCM. In the SCM, Equation (A.1.16) is linear and its slope is a monotonic function of D_e. If the oxidation product is CuO, the curve is still not linear (Figure A.1.2b). However, D_e is 2.2×10^{-13} m^2/s, if we fit the non-linear curve to a linear equation.

$CuSn_{0.05}$ particles:

Equation (A.1.18) can be transformed into the following equation, because the oxidation products are Cu_2O and SnO_2 (Figure 4.15):

$$\frac{\Delta m}{m} = \frac{\frac{4}{3}\pi(R^3 - r_c^3)\rho_{CuSn0.05} \cdot (\frac{Mw_O}{2} + 0.1Mw_O)}{\frac{4}{3}\pi R^3 \rho_{CuSn0.05}} = \frac{0.6Mw_O}{Mw_{CuSn0.05}}[1 - (\frac{r_c}{R})^3] \qquad \text{(A.1.21)}$$

By applying Equations (A.1.16,A.1.21), curves in Figure 4.14 ($\Delta m/m$ vs. t) can be converted into t vs. x. The result is shown in Figure A.1.2c.

For $CuSn_{0.1}$ particles:

Equation (A.1.18) can be transformed into following equation, because the oxidation products are Cu_2O and SnO_2 (Figure 4.15):

$$\frac{\Delta m}{m} = \frac{\frac{4}{3}\pi(R^3 - r_c^3)\rho_{CuSn0.1} \cdot (\frac{Mw_O}{2} + 0.2Mw_O)}{\frac{4}{3}\pi R^3 \rho_{CuSn0.1}} = \frac{0.7Mw_O}{Mw_{CuSn0.1}}[1 - (\frac{r_c}{R})^3] \quad \text{(A.1.22)}$$

By applying Equations (A.1.16,A.1.22), curves in Figure 4.14 ($\Delta m/m$ vs. t) can be converted into t vs. x. The result is illustrated in Figure A.1.2d.

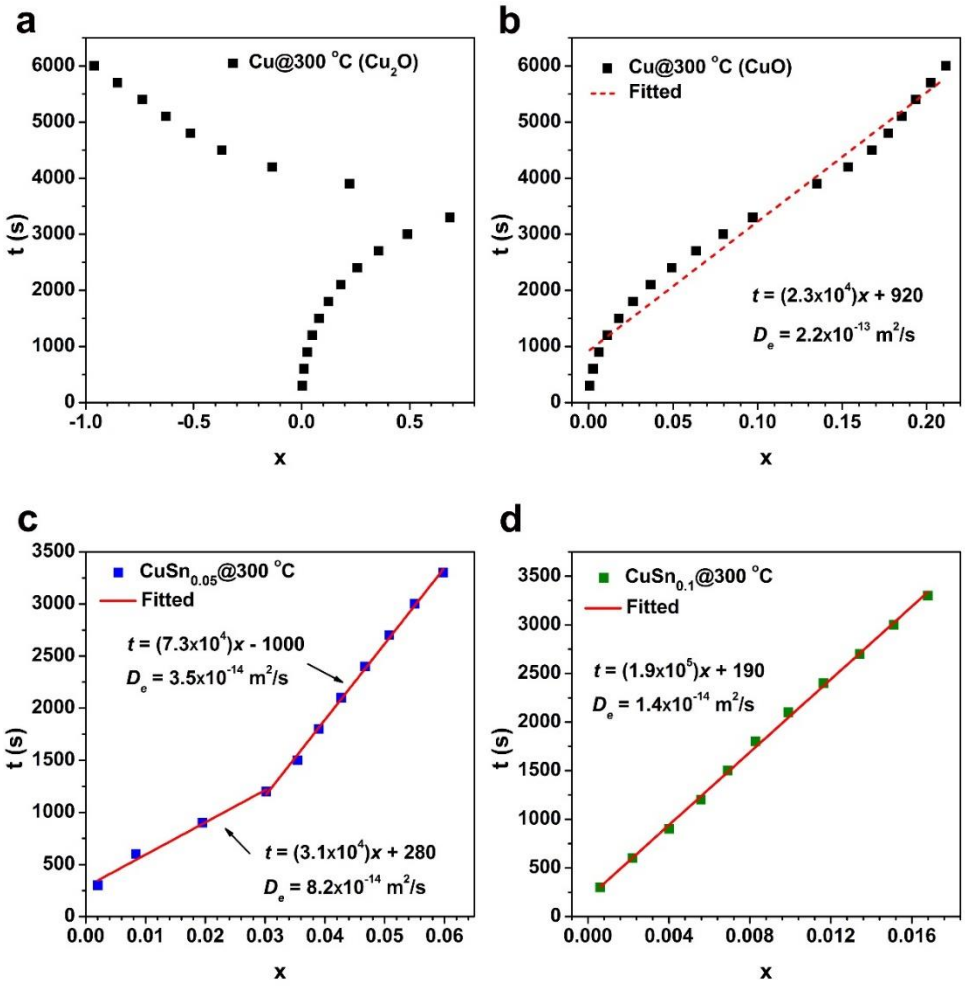

Figure A.1.2. Oxidation time (t) vs x of Cu particles with the assumption that the product of Cu oxidation is Cu_2O (a) and CuO (b) at 300 °C. (c)-(d) Plots of oxidation time (t) vs x of $CuSn_{0.05}$ (c) and $CuSn_{0.1}$ (d) particles. x is a variable defined by Equation (A.1.15). The internal diffusivity of O_2 through oxide ash layer (D_e) is obtained by fitting the curves in (a-d) by Equation (A.1.16). The oxidation is conducted in O_2-He flow with 1.4 vol % O_2. The diffusion coefficients obtained are 10^3 – 10^4 higher than reported values for the diffusion coefficients, which are 10^{-17} m^2/s for both situations of O_2 through Cu_2O and O_2 through SnO_2 and at 300 °C (Hernandez-Ramirez et al. 2008; Li and Mayer 1992).

A2. Modeling on the colloidal spray pyrolysis process in Chapter 6

A2.1 General equations for CSP modeling

In CSP, the oxide colloids were reduced by reducing gases as discussed in the main text. Here, we calculated the time scale of colloid reduction, as explained in Formula 6.2 (Chapter 6).

The oxide-colloid reduction by H_2 can be modeled by two senarios (Levenspiel 1999), as shown in the schematic drawing in Figures 6.1b,6.2d.

i) Diffusion of gaseous H_2 though a layer of metal ash towards the interface of oxide/metal.

ii) Reaction of the gaseous H_2 with oxide at the interface.

For a general approach, we analyzed the colloid reduction process in two situations, where the rate-limiting step is i) the diffusion of H_2 through the metal ash and ii) chemical reaction between the H_2 and oxide core. In addition, the process was assumed to be pseudo-steady state and the colloid radius was assumed to remain constant during the process (discussed in Chapter 6).

i) Diffusion of gaseous H_2 though the metal ash layer controls

Based on the model presented in Figures 6.1b,6.2d, we can build a material balance with respect to H_2:

$$-\frac{dN_{H2}}{dt} = 4\pi r^2 Q_{H2} = 4\pi r_c^2 Q_{c,H2} = constant \ \ [mol \cdot s^{-1}] \quad \text{(A.2.1)}$$

Here, Q_{H2} represents the flux of H_2 through surface of any radius r. $Q_{c,H2}$ is the flux of H_2 to the reaction surface.

$$Q_{H2} = D_e \frac{dC_{H2}}{dr} \ \ [mol \cdot m^{-2} \cdot s^{-1}] \quad \text{(A.2.2)}$$

$$-\frac{dN_{H2}}{dt} = 4\pi r^2 D_e \frac{dC_{H2}}{dr} = constant \quad \text{(A.2.3)}$$

To integrate Equation A.2.3, we can use the following boundary conditions:

$$r = R \qquad C_{H2} = C_{s,H2}$$

$$r = r_c \qquad C_{H2} = 0$$

R is the radius of the colloid. $C_{s,H2}$ is the H_2 concentration on the colloid surface. Then we can have:

$$-\frac{dN_{H2}}{dt}\left(\frac{1}{r_c} - \frac{1}{R}\right) = 4\pi D_e C_{s,H2} \ [mol \cdot m^{-1} \cdot s^{-1}] \quad \text{(A.2.4)}$$

From stoichiometry, Equation A.2.4 can be extended as:

$$-x\frac{dN_{H2}}{dt} = -\frac{dN_{MOx}}{dt} = -\rho_{MOx}\frac{dV}{dt} = -\rho_{MOx}\frac{d\left(\frac{4}{3}\pi r_c^3\right)}{dt} = -4\pi\rho_{MOx} r_c^2 \frac{dr_c}{dt} \quad \text{(A.2.5)}$$

Therefore,

$$-\rho_{MOx} r_c^2 \left(\frac{1}{r_c} - \frac{1}{R}\right)\frac{dr_c}{dt} = xD_e C_{s,H2} \ [mol \cdot m^{-1} \cdot s^{-1}] \quad \text{(A.2.6)}$$

Integrating Equation A.2.6 with the following boundary conditions,

$$r_c = R \qquad t = 0$$

$$r_c = r_c \qquad t = t$$

we obtain:

$$t = \frac{\rho_{MOx} R^2}{6xD_e C_{s,H2}}\left[1 - 3\left(\frac{r_c}{R}\right)^2 + 2\left(\frac{r_c}{R}\right)^3\right] \quad \text{(A.2.7)}$$

The time scale for colloid reduction can be obtained by setting $r_c = 0$ in Equation A.2.7,

$$\tau = \frac{\rho_{MOx} R^2}{6xD_e C_{s,H2}} \quad \text{(A.2.8)}$$

ii) Reaction controls

When colloid reduction is controlled by chemical reactions, the material balance can be analyzed at the interface between oxide/metal. Unlike the case in which diffusion is the rate-controlling step, the interface between the core (oxide) and ash (metal) is not stationary.

The rate expression for oxide reduction by H_2 with respect to H_2 is k_r and the reaction order is n. Therefore, by building the material balance of H_2 on the interface and considering the stoichiometry, we have:

$$-\frac{x}{4\pi r_c^2}\frac{dN_{H2}}{dt} = -\frac{1}{4\pi r_c^2}\frac{dN_{MOx}}{dt} = xk_r C_{s,H2}^n \quad \text{(A.2.9)}$$

In addition, based on Equation A.2.5, we can turn Equation A.2.9 into:

$$-\frac{1}{4\pi r_c^2} 4\pi\rho_{MOx} r_c^2 \frac{dr_c}{dt} = -\rho_{MOx}\frac{dr_c}{dt} = xk_r C_{s,H2}^n \quad \text{(A.2.10)}$$

Integrating the above equation with the following boundary conditions,

$$r_c = R \qquad t = 0$$

$$r_c = r_c \qquad t = t$$

we obtain:

$$t = \frac{\rho_{MOx}}{xk_r C_{s,H2}^n}(R - r_c) \quad \text{(A.2.11)}$$

Setting $r_c = 0$, the time scale for reduction is

$$\tau = \frac{\rho_{MOx} R}{xk_r C_{s,H2}^n} \quad \text{(A.2.12)}$$

A2.2 Detailed procedures to calculate the time of SnO_2 colloid reduction

For the reduction of SnO_2 colloid, the chemical formula is:

$$2H_2 + SnO_2 \rightleftharpoons Sn + 2H_2O \quad \text{(A.2.13)}$$

The volume average droplet diameter produced by the atomizer is 5 μm (Zhong et al. 2013b). To calculate the H_2 concentration on the colloid surface ($C_{s,H2}$), the SnO_2 colloid loadings for each condition are listed in Table 6.1. Every mole of EG will produce 0.81 mol H_2 under reaction conditions similar to this work, based upon experimental results (Zhong et al. 2013b). In addition, each mole of sucrose produces 7.48 mol H_2 (Cho et al. 2013). With this information, the $C_{s,H2}$ was calculated and shown in Table A.2.1.

Table A.2.1. Parameters used in the modeling in Section A.2

	Sn@C particle type		
	Pitaya	Pomegranate	chestnut
Average number of SnO_2 colloids per droplet	7.4×10^{5}	1.2×10^{6}	2.5×10^{6}
Average quantity of EG account for each colloid (mol)	4.2×10^{-19}	2.5×10^{-19}	1.3×10^{-19}
Average quantity of sucrose account for each colloid (mol)	1.8×10^{-20}	1.1×10^{-20}	2.7×10^{-22}
$C_{s,H2}$ (mol/L)	5.4	5.4	4.0

i) Diffusion of gaseous H_2 though the Sn ash layer controls

Equations A.2.5-A.2.8 can be extended as:

$$-2\frac{dN_{H2}}{dt} = -\frac{dN_{SnO2}}{dt} = -\rho_{snO2}\frac{dV}{dt} = -\rho_{snO2}\frac{d\left(\frac{4}{3}\pi r_c^3\right)}{dt} = -4\pi\rho_{snO2}r_c^2\frac{dr_c}{dt} \quad \text{(A.2.14)}$$

$$-\rho_{snO2}r_c^2\left(\frac{1}{r_c}-\frac{1}{R}\right)\frac{dr_c}{dt} = 2D_eC_{s,H2}\ \ [mol\cdot m^{-1}\cdot s^{-1}] \quad \text{(A.2.15)}$$

$$t = \frac{\rho_{SnO2}R^2}{12D_eC_{s,H2}}\left[1-3\left(\frac{r_c}{R}\right)^2+2\left(\frac{r_c}{R}\right)^3\right] \quad \text{(A.2.16)}$$

$$\tau = \frac{\rho_{SnO2}R^2}{12D_eC_{s,H2}} \quad \text{(A.2.17)}$$

Here, ρ_{SnO2} is 4.6×10^4 mol/m^3 (Perry 2011). At our experimental conditions, the set point of the furnaces was 750 ^{o}C. Thus, it is rational to assume that Sn was liquid, since the metaling point of bulk Sn is ~230 ^{o}C (Wronski 1967). The melting point of bulk SnO_2

is believed to be 1630 ^{o}C (Sun et al. 2004). Some researchers even reported that it could be up to 2100 ^{o}C (Galazka et al. 2014). Therefore, *De* represents the H_2 diffusivity in liquid tin. Unfortunately, the *De* of H_2 diffusion through Sn is hard to obtain, because of the large uncertainty in measuring the solubility of H_2 in liquid Sn (Sacris and Parlee 1970). Thus, we used the Stokes-Einstein equation to approximate the *De*:

$$D_e = \frac{kT}{6\pi r_{H2}\mu_{Sn}} \quad \text{(A.2.18)}$$

Here, k is the Boltzmann constant (=1.38×10^{-23} J·K^{-1}). r_{H2} is the radius of H_2 molecule (2.05×10^{-10} m) (Schlapbach and Zuttel 2001). μ_{Sn} is the viscosity of liquid Sn at 750 ^{o}C, which is 0.83 mPa·s (Assael et al. 2010). By Equation A.2.18, *De* is 6.6×10^{-9} m^2·s^{-1} at 750 ^{o}C.

Based on Equation A.2.17, when the diffusion of H_2 through the Sn ash controls the process, the time scales of SnO_2 colloid reduction in generating Sn@C particles are 7.8×10^{-10} s (pitaya-structured), 7.8×10^{-10} s (pomegranate-structured), and 1.1×10^{-9} s (chestnut-structured).

ii) Reaction controls

As it is difficult to find the exact rate expression for SnO_2 reduction by H_2, we used the kinetic equation representing CuO reduction by H_2 as an alternative approach. The reaction order is 0.6 and the rate constant expression with respect to H_2 is (García-Labiano et al. 2004):

$$k_r = 1.0\times10^{-4}\exp\left(\frac{-33000}{8.314\times T}\right)\ [mol^{0.4}m^{-0.2}s^{-1}] \quad \text{(A.2.19)}$$

Therefore, Equations A.2.9-A.2.12 become:

$$-\frac{2}{4\pi r_c^2}\frac{dN_{H2}}{dt} = -\frac{1}{4\pi r_c^2}\frac{dN_{SnO2}}{dt} = 2k_r C_{s,H2}^{0.6} \quad \text{(A.2.20)}$$

$$-\frac{1}{4\pi r_c^2}4\pi\rho_{snO2}r_c^2\frac{dr_c}{dt} = -\rho_{snO2}\frac{dr_c}{dt} = 2k_r C_{s,H2}^{0.6} \quad \text{(A.2.21)}$$

$$t = \frac{\rho_{snO2}}{2k_r C_{s,H2}^{0.6}}(R - r_c) \quad \text{(A.2.22)}$$

$$\tau = \frac{\rho_{snO2}R}{2k_r C_{s,H2}^{0.6}} \quad \text{(A.2.23)}$$

Thus, when chemical reaction controls the SnO_2 colloid reduction, reduction times are 0.14 s (pitaya-structured), 0.14 s (pomegranate-structured), and 0.17 s (chestnut-structured) by using Equation A.2.23. These data are all much larger than the calculation results obtained based on the assumption that the rate-controlling step is the diffusion. Therefore, chemical reaction controls colloid reduction in our situations.

A3. Detailed calculation procedures to obtain the colloid concentration in Chapters 6.

$$n_{SnO_2} = \frac{v \cdot SG \cdot w \cdot \rho_{H_2O}}{Mw} \cdot 10^{-3} \ [mol] \quad \text{(A.2.27)}$$

$$C_{SnO_2} = \frac{n_{SnO_2}}{V} \cdot 1000 \ [mol/L] \quad \text{(A.2.28)}$$

$$N_{colloid,SnO_2} = \frac{v \cdot SG \cdot w \cdot \rho_{H_2O}}{\frac{1}{6}\pi \cdot d^3 \cdot \rho_{SnO_2}} \cdot 10^{21} \quad \text{(A.2.29)}$$

$$\frac{\delta N_{colloid,SnO_2}}{\delta V} = \frac{N_{colloid,SnO_2}}{V} \cdot 1000 \ [\#/L] \quad \text{(A.2.30)}$$

v [ml] is the volume of extracted SnO_2 colloid raw solution. *SG* is the specific gravity of SnO_2 colloid solution (SN15ES) from Nyacol™ at 25 °C, which is 1.15. *w* is the mass fraction of SnO_2 colloid solution (SN15ES) from Nyacol™, which is 0.15. *Mw* [g/mol] is molecular weight of SnO_2. *V* [ml] is the volume of precursor. *d* [nm] is particle size or

particle diameter. ρ_{H2O} [kg/m^3] is the density of bulk H_2O. ρ_{SnO2} [kg/m^3] is the density of bulk SnO_2.

References

Abhinav K, V., Rao R, V. K., Karthik, P. S., Singh, S. P. (2015). Copper conductive inks: synthesis and utilization in flexible electronics. *RSC Advances* 5:63985-64030.

Addison, C. C. and Hathaway, B. J. (1958). 628. The vapour pressure of anhydrous copper nitrate, and its molecular weight in the vapour state. *Journal of the Chemical Society (Resumed)*:3099-3106.

AlOtaibi, B., Fan, S., Wang, D., Ye, J., Mi, Z. (2015). Wafer-Level Artificial Photosynthesis for CO2 Reduction into CH4 and CO Using GaN Nanowires. *ACS Catalysis* 5:5342-5348.

Andresen, A. F. (1958). THE EFFECT OF DISSOLVED TIN ON THE LATTICE PARAMETER OF COPPER. *Transactions of the American Institute of Mining and Metallurgical Engineers* 212:259-260.

Assael, M. J., Kalyva, A. E., Antoniadis, K. D., Michael Banish, R., Egry, I., Wu, J., Kaschnitz, E., Wakeham, W. A. (2010). Reference Data for the Density and Viscosity of Liquid Copper and Liquid Tin. *Journal of Physical and Chemical Reference Data* 39:033105.

Avvaru, B., Patil, M. N., Gogate, P. R., Pandit, A. B. (2006). Ultrasonic atomization: Effect of liquid phase properties. *Ultrasonics* 44:146-158.

Bahadur, J., Sen, D., Mazumder, S., Paul, B., Khan, A., Ghosh, G. (2010). Evaporation-induced self assembly of nanoparticles in non-buckling regime: Volume fraction dependent packing. *Journal of Colloid and Interface Science* 351:357-364.

Bang, J. H. and Suslick, K. S. (2010). Applications of Ultrasound to the Synthesis of Nanostructured Materials. *Advanced Materials* 22:1039-1059.

Bloomberg (2017). Precious and Industrial Metals, Bloomberg Markets, Bloomberg Markets.

Boissiere, C., Grosso, D., Chaumonnot, A., Nicole, L., Sanchez, C. (2011). Aerosol Route to Functional Nanostructured Inorganic and Hybrid Porous Materials. *Advanced Materials* 23:599-623.

Booth, M. H., Brandon, J. K., Brizard, R. Y., Chieh, C., Pearson, W. B. (1977). GAMMA-BRASSES WITH F CELLS. *Acta Crystallographica Section B-Structural Science* 33:30-36.

Cabrera, N. and Mott, N. F. (1949). Theory of the oxidation of metals. *Reports on Progress in Physics* 12:163-184.

Cao, Q., Kim, H.-s., Pimparkar, N., Kulkarni, J. P., Wang, C., Shim, M., Roy, K., Alam, M. A., Rogers, J. A. (2008). Medium-Scale Carbon Nanotube Thin-Film Integrated Circuits on Flexible Plastic Substrates. *Nature* 454:495-500.

Cao, W., Li, W., Yin, R., Zhou, W. (2014). Controlled fabrication of Cu–Sn core–shell nanoparticles via displacement reaction. *Colloids and Surfaces A: Physicochemical and Engineering Aspects* 453:37-43.

Chang, X., Wang, T., Gong, J. (2016). CO2 photo-reduction: insights into CO2 activation and reaction on surfaces of photocatalysts. *Energy & Environmental Science* 9:2177-2196.

Chatain, D., Ghetta, V., Wynblatt, P. (2004). Equilibrium Shape of Copper Crystals Grown on Sapphire. *Interface Science* 12:7-18.

Chatterjee, S. and Gupta, M. (1975). Lattice Parameters of Some Binary and Ternary Copper Alloys. *Journal of Applied Crystallography* 8:492-493.

Chen, Q. and Sieradzki, K. (2013). Spontaneous evolution of bicontinuous nanostructures in dealloyed Li-based systems. *Nat Mater* 12:1102-1106.

Chen, Z., Ye, S., Stewart, I. E., Wiley, B. J. (2014). Copper Nanowire Networks with Transparent Oxide Shells That Prevent Oxidation without Reducing Transmittance. *ACS Nano* 8:9673-9679.

Cho, E. C., Camargo, P. H. C., Xia, Y. (2010). Synthesis and Characterization of Noble-Metal Nanostructures Containing Gold Nanorods in the Center. *Advanced Materials* 22:744-748.

Cho, Y. K., Jung, K. Y., Lee, H., Heo, S. (2013). Synthesis and characterization of C/Cu core–shell particles by hydrogen-free spray pyrolysis assisted with citric acid and sucrose. *Materials Research Bulletin* 48:3424-3430.

Choi, S. H., Ko, Y. N., Lee, J. K., Kang, Y. C. (2015). 3D MoS2-Graphene Microspheres Consisting of Multiple Nanospheres with Superior Sodium Ion Storage Properties. *Adv Funct Mater* 25:1780-1788.

Chuang, S. Y., Dennis, J. S., Hayhurst, A. N., Scott, S. A. (2010). Kinetics of the Oxidation of a Co-precipitated Mixture of Cu and Al2O3 by O2 for Chemical-Looping Combustion. *Energy & Fuels* 24:3917-3927.

Cohen, R. L. and West, K. W. (1972). Solution Chemistry and Colloid Formation in the Tin Chloride Sensitizing Process. *Journal of The Electrochemical Society* 119:433-438.

Comiskey, B., Albert, J. D., Yoshizawa, H., Jacobson, J. (1998). An electrophoretic ink for all-printed reflective electronic displays. *Nature* 394:253-255.

Cussler, E. L. (2009). Diffusion: Mass Transfer in Fluid Systems. Cambridge university press.

Dai, Z. R., Pan, Z. W., Wang, Z. L. (2002). Growth and Structure Evolution of Novel Tin Oxide Diskettes. *Journal of the American Chemical Society* 124:8673-8680.

Damour, T. M., Ehrman, S. H., Karlsson, M. N. A., Karlsson, L. S., Deppert, K. (2005). Experimental Evidence for Nonuniform Flow in a Horizontal Evaporation/Condensation Aerosol Generator. *Aerosol Science and Technology* 39:444-451.

de Andres, P. L., Ramírez, R., Vergés, J. A. (2008). Strong covalent bonding between two graphene layers. *Physical Review B* 77:045403.

Deen, W. M. (1998). Analysis of Transport Phenomena (Topics in Chemical Engineering). Oxford University Press, New York.

Degang, C., Yoshifumi, O., Hirotaka, H., Hiroaki, S., Toshio, O., Seiichi, T., Hiroshi, K. (1998). Surface Protrusions of Chemical Vapor Deposited TiN Films Caused by Cu Contamination of Silicon Substrates. *Japanese Journal of Applied Physics* 37:L607.

Derrien, G., Hassoun, J., Panero, S., Scrosati, B. (2007). Nanostructured Sn–C Composite as an Advanced Anode Material in High-Performance Lithium-Ion Batteries. *Advanced Materials* 19:2336-2340.

Deshpande, V., Kshirsagar, A., Rane, S., Seth, T., Phatak, G. J., Mulik, U. P., Amalnerkar, D. P. (2005). Properties of lead-free conductive thick films of co-precipitated silver–palladium powders. *Materials Chemistry and Physics* 93:320-324.

Dhas, N. A., Raj, C. P., Gedanken, A. (1998). Synthesis, Characterization, and Properties of Metallic Copper Nanoparticles. *Chemistry of Materials* 10:1446-1452.

Duan, Y. (2008). Electronic properties and stabilities of bulk and low-index surfaces of SnO in comparison with SnO2: A first-principles density functional approach with an empirical correction of van der Waals interactions. *Physical Review B* 77:045332.

Ehsan, M. F. and He, T. (2015). In situ synthesis of ZnO/ZnTe common cation heterostructure and its visible-light photocatalytic reduction of CO2 into CH4. *Applied Catalysis B: Environmental* 166–167:345-352.

Eigler, S., Dotzer, C., Hirsch, A. (2012). Visualization of defect densities in reduced graphene oxide. *Carbon* 50:3666-3673.

Ellingham, H. J. T. (1944). Transactions and Communications. *Journal of the Society of Chemical Industry* 63:125-160.

Eom, K., Jung, J., Lee, J. T., Lair, V., Joshi, T., Lee, S. W., Lin, Z., Fuller, T. F. (2015). Improved stability of nano-Sn electrode with high-quality nano-SEI formation for lithium ion battery. *Nano Energy* 12:314-321.

Eslamian, M. and Ashgriz, N. (2006). Effect of precursor, ambient pressure, and temperature on the morphology, crystallinity, and decomposition of powders prepared by spray pyrolysis and drying. *Powder Technology* 167:149-159.

Faddoul, R., Reverdy-Bruas, N., Blayo, A. (2012). Formulation and screen printing of water based conductive flake silver pastes onto green ceramic tapes for electronic applications. *Materials Science and Engineering: B* 177:1053-1066.

Fang, B., Bonakdarpour, A., Reilly, K., Xing, Y., Taghipour, F., Wilkinson, D. P. (2014). Large-Scale Synthesis of TiO2 Microspheres with Hierarchical Nanostructure for Highly Efficient Photodriven Reduction of CO2 to CH4. *ACS Applied Materials & Interfaces* 6:15488-15498.

Feng, Z., Marks, C. R., Barkatt, A. (2003). Oxidation-Rate Excursions During the Oxidation of Copper in Gaseous Environments at Moderate Temperatures. *Oxidation of Metals* 60:393-408.

Fievet, F., Fievet-Vincent, F., Lagier, J.-P., Dumont, B., Figlarz, M. (1993). Controlled nucleation and growth of micrometre-size copper particles prepared by the polyol process. *Journal of Materials Chemistry* 3:627-632.

Fleisch, T. H. and Mains, G. J. (1982). Reduction of copper oxides by UV radiation and atomic hydrogen studied by XPS. *Applications of Surface Science* 10:51-62.

Fogler, H. S. (1999). Elements of chemical reaction engineering. Prentice-Hall International, Inc.

Fotou, G. P., Kodas, T. T., Anderson, B. (2000). Coating Titania Aerosol Particles with ZrO2, Al2O3/ZrO2 and SiO2/ZrO2 in a Gas-Phase Process. *Aerosol Science and Technology* 33:557-571.

Friedlander, S. K. (2000). Smoke, Dust, and Haze. Oxford university press New York.

Fujimoto, T., Terauchi, S.-y., Umehara, H., Kojima, I., Henderson, W. (2001). Sonochemical Preparation of Single-Dispersion Metal Nanoparticles from Metal Salts. *Chemistry of Materials* 13:1057-1060.

Fujita, K., Ando, D., Uchikoshi, M., Mimura, K., Isshiki, M. (2013). New model for low-temperature oxidation of copper single crystal. *Applied Surface Science* 276:347-358.

Galazka, Z., Uecker, R., Klimm, D., Irmscher, K., Pietsch, M., Schewski, R., Albrecht, M., Kwasniewski, A., Ganschow, S., Schulz, D., Guguschev, C., Bertram, R., Bickermann, M., Fornari, R. (2014). Growth, characterization, and properties of bulk SnO2 single crystals. *physica status solidi (a)* 211:66-73.

Gale, W. F. and Totemeier, T. C. (2003). Smithells Metals Reference Book. Butterworth-Heinemann.

García-Labiano, F., de Diego, L. F., Adánez, J., Abad, A., Gayán, P. (2004). Reduction and Oxidation Kinetics of a Copper-Based Oxygen Carrier Prepared by Impregnation for Chemical-Looping Combustion. *Industrial & Engineering Chemistry Research* 43:8168-8177.

Glicksman, H. D., Kodas, T. T., Majumdar, D. (1996). Method for making copper (I) oxide powders by aerosol decomposition, Google Patents.

Glicksman, H. D., Kodas, T. T., Majumdar, D. (1997). Method for making gold powders by aerosol decomposition, Google Patents.

Glicksman, H. D., Kodas, T. T., Pluym, T. C. (1995). Method for making silver-palladium alloy powders by aerosol decomposition, Google Patents.

Glicksman, H. D. and Yang, H. (2004). Aqueous developable photoimageable thick film compositions with photospeed enhancer, Google Patents.

Goriparti, S., Miele, E., De Angelis, F., Di Fabrizio, E., Proietti Zaccaria, R., Capiglia, C. (2014). Review on recent progress of nanostructured anode materials for Li-ion batteries. *Journal of Power Sources* 257:421-443.

Grouchko, M., Kamyshny, A., Magdassi, S. (2009). Formation of air-stable copper-silver core-shell nanoparticles for inkjet printing. *Journal of Materials Chemistry* 19:3057-3062.

Gurav, A., Kodas, T., Pluym, T., Xiong, Y. (1993). Aerosol Processing of Materials. *Aerosol Science and Technology* 19:411-452.

Gürmen, S., Stopić, S., Friedrich, B. (2006). Synthesis of nanosized spherical cobalt powder by ultrasonic spray pyrolysis. *Materials Research Bulletin* 41:1882-1890.

Habisreutinger, S. N., Schmidt-Mende, L., Stolarczyk, J. K. (2013). Photocatalytic Reduction of CO2 on TiO2 and Other Semiconductors. *Angewandte Chemie International Edition* 52:7372-7408.

Hai, H. T., Takamura, H., Koike, J. (2013). Oxidation behavior of Cu–Ag core–shell particles for solar cell applications. *Journal of Alloys and Compounds* 564:71-77.

Hernandez-Ramirez, F., Prades, J. D., Tarancon, A., Barth, S., Casals, O., Jimenez-Diaz, R., Pellicer, E., Rodriguez, J., Morante, J. R., Juli, M. A., Mathur, S., Romano-Rodriguez, A. (2008). Insight into the Role of Oxygen Diffusion in the Sensing Mechanisms of SnO2 Nanowires. *Advanced Functional Materials* 18:2990-2994.

Hong, J., Zhang, W., Ren, J., Xu, R. (2013). Photocatalytic reduction of CO2: a brief review on product analysis and systematic methods. *Analytical Methods* 5:1086-1097.

Hong, Y. J. and Kang, Y. C. (2015). One-pot synthesis of core–shell-structured tin oxide–carbon composite powders by spray pyrolysis for use as anode materials in Li-ion batteries. *Carbon* 88:262-269.

Hsieh, M.-C., Wu, G.-C., Liu, W.-G., Goddard, W. A., Yang, C.-M. (2014). Nanocomposites of Tantalum-Based Pyrochlore and Indium Hydroxide Showing High and Stable Photocatalytic Activities for Overall Water Splitting and Carbon Dioxide Reduction. *Angewandte Chemie International Edition* 53:14216-14220.

Hsien-Hsueh, L., Kan-Sen, C., Kuo-Cheng, H. (2005). Inkjet printing of nanosized silver colloids. *Nanotechnology* 16:2436.

Hsu, H.-C., Shown, I., Wei, H.-Y., Chang, Y.-C., Du, H.-Y., Lin, Y.-G., Tseng, C.-A., Wang, C.-H., Chen, L.-C., Lin, Y.-C., Chen, K.-H. (2013). Graphene oxide as a promising photocatalyst for CO2 to methanol conversion. *Nanoscale* 5:262-268.

Huang, C.-Y. and Sheen, S. R. (1997). Synthesis of nanocrystalline and monodispersed copper particles of uniform spherical shape. *Materials Letters* 30:357-361.

Huang, J. Y., Zhong, L., Wang, C. M., Sullivan, J. P., Xu, W., Zhang, L. Q., Mao, S. X., Hudak, N. S., Liu, X. H., Subramanian, A., Fan, H., Qi, L., Kushima, A., Li, J. (2010). In Situ Observation of the Electrochemical Lithiation of a Single SnO₂ Nanowire Electrode. *Science* 330:1515-1520.

Huang, X. K., Cui, S. M., Chang, J. B., Hallac, P. B., Fell, C. R., Luo, Y. T., Metz, B., Jiang, J. W., Hurley, P. T., Chen, J. H. (2015). A Hierarchical Tin/Carbon Composite as an Anode for Lithium-Ion Batteries with a Long Cycle Life. *Angew Chem Int Edit* 54:1490-1493.

Ide, Y., Inami, N., Hattori, H., Saito, K., Sohmiya, M., Tsunoji, N., Komaguchi, K., Sano, T., Bando, Y., Golberg, D., Sugahara, Y. (2016). Remarkable Charge Separation and Photocatalytic Efficiency Enhancement through Interconnection of TiO2 Nanoparticles by Hydrothermal Treatment. *Angewandte Chemie International Edition* 55:3600-3605.

Im, H. S., Cho, Y. J., Lim, Y. R., Jung, C. S., Jang, D. M., Park, J., Shojaei, F., Kang, H. S. (2013). Phase Evolution of Tin Nanocrystals in Lithium Ion Batteries. *Acs Nano* 7:11103-11111.

Inoue, T., Fujishima, A., Konishi, S., Honda, K. (1979). Photoelectrocatalytic reduction of carbon dioxide in aqueous suspensions of semiconductor powders. *Nature* 277:637-638.

Iskandar, F., Kim, S.-G., Nandiyanto, A. B. D., Kaihatsu, Y., Ogi, T., Okuyama, K. (2009). Direct synthesis of hBN/MWCNT composite particles using spray pyrolysis. *Journal of Alloys and Compounds* 471:166-171.

Istratov, A. A., Flink, C., Hieslmair, H., McHugo, S. A., Weber, E. R. (2000). Diffusion, solubility and gettering of copper in silicon. *Materials Science and Engineering: B* 72:99-104.

Jeong, S., Lee, S. H., Jo, Y., Lee, S. S., Seo, Y.-H., Ahn, B. W., Kim, G., Jang, G.-E., Park, J.-U., Ryu, B.-H., Choi, Y. (2013). Air-Stable, Surface-Oxide Free Cu Nanoparticles for Highly Conductive Cu Ink and Their Application to Printed Graphene Transistors. *Journal of Materials Chemistry C* 1:2704-2710.

Jeong, S., Woo, K., Kim, D., Lim, S., Kim, J. S., Shin, H., Xia, Y., Moon, J. (2008). Controlling the Thickness of the Surface Oxide Layer on Cu Nanoparticles for the Fabrication of Conductive Structures by Ink-Jet Printing. *Advanced Functional Materials* 18:679-686.

Jianfeng, Y., Guisheng, Z., Anming, H., Zhou, Y. N. (2011). Preparation of PVP Coated Cu NPs and the Application for Low-Temperature Bonding. *Journal of Materials Chemistry* 21:15981-15986.

Jiao, J., Wei, Y., Zhao, Y., Zhao, Z., Duan, A., Liu, J., Pang, Y., Li, J., Jiang, G., Wang, Y. (2017). AuPd/3DOM-TiO2 catalysts for photocatalytic reduction of CO2: High efficient separation of photogenerated charge carriers. *Applied Catalysis B: Environmental* 209:228-239.

Jo, Y. H., Park, J. C., Bang, J. U., Song, H., Lee, H. M. (2011). New Synthesis Approach for Low Temperature Bimetallic Nanoparticles: Size and Composition Controlled Sn-Cu Nanoparticles. *Journal of Nanoscience and Nanotechnology* 11:1037-1041.

Johari, P. and Shenoy, V. B. (2011). Modulating Optical Properties of Graphene Oxide: Role of Prominent Functional Groups. *ACS Nano* 5:7640-7647.

Jordan, T. E. (1954). Vapor Pressure of Organic Compounds. Interscience Publishers.

Joshi, B. N., An, S., Kim, Y. I., Samuel, E. P., Song, K. Y., Seong, I. W., Al-Deyab, S. S., Swihart, M. T., Yoon, W. Y., Yoon, S. S. (2017). Flexible freestanding Fe2O3-SnOx-carbon nanofiber composites for Li ion battery anodes. *Journal of Alloys and Compounds* 700:259-266.

Ju, Y., Tasaka, T., Yamauchi, H., Nakagawa, T. (2015). Synthesis of Sn nanoparticles and their size effect on the melting point. *Microsystem Technologies* 21:1849-1854.

Jung, D. S., Hwang, T. H., Lee, J. H., Koo, H. Y., Shakoor, R. A., Kahraman, R., Jo, Y. N., Park, M.-S., Choi, J. W. (2014). Hierarchical Porous Carbon by Ultrasonic Spray Pyrolysis Yields Stable Cycling in Lithium–Sulfur Battery. *Nano Letters* 14:4418-4425.

Jung, D. S., Hwang, T. H., Park, S. B., Choi, J. W. (2013). Spray Drying Method for Large-Scale and High-Performance Silicon Negative Electrodes in Li-Ion Batteries. *Nano Letters* 13:2092-2097.

Jung, D. S., Lee, H. M., Kang, Y. C., Park, S. B. (2011). Air-Stable Silver-Coated Copper Particles of Sub-Micrometer Size. *Journal of Colloid and Interface Science* 364:574-581.

Karabacak, T., DeLuca, J. S., Wang, P.-I., Ten Eyck, G. A., Ye, D., Wang, G.-C., Lu, T.-M. (2006). Low temperature melting of copper nanorod arrays. *Journal of Applied Physics* 99:064304.

Kaspar, J., Terzioglu, C., Ionescu, E., Graczyk-Zajac, M., Hapis, S., Kleebe, H. J., Riedel, R. (2014). Stable SiOC/Sn Nanocomposite Anodes for Lithium-Ion Batteries with Outstanding Cycling Stability. *Adv Funct Mater* 24:4097-4104.

Ke, F. S., Huang, L., Jamison, L., Xue, L. J., Wei, G. Z., Li, J. T., Zhou, X. D., Sun, S. G. (2013). Nanoscale tin-based intermetallic electrodes encapsulated in microporous copper substrate as the negative electrode with a high rate capacity and a long cycleability for lithium-ion batteries. *Nano Energy* 2:595-603.

Kim, H.-S., Lee, K.-H., Kim, S.-G. (2006). Growth of Monodisperse Silver Nanoparticles in Polymer Matrix by Spray Pyrolysis. *Aerosol Science and Technology* 40:536-544.

Kim, I., Kim, Y., Woo, K., Ryu, E.-H., Yon, K.-Y., Cao, G., Moon, J. (2013). Synthesis of oxidation-resistant core-shell copper nanoparticles. *RSC Advances* 3:15169-15177.

Kim, J. H., Babushok, V. I., Germer, T. A., Mulholland, G. W., Ehrman, S. H. (2003). Cosolvent-assisted spray pyrolysis for the generation of metal particles. *Journal of Materials Research* 18:1614-1622.

Kim, J. H., Ehrman, S. H., Germer, T. A. (2004). Influence of Particle Oxide Coating on Light Scattering by Submicron Metal Particles on Silicon Wafers. *Applied Physics Letters* 84:1278-1280.

Kim, S.-W., Kim, M., Lee, W. Y., Hyeon, T. (2002). Fabrication of Hollow Palladium Spheres and Their Successful Application to the Recyclable Heterogeneous Catalyst for Suzuki Coupling Reactions. *Journal of the American Chemical Society* 124:7642-7643.

Kittel, C. (2005). Introduction to Solid State Physics. Wiley, Hoboken, NJ :.

Kobayashi, Y. and Sakuraba, T. (2008). Silica-coating of metallic copper nanoparticles in aqueous solution. *Colloids and Surfaces A: Physicochemical and Engineering Aspects* 317:756-759.

Koci, K., Obalova, L., Solcova, O. (2010). KINETIC STUDY OF PHOTOCATALYTIC REDUCTION OF CO2 OVER TIO2. *Chemical and Process Engineering-Inzynieria Chemiczna I Procesowa* 31:395-407.

Kodas, T. T., Ward, T. L., Glicksman, H. D. (1995). Method for making silver powder by aerosol decomposition, Google Patents.

Koirala, R., Pratsinis, S. E., Baiker, A. (2016). Synthesis of catalytic materials in flames: opportunities and challenges. *Chemical Society Reviews* 45:3053-3068.

Korber, C., Wachau, A., Agoston, P., Albe, K., Klein, A. (2011). Self-Limited Oxygen Exchange Kinetics at SnO2 Surfaces. *Physical Chemistry Chemical Physics* 13:3223-3226.

Kumar, A., Rout, L., Achary, L. S. K., Mohanty, A., Dhaka, R. S., Dash, P. (2016). An investigation into the solar light-driven enhanced photocatalytic properties of a graphene oxide-SnO2-TiO2 ternary nanocomposite. *RSC Advances* 6:32074-32088.

Kumar, K. S., Reinbold, L., Bower, A. F., Chason, E. (2011). Plastic deformation processes in Cu/Sn bimetallic films. *Journal of Materials Research* 23:2916-2934.

Lee, J. U., Lee, W., Yi, J. W., Yoon, S. S., Lee, S. B., Jung, B. M., Kim, B. S., Byun, J. H. (2013). Preparation of highly stacked graphene papers via site-selective functionalization of graphene oxide. *Journal of Materials Chemistry A* 1:12893-12899.

Leenen, M. A. M., Arning, V., Thiem, H., Steiger, J., Anselmann, R. (2009). Printable electronics: flexibility for the future. *physica status solidi (a)* 206:588-597.

Lenggoro, I. W., Hata, T., Iskandar, F., Lunden, M. M., Okuyama, K. (2000). An experimental and modeling investigation of particle production by spray pyrolysis using a laminar flow aerosol reactor. *Journal of Materials Research* 15:733-743.

Lengsfeld, C. S., Delplanque, J. P., Barocas, V. H., Randolph, T. W. (2000). Mechanism Governing Microparticle Morphology during Precipitation by a Compressed Antisolvent: Atomization vs Nucleation and Growth. *The Journal of Physical Chemistry B* 104:2725-2735.

Lengyel, M., Elhassid, D., Atlas, G., Moller, W. T., Axelbaum, R. L. (2014). Development of a scalable spray pyrolysis process for the production of non-hollow battery materials. *Journal of Power Sources* 266:175-178.

Levenspiel, O. (1999). Chemical reaction engineering. Wiley.

Levich, V. G. (1962). Physicochemical Hydrodynamics. Prentice Hall.

Li, H., Gan, S., Wang, H., Han, D., Niu, L. (2015a). Intercorrelated Superhybrid of AgBr Supported on Graphitic-C3N4-Decorated Nitrogen-Doped Graphene: High Engineering Photocatalytic Activities for Water Purification and CO2 Reduction. *Advanced Materials* 27:6906-6913.

Li, J., Li, Y., Wang, Z., Bian, H., Hou, Y., Wang, F., Xu, G., Liu, B., Liu, Y. (2016a). Ultrahigh Oxidation Resistance and High Electrical Conductivity in Copper-Silver Powder. *Scientific Reports* 6:39650.

Li, J. and Mayer, J. W. (1992). Oxidation and reduction of copper oxide thin films. *Materials Chemistry and Physics* 32:1-24.

Li, L., Yan, J., Wang, T., Zhao, Z.-J., Zhang, J., Gong, J., Guan, N. (2015b). Sub-10 nm rutile titanium dioxide nanoparticles for efficient visible-light-driven photocatalytic hydrogen production. *Nature Communications* 6:5881.

Li, M., Zhang, L., Wu, M., Du, Y., Fan, X., Wang, M., Zhang, L., Kong, Q., Shi, J. (2016b). Mesostructured CeO2/g-C3N4 nanocomposites: Remarkably enhanced photocatalytic activity for CO2 reduction by mutual component activations. *Nano Energy* 19:145-155.

Li, W., Wang, Y., Wang, M., Li, W., Tan, J., You, C., Chen, M. (2016c). Synthesis of Stable CucoreAgshell&Ag Particles for Direct Writing Flexible Paper-Based Electronics. *RSC Advances* 6:62236-62243.

Li, W., Zhang, H., Gao, Y., Jiu, J., Li, C.-F., Chen, C., Hu, D., Goya, Y., Wang, Y., Koga, H., Nagao, S., Suganuma, K. (2017). Highly Reliable and Highly Conductive Submicron Cu Particle Patterns Fabricated by Low Temperature Heat-Welding and Subsequent Flash Light Sinter-Reinforcement. *Journal of Materials Chemistry C*.

Li, Y., Wu, Y., Ong, B. S. (2005). Facile Synthesis of Silver Nanoparticles Useful for Fabrication of High-Conductivity Elements for Printed Electronics. *Journal of the American Chemical Society* 127:3266-3267.

Li, Z. J., Lv, W., Zhang, C., Qin, J. W., Wei, W., Shao, J. J., Wang, D. W., Li, B. H., Kang, F. Y., Yang, Q. H. (2014). Nanospace-confined formation of flattened Sn sheets in pre-seeded graphenes for lithium ion batteries. *Nanoscale* 6:9554-9558.

Liao, J. Y. and Manthiram, A. (2014). Mesoporous TiO2-Sn/C Core-Shell Nanowire Arrays as High-Performance 3D Anodes for Li-Ion Batteries. *Adv Energy Mater* 4.

Lide, D. (2007-2008). CRC Handbook of Chemistry and Physics. New York: CRC Press.

Lin, F., Nordlund, D., Li, Y., Quan, M. K., Cheng, L., Weng, T.-C., Liu, Y., Xin, H. L., Doeff, M. M. (2016). Metal segregation in hierarchically structured cathode materials for high-energy lithium batteries. *Nature Energy* 1:15004.

Lin, L.-Y., Nie, Y., Kavadiya, S., Soundappan, T., Biswas, P. (2017). N-doped reduced graphene oxide promoted nano TiO2 as a bifunctional adsorbent/photocatalyst for CO2 photoreduction: Effect of N species. *Chemical Engineering Journal* 316:449-460.

Liu, C. J., Huang, H., Cao, G. Z., Xue, F. H., Camacho, R. A. P., Dong, X. L. (2014). Enhanced Electrochemical Stability of Sn-Carbon Nanotube Nanocapsules as Lithium-Ion Battery Anode. *Electrochim Acta* 144:376-382.

Liu, C. M., Liu, W. L., Chen, W. J., Hsieh, S. H., Tsai, T. K., Yang, L. C. (2005). ITO as a Diffusion Barrier Between Si and Cu. *Journal of The Electrochemical Society* 152:G234-G239.

Liu, J., Chen, H., Ji, H., Li, M. (2016). Highly Conductive Cu–Cu Joint Formation by Low-Temperature Sintering of Formic Acid-Treated Cu Nanoparticles. *ACS Applied Materials & Interfaces* 8:33289-33298.

Liu, W. L., Chen, W. J., Tsai, T. K., Hsieh, S. H., Liu, C. M. (2007a). Effect of Tin-Doped Indium Oxide Film as Capping Layer on the Agglomeration of Copper Film and the Appearance of Copper Silicide. *Applied Surface Science* 253:5516-5520.

Liu, Z., Sun, D. D., Guo, P., Leckie, J. O. (2007b). An Efficient Bicomponent TiO2/SnO2 Nanofiber Photocatalyst Fabricated by Electrospinning with a Side-by-Side Dual Spinneret Method. *Nano Letters* 7:1081-1085.

Long, R., Li, Y., Liu, Y., Chen, S., Zheng, X., Gao, C., He, C., Chen, N., Qi, Z., Song, L., Jiang, J., Zhu, J., Xiong, Y. (2017). Isolation of Cu Atoms in Pd Lattice: Forming Highly Selective Sites for Photocatalytic Conversion of CO2 to CH4. *Journal of the American Chemical Society* 139:4486-4492.

Low, J., Yu, J., Jaroniec, M., Wageh, S., Al-Ghamdi, A. A. (2017). Heterojunction Photocatalysts. *Advanced Materials* 29:1601694.

Loyalka, S. K. (1968). Momentum and Temperature‐Slip Coefficients with Arbitrary Accommodation at the Surface. *The Journal of Chemical Physics* 48:5432-5436.

Lu, L., Shen, Y., Chen, X., Qian, L., Lu, K. (2004). Ultrahigh Strength and High Electrical Conductivity in Copper. *Science* 304:422-426.

Luo, C., Langrock, A., Fan, X., Liang, Y., Wang, C. (2017). P2-type transition metal oxides for high performance Na-ion battery cathodes. *Journal of Materials Chemistry A* 5:18214-18220.

Ma, J., Fang, Z., Yan, Y., Yang, Z., Gu, L., Hu, Y.-S., Li, H., Wang, Z., Huang, X. (2015). Novel Large-Scale Synthesis of a C/S Nanocomposite with Mixed Conducting Networks through a Spray Drying Approach for Li–S Batteries. *Advanced Energy Materials* 5:1500046.

Ma, S., Liu, L., Bromberg, V., Singler, T. J. (2014). Fabrication of Highly Electrically Conducting Fine Patterns via Substrate-Independent Inkjet Printing of Mussel-Inspired Organic Nano-Material. *Journal of Materials Chemistry C* 2:3885-3889.

Mack, E., Osterhof, G. G., Kraner, H. M. (1923). VAPOR PRESSURE OF COPPER OXIDE AND OF COPPER. *Journal of the American Chemical Society* 45:617-623.

Mao, J., Peng, T., Zhang, X., Li, K., Zan, L. (2012). Selective methanol production from photocatalytic reduction of CO2 on BiVO4 under visible light irradiation. *Catalysis Communications* 28:38-41.

Matienzo, L. J., Das, R. N., Egitto, F. D. (2008). Electrically Conductive Adhesives for Electronic Packaging and Assembly Applications. *Journal of Adhesion Science and Technology* 22:853-869.

Matsnnaga, S. and Homma, T. (1976). Influence on the oxidation kinetics of metals by control of the structure of oxide scales. *Oxidation of Metals* 10:361-376.

Mayadas, A. F. and Shatzkes, M. (1970). Electrical-Resistivity Model for Polycrystalline Films: the Case of Arbitrary Reflection at External Surfaces. *Physical Review B* 1:1382-1389.

Mei, Z., Sunwoo, A. J., Morris, J. W. (1992). Analysis of low-temperature intermetallic growth in copper-tin diffusion couples. *Metallurgical Transactions A* 23:857-864.

Miettinen, J. (2008). Thermodynamic description of the Cu–Fe–Sn system at the Cu–Fe side. *Calphad* 32:500-505.

Mkhoyan, K. A., Contryman, A. W., Silcox, J., Stewart, D. A., Eda, G., Mattevi, C., Miller, S., Chhowalla, M. (2009). Atomic and Electronic Structure of Graphene-Oxide. *Nano Letters* 9:1058-1063.

Mokkapati, S., Beck, F. J., Polman, A., Catchpole, K. R. (2009). Designing periodic arrays of metal nanoparticles for light-trapping applications in solar cells. *Applied Physics Letters* 95:053115.

Moonen, P. F., Bat, E., Voorthuijzen, W. P., Huskens, J. (2013). Soft-Lithographic Patterning of Room Temperature-Sintering Ag Nanoparticles on Foil. *RSC Advances* 3:18498-18505.

Morinaga, H., Suyama, M., Nose, M., Verhaverbeke, S., Ohmi, T. (1996). A model for the electrochemical deposition and removal of metallic impurities on Si surfaces. *IEICE Transactions on Electronics* E79C:343-362.

Munnik, P., Wolters, M., Gabrielsson, A., Pollington, S. D., Headdock, G., Bitter, J. H., de Jongh, P. E., de Jong, K. P. (2011). Copper Nitrate Redispersion To Arrive at Highly Active Silica-Supported Copper Catalysts. *The Journal of Physical Chemistry C* 115:14698-14706.

Murcia-López, S., Bacariza, M. C., Villa, K., Lopes, J. M., Henriques, C., Morante, J. R., Andreu, T. (2017). Controlled Photocatalytic Oxidation of Methane to Methanol through Surface Modification of Beta Zeolites. *ACS Catalysis* 7:2878-2885.

Nandiyanto, A. B. D. and Okuyama, K. (2011). Progress in developing spray-drying methods for the production of controlled morphology particles: From the nanometer to submicrometer size ranges. *Advanced Powder Technology* 22:1-19.

Nguyen, Q. T., Kidder Jr, J. N., Ehrman, S. H. (2002). Hybrid gas-to-particle conversion and chemical vapor deposition for the production of porous alumina films. *Thin Solid Films* 410:42-52.

Ni, W., Cheng, J. L., Shi, L. Y., Li, X. D., Wang, B., Guan, Q., Huang, L., Gu, G. F., Li, H. (2014). Integration of Sn/C yolk-shell nanostructures into free-standing conductive networks as hierarchical composite 3D electrodes and the Li-ion insertion/extraction properties in a gel-type lithium-ion battery thereof. *J Mater Chem A* 2:19122-19130.

Nie, Y., Wang, W.-N., Jiang, Y., Fortner, J., Biswas, P. (2016). Crumpled reduced graphene oxide-amine-titanium dioxide nanocomposites for simultaneous carbon dioxide adsorption and photoreduction. *Catalysis Science & Technology* 6:6187-6196.

Noor, F., Vorozhtsov, A., Lerner, M., Bandarra Filho, E. P., Wen, D. (2015). Thermal-Chemical Characteristics of Al–Cu Alloy Nanoparticles. *The Journal of Physical Chemistry C* 119:14001-14009.

Nowick, A. S. (2012). Diffusion in solids: recent developments. Elsevier.

O'Connell, R., Alexander, C., Strachan, R., Alway, B., Nambiath, S., Wiebe, J., Wong, L., Rannestad, E., Li, S., Aranda, D., Scott-Gray, N. (2017). World Silver Survey 2017, The Silver Institute.

Ortega, J., Kodas, T. T., Chadda, S., Smith, D. M., Ciftcioglu, M., Brennan, J. E. (1991). Formation of dense barium calcium titanate (Ba0.86Ca0.14TiO3) particles by aerosol decomposition. *Chemistry of Materials* 3:746-751.

Park, B. K., Jeong, S., Kim, D., Moon, J., Lim, S., Kim, J. S. (2007). Synthesis and size control of monodisperse copper nanoparticles by polyol method. *Journal of Colloid and Interface Science* 311:417-424.

Perelaer, J., Smith, P. J., Mager, D., Soltman, D., Volkman, S. K., Subramanian, V., Korvink, J. G., Schubert, U. S. (2010). Printed electronics: the challenges involved in

printing devices, interconnects, and contacts based on inorganic materials. *Journal of Materials Chemistry* 20:8446-8453.

Perry, D. L. (2011). Handbook of Inorganic Compounds. CRC press.

Pingali, K. C., Rockstraw, D. A., Deng, S. (2005). Silver Nanoparticles from Ultrasonic Spray Pyrolysis of Aqueous Silver Nitrate. *Aerosol Science and Technology* 39:1010-1014.

Platteeuw, J. C. and Meyer, G. (1956). The system tin + oxygen. *Transactions of the Faraday Society* 52:1066-1073.

Pluym, T. C., Powell, Q. H., Gurav, A. S., Ward, T. L., Kodas, T. T., Wang, L. M., Glicksman, H. D. (1993). Solid silver particle production by spray pyrolysis. *Journal of Aerosol Science* 24:383-392.

Polat, D. B., Lu, J., Abouimrane, A., Keles, O., Amine, K. (2014). Nanocolumnar Structured Porous Cu-Sn Thin Film as Anode Material for Lithium-Ion Batteries. *ACS Applied Materials & Interfaces* 6:10877-10885.

Qin, J., He, C., Zhao, N., Wang, Z., Shi, C., Liu, E.-Z., Li, J. (2014). Graphene Networks Anchored with Sn@Graphene as Lithium Ion Battery Anode. *ACS Nano* 8:1728-1738.

R, V. K. R., K, V. A., P. S, K., Singh, S. P. (2015). Conductive silver inks and their applications in printed and flexible electronics. *RSC Advances* 5:77760-77790.

Ramisetty, K. A., Pandit, A. B., Gogate, P. R. (2013). Investigations into ultrasound induced atomization. *Ultrasonics Sonochemistry* 20:254-264.

Reddy, M. V., Subba Rao, G. V., Chowdari, B. V. R. (2013). Metal Oxides and Oxysalts as Anode Materials for Li Ion Batteries. *Chemical Reviews* 113:5364-5457.

Sacris, E. M. and Parlee, N. A. D. (1970). The diffusion of hydrogen in liquid Ni, Cu, Ag, and Sn. *Metallurgical Transactions* 1:3377-3382.

Saunders, N. and Miodownik, A. P. (1990). The Cu-Sn (Copper-Tin) system. *Bulletin of Alloy Phase Diagrams* 11:278-287.

Schiotz, J., Di Tolla, F. D., Jacobsen, K. W. (1998). Softening of Nanocrystalline Metals at Very Small Grain Sizes. *Nature* 391:561-563.

Schirmer, N. C., Ströhle, S., Tiwari, M. K., Poulikakos, D. (2011). On the Principles of Printing Sub-micrometer 3D Structures from Dielectric-Liquid-Based Colloids. *Advanced Functional Materials* 21:388-395.

Schlapbach, L. and Zuttel, A. (2001). Hydrogen-storage materials for mobile applications. *Nature* 414:353-358.

Schoeller, H. and Cho, J. (2011). Oxidation and reduction behavior of pure indium. *Journal of Materials Research* 24:386-393.

Schulz, H., Mädler, L., Strobel, R., Jossen, R., Pratsinis, S. E., Johannessen, T. (2005). Independent Control of Metal Cluster and Ceramic Particle Characteristics During One-step Synthesis of Pt/TiO2. *Journal of Materials Research* 20:2568-2577.

semiwafer.com Silicon Wafer.

Sen, D., Mazumder, S., Melo, J. S., Khan, A., Bhattyacharya, S., D'Souza, S. F. (2009). Evaporation Driven Self-Assembly of a Colloidal Dispersion during Spray Drying: Volume Fraction Dependent Morphological Transition. *Langmuir* 25:6690-6695.

Sharma, M. K., Qi, D., Buchner, R. D., Scharmach, W. J., Papavassiliou, V., Swihart, M. T. (2014). Flame-driven Aerosol Synthesis of Copper–Nickel Nanopowders and Conductive Nanoparticle Films. *ACS Applied Materials & Interfaces* 6:13542-13551.

Shen, W., Zhang, X., Huang, Q., Xu, Q., Song, W. (2014a). Preparation of Solid Silver Nanoparticles for Inkjet Printed Flexible Electronics with High Conductivity. *Nanoscale* 6:1622-1628.

Shen, Y., Søndergaard, M., Christensen, M., Birgisson, S., Iversen, B. B. (2014b). Solid State Formation Mechanism of Li4Ti5O12 from an Anatase TiO2 Source. *Chemistry of Materials* 26:3679-3686.

Shirai, H., Nguyen, M. T., Ishida, Y., Yonezawa, T. (2016). A New Approach for Additive-Free Room Temperature Sintering of Conductive Patterns Using Polymer-Stabilized Sn Nanoparticles. *Journal of Materials Chemistry C* 4:2228-2234.

Shown, I., Hsu, H.-C., Chang, Y.-C., Lin, C.-H., Roy, P. K., Ganguly, A., Wang, C.-H., Chang, J.-K., Wu, C.-I., Chen, L.-C., Chen, K.-H. (2014). Highly Efficient Visible Light Photocatalytic Reduction of CO2 to Hydrocarbon Fuels by Cu-Nanoparticle Decorated Graphene Oxide. *Nano Letters* 14:6097-6103.

Smithells, C. J., Gale, W. F., Totemeier, T. C. (2004). Smithells Metals Reference Book. Elsevier Butterworth-Heinemann, Amsterdam ;.

Smits, F. M. (1958). Measurement of Sheet Resistivities with the Four-Point Probe. *Bell System Technical Journal* 37:711-718.

Song, H., Zhang, L., He, C., Qu, Y., Tian, Y., Lv, Y. (2011). Graphene sheets decorated with SnO2 nanoparticles: in situ synthesis and highly efficient materials for cataluminescence gas sensors. *Journal of Materials Chemistry* 21:5972-5977.

Song, Y. L., Tsai, S. C., Chen, C. Y., Tseng, T. K., Tsai, C. S., Chen, J. W., Yao, Y. D. (2004). Ultrasonic Spray Pyrolysis for Synthesis of Spherical Zirconia Particles. *Journal of the American Ceramic Society* 87:1864-1871.

Songping, W. and Shuyuan, M. (2006). Preparation of micron size copper powder with chemical reduction method. *Materials Letters* 60:2438-2442.

Speight, J. (2004). Lange's Handbook of Chemistry. McGraw-Hill Professional, New York.

Srinivasan, S. and Anantharaman, T. R. (1963). ACCURATE EVALUATION OF LATTICE PARAMETERS OF ALPHA-BRASSES. *Current Science* 32:262-263.

Stern, K. H. (1972). High Temperature Properties and Decomposition of Inorganic Salts Part 3, Nitrates and Nitrites. *Journal of Physical and Chemical Reference Data* 1:747-772.

Strobel, R., Alfons, A., Pratsinis, S. E. (2006). Aerosol flame synthesis of catalysts. *Advanced Powder Technology* 17:457-480.

Strobel, R. and Pratsinis, S. E. (2007). Flame aerosol synthesis of smart nanostructured materials. *Journal of Materials Chemistry* 17:4743-4756.

Suenaga, K. and Koshino, M. (2010). Atom-by-atom spectroscopy at graphene edge. *Nature* 468:1088-1090.

Sun, S. H., Meng, G. W., Zhang, M. G., An, X. H., Wu, G. S., Zhang, L. D. (2004). Synthesis of SnO 2 nanostructures by carbothermal reduction of SnO 2 powder. *Journal of Physics D: Applied Physics* 37:409.

Sun, Z., Zheng, H., Li, J., Du, P. (2015). Extraordinarily efficient photocatalytic hydrogen evolution in water using semiconductor nanorods integrated with crystalline Ni2P cocatalysts. *Energy & Environmental Science* 8:2668-2676.

Tahir, M. and Amin, N. S. (2015). Indium-doped TiO2 nanoparticles for photocatalytic CO2 reduction with H2O vapors to CH4. *Applied Catalysis B: Environmental* 162:98-109.

Talbot, E. L., Yang, L., Berson, A., Bain, C. D. (2014). Control of the Particle Distribution in Inkjet Printing through an Evaporation-Driven Sol–Gel Transition. *ACS Applied Materials & Interfaces* 6:9572-9583.

Talbot, L., Cheng, R. K., Schefer, R. W., Willis, D. R. (2006). Thermophoresis of particles in a heated boundary layer. *Journal of Fluid Mechanics* 101:737-758.

Talley, C. E., Jackson, J. B., Oubre, C., Grady, N. K., Hollars, C. W., Lane, S. M., Huser, T. R., Nordlander, P., Halas, N. J. (2005). Surface-Enhanced Raman Scattering from Individual Au Nanoparticles and Nanoparticle Dimer Substrates. *Nano Letters* 5:1569-1574.

Tan, L.-L., Ong, W.-J., Chai, S.-P., Goh, B. T., Mohamed, A. R. (2015). Visible-light-active oxygen-rich TiO2 decorated 2D graphene oxide with enhanced photocatalytic activity toward carbon dioxide reduction. *Applied Catalysis B: Environmental* 179:160-170.

Tao, X., Wu, R., Xia, Y., Huang, H., Chai, W., Feng, T., Gan, Y., Zhang, W. (2014). Biotemplated Fabrication of Sn@C Anode Materials Based on the Unique Metal Biosorption Behavior of Microalgae. *ACS Applied Materials & Interfaces* 6:3696-3702.

Temple, T. L. and Bagnall, D. M. (2011). Optical properties of gold and aluminium nanoparticles for silicon solar cell applications. *Journal of Applied Physics* 109:084343.

Tian, H., Xin, F., Wang, X., He, W., Han, W. (2015). High capacity group-IV elements (Si, Ge, Sn) based anodes for lithium-ion batteries. *Journal of Materiomics* 1:153-169.

Tran, P. D., Wong, L. H., Barber, J., Loo, J. S. C. (2012). Recent advances in hybrid photocatalysts for solar fuel production. *Energy & Environmental Science* 5:5902-5918.

Tsai, S. C., Cheng, C. H., Ning, W., Song, Y. L., Lee, C. T., Tsai, C. S. (2009). Silicon-based megahertz ultrasonic nozzles for production of monodisperse micrometer-sized

droplets. *Ultrasonics, Ferroelectrics and Frequency Control, IEEE Transactions on* 56:1968-1979.

Tsai, S. C., Song, Y. L., Tsai, C. S., Yang, C. C., Chiu, W. Y., Lin, H. M. (2004). Ultrasonic spray pyrolysis for nanoparticles synthesis. *Journal of Materials Science* 39:3647-3657.

Wang, K., Cai, R., Yuan, T., Yu, X., Ran, R., Shao, Z. (2009). Process investigation, electrochemical characterization and optimization of LiFePO4/C composite from mechanical activation using sucrose as carbon source. *Electrochimica Acta* 54:2861-2868.

Wang, Q., Hisatomi, T., Jia, Q., Tokudome, H., Zhong, M., Wang, C., Pan, Z., Takata, T., Nakabayashi, M., Shibata, N., Li, Y., Sharp, I. D., Kudo, A., Yamada, T., Domen, K. (2016). Scalable water splitting on particulate photocatalyst sheets with a solar-to-hydrogen energy conversion efficiency exceeding 1%. *Nature Materials* 15:611-615.

Wang, T., Chen, X., Lu, G.-Q., Lei, G.-Y. (2007a). Low-Temperature Sintering with Nano-Silver Paste in Die-Attached Interconnection. *Journal of Electronic Materials* 36:1333-1340.

Wang, W.-N., Park, J., Biswas, P. (2011). Rapid synthesis of nanostructured Cu-TiO2-SiO2 composites for CO2 photoreduction by evaporation driven self-assembly. *Catalysis Science & Technology* 1:593-600.

Wang, W.-N., Purwanto, A., Lenggoro, I. W., Okuyama, K., Chang, H., Jang, H. D. (2008). Investigation on the Correlations between Droplet and Particle Size Distribution in Ultrasonic Spray Pyrolysis. *Industrial & Engineering Chemistry Research* 47:1650-1659.

Wang, W.-N., Widiyastuti, W., Wuled Lenggoro, I., Oh Kim, T., Okuyama, K. (2007b). Photoluminescence Optimization of Luminescent Nanocomposites Fabricated by Spray Pyrolysis of a Colloid-Solution Precursor. *Journal of The Electrochemical Society* 154:J121-J128.

Winter, M. and Besenhard, J. O. (1999). Electrochemical lithiation of tin and tin-based intermetallics and composites. *Electrochim Acta* 45:31-50.

Wronski, C. R. M. (1967). The size dependence of the melting point of small particles of tin. *British Journal of Applied Physics* 18:1731.

Wu, C.-J., Sheng, Y.-J., Tsao, H.-K. (2016). Copper Conductive Lines on Flexible Substrates Fabricated at Room Temperature. *Journal of Materials Chemistry C* 4:3274-3280.

Wu, S. P., Gao, R. Y., Xu, L. H. (2009). Preparation of micron-sized flake copper powder for base-metal-electrode multi-layer ceramic capacitor. *Journal of Materials Processing Technology* 209:1129-1133.

Xia, B., Lenggoro, I. W., Okuyama, K. (2000). The roles of ammonia and ammonium bicarbonate in the preparation of nickel particles from nickel chloride. *Journal of Materials Research* 15:2157-2166.

Xia, B., Lenggoro, I. W., Okuyama, K. (2001a). Preparation of Ni particles by ultrasonic spray pyrolysis of NiCl2·6H2O precursor containing ammonia. *Journal of Materials Science* 36:1701-1705.

Xia, B., Lenggoro, I. W., Okuyama, K. (2001b). Preparation of Nickel Powders by Spray Pyrolysis of Nickel Formate. *Journal of the American Ceramic Society* 84:1425-1432.

Xie, Y., Liang, Y., Chen, D., Wu, X., Dai, L., Liu, Q. (2014). Vortical superlattices in a gold nanorods' self-assembled monolayer. *Nanoscale* 6:3064-3068.

Xu, Y., Liu, Q., Zhu, Y., Liu, Y., Langrock, A., Zachariah, M. R., Wang, C. (2013a). Uniform Nano-Sn/C Composite Anodes for Lithium Ion Batteries. *Nano Letters* 13:470-474.

Xu, Y. H., Liu, Q., Zhu, Y. J., Liu, Y. H., Langrock, A., Zachariah, M. R., Wang, C. S. (2013b). Uniform Nano-Sn/C Composite Anodes for Lithium Ion Batteries. *Nano Lett* 13:470-474.

Xu, Z., Lai, E., Shao-Horn, Y., Hamad-Schifferli, K. (2012). Compositional dependence of the stability of AuCu alloy nanoparticles. *Chemical Communications* 48:5626-5628.

Yamauchi, T., Tsukahara, Y., Sakata, T., Mori, H., Yanagida, T., Kawai, T., Wada, Y. (2010). Magnetic Cu-Ni (core-shell) nanoparticles in a one-pot reaction under microwave irradiation. *Nanoscale* 2:515-523.

Yan, Y., Ben, L. B., Zhan, Y. J., Huang, X. J. (2016). Nano-Sn embedded in expanded graphite as anode for lithium ion batteries with improved low temperature electrochemical performance. *Electrochim Acta* 187:186-192.

Yang, Y.-C., Huang, W.-Q., Xu, L., Hu, W., Peng, P., Huang, G.-F. (2017). Hybrid TiO2/graphene derivatives nanocomposites: is functionalized graphene better than pristine graphene for enhanced photocatalytic activity? *Catalysis Science & Technology* 7:1423-1432.

Yaws, C. L. (1995). Handbook of Vapor Pressure: Volume 4:: Inorganic Compounds and Elements. Gulf Professional Publishing.

Yaws, C. L. (1999). Chemical Properties Handbook. McGraw-Hill, New York.

Ye, T., Huang, W., Zeng, L., Li, M., Shi, J. (2017). CeO2-x platelet from monometallic cerium layered double hydroxides and its photocatalytic reduction of CO2. *Applied Catalysis B: Environmental* 210:141-148.

Yiwei, A., Yunxia, Y., Shuanglong, Y., Lihua, D., Guorong, C. (2007). Preparation of spherical silver particles for solar cell electronic paste with gelatin protection. *Materials Chemistry and Physics* 104:158-161.

Yonezawa, T., Tsukamoto, H., Matsubara, M. (2015a). Low-temperature nanoredox two-step sintering of gelatin nanoskin-stabilized submicrometer-sized copper fine particles for preparing highly conductive layers. *RSC Advances* 5:61290-61297.

Yonezawa, T., Uchida, Y., Tsukamoto, H. (2015b). X-ray diffraction and high-resolution TEM observations of biopolymer nanoskin-covered metallic copper fine particles: preparative conditions and surface oxidation states. *Physical Chemistry Chemical Physics* 17:32511-32516.

Yong, Y., Yonezawa, T., Matsubara, M., Tsukamoto, H. (2015). The Mechanism of Alkylamine-Stabilized Copper Fine Particles Towards Improving the Electrical Conductivity of Copper Films at Low Sintering Temperature. *Journal of Materials Chemistry C* 3:5890-5895.

Youn, D. H., Heller, A., Mullins, C. B. (2016). Simple Synthesis of Nanostructured Sn/Nitrogen-Doped Carbon Composite Using Nitrilotriacetic Acid as Lithium Ion Battery Anode. *Chemistry of Materials* 28:1343-1347.

Youngil, L., Jun-rak, C., Kwi Jong, L., Nathan, E. S., Donghoon, K. (2008). Large-scale synthesis of copper nanoparticles by chemically controlled reduction for applications of inkjet-printed electronics. *Nanotechnology* 19:415604.

Yuan, L., Wang, C., Cai, R., Wang, Y., Zhou, G. (2013). Spontaneous ZnO nanowire formation during oxidation of Cu-Zn alloy. *Journal of Applied Physics* 114:023512.

Yue, H., Zhao, Y., Ma, X., Gong, J. (2012). Ethylene Glycol: Properties, Synthesis, and Applications. *Chemical Society Reviews* 41:4218-4244.

Zerjav, G., Arshad, M. S., Djinovic, P., Junkar, I., Kovac, J., Zavasnik, J., Pintar, A. (2017). Improved electron-hole separation and migration in anatase TiO2 nanorod/reduced graphene oxide composites and their influence on photocatalytic performance. *Nanoscale* 9:4578-4592.

Zhang, N., Zhao, Q., Han, X., Yang, J., Chen, J. (2014a). Pitaya-like Sn@C nanocomposites as high-rate and long-life anode for lithium-ion batteries. *Nanoscale* 6:2827-2832.

Zhang, N., Zhao, Q., Han, X. P., Yang, J. G., Chen, J. (2014b). Pitaya-like Sn@C nanocomposites as high-rate and long-life anode for lithium-ion batteries. *Nanoscale* 6:2827-2832.

Zhang, W. M., Hu, J. S., Guo, Y. G., Zheng, S. F., Zhong, L. S., Song, W. G., Wan, L. J. (2008). Tin-nanoparticles encapsulated in elastic hollow carbon spheres for high-performance anode material in lithium-ion batteries. *Adv Mater* 20:1160-+.

Zhang, Y. J., Jiang, L., Wang, C. R. (2015). Preparation of a porous Sn@C nanocomposite as a high-performance anode material for lithium-ion batteries. *Nanoscale* 7:11940-11944.

Zhao, X., Zheng, B., Li, C., Gu, H. (1998). Acetate-derived ZnO ultrafine particles synthesized by spray pyrolysis. *Powder Technology* 100:20-23.

Zhong, K., Peabody, G., Blankenhorn, E., Glicksman, H., Ehrman, S. (2013a). A Spray Pyrolysis Approach for the Generation of Patchy Particles. *Aerosol Science and Technology* 47:i-v.

Zhong, K., Peabody, G., Blankenhorn, E., Glicksman, H., Ehrman, S. (2013b). Spray pyrolysis of phase pure AgCu particles using organic cosolvents. *Journal of Materials Research* 28:2753-2761.

Zhong, K., Peabody, G., Glicksman, H., Ehrman, S. (2012). Particle generation by cosolvent spray pyrolysis: Effects of ethanol and ethylene glycol. *Journal of Materials Research* 27:2540-2550.

Zhu, H. L., Jia, Z., Chen, Y. C., Weadock, N., Wan, J. Y., Vaaland, O., Han, X. G., Li, T., Hu, L. B. (2013). Tin Anode for Sodium-Ion Batteries Using Natural Wood Fiber as a Mechanical Buffer and Electrolyte Reservoir. *Nano Lett* 13:3093-3100.

Zhu, Y., Choi, S. H., Fan, X., Shin, J., Ma, Z., Zachariah, M. R., Choi, J. W., Wang, C. (2017). Recent Progress on Spray Pyrolysis for High Performance Electrode Materials in Lithium and Sodium Rechargeable Batteries. *Advanced Energy Materials* 7:1601578.

Zhu, Z., Wang, S., Du, J., Jin, Q., Zhang, T., Cheng, F., Chen, J. (2014a). Ultrasmall Sn Nanoparticles Embedded in Nitrogen-Doped Porous Carbon As High-Performance Anode for Lithium-Ion Batteries. *Nano Letters* 14:153-157.

Zhu, Z. Q., Wang, S. W., Du, J., Jin, Q., Zhang, T. R., Cheng, F. Y., Chen, J. (2014b). Ultrasmall Sn Nanoparticles Embedded in Nitrogen-Doped Porous Carbon As High-Performance Anode for Lithium-Ion Batteries. *Nano Lett* 14:153-157.

Conference presentations

1. **Oral presentation**, *Photoreduction of CO_2 by SnO_2/graphene oxide composite particles*, CATL 405, 254th ACS National Meeting in Washington, DC, August, 2017
2. **Oral presentation**, *A Novel Spray Process Integrates the Features of Spray Pyrolysis and Drying for Battery Material Generation*, NM6.9.02, 2016 MRS Fall Meeting, Boston, November-December, 2016
3. **Oral presentation**, *Investigation of the Oxidation Behavior of Cu/Sn and Cu/C Composite Particles Fabricated Via Spray Pyrolysis*, 197f, 2016 AIChE Annual Meeting, San Francisco, November, 2016
4. **Oral presentation**, *Copper (Cu) -Tin (Sn) Binary Particles Fabrication Via Spray Pyrolysis and Their Oxidation Behavior*, 14f, 2015 AIChE Annual Meeting, Salt Lake City, November, 2015

Selected publications related to this dissertation

1. **Y. Liang**, W. Wu, P. Wang, S-C. Liou, D. Liu, S. Ehrman, Scalable fabrication of SnO_2/eo-GO nanocomposites for CO_2 photoreduction to CH_4, *Nano Research*, 2018, DOI: 10.1007/s12274-018-1988-x
2. **Y. Liang**, H. Tian, J. Repac, S-C. Liou, W. Han, C. Wang, S. Ehrman, Colloidal spray pyrolysis: A new fabrication technology for nanostructured energy storage materials, *Energy Storage Materials*, 2018, 13, 8-18
3. **Y. Liang**, H. Hou, Y. Yang, H. Glicksman, S. Ehrman, Conductive One- and Two-Dimensional Structures Fabricated Using Oxidation-Resistant Cu-Sn Particles, *ACS Applied Materials & Interfaces*, 2017, 9, 34587–34591

4. **Y. Liang**, S. Oh, X. Wang, H. Glicksman, D. Liu, S. Ehrman, Oxidation-Resistant Micron-Sized Cu-Sn Solid Particles Fabricated by a One-Step and Scalable Method, *RSC Advances*, 2017, 7, 23468-23477

5. **Y. Liang**, R. Felix, H. Glicksman, S. Ehrman, Cu-Sn binary metal particle generation by spray pyrolysis, *Aerosol Science and Technology*, 2017, 51, 430-442